EUROPEAN ORGANIZATION FOR NUCLEAR RESEARCH (CERN)

CERN-EP-2023-197
2024/02/13

CMS-TOP-20-006

Differential cross section measurements for the production of top quark pairs and of additional jets using dilepton events from pp collisions at $\sqrt{s} = 13\,\text{TeV}$

The CMS Collaboration

Abstract

Differential cross sections for top quark pair ($\mathrm{t\bar{t}}$) production are measured in proton-proton collisions at a center-of-mass energy of 13 TeV using a sample of events containing two oppositely charged leptons. The data were recorded with the CMS detector at the CERN LHC and correspond to an integrated luminosity of 138 fb^{-1}. The differential cross sections are measured as functions of kinematic observables of the $\mathrm{t\bar{t}}$ system, the top quark and antiquark and their decay products, as well as of the number of additional jets in the event. The results are presented as functions of up to three variables and are corrected to the parton and particle levels. When compared to standard model predictions based on quantum chromodynamics at different levels of accuracy, it is found that the calculations do not always describe the observed data. The deviations are found to be largest for the multi-differential cross sections.

Submitted to the Journal of High Energy Physics

1 Introduction

Measurements of top quark pair ($t\bar{t}$) production play a crucial role in testing the validity of the standard model (SM) and in searching for new phenomena [1]. The large data set of proton-proton (pp) collisions delivered during Run 2 at the CERN LHC in the years 2016 through 2018 enables precision studies of $t\bar{t}$ differential production cross sections as functions of kinematic variables of various objects produced in the events. The differential measurements provide sensitivity to many new physics scenarios for which the $t\bar{t}$ event topologies and kinematical distributions are different from those in the SM. The present analysis focuses on events in the $t\bar{t}$ dilepton decay channel, shown in Fig. 1, where both W bosons decay into a charged lepton and a neutrino. Kinematic observables of the following objects are studied in the analysis: the $t\bar{t}$ system, the top quark (t) and antiquark ($\bar{t}$), the charged leptons (ℓ and $\bar{\ell}$) and bottom quarks (b and $\bar{b}$) produced in the decay chain, and the additional jets in the event. Electrons and muons produced directly in the W boson decays are considered as signal, while τ leptons are not. The bottom quarks are experimentally accessible through the associated b jets.

In the SM context, the measured cross sections can be used to check predictions of perturbative quantum chromodynamics (pQCD) and electroweak theory. During the last decade, a variety of next-to-next-to-leading order (NNLO) predictions [2–7] have become available for kinematic observables of the $t\bar{t}$ system, top quark and antiquark, and recently also of the final-state leptons and b jets [8]. The situation is different for $t\bar{t}$ events with additional energetic jets in the final state, which, at LHC energies, contribute a large fraction to the total $t\bar{t}$ cross section. The NNLO corrections are not yet established for these high multiplicity radiative processes; nevertheless, a comparison of the available pQCD models to data provides an important benchmark test.

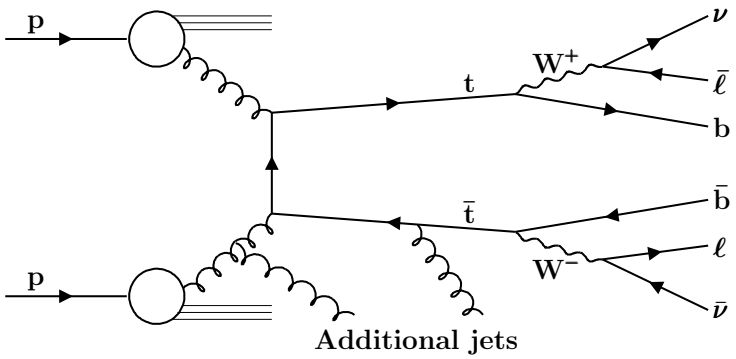

Figure 1: Illustration of a pp collision with $t\bar{t}$ plus additional jet production and subsequent dilepton decay of the $t\bar{t}$ system.

Differential cross sections for $t\bar{t}$ production have been measured previously in pp collisions at the LHC at $\sqrt{s} = 7\,\text{TeV}$ [9–13], 8 TeV [13–20], and 13 TeV [21–31], in the channels with either both, one, or neither of the W bosons emitted in the decays of t and $\bar{t}$ decaying leptonically. The nominal predictions of modern pQCD calculations generally fail to describe several kinematic distributions. For instance, most theoretical models predict a spectrum for the transverse momentum p_T of the top quark, that is harder than observed [25, 26].

We present measurements of differential $t\bar{t}$ cross sections in pp collisions at $\sqrt{s} = 13\,\text{TeV}$ using data taken with the CMS detector during the Run-2 operation of the LHC. The analysis is based on an integrated luminosity of 138 fb^{-1}, where 36.3 fb^{-1} were recorded in 2016, 41.5 fb^{-1} in 2017, and 59.7 fb^{-1} in 2018. The dilepton decay channel has a relatively small branching fraction and significantly lower background compared to other $t\bar{t}$ decay channels. As a consequence of the excellent lepton energy resolution, the precise measurement of kinematic

observables based on lepton pairs is unique to the dilepton channel. However, because of the presence of two neutrinos in the final state, the measurement of top quark kinematic observables in the dilepton channel requires specialized kinematic reconstruction techniques.

The analysis follows the procedures and strategies of Refs. [26, 27] for which only the 2016 data were used. All measurements are compared to predictions from Monte Carlo (MC) generators with next-to-leading order (NLO) accuracy in QCD at the matrix element level interfaced to parton shower simulations. Selected cross section measurements are also compared to a variety of predictions with precision beyond NLO.

The distributions studied in this paper are of basic kinematic observables including the p_{T}, and pseudorapidities η or rapidities y of single objects, e.g. $p_{\mathrm{T}}(\mathrm{t})$ and $y(\mathrm{t})$, or of compound systems, e.g. $p_{\mathrm{T}}(\mathrm{t\bar{t}})$ and $y(\mathrm{t\bar{t}})$. Distributions of invariant masses of compound objects are also investigated, e.g. $m(\mathrm{t\bar{t}})$, as well as the azimuthal or rapidity differences between two objects, e.g. $|\Delta\phi(\mathrm{t},\bar{\mathrm{t}})|$, $|y(\mathrm{t})| - |y(\bar{\mathrm{t}})|$, and $|\Delta\eta(\mathrm{t},\bar{\mathrm{t}})|$, where ϕ is the azimuthal angle in radians. Cross sections are measured at the particle level in a fiducial phase space that is close to that of the detector acceptance. In addition, we extract cross sections for kinematic observables of the top quark and antiquark and the $\mathrm{t\bar{t}}$ system defined at the parton level in the full phase space, which allows a comparison to a larger set of higher-order pQCD calculations. Both absolute and normalized differential cross sections are presented. The latter are obtained by dividing the former by the sum of the cross sections measured in the differential bins, leading to a reduction of systematic uncertainties. Cross sections are measured as functions of one kinematic variable (single-differential), or multi-differentially as functions of two or three variables (double- or triple-differential). The improvements of this analysis compared to Refs. [26, 27] fall into two categories:

1. Measurements are expanded by considering new kinematic observables, using refined binnings and extending the phase space range. An example of a new kinematic observable is the ratio $p_{\mathrm{T}}(\mathrm{t})/m(\mathrm{t\bar{t}})$, revealing interesting details of the $\mathrm{t\bar{t}}$ production dynamics. A finer binning and extended phase space range is used, in particular for the kinematic distributions of leptons and b jets. For measurements with additional jets in the events, a systematic survey of the correlations of the top quark and $\mathrm{t\bar{t}}$ kinematic variables with the number of additional jets in the events is performed in the dilepton channel for the first time.

2. The statistical and systematic uncertainties of the measurements are generally reduced by a factor of about two, the latter profiting from the following improvements: using refined procedures and algorithms, such as for identifying b jets and measuring their p_{T}; applying precise calibrations determined separately for each year of data taking, such as for the jet energy scale; having better estimates for some important background process contributions using in situ constraints from data; exploiting MC simulated samples with reduced statistical uncertainties to correct the data for detector effects and for assessing systematic uncertainties.

The paper is structured as follows: Section 2 provides a brief description of the CMS detector. Details of the event simulation are given in Section 3. The event selection is detailed in Section 4, followed by a description of the kinematic reconstruction in Section 5 where comparisons between data and simulations are shown. The signal extraction and unfolding procedure are explained in Section 6, together with the definitions of the parton and particle level phase spaces. The method to extract the differential cross sections is discussed in Section 7, and the

assessment of the systematic uncertainties is presented in Section 8. Results and comparisons to theoretical predictions are shown in Section 9. Finally, Section 10 provides a summary. Tabulated results can be found in HEPData [32].

2 The CMS detector

The central feature of the CMS apparatus is a superconducting solenoid of 6 m internal diameter, providing a magnetic field of 3.8 T. Within the solenoid volume are a silicon pixel and strip tracker, a lead tungstate crystal electromagnetic calorimeter (ECAL), and a brass and scintillator hadron calorimeter (HCAL), each composed of a barrel and two endcap sections. Forward calorimeters extend the η coverage provided by the barrel and endcap detectors. Muons are measured in gas-ionization detectors embedded in the steel flux-return yoke outside the solenoid. Events of interest are selected using a two-tiered trigger system [33]. The first level (L1), composed of custom hardware processors, uses information from the calorimeters and muon detectors to select events at a rate of around 100 kHz within a time interval of less than 4 μs. The second level, known as the high-level trigger (HLT), consists of a farm of processors running a version of the full event reconstruction software optimized for fast processing, and reduces the event rate to around 1 kHz before data storage. A more detailed description of the CMS detector, together with a definition of the coordinate system used and the relevant kinematic variables, can be found in Ref. [34].

3 Event simulation

Simulations of physics processes are performed with MC event generators for three main purposes. First, to obtain representative predictions of $\mathrm{t\bar{t}}$ production cross sections to be compared to the measurements. Second, to determine corrections for the effects of hadronization, reconstruction, and selection efficiencies, as well as resolutions. These corrections are obtained by passing generated $\mathrm{t\bar{t}}$ signal events through a detector simulation, and are applied for the unfolding of the data. Last, to obtain predictions for the backgrounds by passing generated background events through the detector simulation. All MC programs used in this analysis perform the event generation in several stages: matrix element (ME) level, parton showering matched to ME, hadronization, and the underlying event (UE), including multi-parton interactions (MPIs). For all simulations, the proton structure is described by the NNPDF3.1 NNLO set [35, 36] of parton distribution functions (PDFs), unless stated otherwise. For all simulations with top quark production, the value of the top quark mass parameter is fixed to $m_{\mathrm{t}}^{\mathrm{MC}} = 172.5\,\mathrm{GeV}$. The $\mathrm{t\bar{t}}$ signal process is simulated with ME calculations at NLO in QCD. For the nominal signal simulation, the POWHEG (version 2) [37–40] generator is taken. The h_{damp} parameter of POWHEG, which regulates the damping of real emissions in the NLO calculation when matching to the parton shower, is set to $h_{\mathrm{damp}} = 1.379\, m_{\mathrm{t}}^{\mathrm{MC}}$ [41]. The PYTHIA program (version 8.230) [42] with the CP5 tune [41] is used to model parton showering, hadronization, and the UE. This setup, referred to as POWHEG+PYTHIA8, is used for the detector corrections of the $\mathrm{t\bar{t}}$ signal process in the data, with appropriate variations for assessing the theoretical model uncertainties, described in Section 8.2. The generator-level cross sections of POWHEG+PYTHIA8 are also used as theoretical predictions that are compared in Section 9 to the measured $\mathrm{t\bar{t}}$ cross sections, as well as the predictions from two other models. The first alternative model is based on the MADGRAPH5_aMC@NLO (version 2.4.2) [43] generator, interfaced with PYTHIA using the CP5 tune. At the ME level, up to two extra partons are included at NLO. The events are matched to PYTHIA using the FxFx prescription [44], and MADSPIN [45] is used to model the decays of the top quarks, while preserving their spin correlation. The whole setup is referred

to as MG5_aMC@NLO[FxFx]+PYTHIA 8. The second alternative model is POWHEG interfaced to HERWIG 7 [46] using the CH3 tune [47] and is referred to as POWHEG+HERWIG7.

The main background contributions originate from single top quarks produced in association with a W boson (tW), Z/γ^* bosons produced with additional jets (Z+jets), W boson production with additional jets (W+jets), and diboson (WW, WZ, and ZZ) events. Other backgrounds are negligible.

For all background samples, parton showering, hadronization, and the UE are simulated with PYTHIA. For single top quark production, the *t*-channel and tW processes are simulated at NLO with POWHEG [48–50], and the *s*-channel process at LO with MADGRAPH5_aMC@NLO. In all three cases the PYTHIA 8 CP5 tune is used. For all other background samples discussed in the following, the CP5 tune is applied for the 2017 and 2018 samples, and the CUETP8M1 tune [51–53] for the 2016 samples. For the latter, the PDF set NNPDF3.0 [54] is used with the order (e.g. NLO) of the respective simulation. The Z+jets process is simulated at NLO using MG5_aMC@NLO[FxFx]with up to two additional partons at the ME level. The W+jets process is simulated at leading order (LO) using MADGRAPH5_aMC@NLO with up to four additional partons at the ME level and matched to PYTHIA using the MLM prescription [55, 56]. Diboson events are simulated at LO with PYTHIA.

Predictions are normalized based on their inclusive theoretical cross sections and the integrated luminosity of the data sample. For *s*- and *t*-channel single top quark production, the cross sections are calculated at NLO with HATHOR (version 2.1) [57]. For single top quark production in the tW channel, the approximate NNLO calculations from Ref. [58] are used. For Z+jets and W+jets processes, NNLO predictions obtained with FEWZ [59] are taken, and for diboson production the NLO calculations from Ref. [60] are applied. The $t\bar{t}$ simulation is normalized to a cross section of $831\,^{+20}_{-30}\,(\text{scale}) \pm 4\,(\text{PDF} + \alpha_s)$ pb calculated with the TOP++ (version 2.0) program [61] at NNLO, including resummation of next-to-next-to-leading logarithm (NNLL) soft-gluon terms [62–67], and assuming a top quark pole mass of 172.5 GeV.

The CMS detector response is simulated using GEANT4 [68]. The effect of additional pp interactions within the same or nearby bunch crossings (pileup) is taken into account by adding simulated minimum-bias interactions to the simulated data. Events in the simulation are then weighted to reproduce the pileup distribution in the data, which is estimated from the measured bunch-to-bunch instantaneous luminosity and assuming a total inelastic pp cross section of 69.2 mb [69]. Separate simulations are employed for the data taken in the three years 2016–2018, in order to match the varying detector performance and data-taking conditions. At every step of the analysis, the simulated samples from different years are added together and used as one single sample, both at the detector and the generator levels.

Correction factors described in Sections 6 and 8, subsequently referred to as scale factors, are used to reconcile the number of expected events from simulation with what is observed in data. They are applied, for example, to correct a detector efficiency in the simulation to match the one observed in data, or to scale a background prediction.

4 Event selection

The event selection closely follows that of Ref. [26]. Events are selected corresponding to the decay chain where both top quarks decay into a W boson and a bottom quark, and each of the W bosons decays directly into an electron or a muon and a neutrino. This specification defines the signal process, while all other $t\bar{t}$ events, including those with at least one electron or muon

originating from the decay of a τ lepton, are treated as background which is taken into account, as detailed in Section 6. The signal includes three distinct channels: two same-flavor channels corresponding to two electrons (e^+e^-) or two muons ($\mu^+\mu^-$), and the different-flavor channel corresponding to one electron and one muon ($e^\pm\mu^\mp$). Results are obtained by combining the three channels and adding, at every step of the analysis, the samples from the years 2016–2018.

At the HLT level, events are selected either by single-lepton or dilepton triggers. The former require the presence of at least one electron or muon, and the latter the presence of either two electrons, two muons, or an electron and a muon. For all employed triggers, the leptons are required to fulfill isolation criteria that are looser than those applied later in the offline analysis. For the single-electron triggers, a p_T threshold of 27 (32) GeV is applied in 2016 (2017–2018), while for single-muon triggers the p_T threshold is 24 (27) GeV in 2016/2018 (2017). The dilepton triggers select events based on the leptons with the highest (leading) and second-highest (trailing) p_T in the event. The same-flavor dilepton triggers require either an electron pair with $p_T > 23$ (12) GeV for the leading (trailing) electron or a muon pair with $p_T > 17$ (8) GeV for the leading (trailing) muon. The different-flavor dilepton triggers require either an electron with $p_T > 23$ GeV and a muon with $p_T > 8$ GeV, or a muon with $p_T > 23$ GeV and an electron with $p_T > 12$ GeV. The analysis mainly relies on the dilepton triggers, while the single-lepton triggers help to improve the overall trigger efficiency by about 10%.

The particle-flow (PF) algorithm [70] aims to reconstruct and identify each individual particle with an optimized combination of information from the various elements of the CMS detector. The energy of muons is obtained from the curvature of the corresponding track. The energy of electrons is inferred from a combination of the electron momentum at the primary interaction vertex as determined by the tracker, the energy of the corresponding ECAL cluster, and the energy sum of all bremsstrahlung photons spatially compatible with originating from the electron track. The energy of photons is directly obtained from the ECAL measurement. The energy of charged hadrons is determined from a combination of their momentum measured in the tracker and the matching ECAL and HCAL energy deposits, corrected for the response function of the calorimeters to hadronic showers. Finally, the energy of neutral hadrons is obtained from the corresponding corrected ECAL and HCAL energies.

The measurements presented in this paper depend on the reconstruction and identification of electrons, muons, jets, and missing transverse momentum $\vec{p}_T^{\,\text{miss}}$ associated with neutrinos. Electrons and muons are selected if they are compatible with originating from the primary pp interaction vertex. The primary vertex (PV) is taken to be the vertex corresponding to the hardest scattering in the event, evaluated using tracking information alone, as described in Section 9.4.1 of Ref. [71].

For both electrons and muons, the "tight" identification criteria as described in Refs. [72, 73] are applied. Reconstructed electrons [72] are required to have $p_T > 25$ (20) GeV for the leading (trailing) candidate and $|\eta| < 2.4$. Electron candidates with ECAL clusters in the transition region between the ECAL barrel and endcap, $1.44 < |\eta_{\text{cluster}}| < 1.57$, are excluded since the reconstruction of an electron object in this region is not optimal. A relative isolation I_{rel} is defined as the p_T sum of all neutral and charged hadrons, and photon candidates within a distance of 0.3 from the electron in η-ϕ space, divided by the p_T of the electron candidate. A maximum value of I_{rel} is allowed, in the range 0.05–0.10, depending on the p_T and η of the electron candidate. Further electron identification requirements are applied to reject misidentified electron candidates and candidates originating from photon conversions. Reconstructed muons [73] are required to have $p_T > 25$ (20) GeV for the leading (trailing) candidate and $|\eta| < 2.4$. An isolation requirement of $I_{\text{rel}} < 0.15$ is applied, including particles within a distance of 0.4 in η-

ϕ space from the muon candidate. Furthermore, muon identification requirements are applied to reject misidentified muon candidates and muons originating from in-flight decays. For both electron and muon candidates, I_{rel} is corrected for residual pileup effects. Finally, for the targeted prompt leptons in the $\mathrm{t\bar{t}}$ dilepton decay channel, the total selection efficiencies are about 90% for muons and 70% for electrons.

Jets are reconstructed by clustering the PF candidates using the anti-k_{T} jet algorithm [74, 75] with a distance parameter of 0.4. The jet energies are corrected following the procedures described in Ref. [76]. After correcting for all residual energy deposits from charged and neutral particles from pileup, p_{T}- and η-dependent jet energy adjustments are applied to correct for the detector response. Jets are required to have $p_{\mathrm{T}} > 30\,\text{GeV}$ and $|\eta| < 2.4$ and a distance in η-ϕ space of at least 0.4 to the closest selected lepton.

The b jets are identified with the deep neural network algorithm DEEPCSV [77], based on tracking and secondary vertex information. The chosen working point of the network discriminator has a b-jet tagging efficiency of $\approx$80–90% and a mistagging efficiency of $\approx$1% for jets originating from gluons, as well as u, d, or s quarks, and $\approx$30–40% for jets originating from c quarks. The energy measurement of the b-tagged jets is improved using a deep neural network estimator [78] that performs a regression after all other jet energy corrections have been applied.

The $\vec{p}_{\mathrm{T}}^{\,\text{miss}}$ is computed as the negative vector sum of the transverse momenta of all the PF candidates in an event, and its magnitude is denoted as $p_{\mathrm{T}}^{\text{miss}}$ [79]. The $\vec{p}_{\mathrm{T}}^{\,\text{miss}}$ is updated when accounting for corrections to the energy scale of reconstructed jets in the event. The pileup per particle identification algorithm [80] is applied to reduce the pileup dependence of the $\vec{p}_{\mathrm{T}}^{\,\text{miss}}$ observable. The $\vec{p}_{\mathrm{T}}^{\,\text{miss}}$ is computed from the PF candidates weighted by their probability to originate from the primary interaction vertex [79].

Events are selected offline if they contain exactly two isolated, oppositely charged electrons or muons, ($\mathrm{e^+e^-}$, $\mu^+\mu^-$, $\mathrm{e^\pm}\mu^\mp$) and at least two jets, with at least one of these jets being b tagged. Events with an invariant mass of the lepton pair $m(\ell\bar{\ell})$ below 20 GeV are removed in order to suppress contributions from resonance decays and low-mass Drell–Yan processes. Backgrounds from Z+jets processes in the $\mathrm{e^+e^-}$ and $\mu^+\mu^-$ channels are further reduced by requiring $m(\ell\bar{\ell}) < 76\,\text{GeV}$ or $m(\ell\bar{\ell}) > 106\,\text{GeV}$, and $p_{\mathrm{T}}^{\text{miss}} > 40\,\text{GeV}$.

In this analysis, the $\mathrm{t\bar{t}}$ production cross section is also measured as a function of the extra jet multiplicity N_{jet}. Extra jets (also referred to as additional jets) are jets arising primarily from hard QCD radiation and not from the top quark decays. At the reconstruction level, the extra jets are defined in dilepton $\mathrm{t\bar{t}}$ candidate events as jets with $p_{\mathrm{T}} > 40\,\text{GeV}$ and $|\eta| < 2.4$ that are isolated from the leptons and from the b jets originating from the top quark decays. The extra jet is considered isolated when having a distance to the leptons in η-ϕ space of at least 0.4, and a distance to each b jet of at least 0.8. The requirements on p_{T} and isolation of extra jets largely eliminate the expected contributions from gluons radiated off b quarks produced in the top quark decays.

5 Kinematic reconstruction of the $\mathrm{t\bar{t}}$ system

The four-momenta of the top quark and antiquark are determined from the four-momenta of their decay products using a kinematic reconstruction method referred to as the "full kinematic reconstruction" [14]. In this reconstruction, the two pairs consisting of a lepton and a b jet from the decay are identified, and the top quark (antiquark) is associated with the pair containing

the lepton with positive (negative) charge. The three-momenta of the neutrino (ν) and antineutrino ($\overline{\nu}$) are reconstructed using algebraic equations deduced from the following six kinematic constraints: the conservation of the total p_{T} in the event, and the masses of the W bosons and of the top quark and antiquark. The mass values used in the constraints are 172.5 GeV for the top quark and antiquark, and 80.4 GeV for the W bosons. The $\vec{p}_{\mathrm{T}}^{\,\mathrm{miss}}$ in the event is assumed to originate solely from the two neutrinos. An ambiguity can arise due to multiple algebraic solutions of the constraint equations for the neutrino momenta, which is resolved by taking the solution with the smallest invariant mass of the $\mathrm{t\bar{t}}$ system [81]. The reconstruction is performed 100 times. Each time, the measured energies and directions of the reconstructed leptons and jets are randomly smeared in accordance with their resolutions. This procedure recovers events that initially yield no solution because of measurement fluctuations. The three-momenta of the two neutrinos are determined as a weighted average over all smeared solutions. For each solution, the weight is calculated based on the expected true spectrum of the invariant mass of the lepton and the b jet originating from the decay of a top quark $m(\ell\mathrm{b})$ and taking the product of the two weights for the top quark and antiquark decay chains. All possible lepton-jet combinations in the event that satisfy the requirement $m(\ell\mathrm{b}) < 180\,\mathrm{GeV}$ are considered. Combinations are ranked based on the presence of b-tagged jets in the assignments, i.e. a combination with both leptons assigned to b-tagged jets is preferred over those with one or no b-tagged jet. Among assignments with an equal number of b-tagged jets, the one with the highest sum of weights is taken. Events with no solution after smearing are rejected. The efficiency of the full kinematic reconstruction is defined as the number of events for which a solution is found divided by the total number of selected $\mathrm{t\bar{t}}$ events after the full event selection described in Section 4. Consistent results are observed in data and simulation. The efficiency for signal events is about 90%. After applying the complete event selection and the full kinematic reconstruction, about 1.2 million events are observed, with shares of 56, 14, and 30% for the $\mathrm{e}^{\pm}\mu^{\mp}$, $\mathrm{e}^{+}\mathrm{e}^{-}$, and $\mu^{+}\mu^{-}$ channels, respectively. Combining all decay channels, the estimated signal fraction in data is about 80%.

Distributions of the reconstructed top quark and $\mathrm{t\bar{t}}$ kinematic variables, obtained with the full kinematic reconstruction, are shown in Fig. 2 and the upper plots in Fig. 3. Furthermore, the multiplicity of jets in the events is presented in Fig. 2. The $p_{\mathrm{T}}(\mathrm{t})$ and $y(\mathrm{t})$ spectra include contributions from both the top quark and antiquark. The expected signal and background contributions are estimated as described in Section 6, using the MC simulations for the various processes introduced in Section 3. The expected events labeled as "Minor bg" constitute minor background contributions from diboson and W+jets processes. In general, the data are reasonably well described by the simulation that overestimates, however, the total number of events by about 5%. Some trends are visible, in particular for $p_{\mathrm{T}}(\mathrm{t})$, where the simulation predicts a somewhat harder spectrum than that observed in data, as seen in previous differential $\mathrm{t\bar{t}}$ cross section measurements [14, 17, 19, 21, 24–26].

The $m(\mathrm{t\bar{t}})$ value obtained using the full kinematic reconstruction described above is sensitive to the value of the top quark mass used as a kinematic constraint. An alternative algorithm is employed that reconstructs the $\mathrm{t\bar{t}}$ kinematic variables without using the top quark mass constraint. This algorithm is referred to as the "loose kinematic reconstruction". It is used in this analysis for measuring differential $\mathrm{t\bar{t}}$ cross sections as a function of $m(\mathrm{t\bar{t}})$, in order to preserve the sensitivity of the data for a future top quark mass extraction, as performed in Ref. [27]. In contrast to the full kinematic reconstruction, this algorithm tackles the reconstruction of the $\nu\overline{\nu}$ system as a whole. The ℓb pairs are selected and ranked as described for the full kinematic reconstruction. Among combinations with equal number of b-tagged jets, the ones with the leading and trailing p_{T} jets are chosen. The kinematic variables of the $\nu\overline{\nu}$ system are obtained

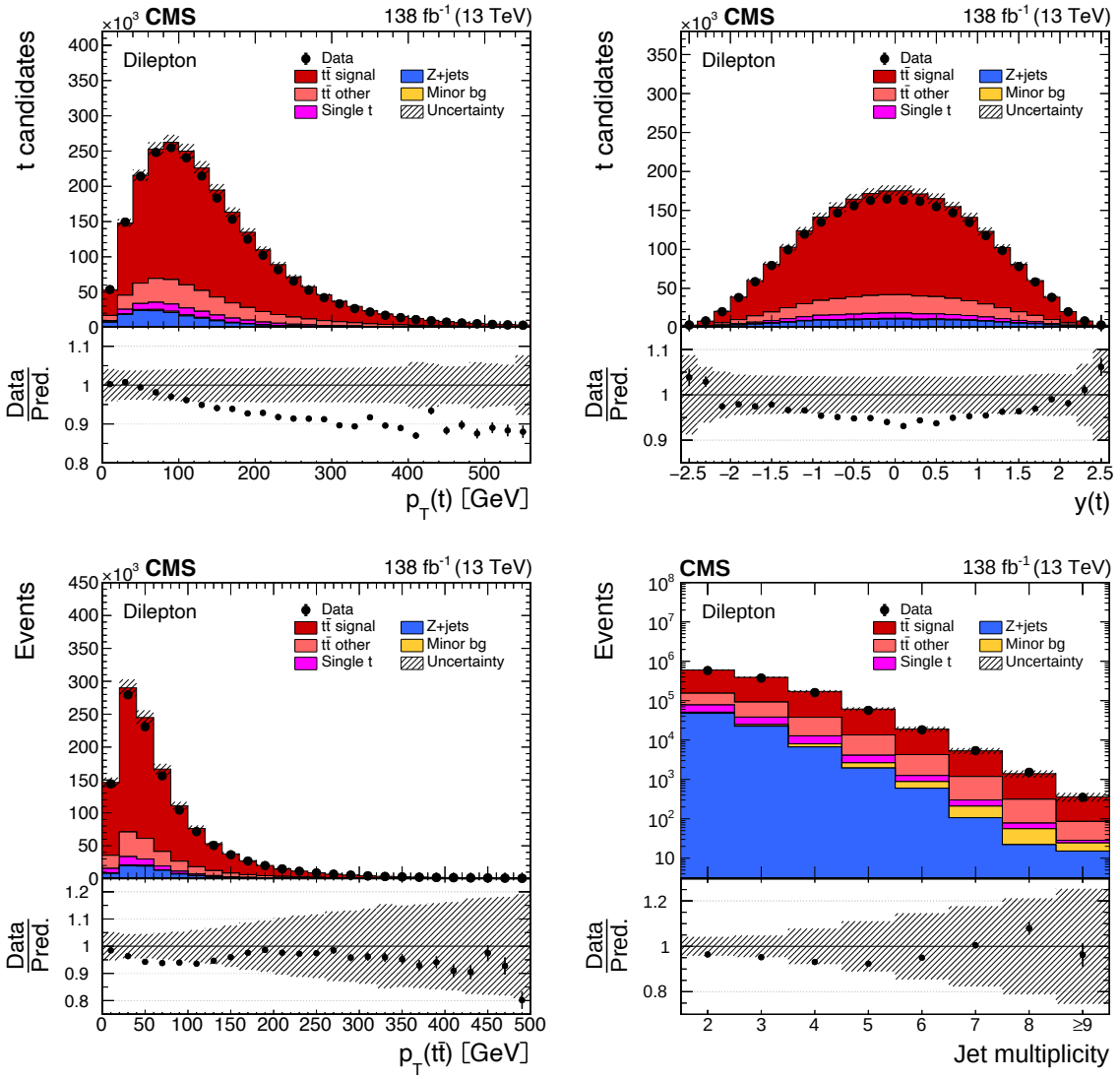

Figure 2: Distributions of $p_{\mathrm{T}}(\mathrm{t})$ (upper left), $y(\mathrm{t})$ (upper right), $p_{\mathrm{T}}(\mathrm{t\bar{t}})$ (lower left), and jet multiplicity (lower right) obtained in selected events with the full kinematic reconstruction. For the first two distributions, "t" refers to both top quark and antiquark. The three dilepton channels ($\mathrm{e^+e^-}$, $\mu^+\mu^-$, and $\mathrm{e^\pm}\mu^\mp$) are added together. The data with vertical bars corresponding to their statistical uncertainties are plotted together with distributions of simulated signal and background processes. The hatched regions depict the systematic shape uncertainties in the signal and backgrounds (as detailed in Section 8). The lower panel in each plot shows the ratio of the observed data event yields to those expected in the simulation.

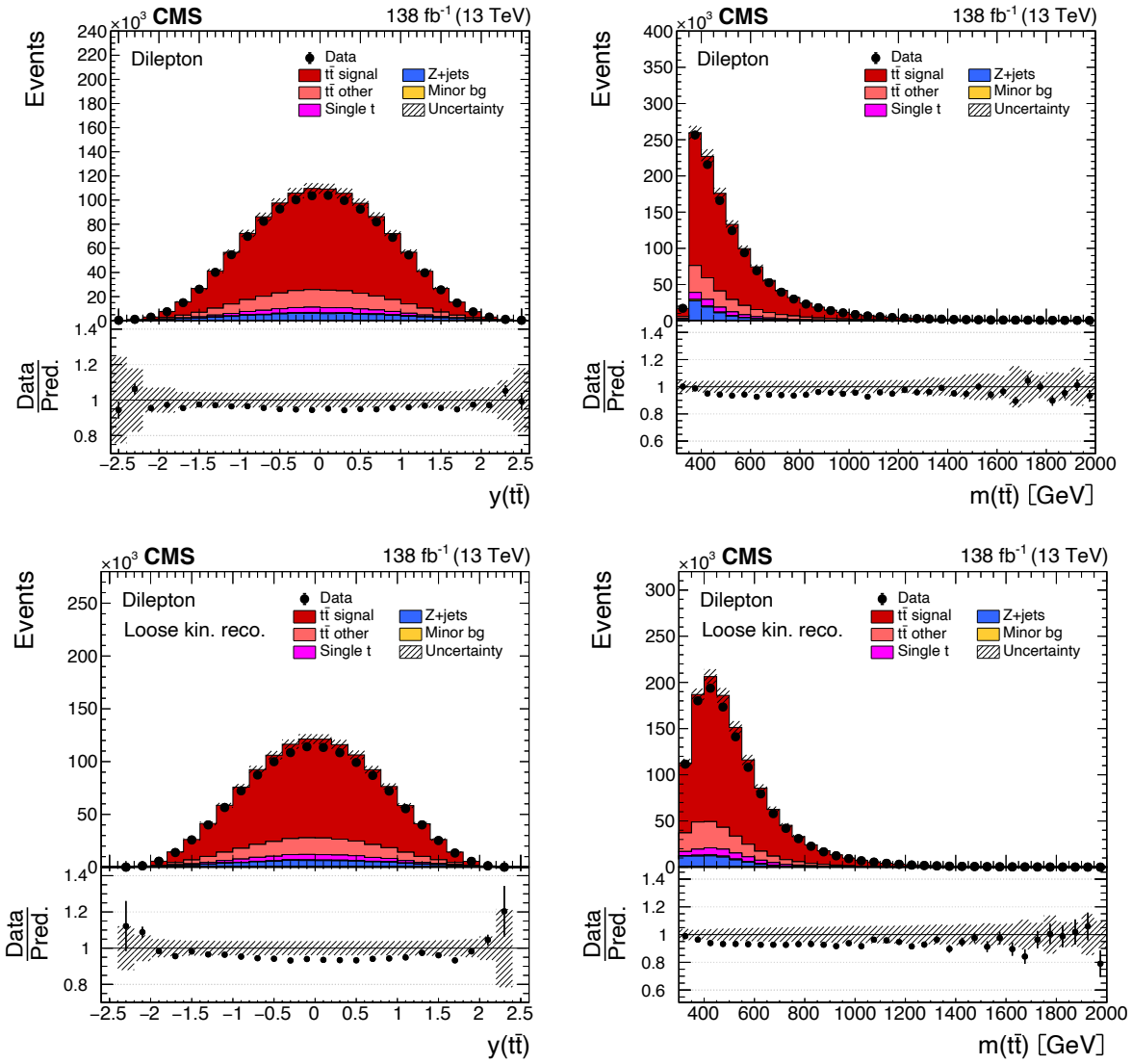

Figure 3: Distributions of $y(\mathrm{t\bar{t}})$ (left) and $m(\mathrm{t\bar{t}})$ (right) obtained in selected events with the full (upper) and the loose kinematic reconstruction (lower). Further details can be found in the caption of Fig. 2.

as follows: its $\vec{p}_{\mathrm{T}}$ is set equal to $\vec{p}_{\mathrm{T}}^{\,\mathrm{miss}}$ and its unknown longitudinal momentum and energy are set equal to the values of the lepton pair. Additional constraints are applied on the invariant mass of the neutrino pair, $m(\nu\bar{\nu}) \geq 0$, and on the invariant mass of the W bosons, $m(\mathrm{W^+W^-}) \geq 2m_{\mathrm{W}}$. These constraints have only minor impact on the performance of the reconstruction. This method yields $\mathrm{t\bar{t}}$ kinematic resolutions and reconstruction efficiency similar to those of the full kinematic reconstruction. As in the case of the full kinematic reconstruction, events with no valid solution for the loose kinematic reconstruction are excluded from further analysis. The presence of a solution for the full kinematic reconstruction in an event is also required for the cross section measurements as functions of lepton and b jet kinematic variables discussed in Section 9.2. Figure 3 (lower row) displays the distributions of the reconstructed $\mathrm{t\bar{t}}$ invariant mass and rapidity using the loose kinematic reconstruction. These distributions are similar to the ones obtained with the full kinematic reconstruction, shown in the upper row, except for $m(\mathrm{t\bar{t}})$ in the threshold region that is smeared out due the omission of the top quark mass constraint.

The loose kinematic reconstruction is used for a subset of measurements presented in Section 9, namely, for single-differential cross sections as functions of $m(\mathrm{t\bar{t}})$, and for all multi-differential cross sections composed of combinations of $m(\mathrm{t\bar{t}})$ with $p_{\mathrm{T}}(\mathrm{t\bar{t}})$, $y(\mathrm{t\bar{t}})$, or N_{jet}. For all other cross sections as functions of kinematic observables of the $\mathrm{t\bar{t}}$ system or of the top quark and antiquark, the full kinematic reconstruction is used.

6 Signal extraction and unfolding

The number of signal events is obtained for each histogram bin by subtracting the expected number of background events from the observed number of events.

The expected background contribution from single top quark, W+jets, and diboson processes are taken directly from the MC simulations. The Z+jets contribution is also estimated from the MC simulation, but corrected by global normalization scale factors, which are determined from a binned template fit to the data, using the method described in Ref. [82], as implemented in the TFRACTIONFITTER class in ROOT [83]. In this procedure, the event fraction of Z+jets process and of the sum of all other contributions are fitted to the $m(\ell\bar{\ell})$ distributions in the data, within the Z boson peak signal region $76 < m(\ell\bar{\ell}) < 106\,\mathrm{GeV}$. The template distributions are obtained from the MC-simulated samples. Separate normalization scale factors are fitted for the simulations of the Z+jets process in the $\mathrm{e^+e^-}$ and $\mu^+\mu^-$ channels and the scale factor for the $\mathrm{e^\pm}\mu^\mp$ channel is calculated as the geometric mean of these factors. The nominal scale factors are determined for a data selection with relaxed requirements, omitting those on $p_{\mathrm{T}}^{\mathrm{miss}}$, the number of b-tagged jets, and the presence of a solution for the kinematic reconstruction, in order to have a clean sample of Z+jets events. The scale factors are compatible, within a few percent, with unity. The $m(\ell\bar{\ell})$ window chosen for the fits ensures that there is no overlap with the sample used for the analysis and is still large enough to provide a good separation of Z+jets from the other processes. As a cross-check, the template fits are performed over a wider $m(\ell\bar{\ell})$ range, starting at 20 GeV and extending to values much above the Z boson peak signal region, and only small scale factor variations are observed of the order of one percent.

After the subtraction of non-$\mathrm{t\bar{t}}$ backgrounds, the resulting event yields are corrected for the contributions from $\mathrm{t\bar{t}}$ final states other than the signal, dominated by events with one or both of the W bosons decaying into τ leptons with subsequent decay into electrons or muons. These events arise from the same $\mathrm{t\bar{t}}$ production process as the signal and thus the normalization of this background is fixed to that of the signal. For each bin, the number of events obtained after the subtraction of all other background sources is multiplied by the ratio of the number of selected $\mathrm{t\bar{t}}$ signal events to the total number of selected $\mathrm{t\bar{t}}$ events (i.e. the signal and all other $\mathrm{t\bar{t}}$ events) in simulation.

The numbers of signal events are obtained by adding together the event yields in the $\mathrm{e^+e^-}$, $\mu^+\mu^-$, and $\mathrm{e^\pm}\mu^\mp$ channels, subtracting the background, and correcting for detector effects using the TUNFOLD package [84]. The addition of the three channels before applying detector corrections is justified by the fact that background levels are small in all channels and kinematic resolutions are comparable. The measurements in the separate channels yield consistent results.

In the unfolding procedure the response matrix plays an important role. An element of this matrix specifies the probability for an event originating from one bin of the true distribution to be observed in a specific bin of the reconstructed observables. The response matrix models the effects of acceptance, detector efficiencies, and resolutions in a given phase space. It is calculated for each measured distribution using the $\mathrm{t\bar{t}}$ signal simulation, and is defined either at

the particle level in a fiducial phase space or at the parton level in the full phase space, using the corresponding generator-level definitions discussed in Section 6.1. At the detector level, the number of bins used per kinematic variable is typically two times larger than the number of bins used at the generator level. In TUNFOLD, the distribution of unfolded event numbers is extracted from the measured distribution at the detector level by performing a χ^2 fit. An additional χ^2 term is included representing Tikhonov regularization [85], based on second-order derivatives and using the nominal $\mathrm{t\bar{t}}$ simulation as the bias vector. The regularization reduces unphysically large high-frequency components of the unfolded spectrum. The regularization strength that minimizes the global correlation coefficient [86] is chosen.

6.1 Generator-level definitions

The definitions of the generator level that are used in the construction of the response matrices follow, to a large extent, those applied in Refs. [26, 27, 87].

For the parton-level results, the momenta of the parton-level top quarks are defined after QCD radiation, but before the top quark decays. The unfolded signal event numbers are corrected for the branching fractions $\mathrm{W} \to \ell\nu$. The parton-level results are extrapolated to the full phase space using the default $\mathrm{t\bar{t}}$ simulation. The extrapolation is implicitly performed by counting each simulated event in the response matrix that enters a specific parton-level bin of a differential cross section.

For the particle-level results, the generator-level objects are defined by the stable particles (i.e. those with lifetime $\tau > 0.3 \times 10^{-10}$ s) in the simulation. The selection of these objects is intended to match as closely as possible the detector-level requirements used to select $\mathrm{t\bar{t}}$ events. It is described together with the generator-level top quark kinematic reconstruction procedure in Refs. [26, 87], and is summarized below.

- All simulated electrons and muons, including those from τ lepton decays, but not originating from the decay of a hadron, are corrected ("dressed") for bremsstrahlung effects by adding the momentum of a photon to that of the closest lepton if their separation in η-ϕ space is < 0.1. Leptons are required to have $p_{\mathrm{T}} > 20\,\mathrm{GeV}$ and $|\eta| < 2.4$.
- Only neutrinos originating from nonhadronic decays (i.e. prompt neutrinos) are used.
- Jets are clustered using the anti-k_{T} jet algorithm [74, 75] with a distance parameter of 0.4. All stable particles, with the exception of the dressed leptons and prompt neutrinos, are clustered. Jets with $p_{\mathrm{T}} > 30\,\mathrm{GeV}$ and $|\eta| < 2.4$ are selected if there is no electron or muon, as defined above, within a distance of 0.4 in η-ϕ space.
- b jets are defined as those jets that contain a b hadron using the ghost-matching technique [88]: as a result of the short lifetime of b hadrons, only their decay products are considered for the jet clustering. However, to allow their association with a jet, the b hadrons are also included with their momenta scaled down to a negligible value. This preserves the information of their directions, but removes their impact on the jet clustering.
- The following additional event-level requirements are applied to define the fiducial phase space region in which the particle-level cross sections are measured: we require that the W bosons produced from decays of the top quark and antiquark in a $\mathrm{t\bar{t}}$ event themselves decay to an electron or a muon; we reject events where these W bosons decay to τ leptons; we require exactly two selected lepton candidates with

opposite charges, $m(\ell\bar{\ell}) > 20\,\text{GeV}$, and at least two b jets.

- The top quark reconstruction at the particle level proceeds as follows. Prompt neutrinos are combined with the dressed leptons to form W boson candidates. We take the permutation of neutrinos and leptons that minimizes the sum of the absolute values of the differences between the mass of each neutrino-lepton pair and the nominal W boson mass of 80.4 GeV. Subsequently, the W boson candidates are combined with b jets to form particle-level top quark candidates by minimizing the sum of the absolute values of the differences between the mass of each pair and the nominal top quark mass of 172.5 GeV.

Due to the finite detector resolution, events that are outside the fiducial phase space region at the generator level can be measured inside the accepted region at the detector level. These events are subtracted, before the unfolding, by a fractional correction of the observed number of events after subtracting all other backgrounds. The correction, performed separately for each detector-level bin, is defined as the number of events in the $\mathrm{t\bar{t}}$ signal simulation that pass both the detector- and particle-level selection criteria, divided by the number of all events fulfilling the detector-level requirements.

When measuring the differential cross sections as functions of N_{jet} (see Section 9.3), the top quark and antiquark are measured either at the parton level in the full phase space or at the particle level in a fiducial phase space, as described above, while the additional jets are measured at the particle level only. The definition of these extra jets differs slightly from the one given above: they have to be isolated from the charged leptons (e or μ) and b quarks originating from the top quark decays, as represented by the corresponding particle level leptons and b jets, with a minimal distance to these leptons (b quarks) of 0.4 (0.8) in η-ϕ space. The larger distance to the b quarks is required to avoid selecting jets coming from gluon radiation from the b quarks as additional jets. In addition, the additional jets are required to have $p_{\text{T}} > 40\,\text{GeV}$ and $|\eta| < 2.4$. Specifically for the measurements of the top quark and antiquark at the parton level, two more differences in the definition of the extra jets are introduced [27]. The neutrinos from decays of hadrons are excluded in the clustering of these jets, and the charged leptons and b quarks used in the jet isolation are taken directly after the W boson and top quark decays, respectively.

7 Cross section measurement

For a given variable X, the absolute differential $\mathrm{t\bar{t}}$ cross section $\mathrm{d}\sigma_i/\mathrm{d}X$ is extracted via the relation

$$\frac{\mathrm{d}\sigma_i}{\mathrm{d}X} = \frac{1}{\mathcal{L}}\frac{x_i}{\Delta_i^X}, \tag{1}$$

where $\mathcal{L}$ is the integrated luminosity, x_i is the number of unfolded signal events observed in bin i, and Δ_i^X is the bin width. The numbers x_i are calculated with respect to the $\mathrm{t\bar{t}}$ parton or particle generator levels defined in Section 6.1. The normalized differential cross section is obtained by dividing the absolute differential cross section by the measured total cross section σ in the same phase space, which is evaluated by summing the binned cross section measurements over all bins of the observable X. For differential cross sections measured simultaneously as functions of two or three variables, the following criteria are adopted for optimizing their display. The measured cross sections are divided by the bin width of the variable that is chosen as the last one. They present single-differential cross sections as functions of the last variable in different ranges of the first, or first and second variables, and are referred to as double- or triple-differential cross sections, respectively.

The bin widths are chosen based on the resolutions of the kinematic variables, such that the purity and the stability of each bin are generally above 30% for single-differential cross sections and above 20% for double- or triple-differential cross sections. For a given bin, the purity is defined as the fraction of events in the $\mathrm{t\bar{t}}$ signal simulation that are generated and reconstructed in the same bin with respect to the total number of events reconstructed in that bin. To evaluate the stability, the number of events in the $\mathrm{t\bar{t}}$ signal simulation that are generated and reconstructed in a given bin are divided by the total number of reconstructed events generated in the bin.

The cross section measurement based on the signal extraction and unfolding procedure described in Section 6 is validated with closure tests. Large numbers (~ 1000) of pseudo-data sets are generated from the $\mathrm{t\bar{t}}$ signal MC simulations and analyzed as if they were real data. The unfolded differential cross sections are found to be unbiased and to provide proper 68% confidence intervals within ± 1 estimated standard deviation uncertainties. A second test is performed by unfolding pseudo-data sets, generated using reweighted $\mathrm{t\bar{t}}$ signal simulations, with the response matrix and bias vector taken from the nominal simulation. The reweighting is performed as a function of the differential cross section kinematic observables at the generator level and is used to introduce controlled shape variations, e.g., making the $p_{\mathrm{T}}(\mathrm{t})$ spectrum harder or softer. This test probes the robustness of the unfolding procedure with respect to the underlying physics model in the simulation, which impacts both the response matrix and the regularization bias vector. Figure 4 shows two examples of these tests, performed for cross sections as functions of $p_{\mathrm{T}}(\mathrm{t})$ and $m(\ell\bar{\ell})$. The applied reweightings follow approximately parabolic functions and lead to shape distortions of about $\pm 20\%$ at thresholds and end points of the kinematic spectra, comprising the differences observed between data and the nominal simulation (as shown by figures in Section 9). The unfolding is performed with the standard regularization procedure and alternatively with switching it off; the obtained cross sections are found to deviate at most by a few permille, showing that biases induced by the regularization are small. The unfolded cross sections vary visibly from the true values only in the kinematic threshold regions, with maximum differences of the order of 1%. Effects of similar size are also seen for other single- and multi-differential cross sections and demonstrate an overall good robustness of the unfolding procedure. The simple reweighting approach discussed here is not suitable for quantifying the measurement uncertainty from the underlying physics model; this is done, instead, by the dedicated set of variations applied to the $\mathrm{t\bar{t}}$ signal simulation detailed in Section 8.2.

8 Systematic uncertainties

The systematic uncertainties in the measured differential cross sections are grouped into three categories: experimental uncertainties from the imperfect modeling of the detector response, theoretical uncertainties from the modeling of the signal, and the uncertainties in the numbers of events from background processes. The systematic uncertainty is assessed source by source by changing in the simulation the corresponding efficiency, resolution, or scale by its uncertainty, following largely the prescriptions used in Refs. [26, 27]. For each change made, the cross section is recalculated, which for most sources involves a repetition of the full analysis with the varied simulations. The difference with respect to the nominal result in each bin is taken as the systematic uncertainty.

Separate simulations are employed for the data taken in the three years 2016, 2017, and 2018, in order to match the varying detector performance and data-taking conditions. The correlations of systematic uncertainties among the measurements in the different periods must be specified.

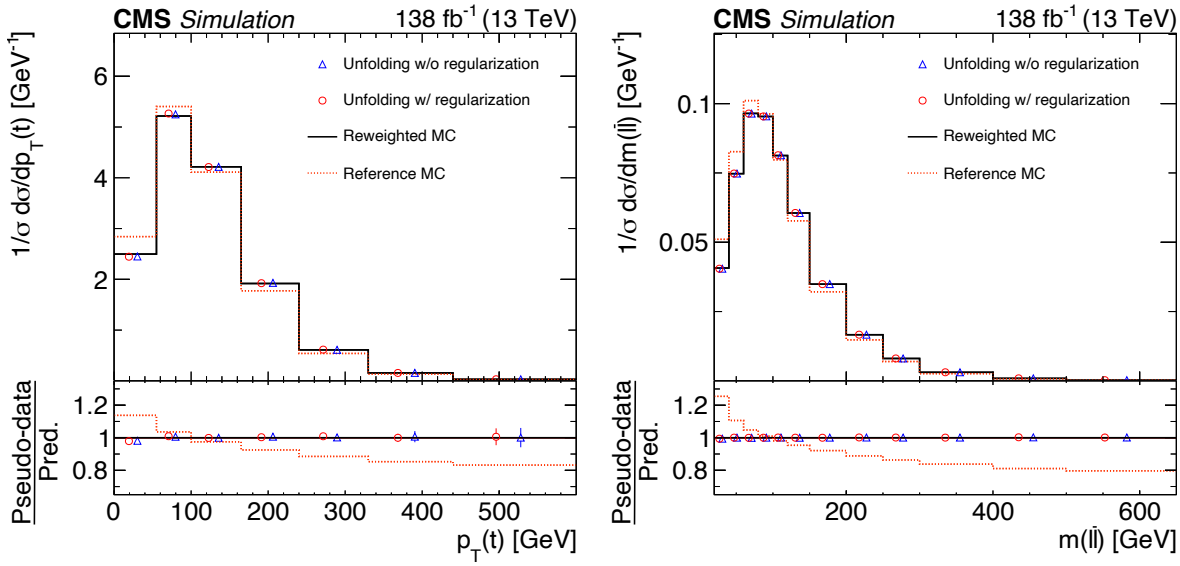

Figure 4: Reweighting test for the extraction of the normalized differential cross sections as functions of $p_{\mathrm{T}}(\mathrm{t})$ (left) and $m(\ell\overline{\ell})$ (right). The former cross section is measured at the parton level in the full phase space and the latter at the particle level in a fiducial phase space. The nominal $\mathrm{t\overline{t}}$ signal MC spectra are shown as dotted red histograms and the assumed true spectra, obtained from reweighting, as solid black histograms. The unfolded spectra, using pseudo-data based on the true spectra but using the nominal spectra for the detector corrections and bias vector in the regularization, are presented as open red circles. The unfolded spectra with the regularization switched off are also shown (open blue triangles). The statistical uncertainties in the unfolded cross sections are represented by a vertical bar on the corresponding points. The lower panel in each plot shows the ratios of the pseudo-data to the predicted spectra.

For theoretical uncertainties we assume a 100% correlation, as the same theoretical models and variations are used for all periods. For experimental uncertainties we use either uncorrelated, partial, or full correlations. For the case of partial correlations we make use of the varied and nominal simulations for each year. The correlated part of the uncertainty is assessed by using the varied simulations for all three years, but rescaling the resulting systematic uncertainty by a factor $\sqrt{\rho}$, where ρ specifies the level of correlation, e.g. 50%. For the uncorrelated part, we separately vary the simulation for each year, keeping the nominal simulation for the other two years, and add the resulting uncertainties in quadrature, after rescaling them by a factor $\sqrt{1-\rho}$.

8.1 Experimental uncertainties

The following sources are considered:

- The uncertainties in the integrated luminosities of the 2016, 2017, and 2018 data samples are 1.2, 2.3, and 2.5%, respectively, and are 30% correlated between the years [89–91]. The resulting total normalization uncertainty on the absolute cross sections is 1.6%.
- The uncertainty in the amount of pileup is assessed by varying the value of the total pp inelastic cross section, which is used to estimate the mean number of additional pp interactions, by its measurement uncertainty of $\pm$4.6% [69], leading to a 100% correlated uncertainty among the three years.
- The efficiencies for the dilepton and single-lepton triggers are measured with independent triggers based on a $p_{\mathrm{T}}^{\mathrm{miss}}$ requirement. Scale factors are calculated in bins of lepton p_{T}, independently for the years 2016, 2017, and 2018. They agree with unity typically within 1%. The scale factors are varied within their uncertainties. The uncertainties are assumed to be uncorrelated among the years.
- Lepton identification and isolation efficiencies are determined using the "tag-and-probe" method with Z+jets event samples [92, 93]. The efficiencies are assessed in two-dimensional bins of lepton η and p_{T}. The corresponding scale factors typically agree with unity within 10% for electrons and 3% for muons. The scale factors are varied within their calibration uncertainties and a 100% correlation among the years is assumed. An implicit assumption made in the analysis is that the scale factors derived from the Z+jets sample are applicable to the $\mathrm{t\bar{t}}$ samples, where the efficiency for lepton isolation is reduced due to the typically larger number of jets present in the events. An additional uncertainty of 1% (0.5%) is added for electrons (muons) to take into account a possible violation of this assumption. This uncertainty is verified with studies of $\mathrm{t\bar{t}}$-enriched samples using a similar event selection as for the present analysis [94]. In these studies, the lepton isolation criteria are relaxed for one lepton and the efficiency for passing the criteria is measured both in data and simulation.
- The uncertainty arising from the jet energy scale (JES) is assessed by varying the individual sources of JES uncertainty in bins of p_{T} and η and taking the quadrature sum of the effects [76]. The JES uncertainties also include several minor sources related to pileup. The JES variations are also propagated to the uncertainties in $\vec{p}_{\mathrm{T}}^{\,\mathrm{miss}}$. The correlation among the years is evaluated separately for each source.
- The uncertainty from the jet energy resolution (JER) is evaluated by the variation of the simulated JER by $\pm$1 standard deviation in different η regions [76]. An additional uncertainty in the calculation of $\vec{p}_{\mathrm{T}}^{\,\mathrm{miss}}$ is estimated by varying the energies of reconstructed particles not clustered into jets. Both sources of uncertainty are

assumed to be uncorrelated among the different years.

- During the 2016–2017 data-taking periods, a gradual shift in the timing of the inputs of the ECAL L1 trigger in the forward endcap region ($|\eta| > 2.4$) led to a particular trigger inefficiency. A correction for this effect was determined using an unbiased data sample and is found to be relevant in events containing high-p_T jets pointing to the most forward ECAL region ($2.4 < |\eta| < 3.0$). While no reconstructed objects at this pseudorapidity enter the measurements, the systematic variation of 20% in this correction for affected events nevertheless leads to a small measurement uncertainty.
- Scale factors for the b tagging efficiency of individual b jets and the mistagging efficiencies of c quark, and light-flavor and gluon jets are measured using dedicated calibration samples [77]. The factors are parameterized as functions of jet p_T and η. For the systematic uncertainty evaluation the scale factors are varied within their estimated uncertainties [77]. The variations for b and c jets are treated as fully correlated and uncorrelated to those applied for light jets. The statistical uncertainties in the scale factors are uncorrelated among the years and the uncertainties for light jets are also assumed to be uncorrelated among these periods. All other b tagging uncertainties are treated as fully correlated among the years.

8.2 Theoretical uncertainties

The uncertainties in the modeling of the $t\bar{t}$ events, comprising signal and other final states, are assessed with appropriate variations of the nominal simulation based on POWHEG+PYTHIA 8 and the CP5 tune, introduced in Section 3:

- The uncertainty arising from missing higher-order terms in the simulation of the signal process at the ME level is estimated by varying the renormalization and factorization scales (denoted as μ_r and μ_f, respectively) in the POWHEG simulation up and down by factors of two with respect to the nominal values. The nominal scales are defined in the POWHEG sample as $\mu_r = \mu_f = \sqrt{(m_t^{MC})^2 + p_{T,t}^2}$. Here, $p_{T,t}$ denotes the p_T of the top quark in the $t\bar{t}$ rest frame. In total, six variations are applied: two with μ_r fixed, two with μ_f fixed, and two with both scales varied in the same direction (up or down). For each measurement bin, the maximum of the resulting measurement variations is taken as the final uncertainty.
- For the parton shower simulation, uncertainties are separately assessed for initial- and final-state radiation, by varying the respective scales up and down by factors of two.
- The uncertainty originating from the scheme used to match the ME-level calculation to the parton shower simulation is derived by varying the h_{damp} parameter in POWHEG from its nominal value of $1.379\, m_t^{MC}$ to $0.8738\, m_t^{MC}$ and $2.305\, m_t^{MC}$, according to the tuning results of Ref. [41].
- The uncertainty from the choice of PDFs is assessed by reweighting the $t\bar{t}$ signal simulation according to the ± 1 standard deviation along the directions of the 100 eigenvectors of the NNPDF3.1 error PDF sets [36] and adding the resulting measurement variations in quadrature. In addition, the value of the strong coupling α_S is independently varied within its uncertainty in the PDF set.
- The dependence of the measurement on the assumed top quark mass is estimated by varying m_t^{MC} in the $t\bar{t}$ simulation by ± 1 GeV around the nominal value of 172.5 GeV.
- The uncertainty related to modeling of the UE is estimated by varying the CP5 tune

parameters within their uncertainties determined in the tuning process [41].

- The nominal PYTHIA setup includes a model of color reconnection (CR) based on MPIs with early resonance decays switched off. The analysis is repeated with three other CR models within PYTHIA: the MPI-based scheme with early resonance decays switched on, a gluon-move scheme [95], and a QCD-inspired scheme [96]. The total CR related uncertainty is taken to be the maximum deviation from the nominal result.
- The b jet energy response is different for semileptonic decays of b hadrons and thus their branching fractions are varied within world average uncertainties [1]. The parton level cross sections are corrected for the branching fractions for $W \to \ell\nu$ which are taken from Ref. [1] and varied according to their uncertainty of 1.5%.

The uncertainties associated with the values of h_{damp}, m_{t}^{MC}, and the CR treatment are evaluated using separate $\text{t}\bar{\text{t}}$ simulations incorporating the varied values, while all other theoretical uncertainties are assessed by applying appropriate event weights in the nominal simulations.

8.3 Background uncertainties

The contributions from non-$\text{t}\bar{\text{t}}$ background processes are overall at the level of a few percent, and the uncertainties are treated as global normalization uncertainties in the MC simulated processes. The uncertainty in the Z+jets background normalization is assessed by repeating the template fits to $m(\ell\bar{\ell})$ distributions, described in Section 4, with varied event selections. The nominal fits are performed with a selection dropping all requirements on $p_{\text{T}}^{\text{miss}}$, the number of b-tagged jets, and the $\text{t}\bar{\text{t}}$ kinematic reconstruction. In the first varied scenario, the $p_{\text{T}}^{\text{miss}} > 40\,\text{GeV}$ requirement is switched on again for the e^+e^- and $\mu^+\mu^-$ channels, in the next one it is additionally required to have at least one b-tagged jet in the event, and in the last one the criterion of finding a solution to the full kinematic reconstruction is imposed. The variations are studied separately for each channel (e^+e^- and $\mu^+\mu^-$) and each year. The maximum scale factor variation observed among all channels, years, and event selections is used to derive a $\pm 20\%$ systematic uncertainty in the Z+jets normalization.

For the single top quark, W+jets, and diboson backgrounds, a normalization uncertainty of $\pm 30\%$ is taken, following the prescription from our previous analyses [26, 27]. This value is confirmed for the tW background (dominant contribution among these processes) by investigating the ratio of the number of events with one and two b-tagged jets in the $\text{e}^{\pm}\mu^{\mp}$ sample, which is higher for the tW process than for $\text{t}\bar{\text{t}}$ events.

8.4 Summary of uncertainties

The total systematic uncertainty in each measurement bin is assessed by adding all contributions described above in quadrature, separately for positive and negative cross section variations. If a systematic uncertainty leads to two cross section variations of the same sign, the largest one is taken and the opposite variation is set to zero. The total uncertainties for the measured cross sections range 2–20%, depending on the observable and the bin. They are dominated by the systematic uncertainties.

The uncertainties are illustrated in Figs. 5–6, showing the relative contributions from the various sources for selected differential cross sections. Individual sources affecting a particular uncertainty (e.g. JES) are added in quadrature and shown as a single component. Additional experimental systematic uncertainties and all contributions from theoretical uncertainties are also added in quadrature, respectively, and shown as single components. For most bins in a

majority of the distributions, the JES is the dominant systematic uncertainty. Important contributions arise from other experimental sources, as well as from theoretical and background uncertainties. Among the significant experimental sources of uncertainties are the lepton and b tagging efficiencies, and for measurements of absolute cross sections, the integrated luminosity. For the theoretical uncertainties, the following sources contribute significantly, with relative magnitudes depending on the observables and phase space region: ME level and final-state radiation scales, h_{damp} parameter, top quark mass, underlying event, and CR.

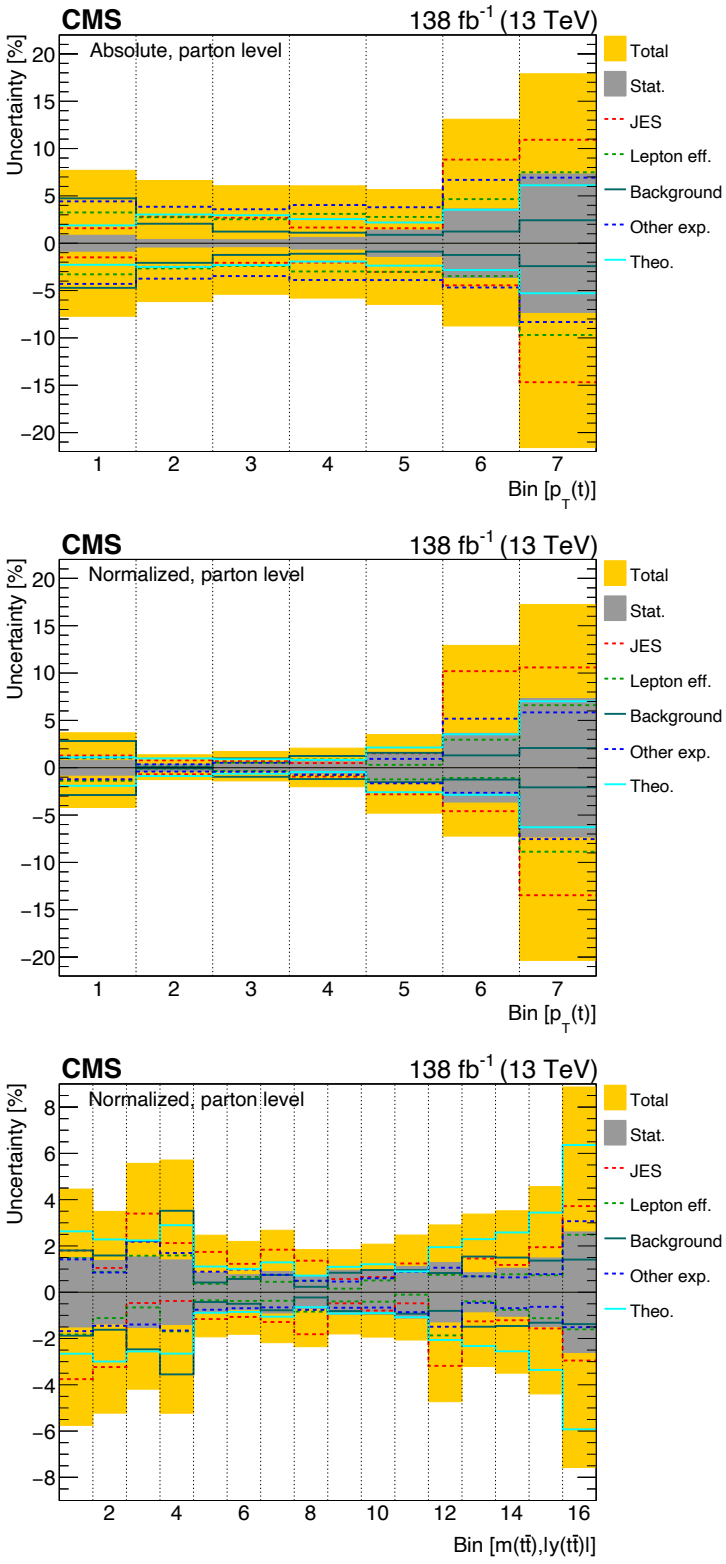

Figure 5: The various sources of systematic uncertainty and their relative contributions to the overall uncertainty are shown for several parton-level measurements: absolute $p_{\mathrm{T}}(\mathrm{t})$ (upper), normalized $p_{\mathrm{T}}(\mathrm{t})$ (middle), and normalized $[m(\mathrm{t\bar{t}}), |y(\mathrm{t\bar{t}})|]$ (lower). The statistical uncertainties and the total uncertainties (statistical and systematic uncertainties added in quadrature) are shown as grey and yellow bands, respectively. The ranges of the observables for a given bin number can be read off from the corresponding cross section distributions in Figs. 7 and 16.

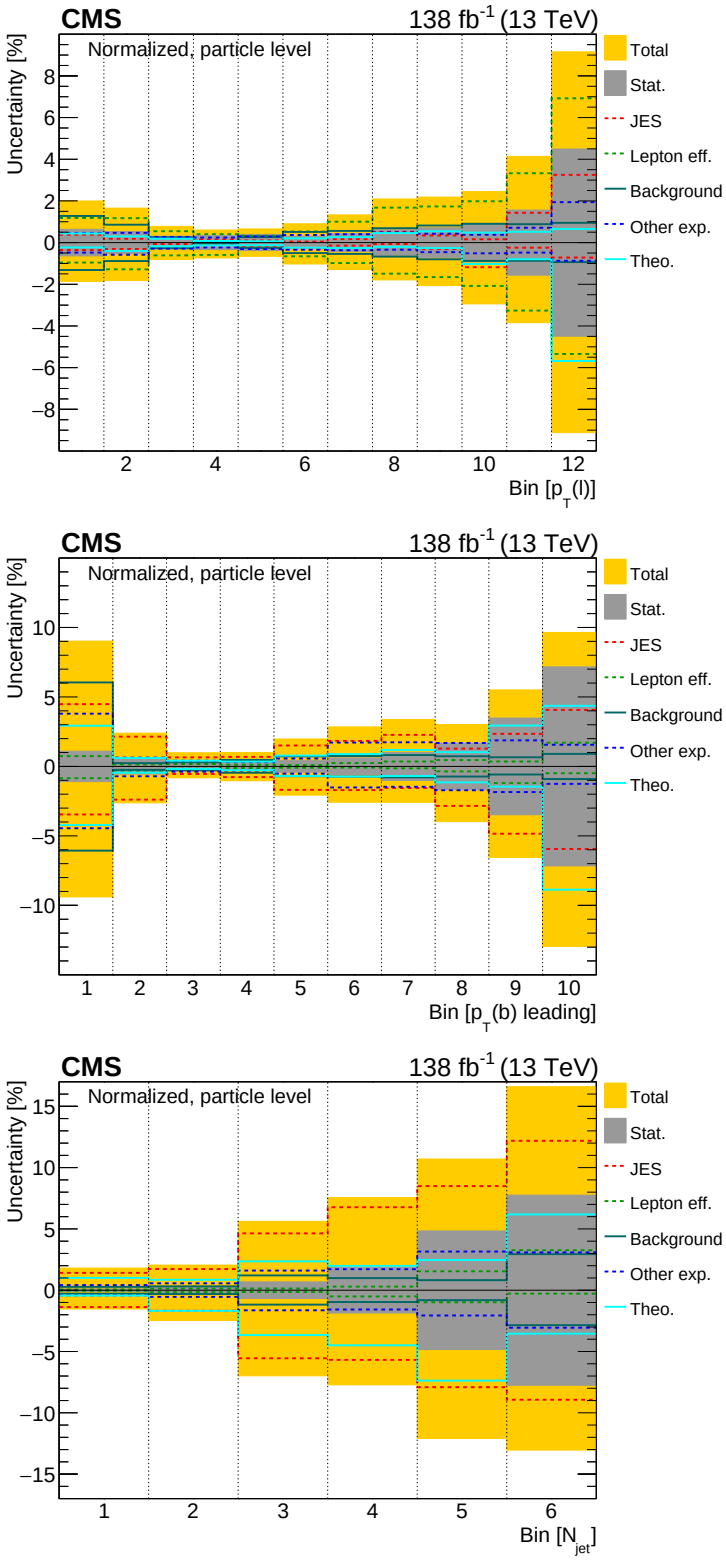

Figure 6: The various sources of systematic uncertainty and their relative contributions to the overall uncertainty are shown for several normalized particle-level measurements: p_{T} of the lepton (upper), p_{T} of the leading b jet (middle), and N_{jet} (lower). The statistical uncertainties and the total uncertainties (statistical and systematic uncertainties added in quadrature) are shown as grey and yellow bands, respectively. The ranges of the observables for a given bin number can be read off from the corresponding cross section distributions in Figs. 23, 24, and 30.

9 Results

Cross sections for $t\bar{t}$ and top quark kinematic variables are discussed in Section 9.1, for lepton and b jet variables in Section 9.2, and for events with additional jets in Section 9.3. The three predictions based on MC simulations introduced in Section 3: POWHEG+PYTHIA 8 ('POW+PYT'), POWHEG+HERWIG 7 ('POW+HER'), and MG5_aMC@NLO[FxFx]+PYTHIA 8 ('FxFx+PYT'), are used for comparisons to data. The POW+PYT and POW+HER theoretical predictions differ by the parton-shower method, hadronization and event tune (p_T-ordered parton showering, string hadronization model, and CP5 tune in POW+PYT, or angular ordered parton showering, cluster hadronization model, and CH3 tune in POW+HER), while the POW+PYT and FxFx+PYT predictions adopt different matrix elements (inclusive $t\bar{t}$ production at NLO in POW+PYT, or $t\bar{t}$ with up to two extra partons at NLO in FxFx+PYT) and different methods for matching with parton shower (correcting the first parton shower emission to the NLO result in POW+PYT, or subtracting from the exact NLO result its parton shower approximation in FxFx+PYT). In Section 9.4, several theoretical calculations with beyond-NLO precision are introduced and their predictions compared to the data for a subset of the measured cross sections. Finally, a study of the sensitivity of the normalized cross sections to the PDFs is presented in Section 9.5. For each data-to-theory comparison, a χ^2 statistic and the number of degrees of freedom (dof) are reported. One statistic, denoted in the following as "standard χ^2", probes directly the quality of the nominal predictions. It takes all measurement uncertainties into account, including bin-to-bin correlations, but neglects the uncertainties in the theoretical predictions. Additional χ^2 values that include prediction uncertainties are also provided for a subset of the models: for POW+PYT, the full set of uncertainties discussed in Section 8.2 is applied to the generator-level predictions, and for the beyond NLO models, the theory scale uncertainties discussed in Section 9.4 are considered; these prediction uncertainties are also shown in the corresponding result figures. The exact definition of the χ^2 values is given in Appendix A. Normalized cross sections and tables providing the χ^2 values are presented in this section, while absolute cross sections and corresponding χ^2 tables are summarized in Appendix B. The p-values denoting the probability for finding a χ^2 of equal or larger size than observed are tabulated, for all results, in Appendix C.

9.1 Results for top quark and $t\bar{t}$ kinematic observables at the parton and particle levels

The studies presented in this subsection aim to provide a comprehensive survey of the kinematic spectra of the top quark and antiquark, the $t\bar{t}$ system, and their correlations.

9.1.1 Single-differential cross sections

The single-differential cross sections are shown in Figs. 7–12. The χ^2 values of the model-to-data comparisons are listed in Tables 1–2, and the corresponding p-values in Tables 25–26. First, we present measurements where the top quark and antiquark kinematics are studied. Figure 7 illustrates the distributions of $p_T(t)$ and $p_T(\bar{t})$. Both the POW+PYT and, in particular, the FxFx+PYT models predict harder spectra than observed, while POW+HER provides a reasonable description of the data, as supported by the p-value of the χ^2 test. The discrepancy between POW+PYT and the data is smaller than what was observed in our previous analysis [26]. This reduction can be attributed to the use of the more-recent tune CP5 [41] for the PYTHIA part of the calculation, whereas in the previous analysis the CUETP8M2T4 tune [51–53] was applied. Figure 8 depicts the $y(t)$ and $y(\bar{t})$ distributions. All models predict a slightly more central distribution than observed in data. One general observation can be made at this point: the comparisons of predictions and data for the cross sections at the parton and particle

levels show similar patterns. This is also the case for most other cross sections presented in this paper; consequently, a separate discussion of the parton- and particle-level cross sections will be only given in case of significant differences.

Figure 9 shows the distributions of the complete set of $t\bar{t}$ kinematic observables: $p_T(t\bar{t})$, $m(t\bar{t})$, and $y(t\bar{t})$. For $p_T(t\bar{t})$, the phase space covered in our previous analysis [26] is extended up to 1 TeV. The description of the $p_T(t\bar{t})$ distribution is particularly difficult, since nonzero values indicate the presence of extra QCD radiation in the event recoiling against the $t\bar{t}$ system, which directly probes higher-order processes in the calculation. The three MC models differ in the predicted shape of the $p_T(t\bar{t})$ distribution and none of them is able to describe the data accurately. The best description is provided by POW+PYT, which tends to overshoot the data only in the higher-$p_T(t\bar{t})$ range. The FxFx+PYT model predicts too many events in the intermediate $p_T(t\bar{t})$ ranges, while POW+HER predicts too few. The description by POW+HER is somewhat improved compared to what was observed in our previous analysis [26], which can also be attributed to using a newer version of the HERWIG MC generator, HERWIG 7 [46], instead of HERWIG++ [97]. It is interesting to note that also in two recent measurements [25, 28] by the ATLAS and CMS Collaborations, the $p_T(t\bar{t})$ distribution was found to be rather poorly described by several models. In the present analysis, the $m(t\bar{t})$ spectrum is overall reasonably well described by the models, with the exception of the first bin near the threshold where the predictions lie somewhat below the data. This region is known to be particularly sensitive to the value of the top quark mass assumed in the calculations. To investigate this discrepancy in more detail, the POW+PYT prediction is also shown for two other values of the top quark mass parameter, $m_t^{MC} = 169.5\,\text{GeV}$ and $m_t^{MC} = 175.5\,\text{GeV}$, compared to the value of 172.5 GeV taken in the nominal simulation. For the lower value, the cross section prediction moves up in the lowest $m(t\bar{t})$ bin by about 20% and the whole mass spectrum is a bit softer than in the data, however still providing a χ^2 with a good p-value. Using the higher value, the resulting predicted $m(t\bar{t})$ spectrum is clearly harder than what is observed in data. This discrepancy is also reflected by an increase of the χ^2 value of about 13 units compared to using the central mass value, proving the high sensitivity of the $m(t\bar{t})$ distribution to the top quark mass value, as explored in the CMS analysis [98]. The $y(t\bar{t})$ distribution of the data is described reasonably well by all models.

Moving on to studies of kinematic correlations between top quark and antiquark, we show in Fig. 10 the distribution of the absolute value of the azimuthal angle difference between the top quark and antiquark $|\Delta\phi(t,\bar{t})|$, and the difference of the absolute values of the top quark and antiquark rapidities $|y(t)| - |y(\bar{t})|$, related to the charge asymmetry [99]. For $|\Delta\phi(t,\bar{t})|$, angles smaller than π are directly sensitive to additional QCD radiation in the event. The models provide a good description of the data. The $|y(t)| - |y(\bar{t})|$ spectrum of the data is not perfectly described by the MC models, as they predict more events at small rapidity separations and fewer at larger values $|y(t)| - |y(\bar{t})| \approx 2$.

Figure 11 presents the distributions of two ratios: $p_T(t)/m(t\bar{t})$ and $p_T(t\bar{t})/m(t\bar{t})$. The study of the first quantity is inspired by the observation in Ref. [27] that at large $m(t\bar{t})$ the effect of the models predicting harder $p_T(t)$ spectra is enhanced. Indeed, all three tested models predict a significantly harder spectrum for the ratio of the two variables and the χ^2 values indicate a poor data description. The distribution of the second ratio, $p_T(t\bar{t})/m(t\bar{t})$, is expected to be sensitive to p_T resummation effects. The description by the three models follows largely the trends observed for $p_T(t\bar{t})$.

Finally, we study two observables ξ_1 and ξ_2, defined as $\xi_1 = [E(t\bar{t}) - p_z(t\bar{t})]/2E_p$ and $\xi_2 = [E(t\bar{t}) + p_z(t\bar{t})]/2E_p$, with E_p denoting the proton beam energy, and $p_z(t\bar{t})$ the magnitude of

the $t\bar{t}$ momentum along the beam axis. In the leading order pQCD picture of the $pp \to t\bar{t}$ process, these variables represent the proton momentum fractions of the two partons entering the hard interaction. Figure 12 depicts the $\log(\xi_1)$ and $\log(\xi_2)$ distributions. Overall, these PDF-sensitive distributions are reasonably well described by all the models. Of special interest is the last bin covering proton momentum fractions above $\approx$0.2, where the uncertainties in the PDFs, in particular for the gluon distribution, start to grow.

The description of the kinematic distributions of top quark, antiquark, and $t\bar{t}$ system by the three MC models can be summarized as follows. The models tend to predict, for the individual quarks, harder p_T spectra and slightly more-central rapidity distributions than those observed in data. A reasonable description is provided for the $t\bar{t}$ rapidity and invariant mass spectra. The latter is described less well by the POW+PYT simulation that uses a larger value of m_t^{MC}, as it predicts a harder spectrum than that observed in data. The $|\Delta\phi(t,\bar{t})|$ distribution is modeled well, and smaller rapidity separations are predicted than observed in data on average. The FxFx+PYT model provides overall the least accurate description of the data, in particular by predicting harder p_T spectra for the top quark, antiquark, and the $t\bar{t}$ system. Among all the models, POW+HER predicts the softest p_T spectra for the top quark, antiquark, and the $t\bar{t}$ system, which matches the data well for the former two, but are too soft for the latter. The POW+PYT model provides the best description of the p_T distribution of the $t\bar{t}$ system. The standard χ^2 values indicate a rather poor description of several distributions by some of the models, while the χ^2 values that also include the prediction uncertainties (as for example, those evaluated for POW+PYT, see Tables 1–2) are found to be significantly smaller. Only for a few distributions, e.g. $p_T(t)/m(t\bar{t})$, the p-values of the χ^2 remain too low for a reasonable description of the data, as is typically the case for those distributions with the largest visible discrepancies.

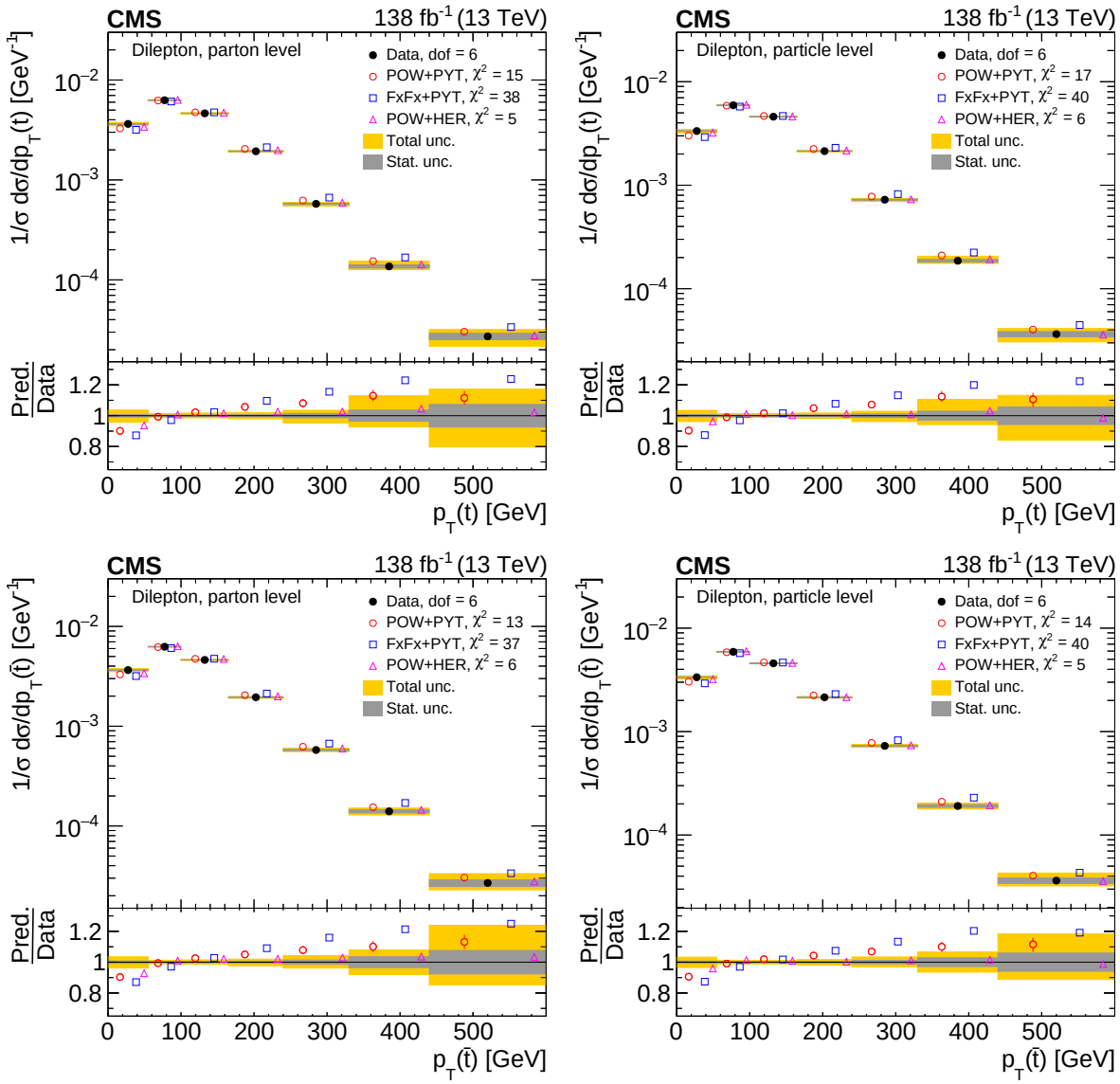

Figure 7: Normalized differential $\mathrm{t\bar{t}}$ production cross sections as functions of $p_{\mathrm{T}}(\mathrm{t})$ (upper) and $p_{\mathrm{T}}(\bar{\mathrm{t}})$ (lower), measured at the parton level in the full phase space (left) and at the particle level in a fiducial phase space (right). The data are shown as filled circles with grey and yellow bands indicating the statistical and total uncertainties (statistical and systematic uncertainties added in quadrature), respectively. For each distribution, the number of degrees of freedom (dof) is also provided. The cross sections are compared to various MC predictions (other points). The estimated uncertainties in the POWHEG+PYTHIA 8 ('POW-PYT') simulation are represented by a vertical bar on the corresponding points. For each MC model, a value of χ^2 is reported that takes into account the measurement uncertainties. The lower panel in each plot shows the ratios of the predictions to the data.

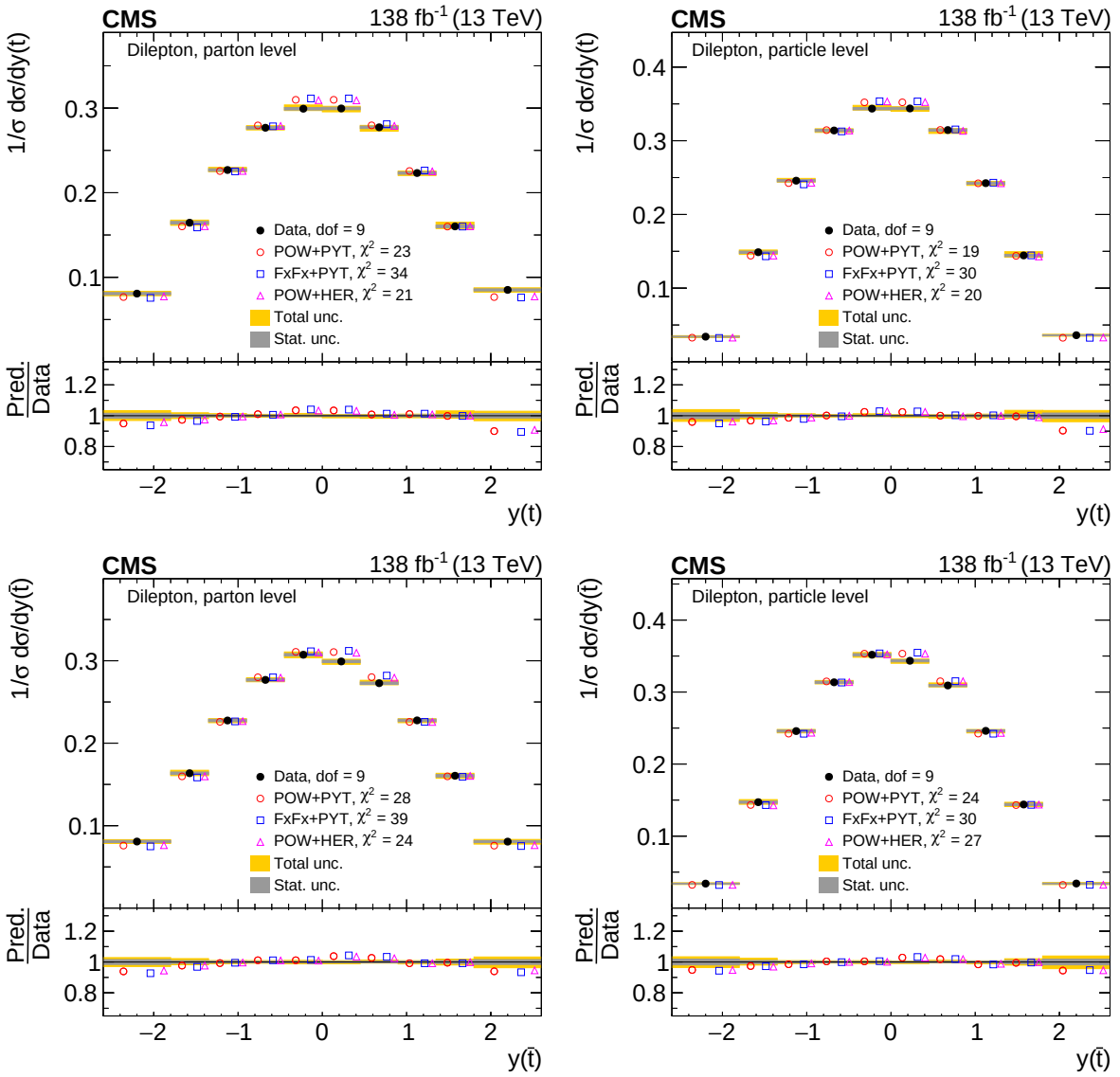

Figure 8: Normalized differential $t\bar{t}$ production cross sections as functions of $y(t)$ (upper) and $y(\bar{t})$ (lower) are shown for data (filled circles) and various MC predictions (other points). Further details can be found in the caption of Fig. 7.

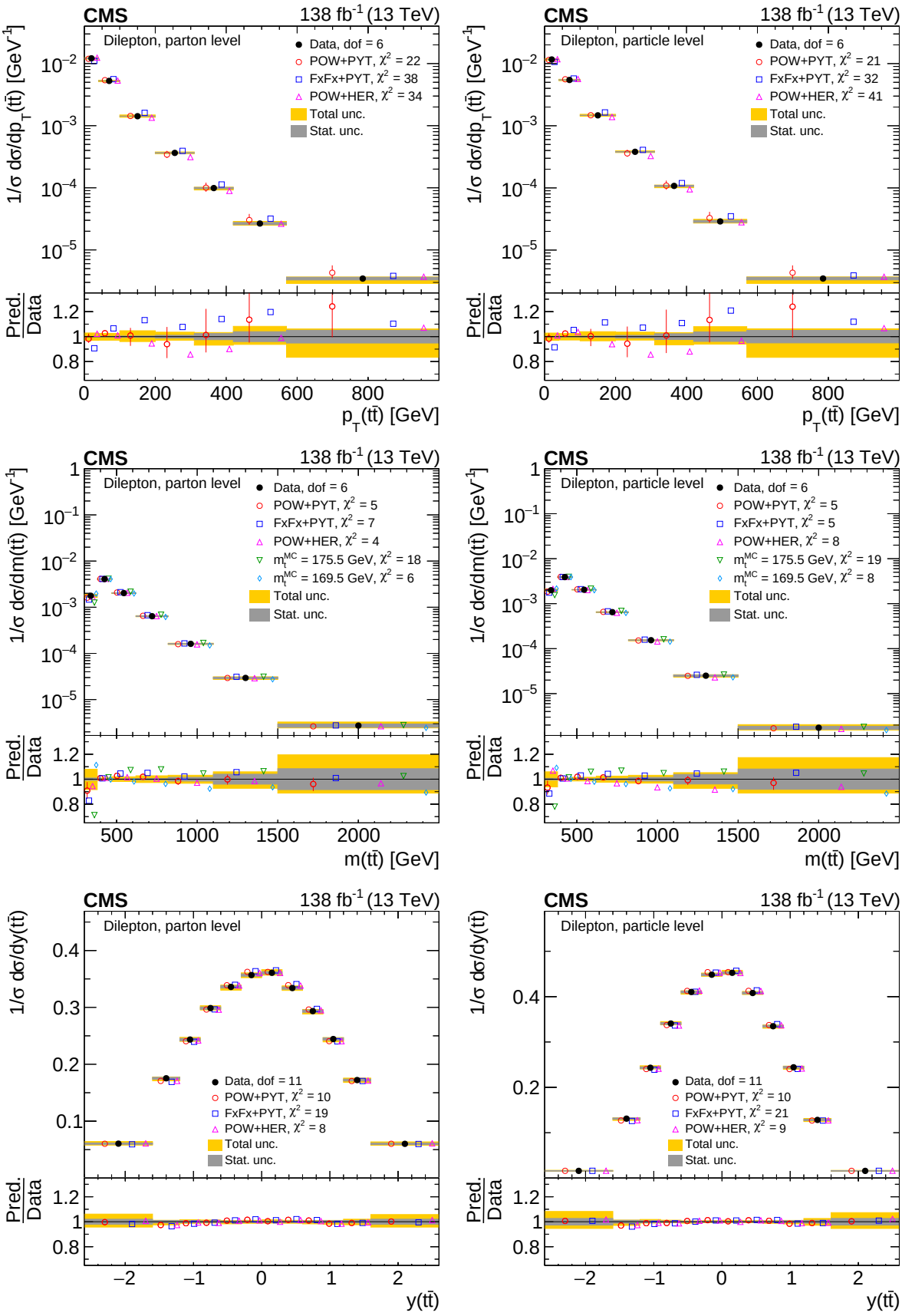

Figure 9: Normalized differential $\mathrm{t\bar{t}}$ production cross sections as functions of $p_{\mathrm{T}}(\mathrm{t\bar{t}})$ (upper), $m(\mathrm{t\bar{t}})$ (middle) and $y(\mathrm{t\bar{t}})$ (lower) are shown for data (filled circles) and various MC predictions (other points). The $m(\mathrm{t\bar{t}})$ distributions are also compared to POWHEG+PYTHIA 8 ('POW-PYT') simulations with different values of $m_{\mathrm{t}}^{\mathrm{MC}}$. Further details can be found in the caption of Fig. 7.

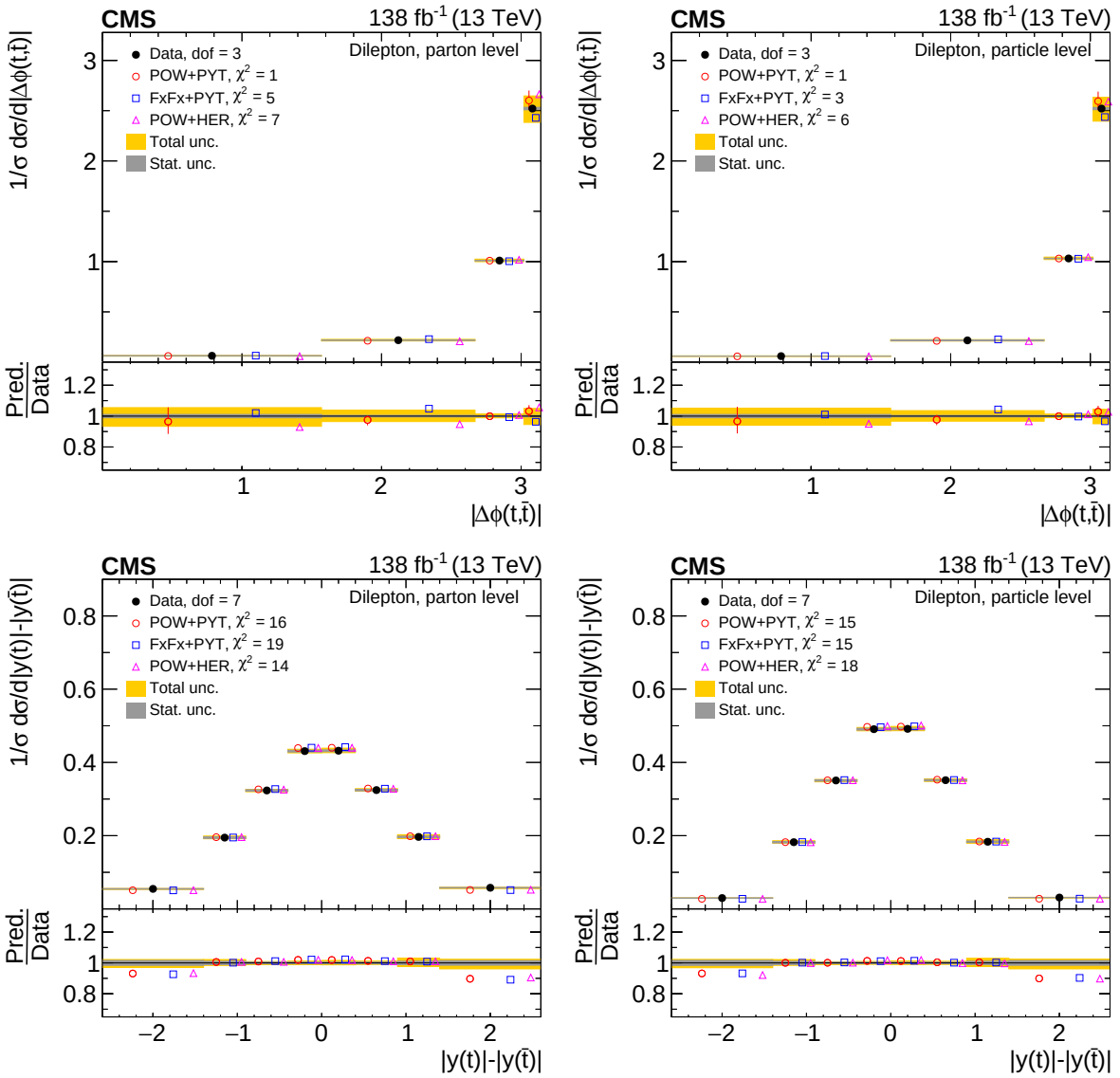

Figure 10: Normalized differential $t\bar{t}$ production cross sections as functions of $|\Delta\phi(t,\bar{t})|$ (upper) and $|y(t)| - |y(\bar{t})|$ (lower) are shown for data (filled circles) and various MC predictions (other points). Further details can be found in the caption of Fig. 7.

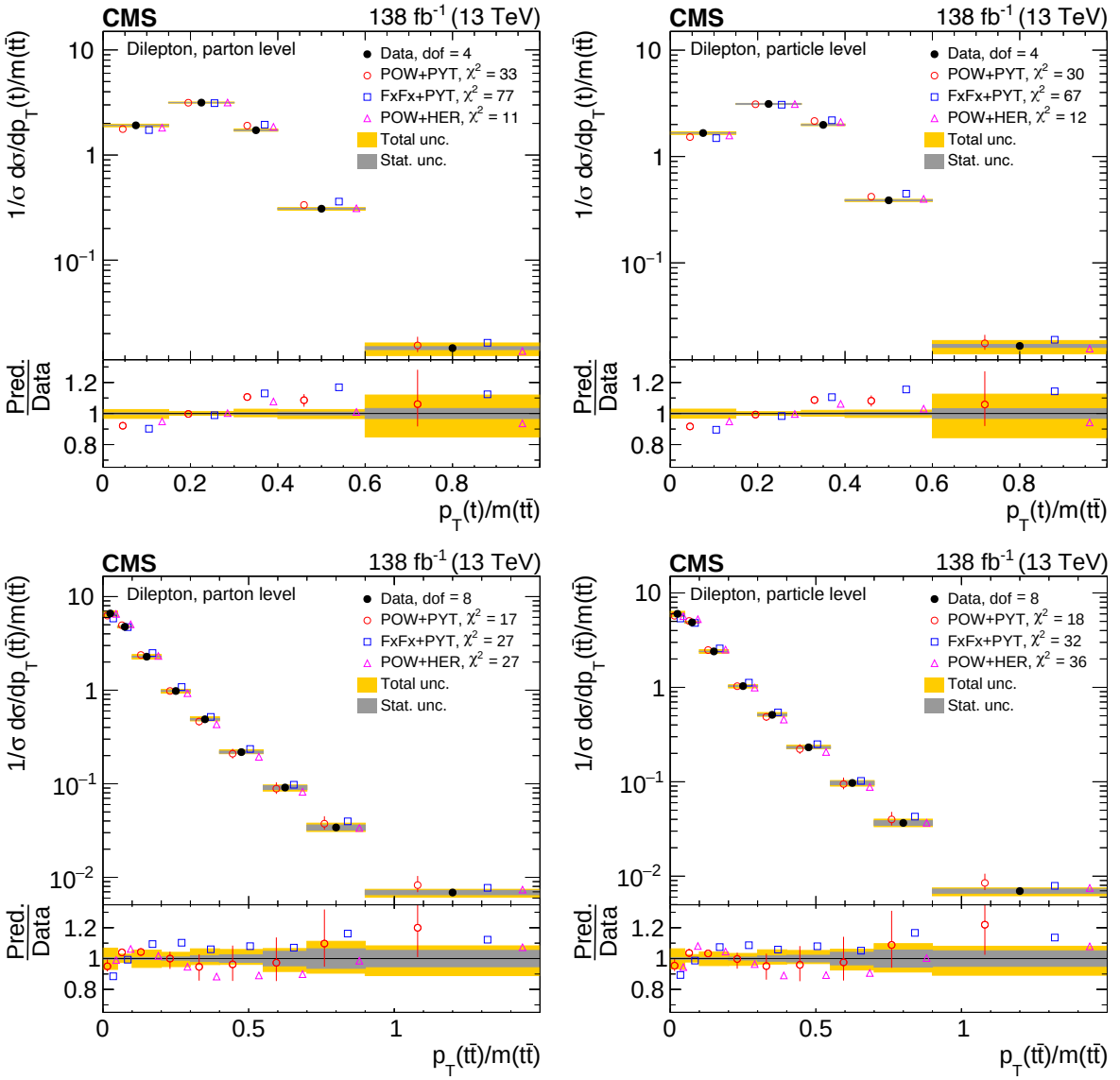

Figure 11: Normalized differential $\mathrm{t\bar{t}}$ production cross sections as functions of $p_{\mathrm{T}}(\mathrm{t})/m(\mathrm{t\bar{t}})$ (upper) and $p_{\mathrm{T}}(\mathrm{t\bar{t}})/m(\mathrm{t\bar{t}})$ (lower) are shown for data (filled circles) and various MC predictions (other points). Further details can be found in the caption of Fig. 7.

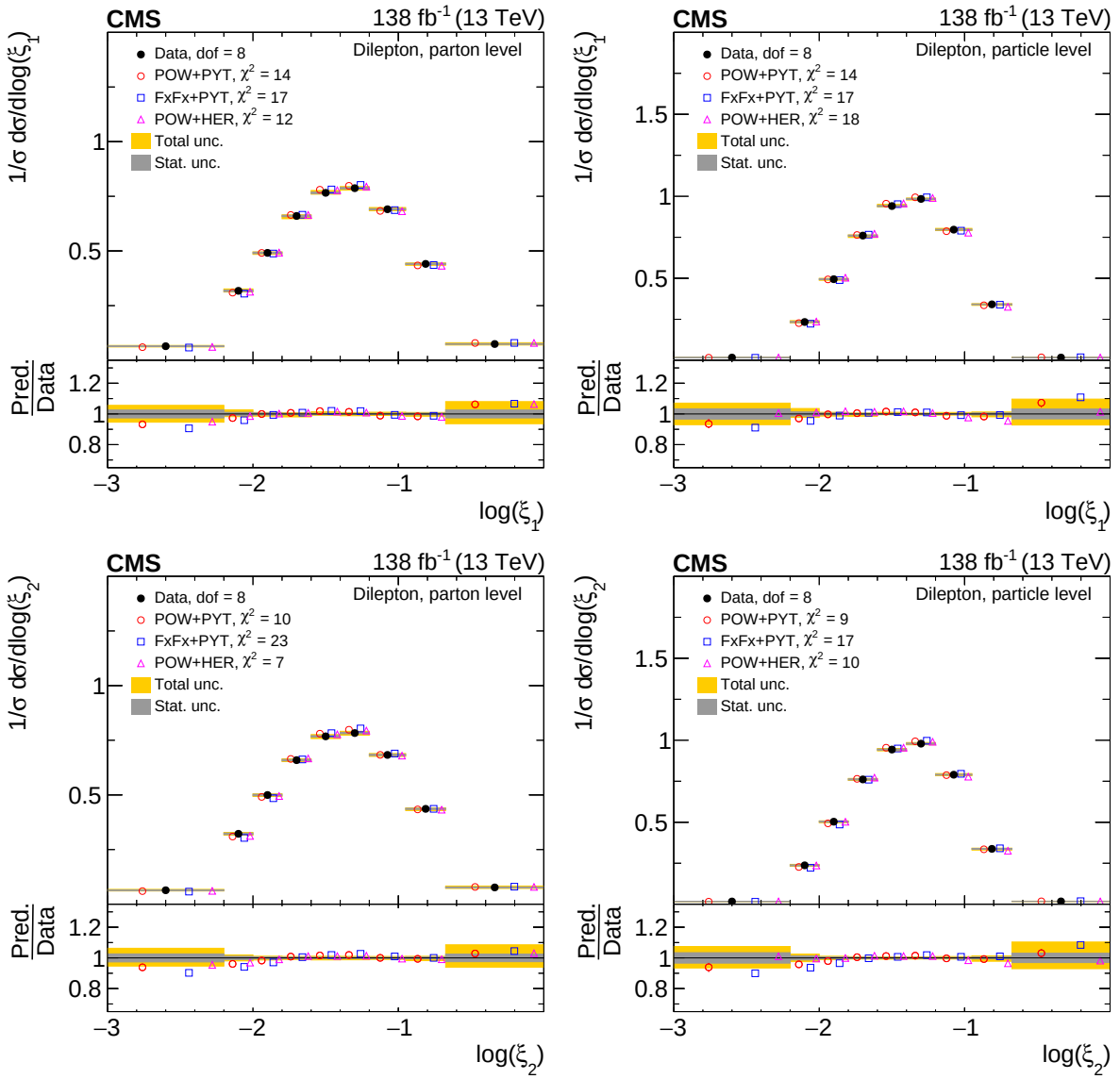

Figure 12: Normalized differential $t\bar{t}$ production cross sections as functions of $\log(\xi_1)$ (upper) and $\log(\xi_2)$ (lower) are shown for data (filled circles) and various MC predictions (other points). Further details can be found in the caption of Fig. 7.

Table 1: The χ^2 values and dof of the measured normalized single-differential cross sections for $t\bar{t}$ and top quark kinematic observables at the parton level are shown with respect to the predictions of various MC generators. The χ^2 values are calculated taking only measurement uncertainties into account and excluding theory uncertainties. For POW+PYT, the χ^2 values including theory uncertainties are indicated with the brackets (w. unc.).

Cross section variables	dof	χ^2		
		POW+PYT (w. unc.)	FxFx+PYT	POW+HER
$p_T(t)$	6	15 (11)	38	5
$p_T(\bar{t})$	6	13 (9)	37	6
$y(t)$	9	23 (20)	34	21
$y(\bar{t})$	9	28 (25)	39	24
$p_T(t\bar{t})$	6	22 (7)	38	34
$y(t\bar{t})$	11	10 (8)	19	8
$m(t\bar{t})$	6	5 (3)	7	4
$\lvert\Delta\phi(t,\bar{t})\rvert$	3	1 (0)	5	7
$\lvert y(t)\rvert - \lvert y(\bar{t})\rvert$	7	16 (9)	19	14
$p_T(t)/m(t\bar{t})$	4	33 (20)	77	11
$p_T(t\bar{t})/m(t\bar{t})$	8	17 (6)	27	27
$\log(\xi_1)$	8	14 (10)	17	12
$\log(\xi_2)$	8	10 (7)	23	7

Table 2: The χ^2 values and dof of the measured normalized single-differential cross sections for $t\bar{t}$ and top quark kinematic observables at the particle level are shown with respect to the predictions of various MC generators. The χ^2 values are calculated taking only measurement uncertainties into account and excluding theory uncertainties. For POW+PYT, the χ^2 values including theory uncertainties are indicated with the brackets (w. unc.).

Cross section variables	dof	χ^2		
		POW+PYT (w. unc.)	FxFx+PYT	POW+HER
$p_T(t)$	6	17 (12)	40	6
$p_T(\bar{t})$	6	14 (9)	40	5
$y(t)$	9	19 (16)	30	20
$y(\bar{t})$	9	24 (20)	30	27
$p_T(t\bar{t})$	6	21 (7)	32	41
$y(t\bar{t})$	11	10 (7)	21	9
$m(t\bar{t})$	6	5 (3)	5	8
$\lvert\Delta\phi(t,\bar{t})\rvert$	3	1 (0)	3	6
$\lvert y(t)\rvert - \lvert y(\bar{t})\rvert$	7	15 (10)	15	18
$p_T(t)/m(t\bar{t})$	4	30 (20)	67	12
$p_T(t\bar{t})/m(t\bar{t})$	8	18 (7)	32	36
$\log(\xi_1)$	8	14 (9)	17	18
$\log(\xi_2)$	8	9 (6)	17	10

9.1.2 Multi-differential cross section measurements

Studies of differential $t\bar{t}$ cross sections performed as functions of several kinematic observables shed light on the details of the $t\bar{t}$ production dynamics and can help to better understand the origin of model-to-data discrepancies seen in single-differential cross sections. The double-differential measurements performed in this analysis, e.g. as functions of $|y(t)|$ and $p_T(t)$, are denoted in the following as $[|y(t)|,\ p_T(t)]$, etc., and an analogous notation is adopted for triple-differential cross sections. The cross section results are shown in Figs. 13–22. The upper and lower plots show the cross sections at the parton and particle levels, respectively. The χ^2 values of model-to-data comparisons are listed in Tables 3–4, and the corresponding p-values in Tables 27–28.

In the first set of studies, we investigate how the $p_T(t)$ distribution is correlated with other event kinematic observables. In Fig. 13, the $p_T(t)$ distribution is compared in different ranges of $|y(t)|$ to predictions from the same three MC models discussed above. The data distribution is softer than that of the predictions over the entire $y(t)$ range. The POW+HER prediction that gave a reasonable description of the single-differential $p_T(t)$ cross section (Fig. 7), still provides the best description, but exhibits a stronger positive $p_T(t)$ slope with respect to the data in the lowest and highest $|y(t)|$ ranges. Figure 14 shows the $p_T(t)$ distributions in different $m(t\bar{t})$ ranges. Similar to the result of the previous analysis [27], this is among the double-differential cross sections poorly described by the models. While the POW+HER model describes the $p_T(t)$ distribution in the lowest $m(t\bar{t})$ range near threshold reasonably well, it joins POW+PYT and FxFx+PYT in a trend that grows with increasing $m(t\bar{t})$ to predict a $p_T(t)$ spectrum that is harder than observed in the data. Figure 15 illustrates the $p_T(t\bar{t})$ spectrum in different $p_T(t)$ ranges. Larger $p_T(t)$ values can be kinematically correlated with higher $p_T(t\bar{t})$ values when the $t\bar{t}$ system is recoiling against additional QCD radiation in the event. The FxFx+PYT model predicts a harder $p_T(t\bar{t})$ spectrum than observed in the data for all $p_T(t)$ ranges. The POW+PYT and POW+HER predictions tend to overshoot the data in the higher $p_T(t)$ ranges at the lower $p_T(t\bar{t})$ values.

Next we investigate the $t\bar{t}$ kinematic observables. Figure 16 illustrates the $[m(t\bar{t}),\ |y(t\bar{t})|]$ distributions. Both variables are kinematically correlated with the observables ξ_1 and ξ_2 introduced above, and their combination is known to provide optimal information for constraining the PDFs [19]. For low- and medium-$m(t\bar{t})$ regions, the predictions are slightly more central than the data, though in the highest $m(t\bar{t})$ range the opposite effect is observed. In Fig. 17, the spectrum of $p_T(t\bar{t})$ is shown in bins of $|y(t\bar{t})|$. These two observables are rather uncorrelated, and thus it is not surprising that the description of the $p_T(t\bar{t})$ distribution by the models is similar in all $|y(t\bar{t})|$ ranges. Figure 18 presents the $[m(t\bar{t}),\ p_T(t\bar{t})]$ distributions. This is an interesting observable combination since the phase space for QCD radiation that is driving the $p_T(t\bar{t})$ observable is increasing with higher $m(t\bar{t})$. The trends observed in the single-differential $p_T(t\bar{t})$ distribution (see Fig. 9), namely, that FxFx+PYT (POW+HER) predicts a too hard (soft) spectrum, are somewhat enhanced in the higher $m(t\bar{t})$ ranges. Figure 19 shows the first simultaneous study of all three $t\bar{t}$ kinematic observables: p_T, mass, and rapidity. Overall, POW+PYT provides a fairly reasonable description, though FxFx+PYT and POW+HER show deficiencies in specific $m(t\bar{t})$ and $p_T(t\bar{t})$ phase space regions, with mostly small or moderate dependencies on $y(t\bar{t})$.

Finally, we perform several studies of $m(t\bar{t})$, investigating its correlation to several other kinematic observables. Figure 20 illustrates the distributions of $|y(t)|$. The trend that the predictions exhibit a more-central rapidity distribution than the data increases slightly with higher $m(t\bar{t})$. In Fig. 21, the $|\Delta\eta(t,\bar{t})|$ distributions are shown, which are sensitive to the hard scat-

tering dynamics. The data favor larger rapidity separations than predicted by the models, and the significance of this effect increases at larger $m(t\bar{t})$. The disagreement is the strongest for FxFx+PYT. For a given $m(t\bar{t})$ value, larger $|\Delta\eta(t,\bar{t})|$ are correlated with lower $p_T(t)$ values on average. This gives a hint that the effects of the models predicting harder $p_T(t)$ spectra and smaller $|\Delta\eta(t,\bar{t})|$ distributions, which are enhanced in the higher $m(t\bar{t})$ ranges (Figs. 14 and 21), are related. Figure 22 depicts the $[m(t\bar{t}),\ |\Delta\phi(t,\bar{t})|]$ distributions. At low $m(t\bar{t})$, the data prefer a slightly more back-to-back distribution of the top quark and antiquark compared to the models, but in the highest $m(t\bar{t})$ range, the trend reverses. Of all models considered, the FxFx+PYT simulation provides the best description and POW+HER the worst.

The observations made with the multi-differential cross sections can be summarized as follows. The p_T of the top quark and $t\bar{t}$, and the $t\bar{t}$ invariant mass are, in general, mildly correlated with rapidity of the same objects, and also the quality of their description by the MC models is nearly independent of the rapidity. As expected, larger kinematical correlations are observed between p_T and the mass observables. The trends of harder top quark p_T spectra and smaller rapidity separations between top quark and antiquark, when comparing the models to the data, is clearly enhanced at higher $m(t\bar{t})$. The tendency for FxFx+PYT (POW+HER) to predict p_T spectra for the $t\bar{t}$ system that are too hard (soft) is also stronger at higher $m(t\bar{t})$. In general, the p-values associated with the standard χ^2 values of the model-to-data comparisons are often much lower for the multi-differential $t\bar{t}$ cross sections than for the single-differential results presented in the previous subsection. This result is in line with the observations in recent comparable $t\bar{t}$ differential cross section papers from the ATLAS and CMS Collaborations [25, 28]. Another interesting observation is that the χ^2 values for both the single- and multi-differential $t\bar{t}$ cross sections are, on average, significantly higher than those observed in the corresponding previous measurements [26, 27] based on the 2016 data set only, which can be attributed to a substantially improved measurement precision. The χ^2 values that include the prediction uncertainties for the POW+PYT model (see Tables 3–4) are, in general, significantly lower than the standard ones. However, for several distributions such as $[m(t\bar{t}),\ |\Delta\phi(t,\bar{t})|]$, the values remain too high to indicate a good description of the data.

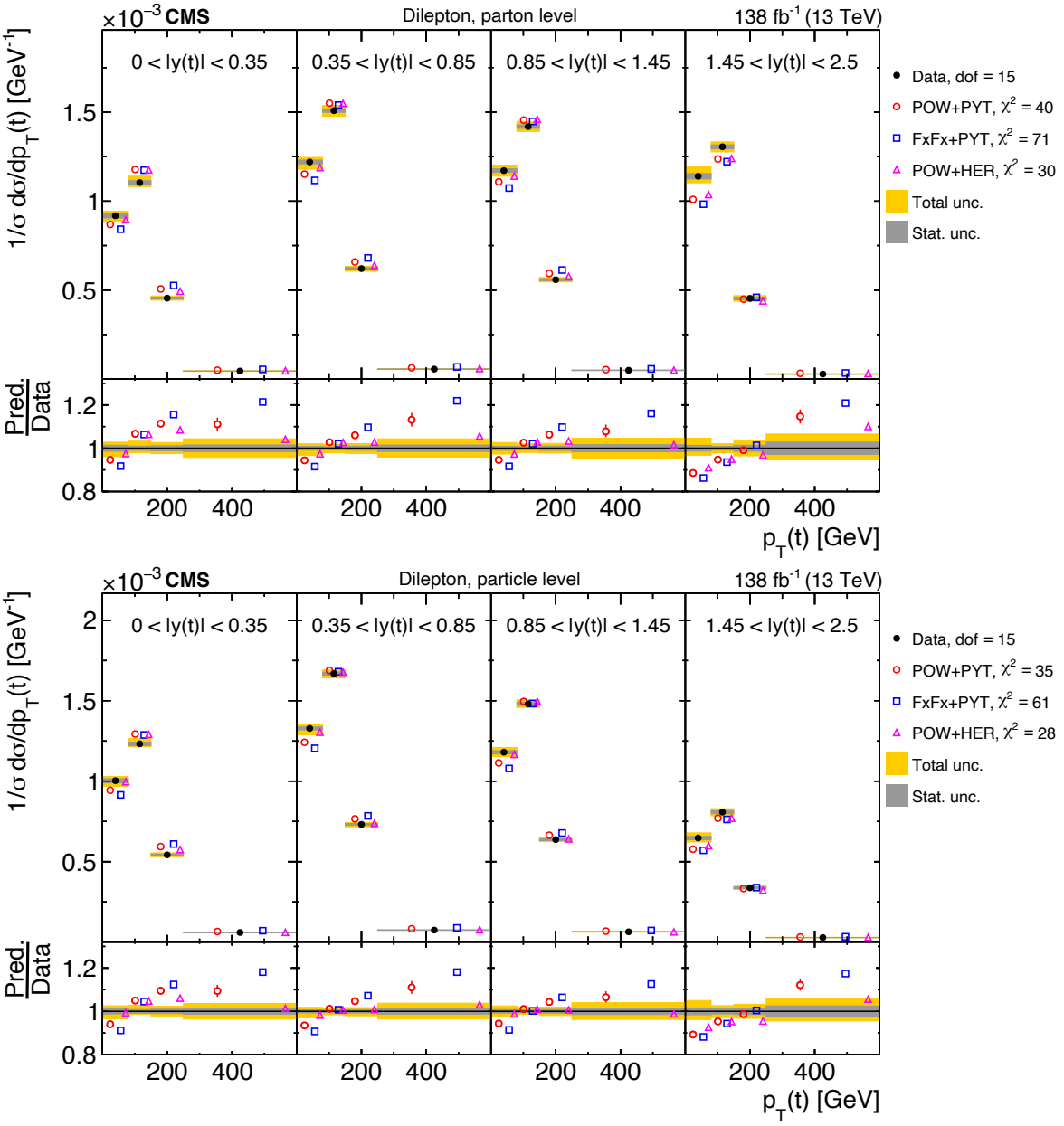

Figure 13: Normalized $[|y(t)|, p_T(t)]$ cross sections measured at the parton level in the full phase space (upper) and at the particle level in a fiducial phase space (lower). The data are shown as filled circles with grey and yellow bands indicating the statistical and total uncertainties (statistical and systematic uncertainties added in quadrature), respectively. For each distribution, the number of degrees of freedom (dof) is also provided. The cross sections are compared to various MC predictions (other points). The estimated uncertainties in the POWHEG+PYTHIA 8 ('POW-PYT') simulation are represented by a vertical bar on the corresponding points. For each MC model, a value of χ^2 is reported that takes into account the measurement uncertainties. The lower panel in each plot shows the ratios of the predictions to the data.

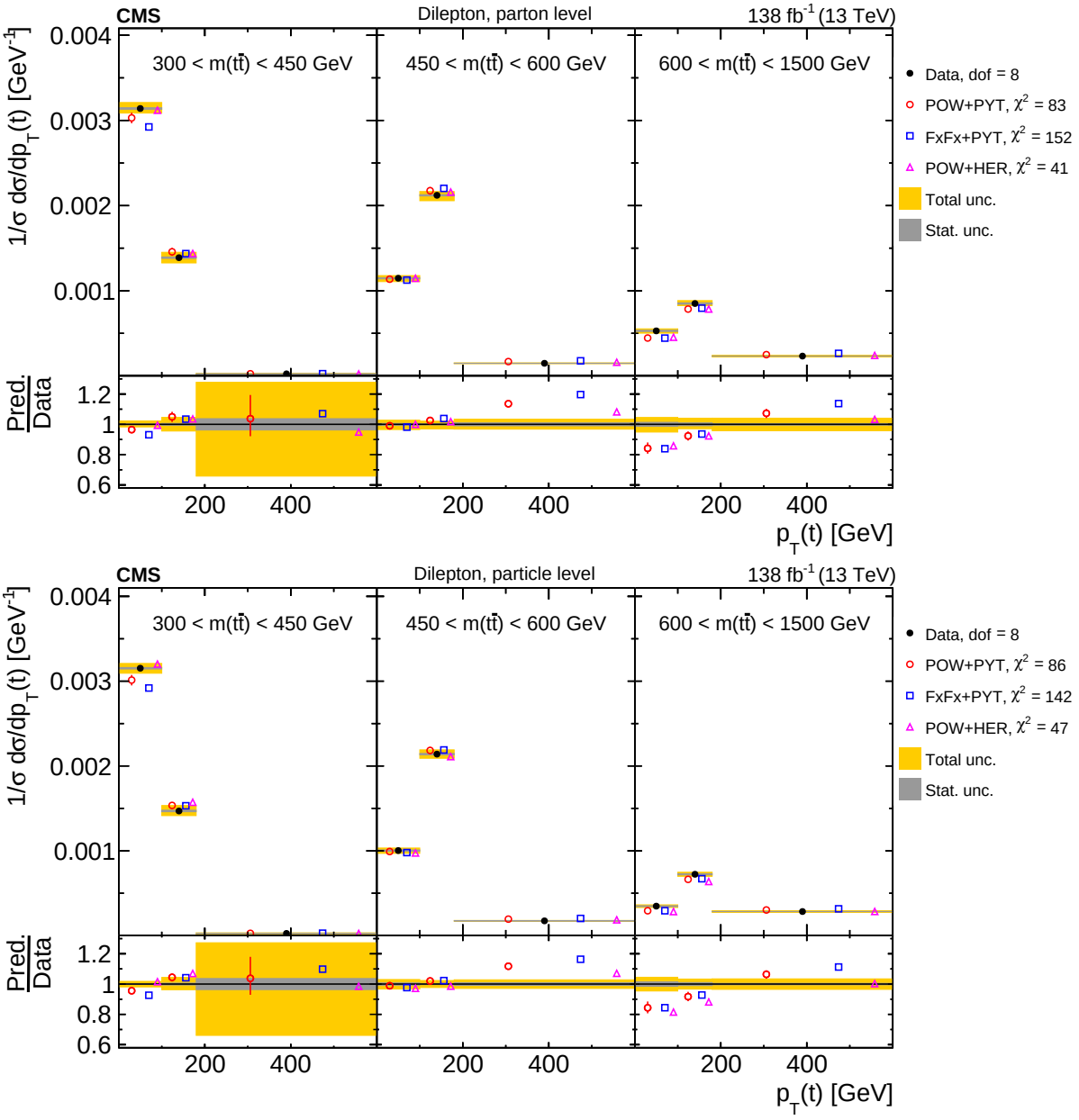

Figure 14: Normalized $[m(t\bar{t}),\ p_T(t)]$ cross sections are shown for data (filled circles) and various MC predictions (other points). Further details can be found in the caption of Fig. 13.

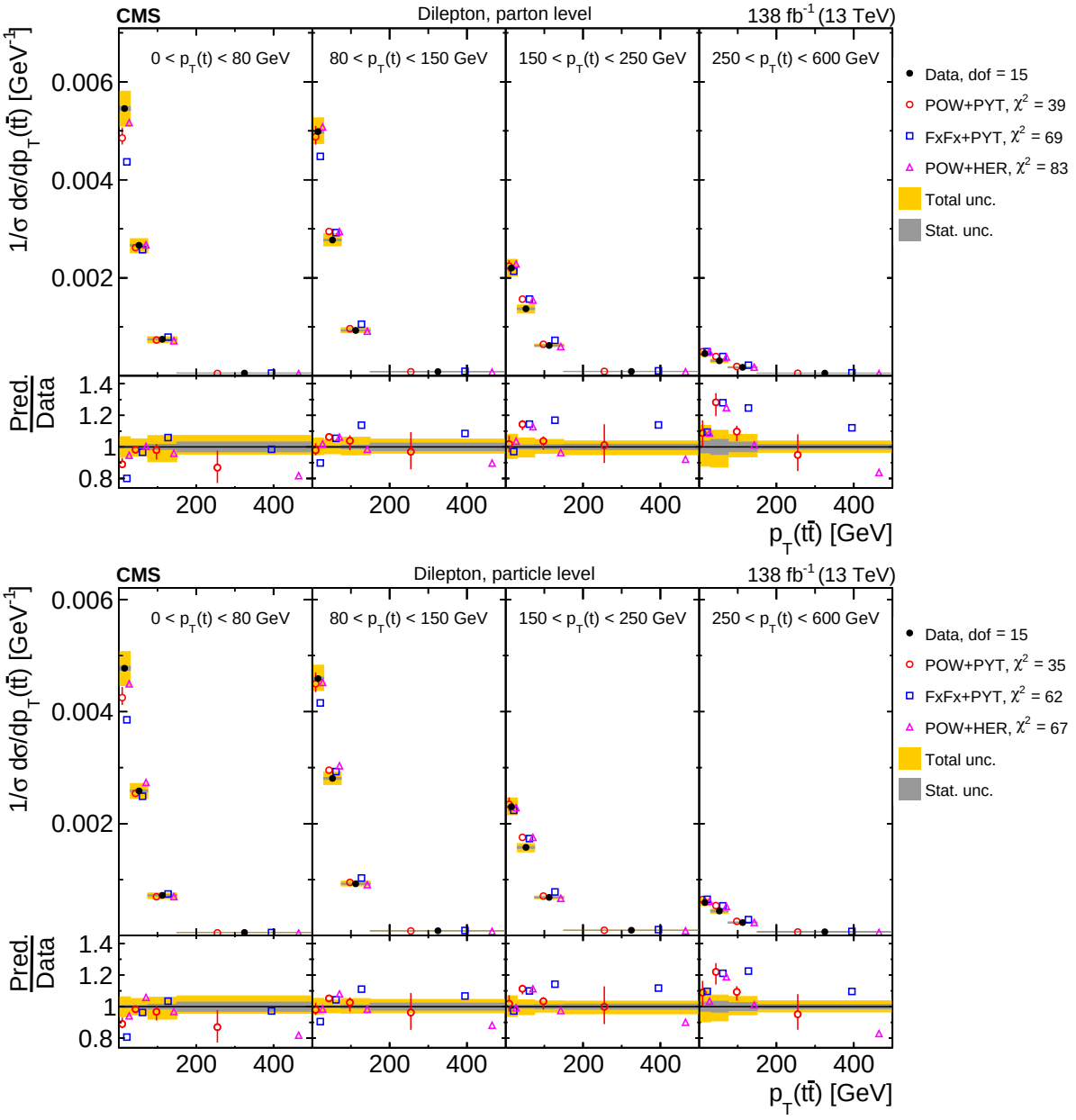

Figure 15: Normalized $[p_{\mathrm{T}}(\mathrm{t}),\ p_{\mathrm{T}}(\mathrm{t\bar{t}})]$ cross sections are shown for data (filled circles) and various MC predictions (other points). Further details can be found in the caption of Fig. 13.

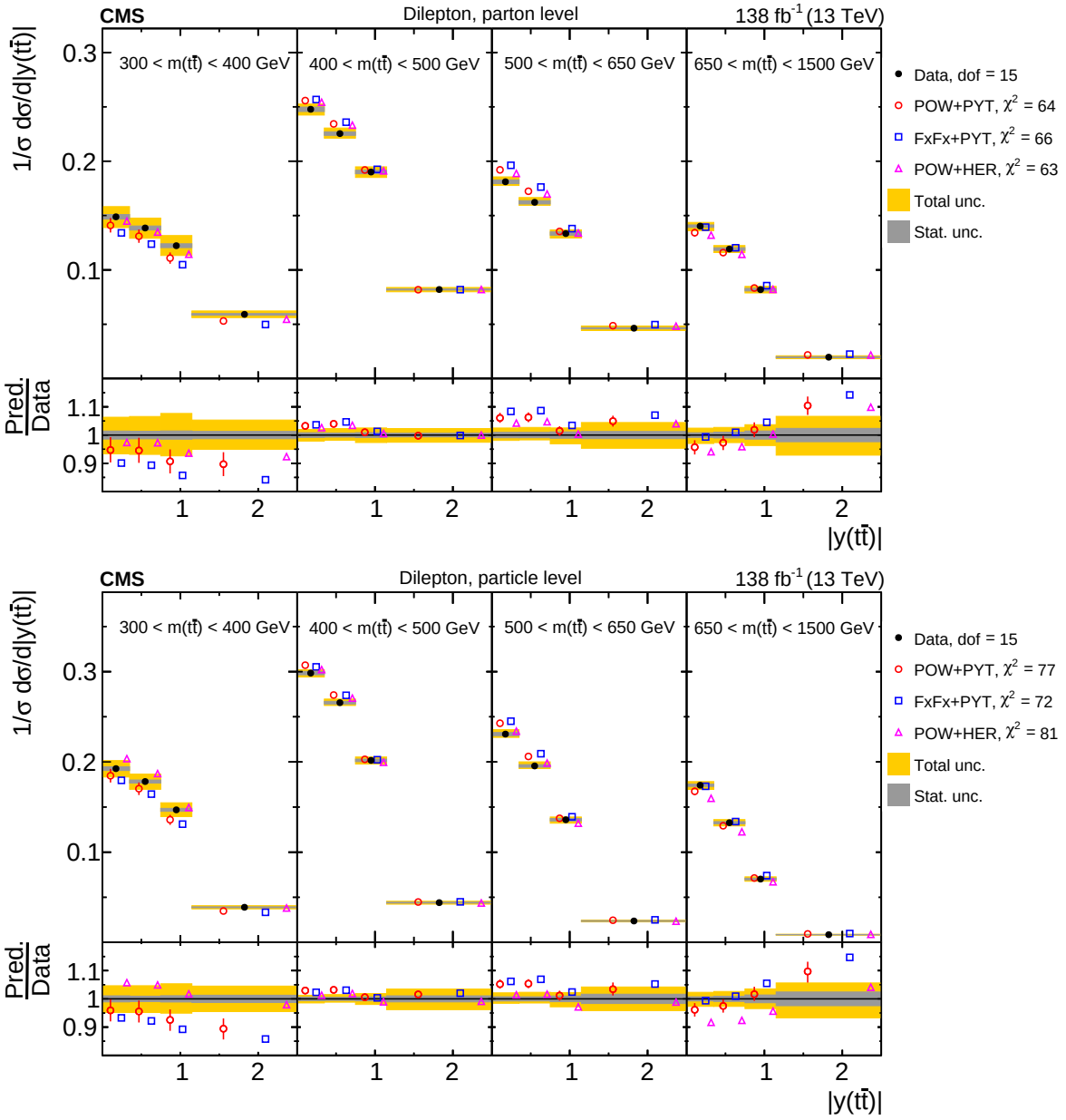

Figure 16: Normalized $[m(t\bar{t}),\ |y(t\bar{t})|]$ cross sections are shown for data (filled circles) and various MC predictions (other points). Further details can be found in the caption of Fig. 13.

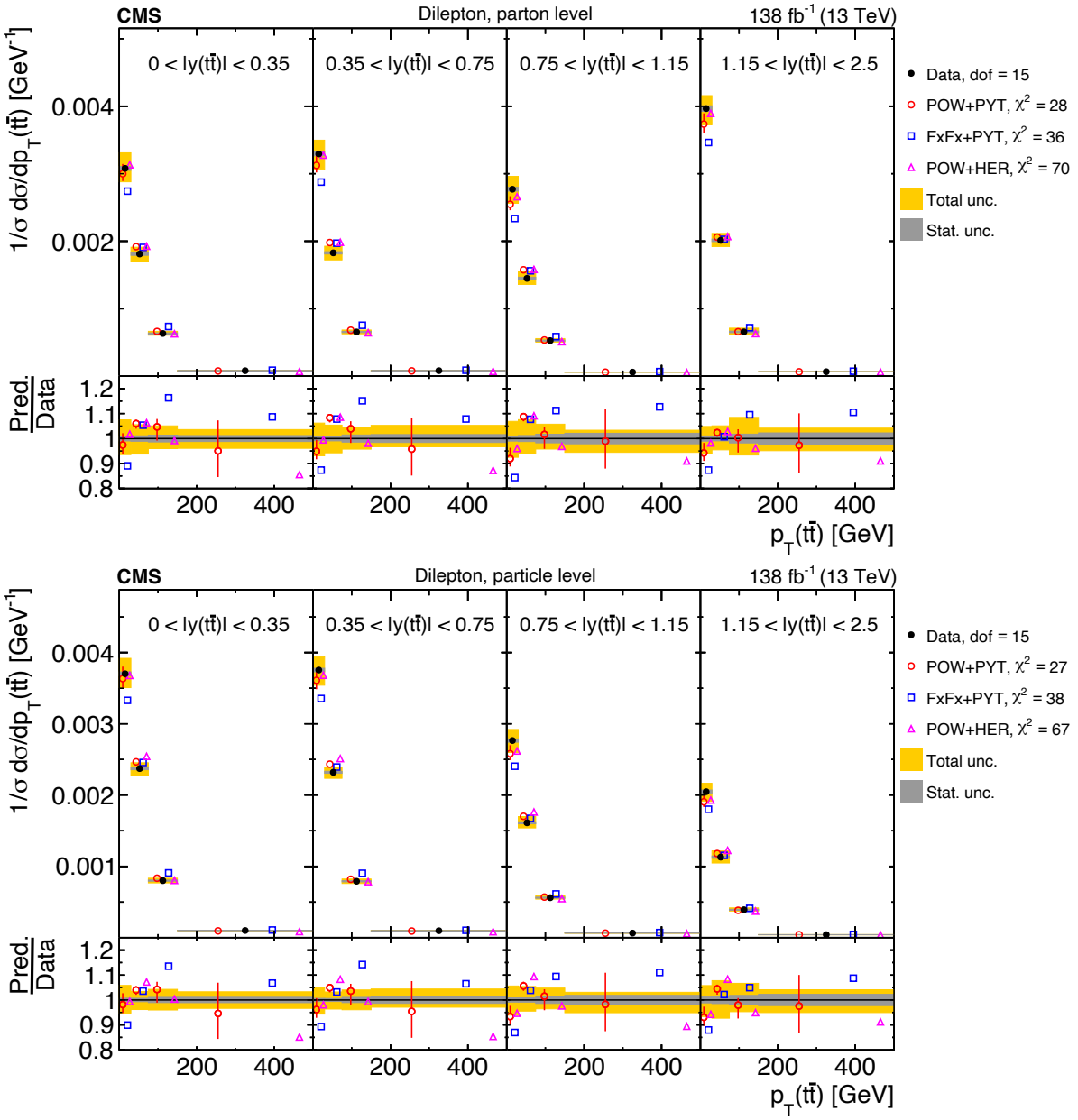

Figure 17: Normalized $[|y(\mathrm{t\bar{t}})|, p_{\mathrm{T}}(\mathrm{t\bar{t}})]$ cross sections are shown for data (filled circles) and various MC predictions (other points). Further details can be found in the caption of Fig. 13.

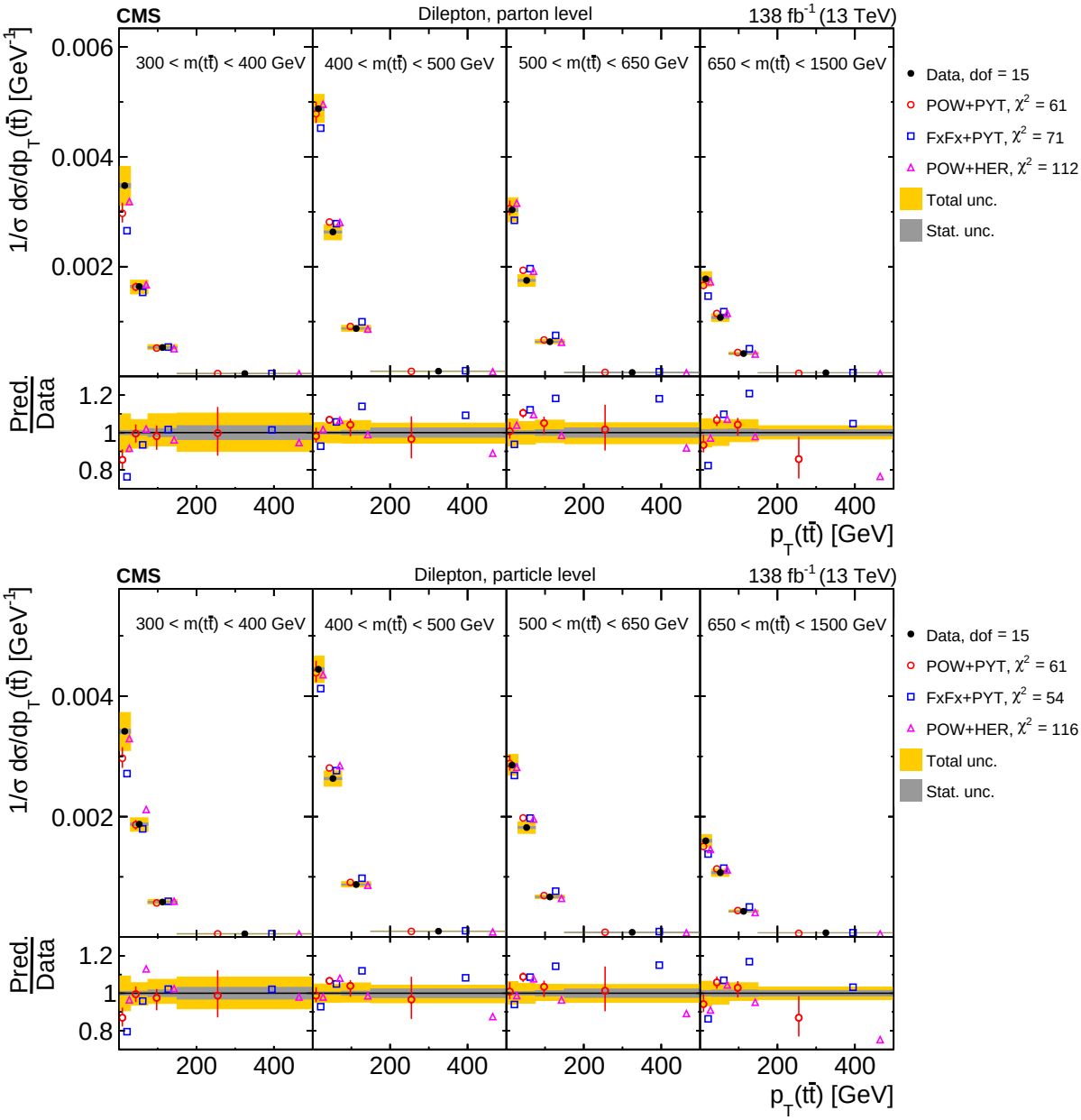

Figure 18: Normalized $[m(t\bar{t}),\ p_{T}(t\bar{t})]$ cross sections are shown for data (filled circles) and various MC predictions (other points). Further details can be found in the caption of Fig. 13.

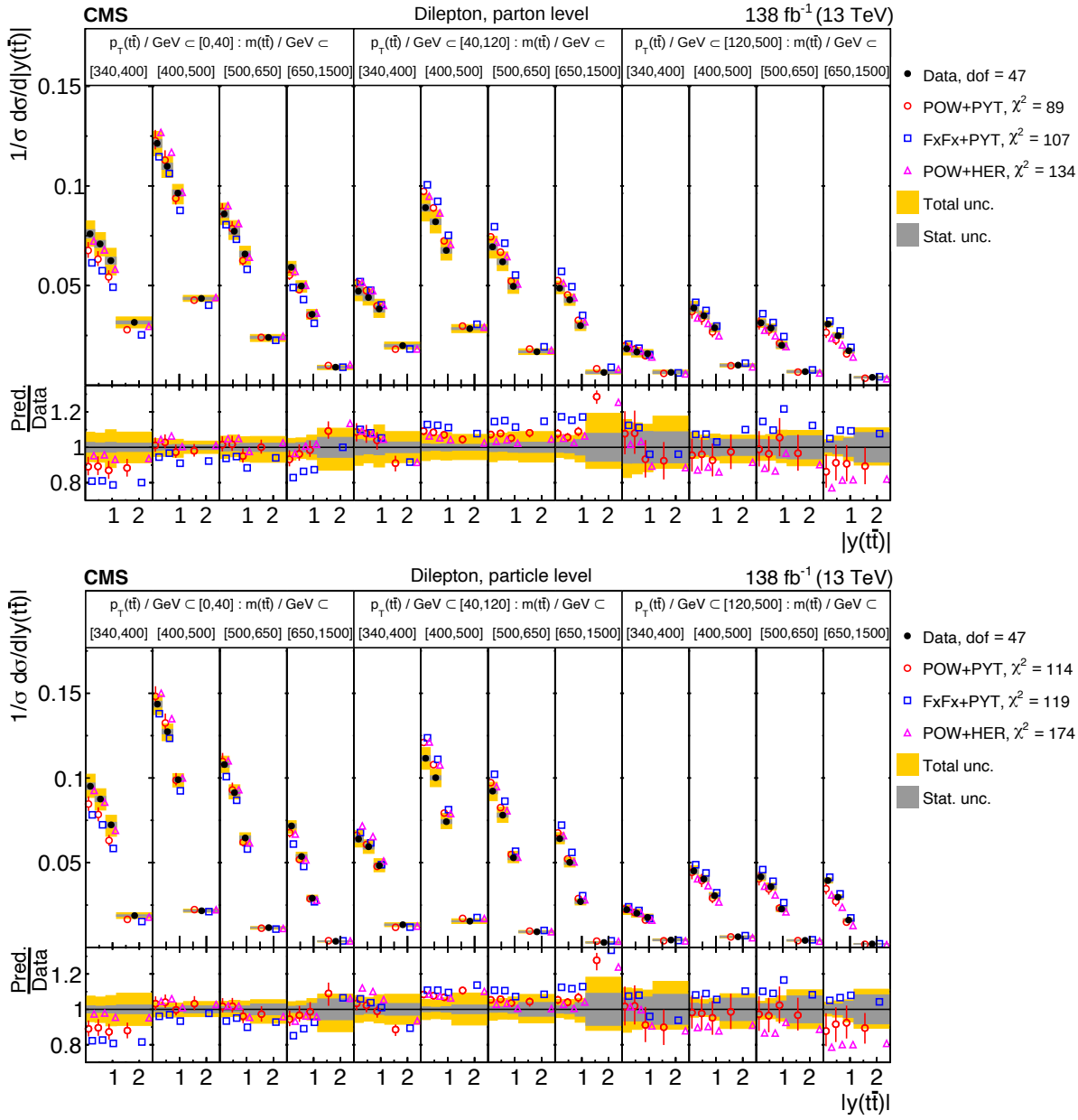

Figure 19: Normalized $[p_{\mathrm{T}}(\mathrm{t\bar{t}}), m(\mathrm{t\bar{t}}), |y(\mathrm{t\bar{t}})|]$ cross sections are shown for data (filled circles) and various MC predictions (other points). Further details can be found in the caption of Fig. 13.

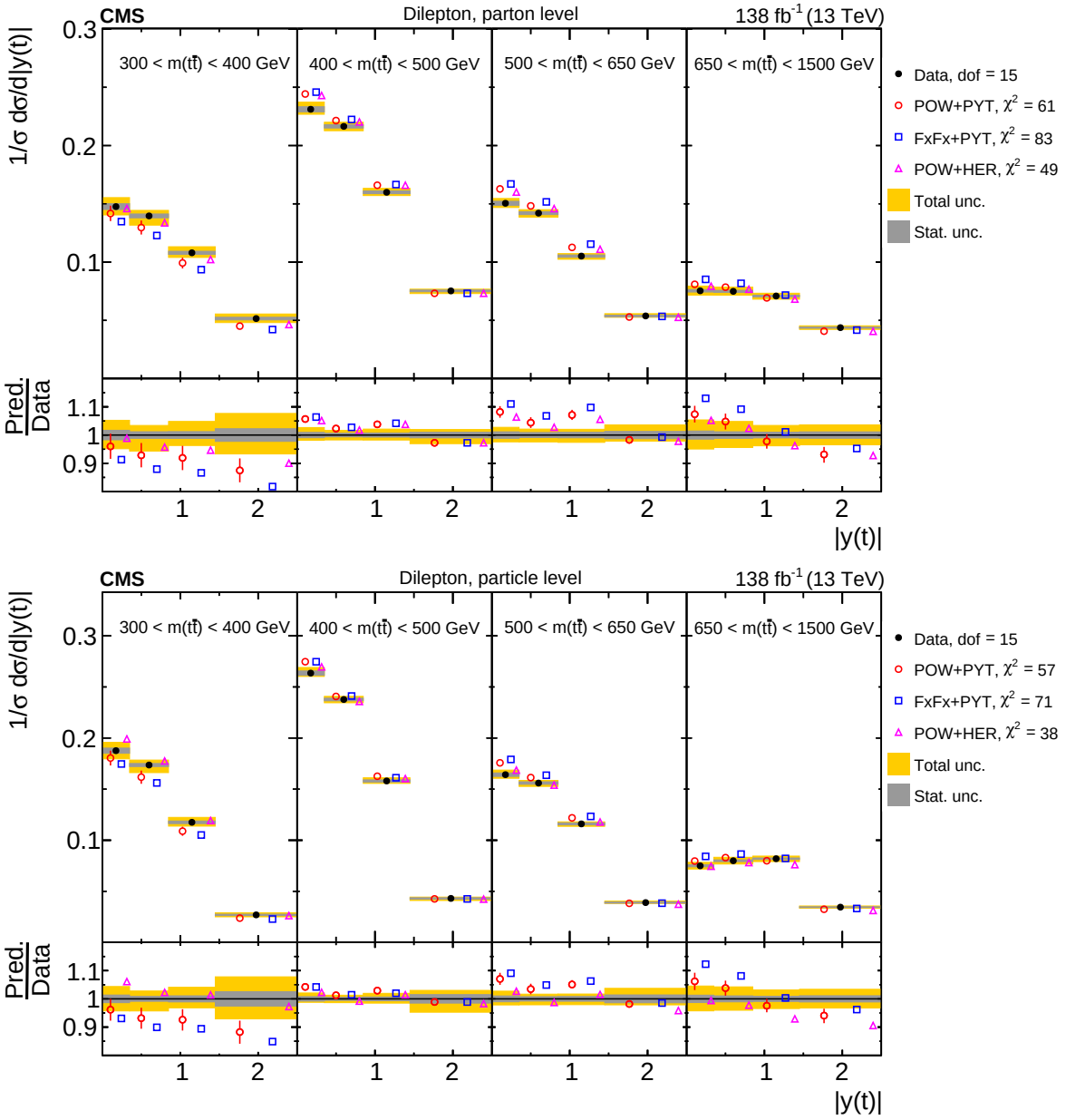

Figure 20: Normalized $[m(t\bar{t}), |y(t)|]$ cross sections are shown for data (filled circles) and various MC predictions (other points). Further details can be found in the caption of Fig. 13.

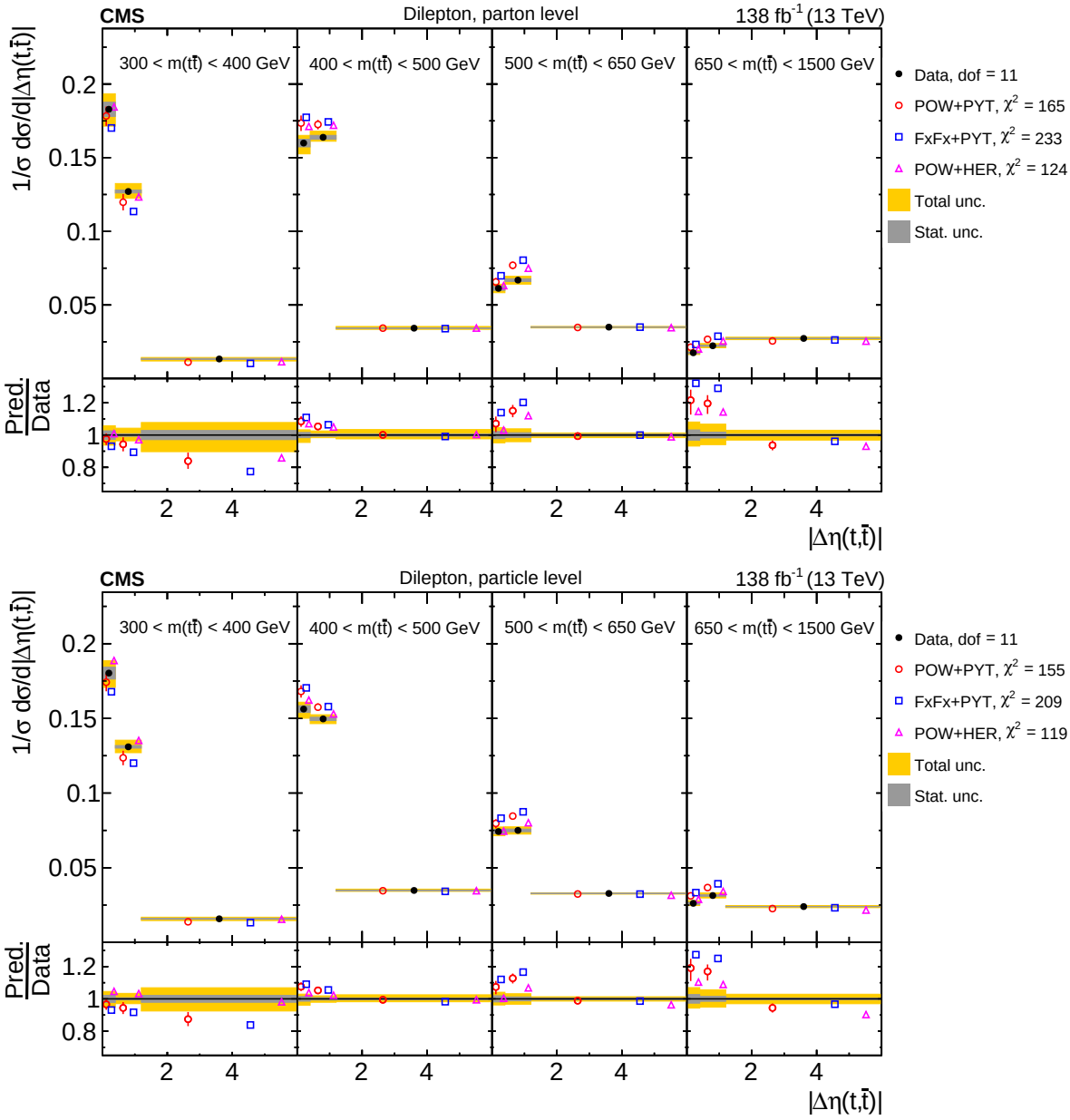

Figure 21: Normalized $[m(\mathrm{t\bar{t}}), |\Delta\eta(\mathrm{t},\bar{\mathrm{t}})|]$ cross sections are shown for data (filled circles) and various MC predictions (other points). Further details can be found in the caption of Fig. 13.

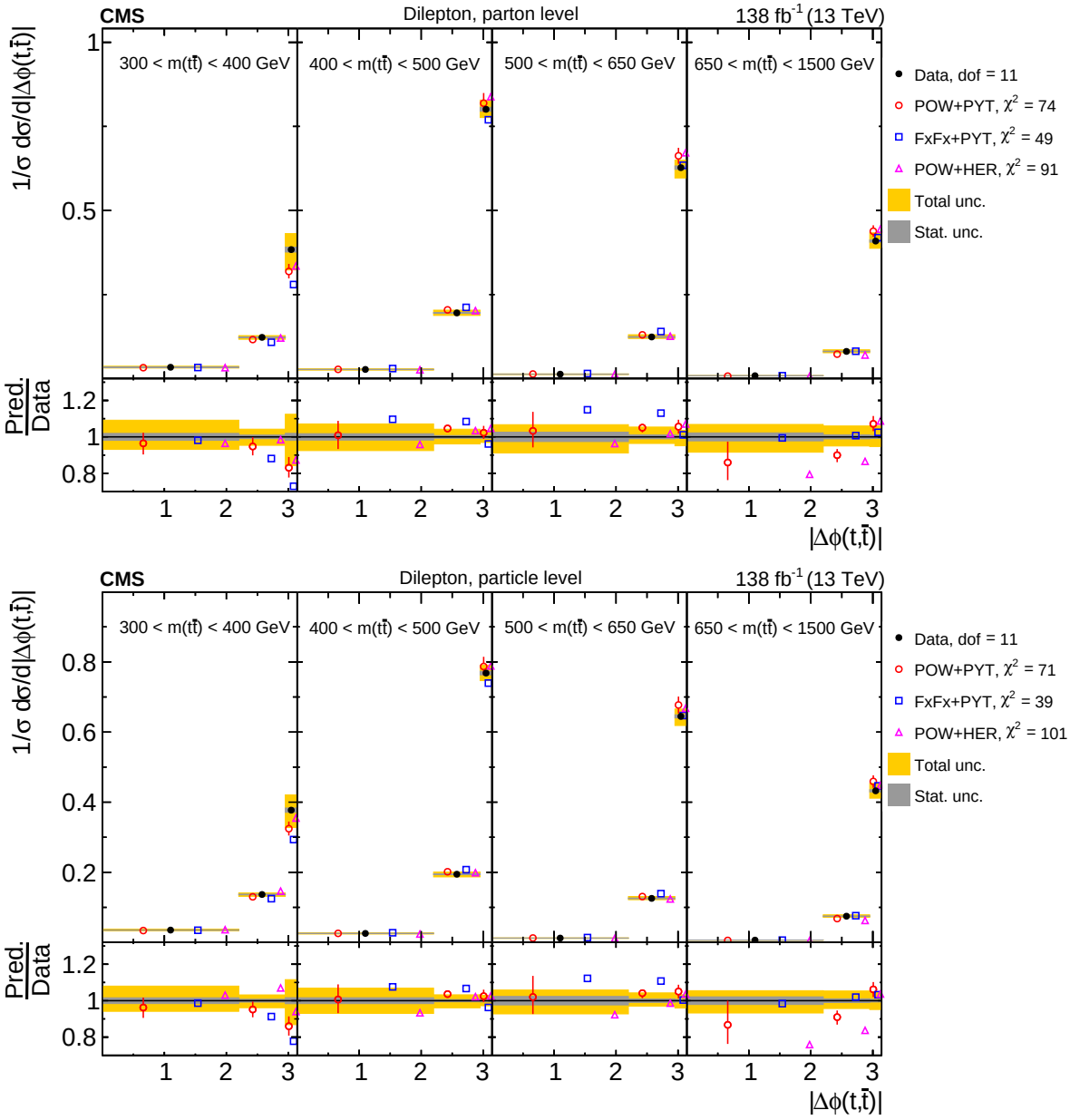

Figure 22: Normalized $[m(t\bar{t}), |\Delta\phi(t,\bar{t})|]$ cross sections are shown for data (filled circles) and various MC predictions (other points). Further details can be found in the caption of Fig. 13.

Table 3: The χ^2 values and dof of the measured normalized multi-differential cross sections for $t\bar{t}$ and top quark kinematic observables at the parton level are shown with respect to the predictions of various MC generators. The χ^2 values are calculated taking only measurement uncertainties into account and excluding theory uncertainties. For POW+PYT, the χ^2 values including theory uncertainties are indicated with the brackets (w. unc.).

Cross section variables	dof	χ^2		
		POW+PYT (w. unc.)	FxFx+PYT	POW+HER
$[\lvert y(t)\rvert,\ p_T(t)]$	15	40 (31)	71	30
$[m(t\bar{t}),\ p_T(t)]$	8	83 (35)	152	41
$[p_T(t),\ p_T(t\bar{t})]$	15	39 (21)	69	83
$[m(t\bar{t}),\ \lvert y(t\bar{t})\rvert]$	15	64 (42)	66	63
$[\lvert y(t\bar{t})\rvert,\ p_T(t\bar{t})]$	15	28 (15)	36	70
$[m(t\bar{t}),\ p_T(t\bar{t})]$	15	61 (43)	71	112
$[p_T(t\bar{t}),\ m(t\bar{t}),\ \lvert y(t\bar{t})\rvert]$	47	89 (64)	107	134
$[m(t\bar{t}),\ \lvert y(t)\rvert]$	15	61 (37)	83	49
$[m(t\bar{t}),\ \lvert\Delta\eta(t,\bar{t})\rvert]$	11	165 (31)	233	124
$[m(t\bar{t}),\ \lvert\Delta\phi(t,\bar{t})\rvert]$	11	74 (47)	49	91

Table 4: The χ^2 values and dof of the measured normalized multi-differential cross sections for $t\bar{t}$ and top quark kinematic observables at the particle level are shown with respect to the predictions of various MC generators. The χ^2 values are calculated taking only measurement uncertainties into account and excluding theory uncertainties. For POW+PYT, the χ^2 values including theory uncertainties are indicated with the brackets (w. unc.).

Cross section variables	dof	χ^2		
		POW+PYT (w. unc.)	FxFx+PYT	POW+HER
$[\lvert y(t)\rvert,\ p_T(t)]$	15	35 (25)	61	28
$[m(t\bar{t}),\ p_T(t)]$	8	86 (36)	142	47
$[p_T(t),\ p_T(t\bar{t})]$	15	35 (19)	62	67
$[m(t\bar{t}),\ \lvert y(t\bar{t})\rvert]$	15	77 (40)	72	81
$[\lvert y(t\bar{t})\rvert,\ p_T(t\bar{t})]$	15	27 (18)	38	67
$[m(t\bar{t}),\ p_T(t\bar{t})]$	15	61 (36)	54	116
$[p_T(t\bar{t}),\ m(t\bar{t}),\ \lvert y(t\bar{t})\rvert]$	47	114 (68)	119	174
$[m(t\bar{t}),\ \lvert y(t)\rvert]$	15	57 (26)	71	38
$[m(t\bar{t}),\ \lvert\Delta\eta(t,\bar{t})\rvert]$	11	155 (30)	209	119
$[m(t\bar{t}),\ \lvert\Delta\phi(t,\bar{t})\rvert]$	11	71 (42)	39	101

9.2 Results for lepton and b jet kinematic variables at the particle level

In this subsection we present selected kinematic distributions of the leptons and b jets produced in the decays of the top quark and antiquark, at the particle level in a fiducial phase space. These distributions are sensitive to both the dynamics of the $\mathrm{t\bar{t}}$ production and its decay. The kinematic observables of these objects are measured very precisely with the CMS detector. The single-differential cross sections studied at the particle level are shown in Figs. 23–25. The model-to-data χ^2 and corresponding p-values are listed in Tables 5 and 29, respectively.

First we investigate the lepton kinematic observables. Figure 23 shows the distributions of the p_T of the lepton (with negative charge), the ratio of the trailing and leading lepton p_T, and the ratio of the lepton and top antiquark p_T. As for the top antiquark (Fig. 7), the MC models predict a harder p_T spectrum for the leptons than observed, with FxFx+PYT exhibiting a stronger discrepancy. For the ratio of the trailing and leading lepton p_T, the models predict distributions that are slightly too soft, with FxFx+PYT again showing a more significant deviation than POW+PYT and POW+HER. The distribution of the ratio of the lepton and top quark p_T shows an interesting excess of data over the predictions for ratios above 0.8, which is an indication of a failure of the models to describe the dynamics of the top quark decay.

Next, we study three b jet observables, as shown in Fig. 24. The leading (trailing) b jet is defined as the b jet from the decay of the $\mathrm{t\bar{t}}$ system with the higher (lower) p_T. The distributions of the leading and trailing b jet p_T are reasonably well described by the POW+PYT and POW+HER models, while FxFx+PYT predicts a spectrum that is too hard. The third studied variable is the ratio between the sum of the p_T of the b and $\mathrm{\bar{b}}$ jets over the sum of the p_T of the top quark and antiquark $(p_\mathrm{T}(\mathrm{b}) + p_\mathrm{T}(\mathrm{\bar{b}}))/(p_\mathrm{T}(\mathrm{t}) + p_\mathrm{T}(\mathrm{\bar{t}}))$. All models predict a distribution that is somewhat too soft.

In the next set of studies, shown in Fig. 25, we analyze the invariant mass spectra of the lepton pair $m(\ell\bar{\ell})$, of the b jet pair $m(\mathrm{b\bar{b}})$, and of the combined system $m(\ell\bar{\ell}\mathrm{b\bar{b}})$. We investigate whether the model descriptions for the mass spectra of these partial decay systems follow the good description observed for the full $\mathrm{t\bar{t}}$ system, $m(\mathrm{t\bar{t}})$ (Fig. 9, middle plot). The $m(\ell\bar{\ell})$ distributions show a clear trend towards a somewhat harder spectrum in the model predictions compared to the data. The $m(\mathrm{b\bar{b}})$ spectra are reasonably well described overall by all three predictions, with a small trend of the data overshooting the predictions near threshold and at large mass values. The $m(\ell\bar{\ell}\mathrm{b\bar{b}})$ distributions show a similar trend. Furthermore, we investigate the sensitivity of the different mass spectra to the value of the top quark mass assumed in the POW+PYT calculation, by showing the predictions for m_t^MC = 169.5 and 175.5 GeV, compared to the nominal prediction using a value of 172.5 GeV. It is clear that the predicted $m(\ell\bar{\ell})$ and $m(\mathrm{b\bar{b}})$ spectra become harder with increasing m_t^MC, although the effects are diluted in the regions of small invariant masses compared to the $m(\mathrm{t\bar{t}})$ distribution shown in Fig. 9. The $m(\ell\bar{\ell}\mathrm{b\bar{b}})$ distribution clearly exhibits a better sensitivity to the m_t^MC value in the small invariant mass region, comparable to the one observed for the $m(\mathrm{t\bar{t}})$ spectrum.

Finally, we study additional dilepton distributions, whose kinematic obervables are among those in the present analysis that are reconstructed with highest precision. Figure 26 shows the $p_\mathrm{T}(\ell\bar{\ell})$ and $|\eta(\ell\bar{\ell})|$ distributions. Overall, they are reasonably well described by the three MC models, with FxFx+PYT predicting a $p_\mathrm{T}(\ell\bar{\ell})$ spectrum that is slightly too hard and an $|\eta(\ell\bar{\ell})|$ distribution that is a bit too central. Figures 27-29 show double-differential cross sections, illustrating the correlations between the dilepton kinematic observables. The $[|\eta(\ell\bar{\ell})|, m(\ell\bar{\ell})]$ distributions show that the tendency of the MC predictions to provide a $m(\ell\bar{\ell})$ spectrum that is harder than in data is a bit enhanced towards high values of $|\eta(\ell\bar{\ell})|$. The $[|\eta(\ell\bar{\ell})|, p_\mathrm{T}(\ell\bar{\ell})]$

spectra are well described by the POW+PYT and POW+HER models, while FxFx+PYT predicts $p_{\mathrm{T}}(\ell\bar{\ell})$ distributions that are somewhat too hard at small $|\eta(\ell\bar{\ell})|$ values. For the $[p_{\mathrm{T}}(\ell\bar{\ell}),\, m(\ell\bar{\ell})]$ distributions the $m(\ell\bar{\ell})$ spectra clearly become harder towards larger values of $p_{\mathrm{T}}(\ell\bar{\ell})$ and this effect is a bit more pronounced in the MC models than in the data.

The observations made with the differential $\mathrm{t\bar{t}}$ cross sections as functions of charged lepton and b jet kinematic observables can be summarized as follows. These measurements are the most accurate of all results presented in this document. Overall, the predictions from the MC models agree rather well with each other. The models predict harder distributions for the lepton p_{T} and the invariant mass of the lepton pair. The distributions of p_{T} of leading and trailing b jets, and of $m(\mathrm{b\bar{b}})$ are reasonably well described, except for FxFx+PYT, which predicts harder p_{T} spectra. Among the invariant mass spectra, the $m(\ell\bar{\ell}\mathrm{b\bar{b}})$ distribution clearly shows the strongest sensitivity to the value of the top quark mass used in the POW+PYT calculation. The single-differential p_{T} and η distributions of the dilepton system are reasonably well described by the models overall, although for double-differential distributions, including also $m(\ell\bar{\ell})$ as a possible second variable, some tensions are visible, in particular for FxFx+PYT. The standard χ^2 values indicate, in general, a poor quality in the description of the data by the nominal predictions. The inclusion of the prediction uncertainties for the POW+PYT model (see Table 5) results in χ^2 tests with reasonable p-values in most cases.

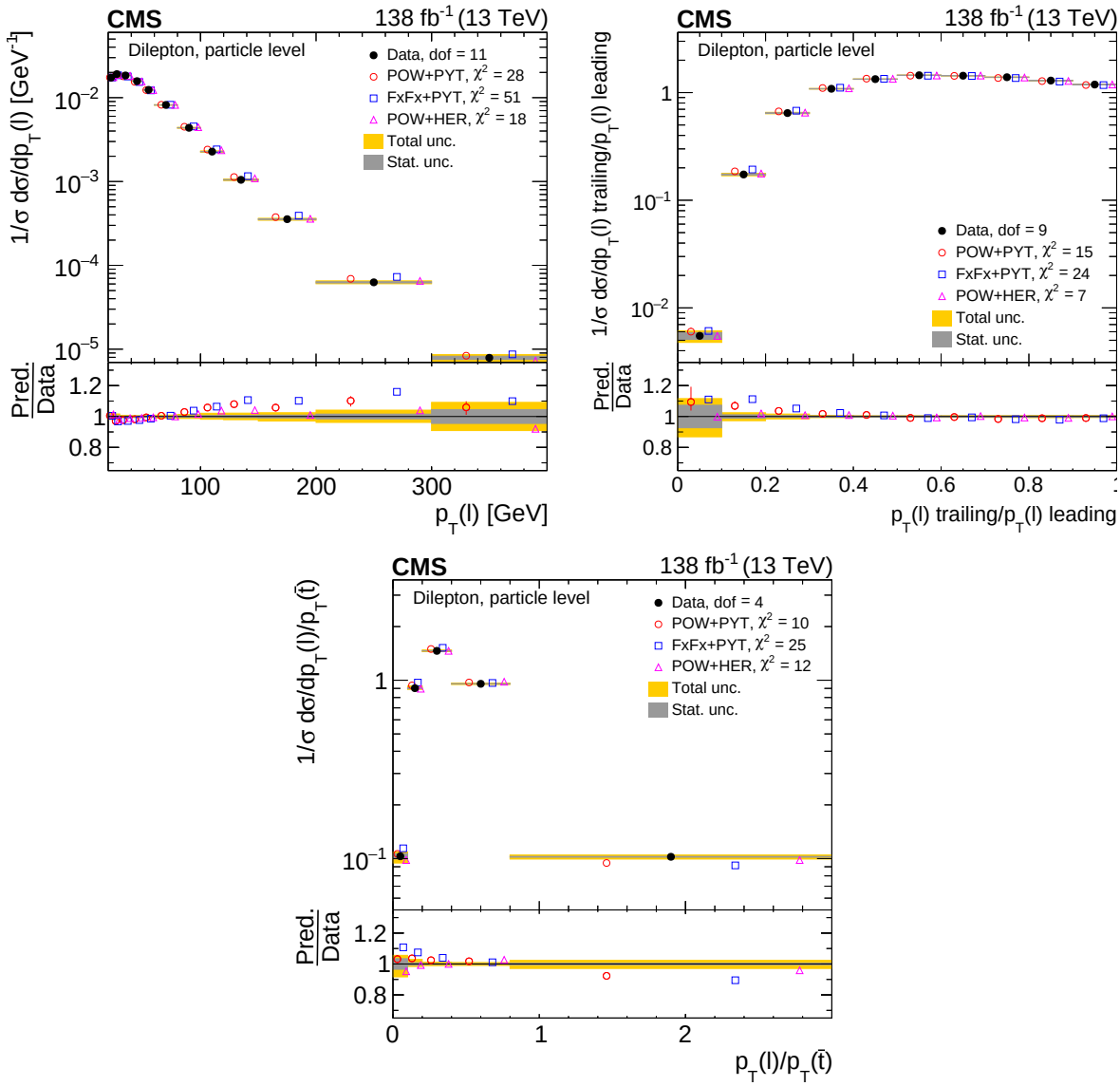

Figure 23: Normalized differential $t\bar{t}$ production cross sections as functions of p_T of the lepton (upper left), of the ratio of the trailing and leading lepton p_T (upper right), and of the ratio of lepton and top antiquark p_T (lower), measured at the particle level in a fiducial phase space. The data are shown as filled circles with grey and yellow bands indicating the statistical and total uncertainties (statistical and systematic uncertainties added in quadrature), respectively. For each distribution, the number of degrees of freedom (dof) is also provided. The cross sections are compared to various MC predictions (other points). The estimated uncertainties in the POWHEG+PYTHIA 8 ('POW-PYT') simulation are represented by a vertical bar on the corresponding points. For each MC model, a value of χ^2 is reported that takes into account the measurement uncertainties. The lower panel in each plot shows the ratios of the predictions to the data.

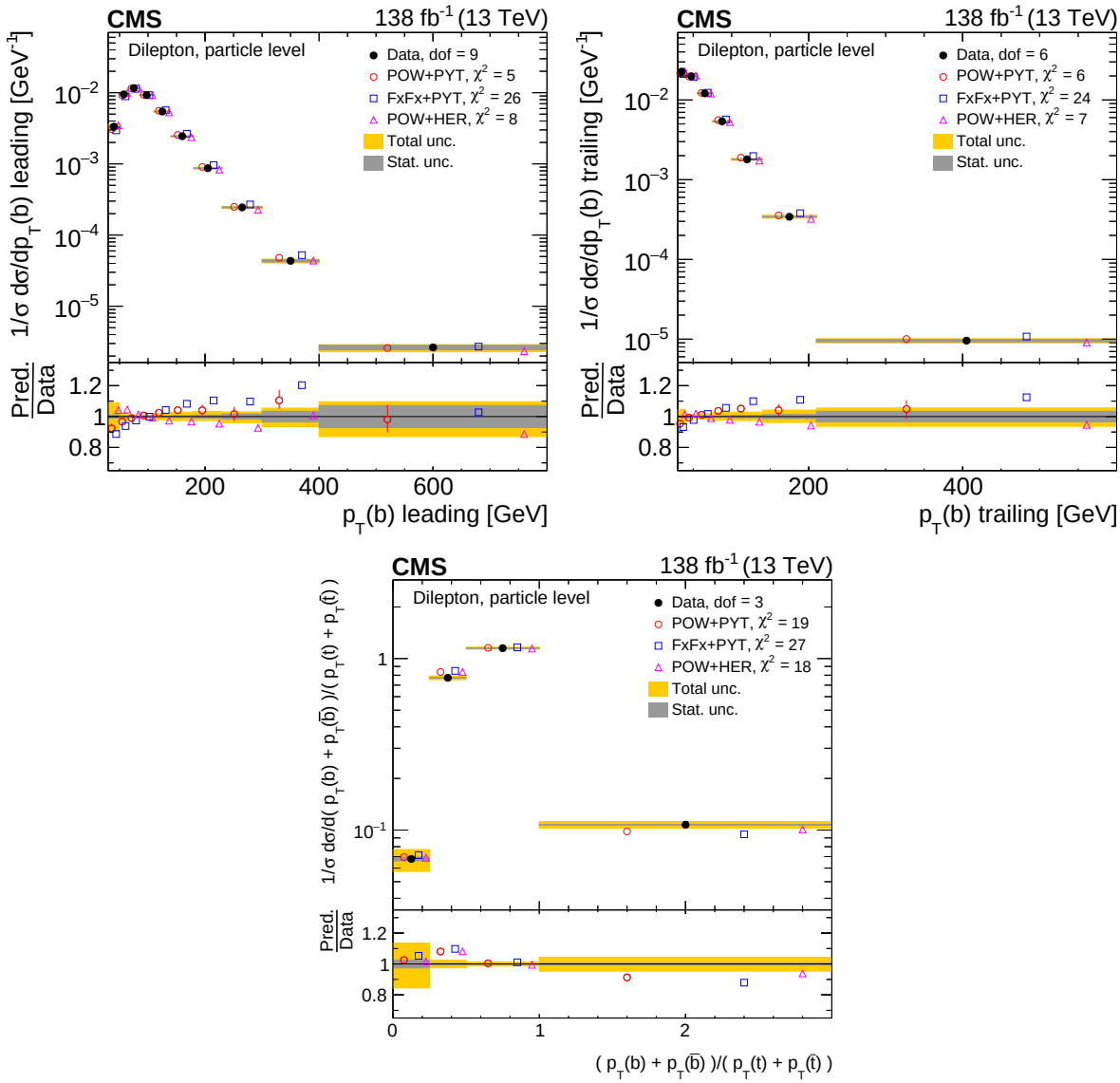

Figure 24: Normalized differential $\mathrm{t\bar{t}}$ production cross sections as functions of the p_{T} of the leading (upper left) and trailing (upper right) b jet, and $(p_{\mathrm{T}}(\mathrm{b}) + p_{\mathrm{T}}(\bar{\mathrm{b}}))/(p_{\mathrm{T}}(\mathrm{t}) + p_{\mathrm{T}}(\bar{\mathrm{t}}))$ (lower). Further details can be found in the caption of Fig. 23.

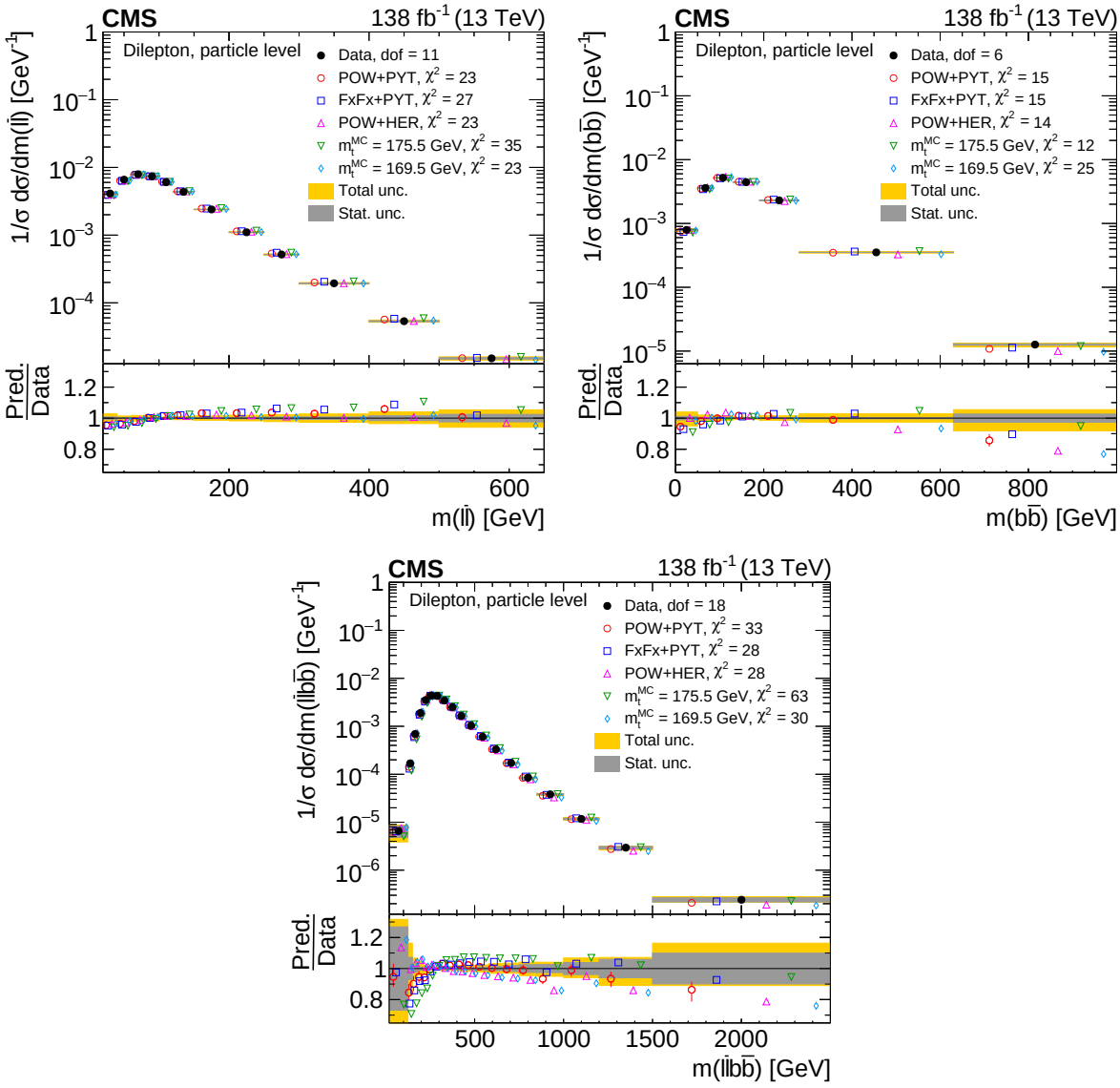

Figure 25: Normalized differential $\mathrm{t\bar{t}}$ production cross sections as functions of $m(\ell\bar{\ell})$ (upper left), $m(\mathrm{b\bar{b}})$ (upper right), and $m(\ell\bar{\ell}\mathrm{b\bar{b}})$ (lower) are shown for data (filled circles) and various MC predictions (other points). The distributions are also compared to POWHEG+PYTHIA 8 ('POW-PYT') simulations with different values of $m_{\mathrm{t}}^{\mathrm{MC}}$. Further details can be found in the caption of Fig. 23.

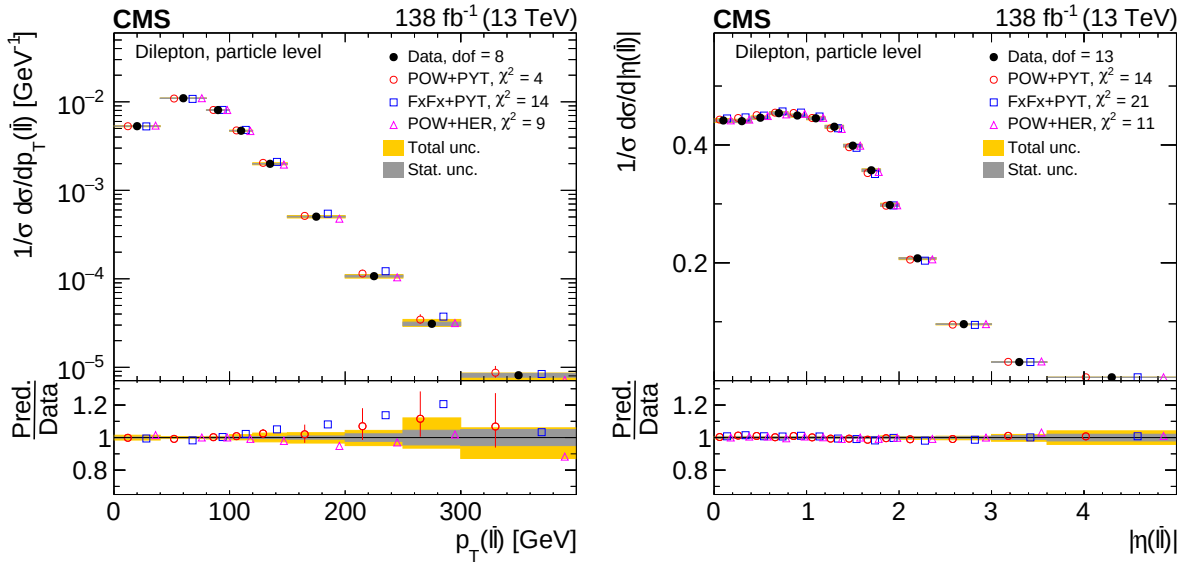

Figure 26: Normalized differential $t\bar{t}$ production cross sections as functions of $p_T(\ell\bar{\ell})$ (left) and $|\eta(\ell\bar{\ell})|$ (right) are shown for data (filled circles) and various MC predictions (other points). Further details can be found in the caption of Fig. 23.

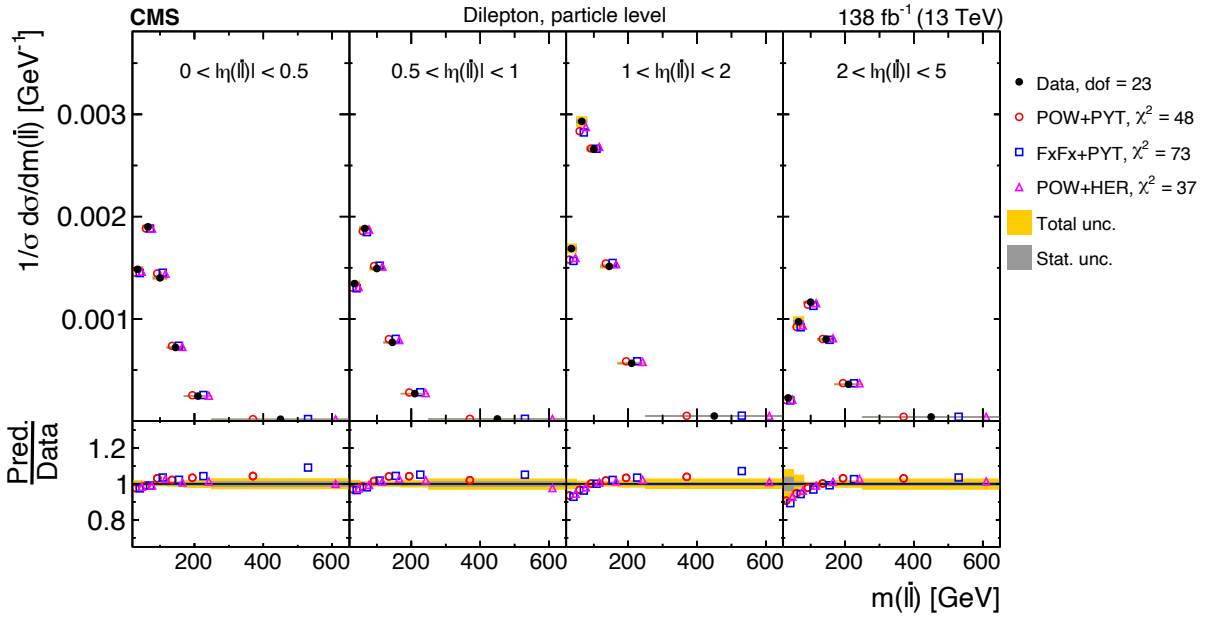

Figure 27: Normalized $[|\eta(\ell\bar{\ell})|, m(\ell\bar{\ell})]$ cross sections are shown for data (filled circles) and various MC predictions (other points). Further details can be found in the caption of Fig. 23.

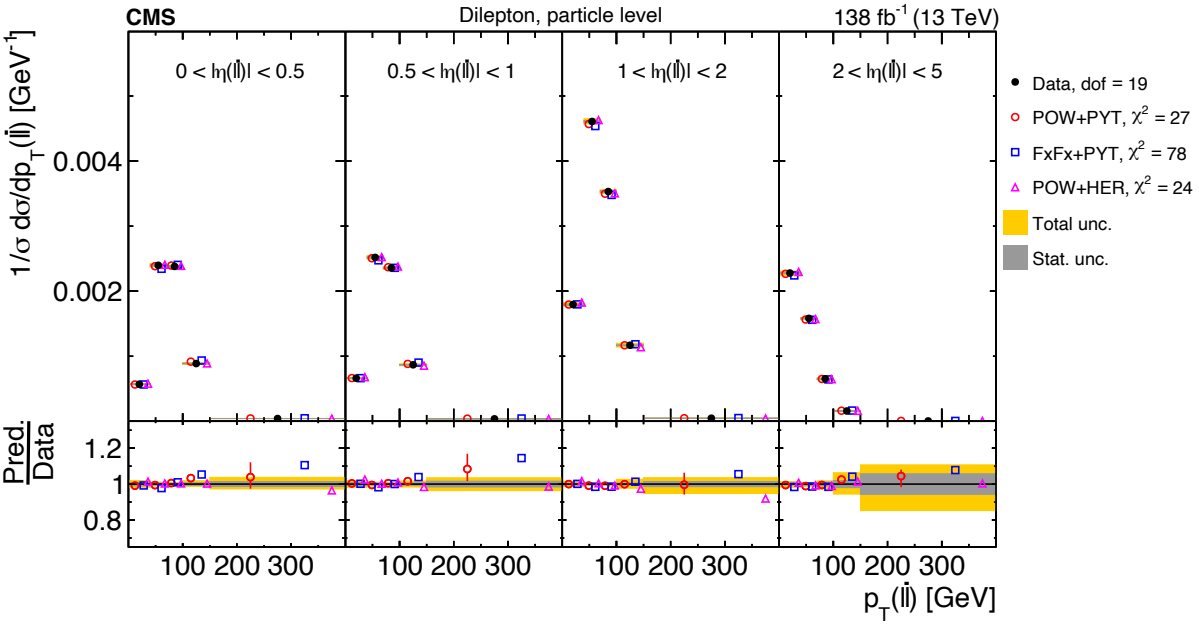

Figure 28: Normalized $[|\eta(\ell\bar{\ell})|,\ p_{\mathrm{T}}(\ell\bar{\ell})]$ cross sections are shown for data (filled circles) and various MC predictions (other points). Further details can be found in the caption of Fig. 23.

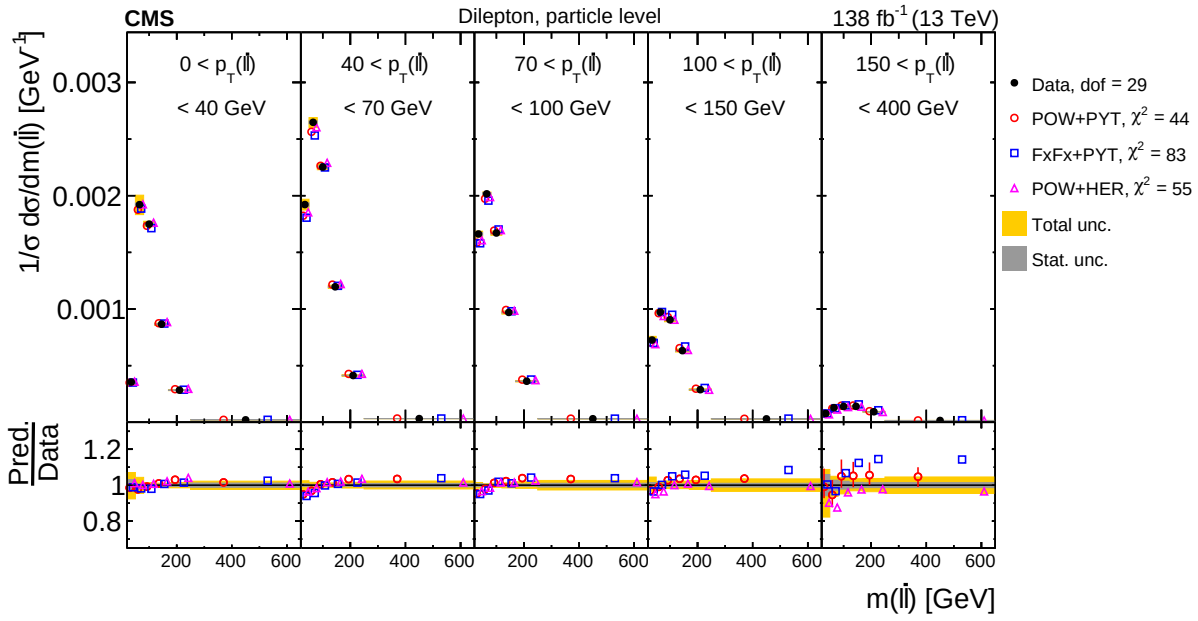

Figure 29: Normalized $[p_{\mathrm{T}}(\ell\bar{\ell}),\ m(\ell\bar{\ell})]$ cross sections are shown for data (filled circles) and various MC predictions (other points). Further details can be found in the caption of Fig. 23.

Table 5: The χ^2 values and dof of the measured normalized single-differential cross sections for lepton and b-jet kinematic observables at the particle level are shown with respect to the predictions of various MC generators. The χ^2 values are calculated taking only measurement uncertainties into account and excluding theory uncertainties. For POW+PYT, the χ^2 values including theory uncertainties are indicated with the brackets (w. unc.).

Cross section variables	dof	χ^2		
		POW+PYT (w. unc.)	FxFx+PYT	POW+HER
$p_T(\ell)$	11	28 (18)	51	18
$p_T(\ell)$ trailing/$p_T(\ell)$ leading	9	15 (11)	24	7
$p_T(\ell)/p_T(\bar{t})$	4	10 (9)	25	12
$p_T(b)$ leading	9	5 (4)	26	8
$p_T(b)$ trailing	6	6 (4)	24	7
$(p_T(b) + p_T(\bar{b}))/(p_T(t) + p_T(\bar{t}))$	3	19 (15)	27	18
$m(\ell\bar{\ell})$	11	23 (20)	27	23
$m(b\bar{b})$	6	15 (12)	15	14
$m(\ell\bar{\ell}b\bar{b})$	18	33 (18)	28	28
$p_T(\ell\bar{\ell})$	8	4 (3)	14	9
$\lvert\eta(\ell\bar{\ell})\rvert$	13	14 (9)	21	11
$[\lvert\eta(\ell\bar{\ell})\rvert, m(\ell\bar{\ell})]$	23	48 (28)	73	37
$[\lvert\eta(\ell\bar{\ell})\rvert, p_T(\ell\bar{\ell})]$	19	27 (14)	78	24
$[p_T(\ell\bar{\ell}), m(\ell\bar{\ell})]$	29	44 (37)	83	55

9.3 Results as a function of additional-jet multiplicity

In the final set of studies, we measure differential $\mathrm{t\bar{t}}$ production cross sections as a function of the multiplicity of additional jets in the events. These investigations provide an exemplary testing ground for the understanding of perturbative QCD. In particular, additional jets provide a second hard kinematic scale in the events, competing with the $\mathrm{t\bar{t}}$ invariant mass, and thus give rise to a multiscale situation that provides a challenge for the perturbative expansion [100]. The definitions of the cross sections are given in Section 6.1. Additional jets are measured at the particle level, and the top quark and antiquark are either measured at the parton level in the full phase space or at the particle level in a fiducial phase space. The cross sections are shown in Figs. 30–39. The upper and lower plots in the figures depict the cross sections at the parton and particle levels, respectively. The χ^2 values of model-to-data comparisons are listed in Tables 6–7 and the corresponding p-values in Tables 30–31.

We first discuss the additional-jet multiplicity N_{jet} distribution and its dependence on the minimum jet p_{T} requirement. This distribution provides a direct view of the amount of higher-order QCD radiation in $\mathrm{t\bar{t}}$ events. Figure 30 shows the N_{jet} cross section distributions for minimum p_{T} values of 40 and 100 GeV, respectively. The data are compared to the same three MC models as discussed above. The POW+PYT MC provides a good description of the N_{jet} distribution for the lower p_{T} value, though for the higher p_{T} value it starts to overshoot the data at larger jet multiplicities $N_{\mathrm{jet}} \geq 2$. The FxFx+PYT model exhibits a low accuracy, nearly independent of the p_{T} requirement. Its cross section prediction is too low for $N_{\mathrm{jet}} = 0$ and too high for $N_{\mathrm{jet}} = 1$, though it is reasonable for larger N_{jet}. The effect is underlined by large χ^2 values. The description of the data by POW+PYT and FxFx+PYT is consistent for the parton- and particle-level cross sections, but for POW+HER a different picture emerges. This model clearly predicts too many extra jets for the parton-level cross section, but describes the data well at the particle level in a fiducial phase space. The parton level is defined for the full phase space. However, there might be a larger contribution from extra jets in POW+HER from events that are predominantly outside the particle-level fiducial phase space for the top quark and antiquark.

Next we investigate the top quark and $\mathrm{t\bar{t}}$ kinematics as a function of N_{jet}. This allows us to map the kinematic correlations to additional jets and to check whether description deficiencies seen, e.g. for the top quark transverse momentum $p_{\mathrm{T}}(\mathrm{t})$ spectrum (Fig. 7), are associated with specific N_{jet} values. Figure 31 shows the $p_{\mathrm{T}}(\mathrm{t})$ distributions. For POW+PYT, the effect of a harder $p_{\mathrm{T}}(\mathrm{t})$ spectrum compared to that observed in data seems to be slightly enhanced in the lower two jet multiplicity bins $N_{\mathrm{jet}} = 0, 1$, though a reasonable description is seen for higher multiplicities $N_{\mathrm{jet}} > 1$. The FxFx+PYT model predicts harder $p_{\mathrm{T}}(\mathrm{t})$ spectra, rather independent of N_{jet}. Among all considered predictions, POW+HER provides the best description of the $p_{\mathrm{T}}(\mathrm{t})$ distributions at the particle level, but fails at the parton level, where its large excess at $N_{\mathrm{jet}} > 1$ is accompanied by a $p_{\mathrm{T}}(\mathrm{t})$ spectrum that falls too steeply. The distributions of $|y(\mathrm{t})|$ are illustrated in Fig. 32. The data prefer slightly less-central $|y(\mathrm{t})|$ distributions than the models, with weak dependence on N_{jet}. Figure 33 shows the $[N_{\mathrm{jet}}, p_{\mathrm{T}}(\mathrm{t\bar{t}})]$ distributions. The two variables are correlated since additional QCD radiation in the event leads to nonzero values of $p_{\mathrm{T}}(\mathrm{t\bar{t}})$, as well as to values $N_{\mathrm{jet}} \geq 1$. For low jet multiplicities, $N_{\mathrm{jet}} = 0, 1$, the POW+PYT model provides a reasonable description of the measured $p_{\mathrm{T}}(\mathrm{t\bar{t}})$ spectrum, though for $N_{\mathrm{jet}} > 1$ it predicts a rise of the cross section that is too steep over the first three $p_{\mathrm{T}}(\mathrm{t\bar{t}})$ ranges from 0 to 100 GeV. The ratio of the FxFx+PYT model to the data always exhibits a positive slope over the first three $p_{\mathrm{T}}(\mathrm{t\bar{t}})$ ranges, irrespectively of N_{jet}. The POW+HER prediction mostly follows the POW+PYT model, except at high $p_{\mathrm{T}}(\mathrm{t\bar{t}})$ where it is a bit lower.

The distributions of $m(\mathrm{t\bar{t}})$ are shown in Fig. 34. The shapes of these distributions are fairly well

modeled by POW+PYT, for all N_{jet} ranges. The FxFx+PYT calculation clearly predicts much harder $m(\mathrm{t\bar{t}})$ spectra for $N_{\text{jet}} = 1$. The POW+HER provides a fair description at the $\mathrm{t\bar{t}}$ particle level, but fails again at the parton level, where it predicts a much softer $m(\mathrm{t\bar{t}})$ distribution for $N_{\text{jet}} > 1$. Figure 35 displays the $|y(\mathrm{t\bar{t}})|$ spectra. The shapes of these distributions are reasonably well described by the models, irrespectively of the N_{jet} range, but specific N_{jet}-dependent normalization problems remain for FxFx+PYT and POW+HER at the particle level. Figure 36 depicts the $\Delta\eta(\mathrm{t}, \bar{\mathrm{t}})$ distributions. The description by the models is poor, which is also indicated by the large χ^2 values with very small p-values. For the first two N_{jet} bins there is a clear trend for the models to predict rapidity separations between top quark and antiquark that are too small, while in the last bin the trend is slightly reversed.

Figures 37–39 show triple-differential cross sections as functions of N_{jet}, $m(\mathrm{t\bar{t}})$, and $|y(\mathrm{t\bar{t}})|$. These cross sections were one of the highlights of our previous analysis [27], where it was demonstrated that they can be used for a simultaneous extraction of the top quark pole mass, α_{S}, and the PDFs, with good precision. We measure the cross sections separately using two ($N_{\text{jet}} = 0$ and $N_{\text{jet}} \geq 1$), three ($N_{\text{jet}} = 0$, $N_{\text{jet}} = 1$, and $N_{\text{jet}} \geq 2$), and four ($N_{\text{jet}} = 0$, $N_{\text{jet}} = 1$, $N_{\text{jet}} = 2$ and $N_{\text{jet}} \geq 3$) bins of N_{jet} for the particle-level jets. These cross sections are denoted as $[N_{\text{jet}}^{0,1+}, m(\mathrm{t\bar{t}}), |y(\mathrm{t\bar{t}})|]$, $[N_{\text{jet}}^{0,1,2+}, m(\mathrm{t\bar{t}}), |y(\mathrm{t\bar{t}})|]$, and $[N_{\text{jet}}^{0,1,2,3+}, m(\mathrm{t\bar{t}}), |y(\mathrm{t\bar{t}})|]$, respectively. The $[N_{\text{jet}}^{0,1,2,3+}, m(\mathrm{t\bar{t}}), |y(\mathrm{t\bar{t}})|]$ cross sections are measured for the first time. A striking feature of the comparisons of the MC models to the data is a growing discrepancy when going from two to three and four bins of N_{jet}. The $[N_{\text{jet}}^{0,1,2,3+}, m(\mathrm{t\bar{t}}), |y(\mathrm{t\bar{t}})|]$ cross sections clearly exhibit the best power for distinguishing the models. Among all tested predictions, the POW+PYT model provides the overall best description. The FxFx+PYT calculation exhibits the same normalization problems versus N_{jet} that are visible in the N_{jet} spectrum (Fig. 30), coupled with a small trend to predict cross sections towards large $m(\mathrm{t\bar{t}})$ that are too high, though the $|y(\mathrm{t\bar{t}})|$ shapes are described reasonably well. The POW+HER model delivers a description at the particle level that is comparable to that of POW+PYT, but fails at the parton level where it overshoots the data for the $N_{\text{jet}} = 2$ and $N_{\text{jet}} > 2$ bins.

The comparisons of MC models and data can be summarized as follows. The POW+PYT calculation clearly provides the best description of the additional-jet multiplicity N_{jet} in $\mathrm{t\bar{t}}$ events. The FxFx+PYT and POW+HER models fail, the former predicting too many events with $N_{\text{jet}} = 1$ and the latter too many events at the parton level in the full phase space with $N_{\text{jet}} > 1$. There are rather weak kinematic correlations of the top quark and $\mathrm{t\bar{t}}$ rapidity spectra with N_{jet}, and the quality of the descriptions of the rapidity spectra by the models is rather independent of N_{jet}. As expected, there are larger kinematic correlations of top quark and $\mathrm{t\bar{t}}$ transverse momenta or $\mathrm{t\bar{t}}$ invariant mass with N_{jet}, showing harder spectra for larger N_{jet}. All models exhibit different level of discrepancies for these distributions that depend on the jet multiplicity. For instance, there is an indication that the problem of harder $p_{\mathrm{T}}(\mathrm{t})$ distributions in the models is localized at small jet multiplicities. The theory-to-data χ^2 values indicate a rather poor description of the data by the nominal model predictions for many of the discussed distributions. The χ^2 values that include the prediction uncertainties for POW+PYT (see Tables 6–7) are significantly reduced, but the corresponding p-values remain too small for a reasonable description of several measured observables.

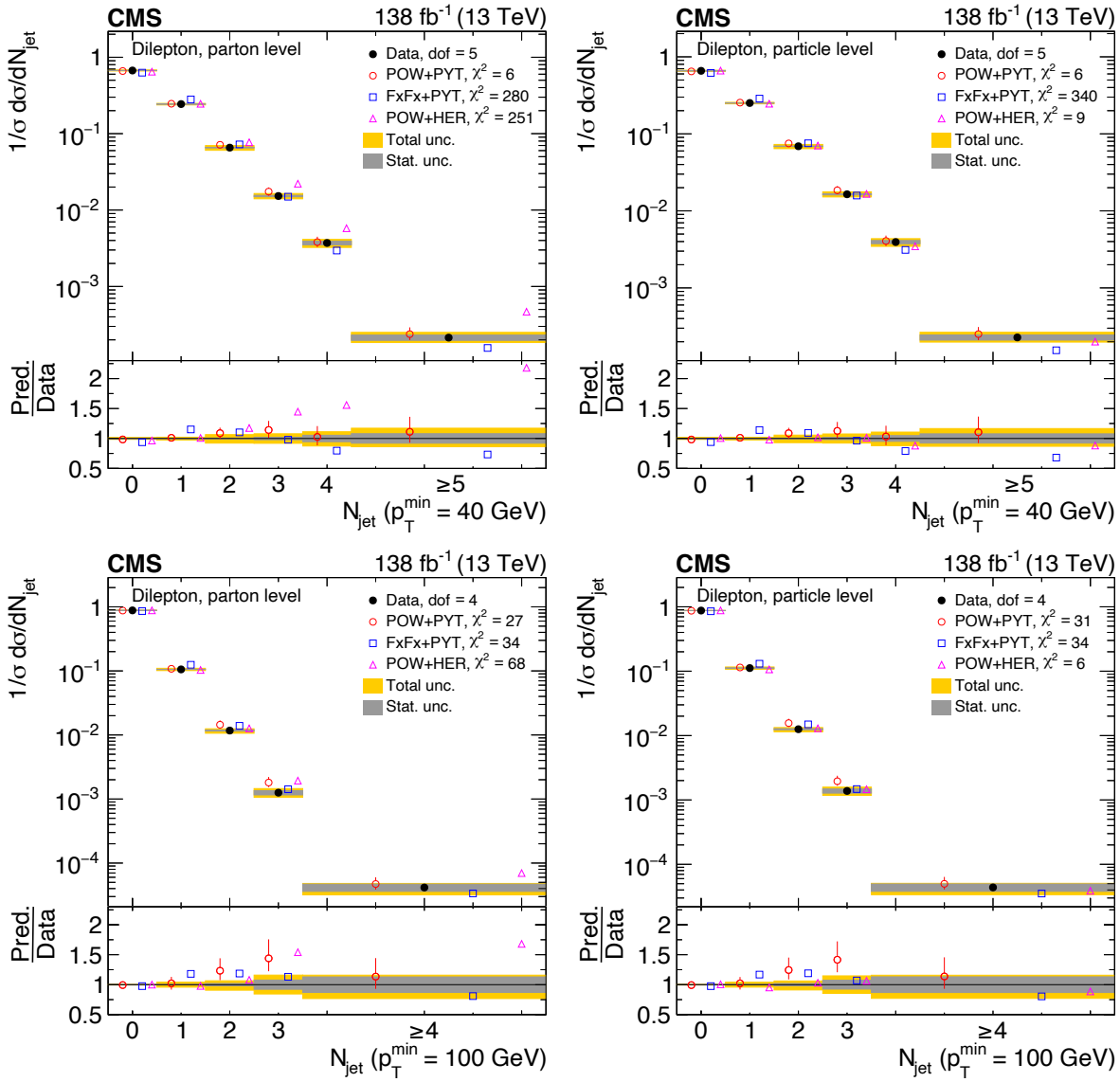

Figure 30: Normalized differential $t\bar{t}$ production cross sections as a function of N_{jet}, for a minimum jet p_T of 40 GeV (upper) and 100 GeV (lower), measured at the parton level in the full phase space (left) and at the particle level in a fiducial phase space (right). The data are shown as filled circles with grey and yellow bands indicating the statistical and total uncertainties (statistical and systematic uncertainties added in quadrature), respectively. For each distribution, the number of degrees of freedom (dof) is also provided. The cross sections are compared to various MC predictions (other points). The estimated uncertainties in the POWHEG+PYTHIA 8 ('POW-PYT') simulation are represented by a vertical bar on the corresponding points. For each MC model, a value of χ^2 is reported that takes into account the measurement uncertainties. The lower panel in each plot shows the ratios of the predictions to the data.

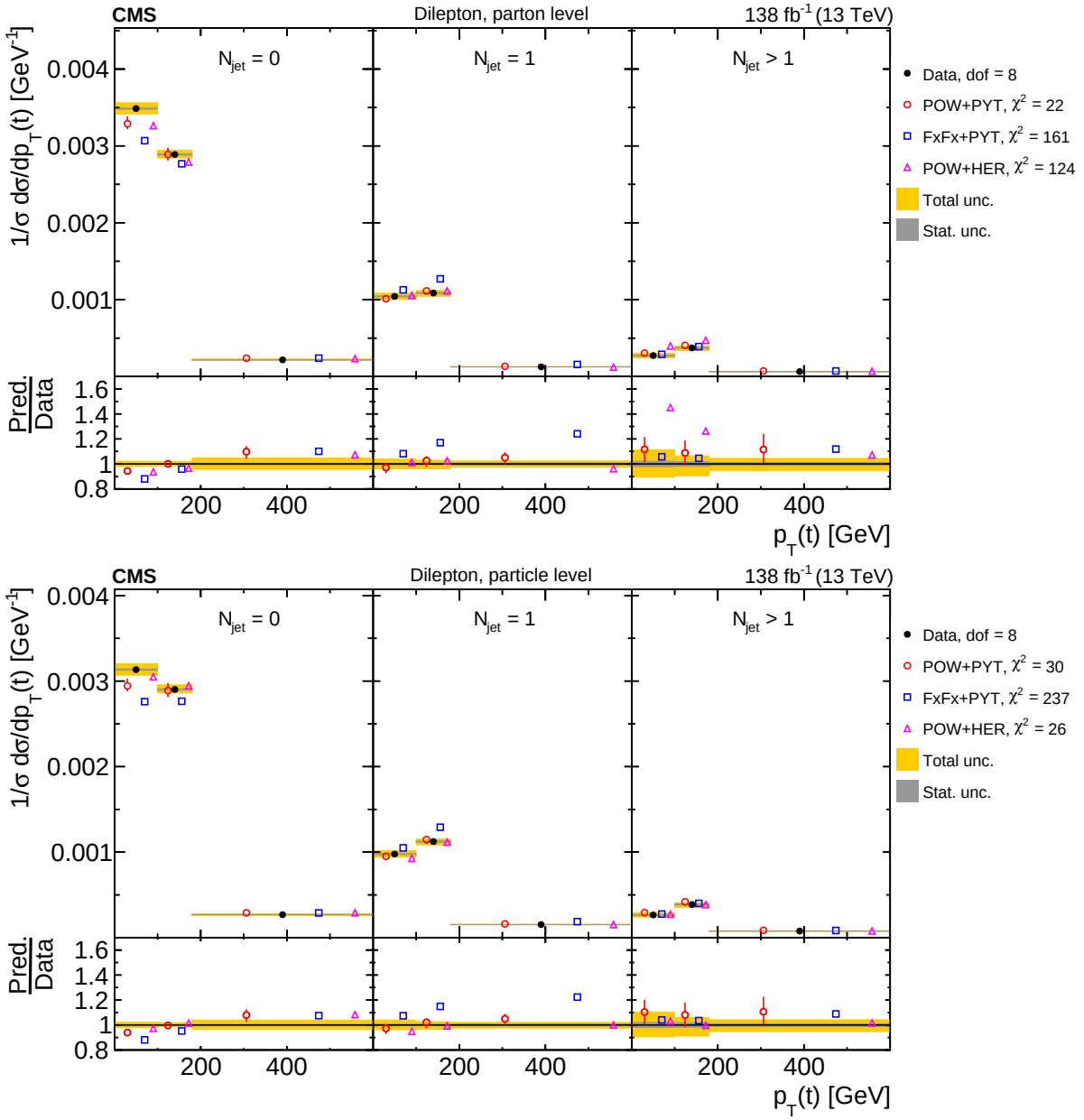

Figure 31: Normalized $[N_{\text{jet}}, p_{\text{T}}(\text{t})]$ cross sections measured at the parton level in the full phase space (upper) and at the particle level in a fiducial phase space (lower). The data are shown as filled circles with grey and yellow bands indicating the statistical and total uncertainties (statistical and systematic uncertainties added in quadrature), respectively. For each distribution, the number of degrees of freedom (dof) is also provided. The cross sections are compared to various MC predictions (other points). The estimated uncertainties in the POWHEG+PYTHIA 8 ('POW-PYT') simulation are represented by a vertical bar on the corresponding points. For each MC model, a value of χ^2 is reported that takes into account the measurement uncertainties. The lower panel in each plot shows the ratios of the predictions to the data.

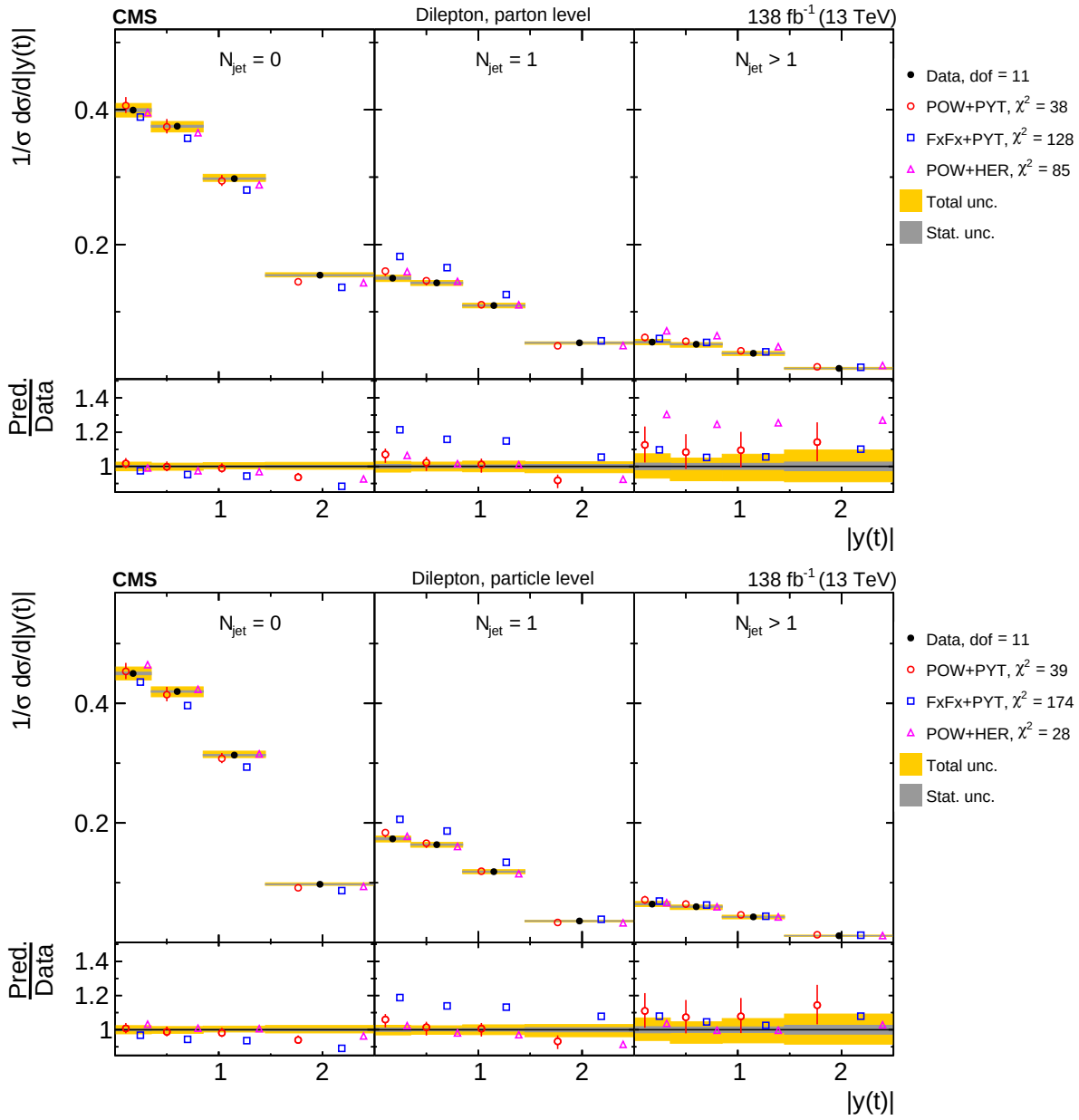

Figure 32: Normalized $[N_{\text{jet}}, |y(t)|]$ cross sections are shown for data (filled circles) and various MC predictions (other points). Further details can be found in the caption of Fig. 31.

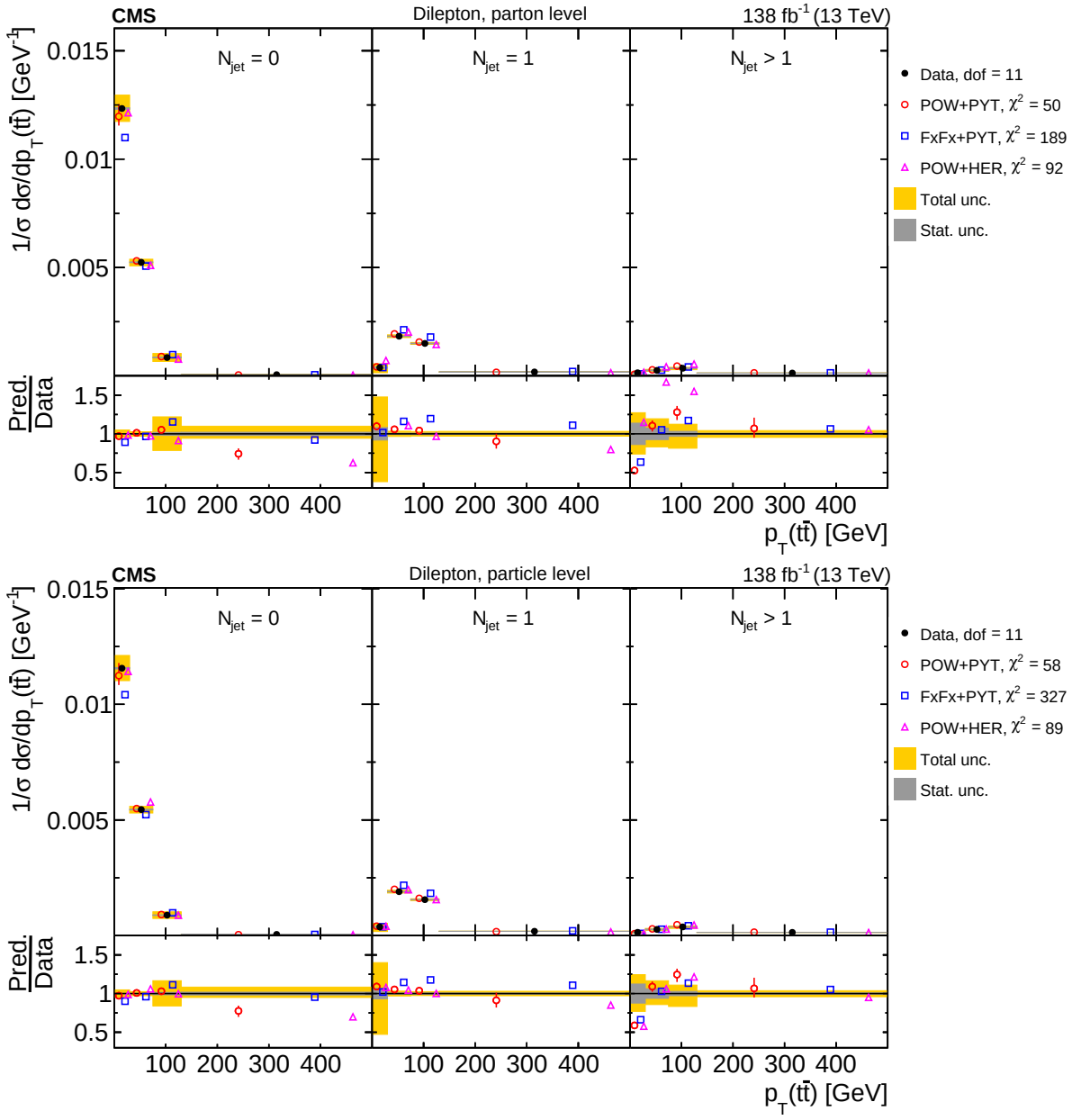

Figure 33: Normalized $[N_{\text{jet}},\ p_{\text{T}}(\text{t}\bar{\text{t}})]$ cross sections are shown for data (filled circles) and various MC predictions (other points). Further details can be found in the caption of Fig. 31.

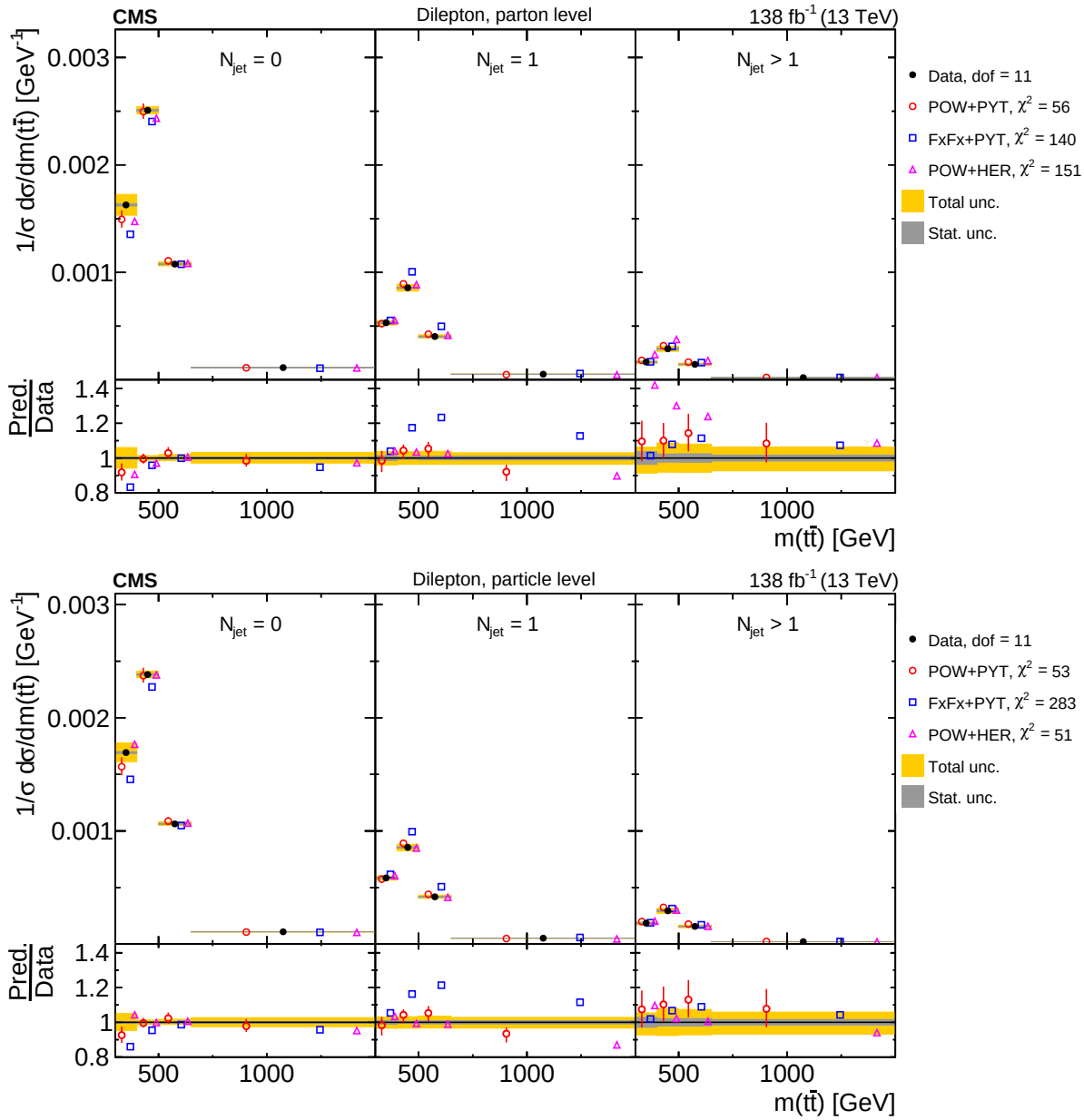

Figure 34: Normalized $[N_{\text{jet}}, m(\text{t}\bar{\text{t}})]$ cross sections are shown for data (filled circles) and various MC predictions (other points). Further details can be found in the caption of Fig. 31.

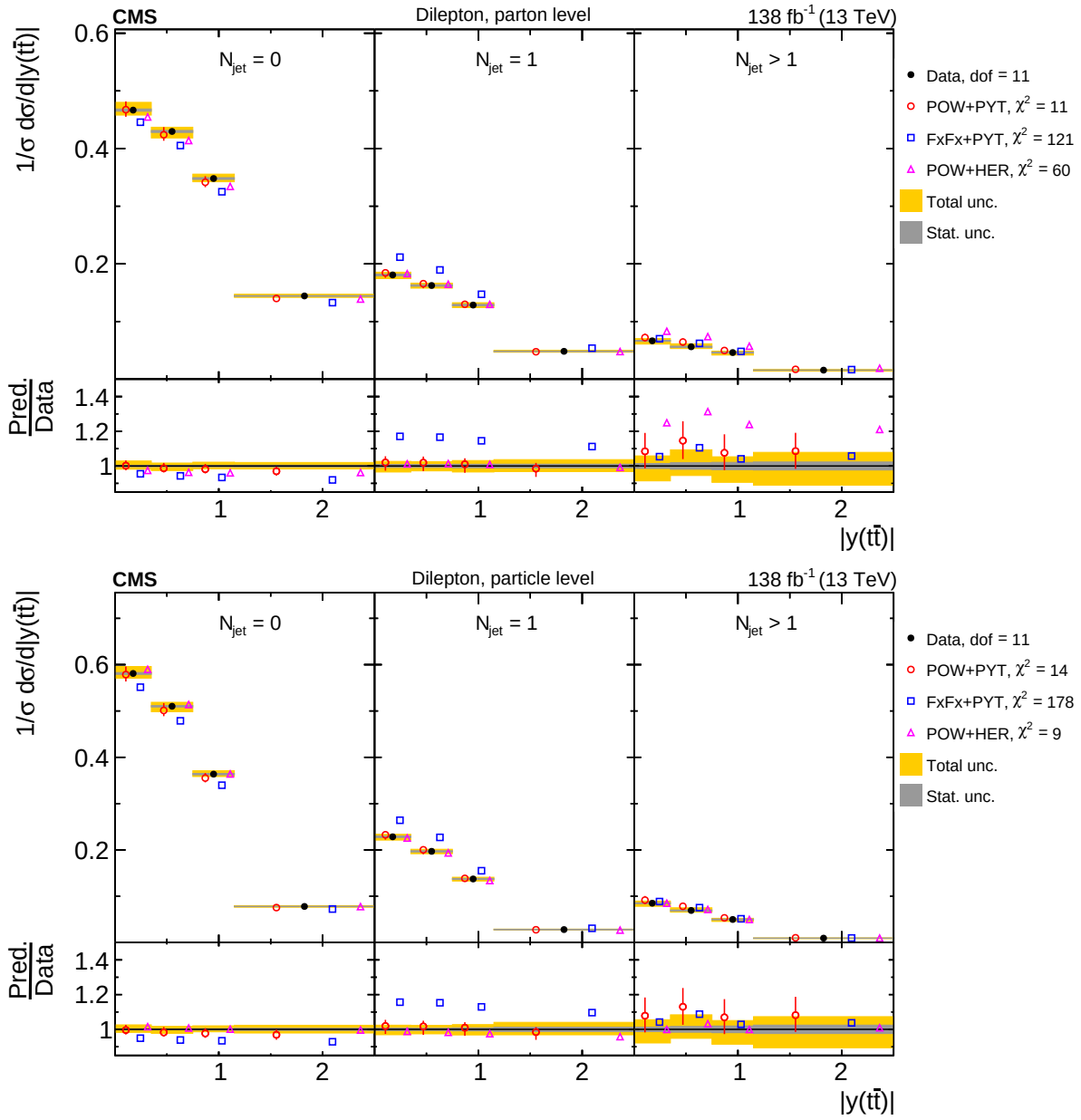

Figure 35: Normalized $[N_{\text{jet}}, |y(\text{t}\bar{\text{t}})|]$ cross sections are shown for data (filled circles) and various MC predictions (other points). Further details can be found in the caption of Fig. 31.

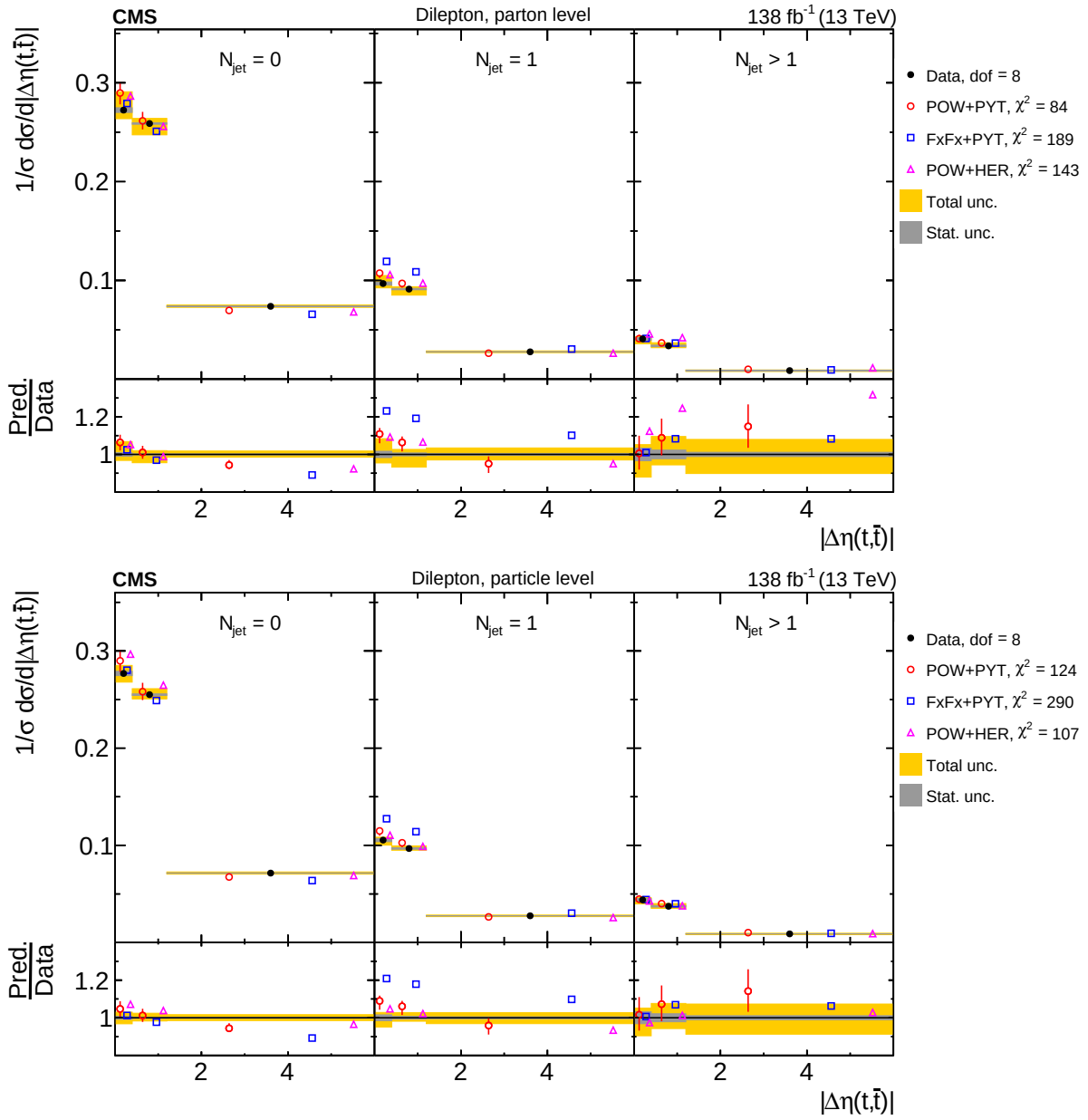

Figure 36: Normalized $[N_{\text{jet}}, |\Delta\eta(\text{t},\bar{\text{t}})|]$ cross sections are shown for data (filled circles) and various MC predictions (other points). Further details can be found in the caption of Fig. 31.

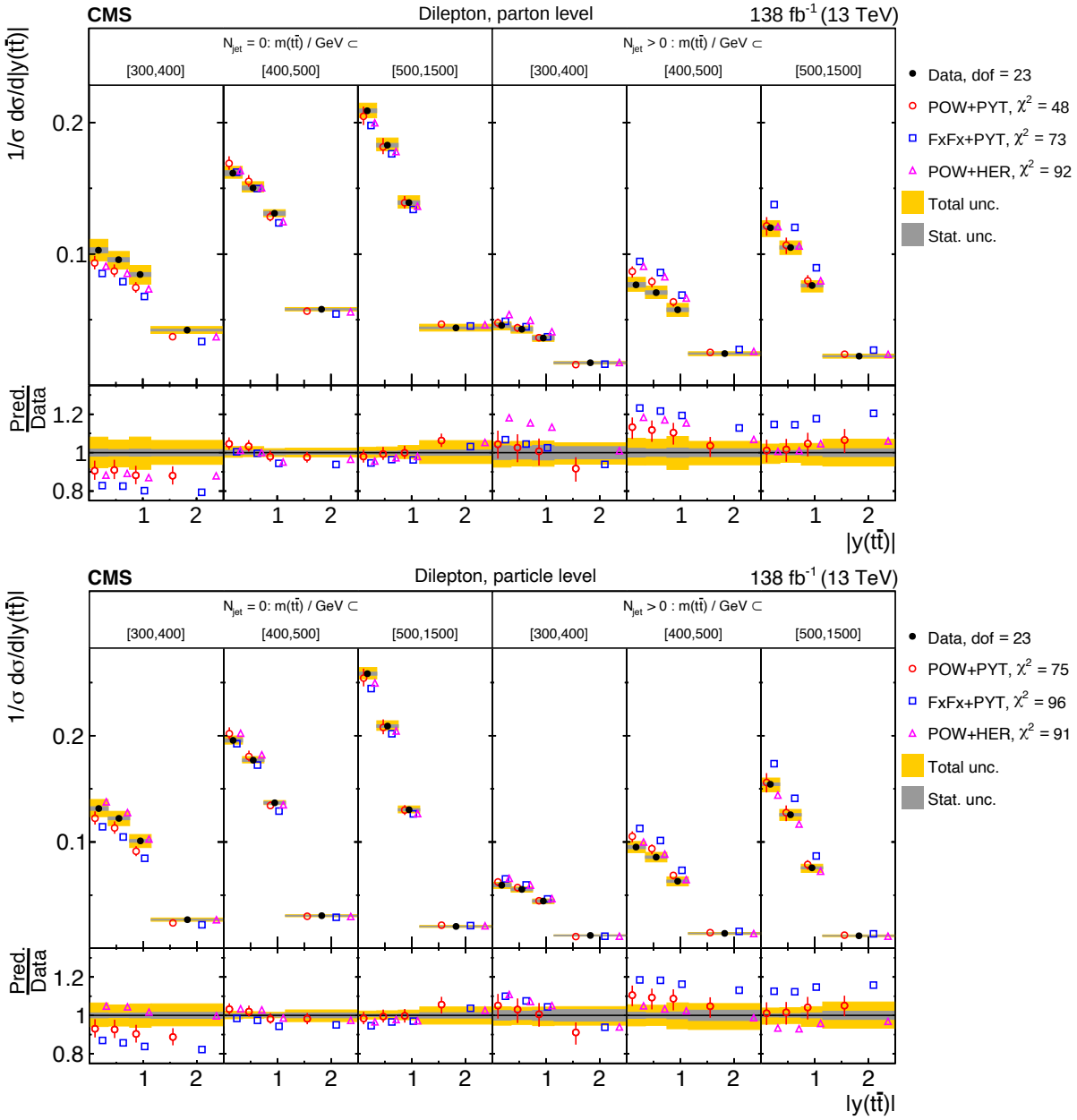

Figure 37: Normalized $[N_{\text{jet}}^{0,1+}, m(\text{t}\bar{\text{t}}), |y(\text{t}\bar{\text{t}})|]$ cross sections are shown for data (filled circles) and various MC predictions (other points). Further details can be found in the caption of Fig. 31.

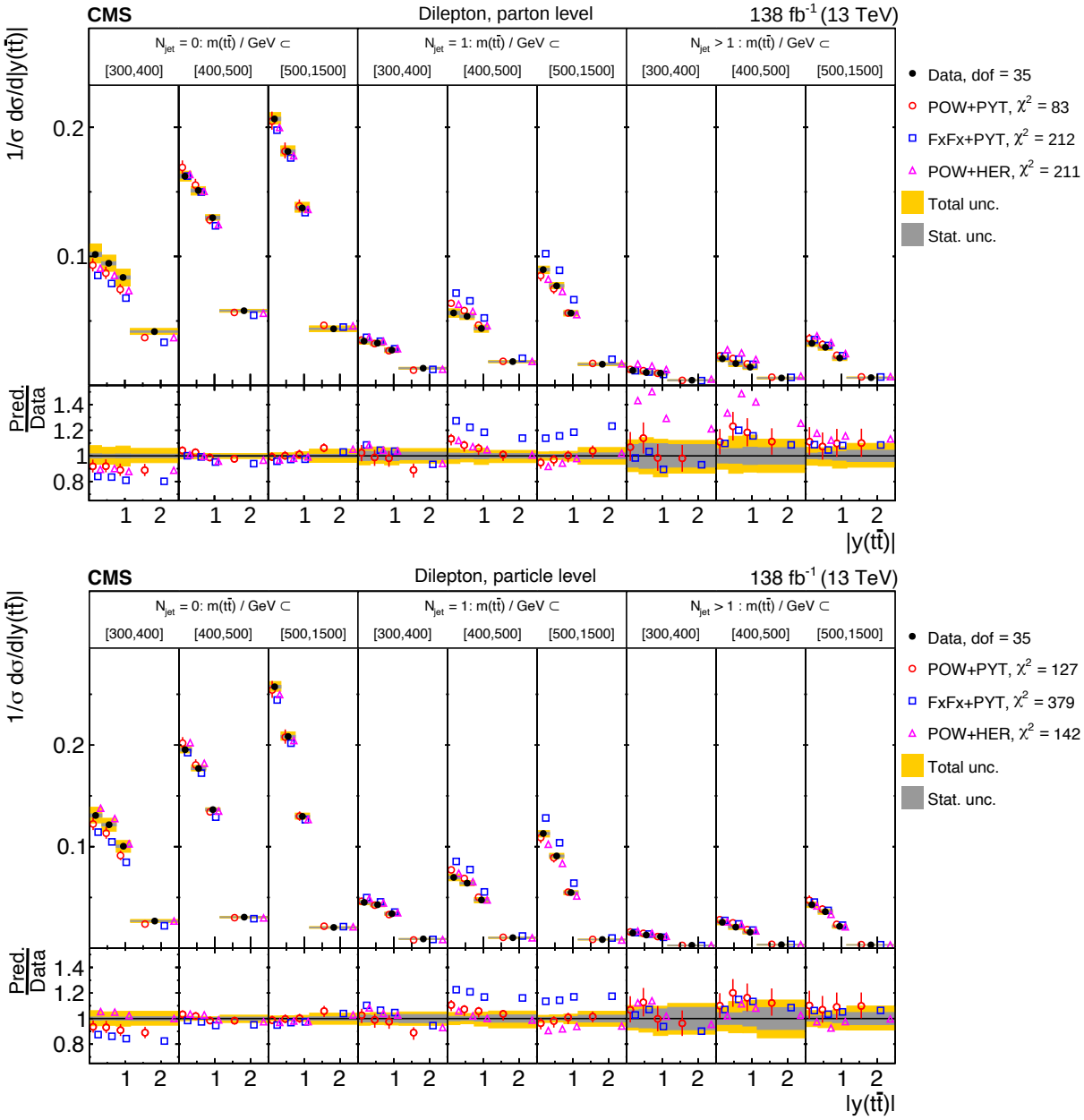

Figure 38: Normalized $[N_{\text{jet}}^{0,1,2+}, m(\text{t}\bar{\text{t}}), |y(\text{t}\bar{\text{t}})|]$ cross sections are shown for data (filled circles) and various MC predictions (other points). Further details can be found in the caption of Fig. 31.

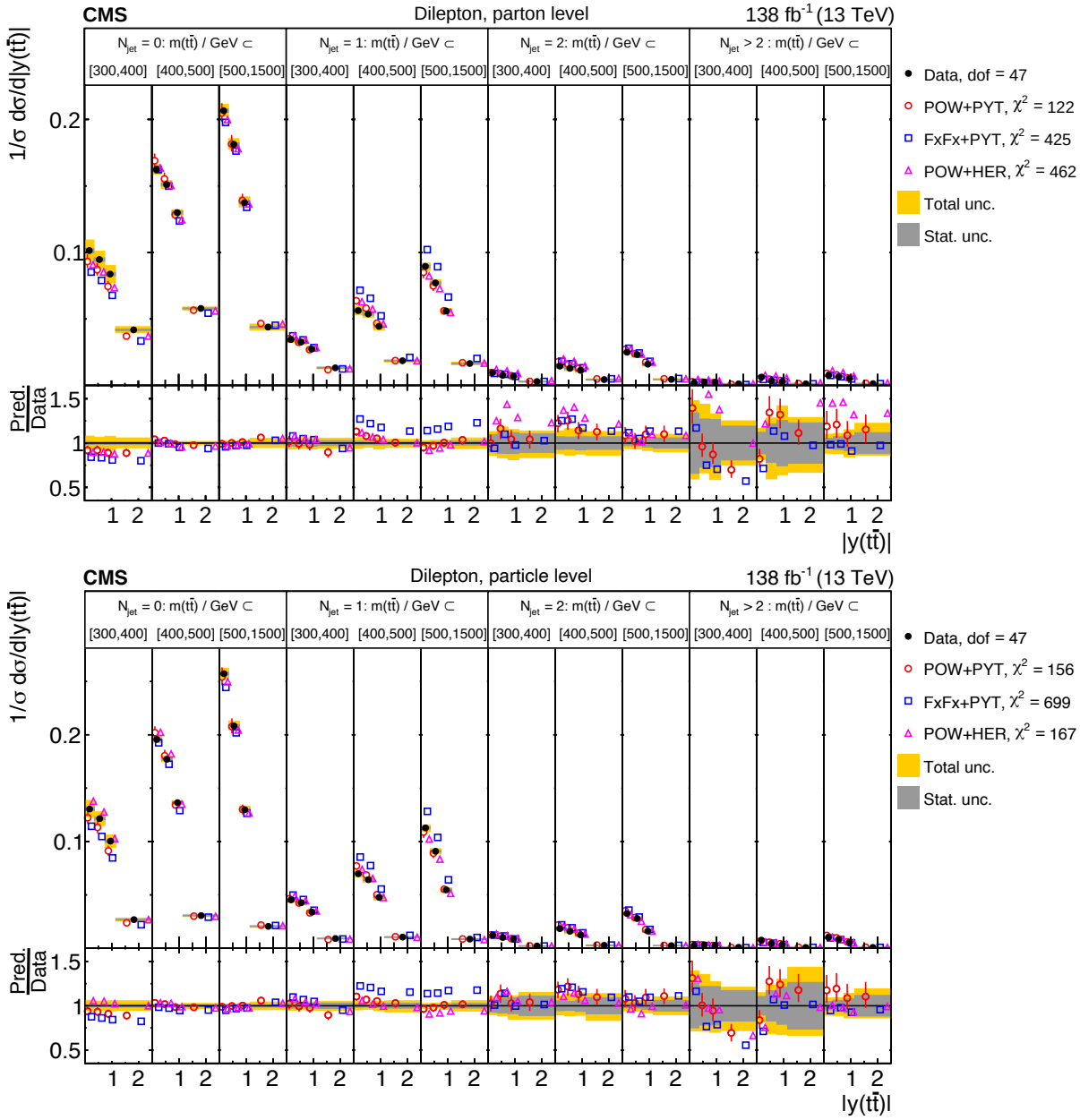

Figure 39: Normalized $[N_{\text{jet}}^{0,1,2,3+}, m(\text{t}\bar{\text{t}}), |y(\text{t}\bar{\text{t}})|]$ cross sections are shown for data (filled circles) and various MC predictions (other points). Further details can be found in the caption of Fig. 31.

Table 6: The χ^2 values and dof of the measured normalized differential cross sections as a function of the additional-jet multiplicity in the events, at the parton level of the top quark and antiquark, are shown with respect to the predictions of various MC generators. The χ^2 values are calculated taking only measurement uncertainties into account and excluding theory uncertainties. For POW+PYT, the χ^2 values including theory uncertainties are indicated with the brackets (w. unc.).

Cross section variables	dof	χ^2		
		POW+PYT (w. unc.)	FxFx+PYT	POW+HER
$N_{\text{jet}}(p_{\text{T}} > 40\,\text{GeV})$	5	6 (3)	280	251
$N_{\text{jet}}(p_{\text{T}} > 100\,\text{GeV})$	4	27 (8)	34	68
$[N_{\text{jet}},\, p_{\text{T}}(\text{t})]$	8	22 (12)	161	124
$[N_{\text{jet}},\, \lvert y(\text{t})\rvert]$	11	38 (29)	128	85
$[N_{\text{jet}},\, p_{\text{T}}(\text{t}\bar{\text{t}})]$	11	50 (37)	189	92
$[N_{\text{jet}},\, m(\text{t}\bar{\text{t}})]$	11	56 (41)	140	151
$[N_{\text{jet}},\, \lvert y(\text{t}\bar{\text{t}})\rvert]$	11	11 (5)	121	60
$[N_{\text{jet}},\, \lvert \Delta\eta(\text{t},\bar{\text{t}})\rvert]$	8	84 (37)	189	143
$[N_{\text{jet}}^{0,1+},\, m(\text{t}\bar{\text{t}}),\, \lvert y(\text{t}\bar{\text{t}})\rvert]$	23	48 (35)	73	92
$[N_{\text{jet}}^{0,1,2+},\, m(\text{t}\bar{\text{t}}),\, \lvert y(\text{t}\bar{\text{t}})\rvert]$	35	83 (57)	212	211
$[N_{\text{jet}}^{0,1,2,3+},\, m(\text{t}\bar{\text{t}}),\, \lvert y(\text{t}\bar{\text{t}})\rvert]$	47	122 (84)	425	462

Table 7: The χ^2 values and dof of the measured normalized differential cross sections as a function of the additional-jet multiplicity in the events, at the particle level of the top quark and antiquark, are shown with respect to the predictions of various MC generators. The χ^2 values are calculated taking only measurement uncertainties into account and excluding theory uncertainties. For POW+PYT, the χ^2 values including theory uncertainties are indicated with the brackets (w. unc.).

Cross section variables	dof	χ^2		
		POW+PYT (w. unc.)	FxFx+PYT	POW+HER
$N_{\text{jet}}(p_{\text{T}} > 40\,\text{GeV})$	5	6 (3)	340	9
$N_{\text{jet}}(p_{\text{T}} > 100\,\text{GeV})$	4	31 (8)	34	6
$[N_{\text{jet}},\, p_{\text{T}}(\text{t})]$	8	30 (13)	237	26
$[N_{\text{jet}},\, \lvert y(\text{t})\rvert]$	11	39 (24)	174	28
$[N_{\text{jet}},\, p_{\text{T}}(\text{t}\bar{\text{t}})]$	11	58 (37)	327	89
$[N_{\text{jet}},\, m(\text{t}\bar{\text{t}})]$	11	53 (35)	283	51
$[N_{\text{jet}},\, \lvert y(\text{t}\bar{\text{t}})\rvert]$	11	14 (5)	178	9
$[N_{\text{jet}},\, \lvert \Delta\eta(\text{t},\bar{\text{t}})\rvert]$	8	124 (41)	290	107
$[N_{\text{jet}}^{0,1+},\, m(\text{t}\bar{\text{t}}),\, \lvert y(\text{t}\bar{\text{t}})\rvert]$	23	75 (45)	96	91
$[N_{\text{jet}}^{0,1,2+},\, m(\text{t}\bar{\text{t}}),\, \lvert y(\text{t}\bar{\text{t}})\rvert]$	35	127 (69)	379	142
$[N_{\text{jet}}^{0,1,2,3+},\, m(\text{t}\bar{\text{t}}),\, \lvert y(\text{t}\bar{\text{t}})\rvert]$	47	156 (94)	699	167

9.4 Comparisons to higher-order theoretical predictions

In this Section, the measured cross sections are compared to the following calculations of beyond-NLO precision in QCD:

- ***a*N^{3}LO**: An approximate next-to-NNLO calculation [2, 3], based on the resummation of soft-gluon contributions at NNLL accuracy in the moment-space approach. This prediction is only available for the $p_{\mathrm{T}}(\mathrm{t})$, $y(\mathrm{t})$, and $[|y(\mathrm{t})|,\ p_{\mathrm{T}}(\mathrm{t})]$ cross sections. The renormalization and factorization scales are set to m_{t} for the $y(\mathrm{t})$ distributions and to m_{T} for $p_{\mathrm{T}}(\mathrm{t})$ and $[|y(\mathrm{t})|,\ p_{\mathrm{T}}(\mathrm{t})]$. Here, m_{t} denotes the top quark mass and m_{T} is defined as $m_{\mathrm{T}} = \sqrt{m_{\mathrm{t}}^2 + p_{\mathrm{T}}(\mathrm{t})^2}$.
- **MATRIX (NNLO)**: A prediction with full NNLO accuracy in QCD obtained with the MATRIX package [7, 101–107]. The dynamic scales are set to $H_{\mathrm{T}}/4$, where H_{T} denotes the sum of the top quark and antiquark m_{T} values.
- **STRIPPER (NNLO)**: A calculation with full NNLO precision in QCD using the STRIPPER framework [5, 8, 108–110]. The dynamic scales are set to $H_{\mathrm{T}}/4$. For parton level cross sections as functions of the $\mathrm{t\bar{t}}$ and top quark kinematic observables, the STRIPPER predictions are expected to be identical to the results obtained with MATRIX. The STRIPPER calculation also provides cross sections at NNLO accuracy for the process $\mathrm{pp} \to \mathrm{t\bar{t}} \to \mathrm{b\bar{b}}\ell\bar{\ell}\nu\bar{\nu} + \mathrm{X}$ [8], that can be compared to the particle level measurements obtained in this analysis as functions of the $\mathrm{t\bar{t}}$, top quark, and lepton and b jet kinematic variables.
- **MiNNLOPS (NNLOPS)**: A prediction with full NNLO precision in QCD, complemented with parton showers and computed using the POWHEG-BOX-V2 [39]. These calculations are obtained using the MiNNLOPS method [111–113], which supplements the MiNLO prescription [114, 115] with the missing pieces to reach NNLO accuracy for inclusive observables. The μ_{r} for the two powers of α_{S} is set to $H_{\mathrm{T}}/4$, and the scale of the modified logarithms is set to half of this value. Parton showering is simulated with PYTHIA 8, and includes the effects of underlying event and hadronization.

In all predictions, the top quark mass is set to $m_{\mathrm{t}} = 172.5\,\mathrm{GeV}$ and the NNPDF3.1 NNLO PDF set [36] is used. In the following, the calculations are collectively referred to as theoretical predictions.

The comparisons of the theoretical predictions to the measured normalized differential cross sections are shown in Figs. 40–62. The predictions are depicted as symbols with vertical bars representing missing higher-order uncertainties, as estimated from six variations of μ_{r} and μ_{f}, following the same variation procedure as described in Section 8.2. These uncertainties are denoted in the following as "theory scale uncertainties". The predictions from POW+PYT are also shown, serving as a reference for the description by the MC models, discussed in Sections 9.1 and 9.2. The χ^2 values of model-to-data comparisons are listed in Tables 8–12, and the corresponding p-values can be found in Tables 32–36. The values are provided only taking measurement uncertainties into account and also including the full (scale) uncertainties for the POW+PYT (beyond-NLO) predictions. The scale uncertainties of the beyond-NLO predictions are found to be quite asymmetric in some cases; this feature is taken into account by using the averaging procedure described in Appendix A when constructing the covariance matrix of the calculation. Comparisons of the predictions to the measured absolute cross sections are provided in Appendix B.2.

For the cross sections as functions of the $\mathrm{t\bar{t}}$ and top quark kinematic observables at the parton and particle levels, shown in Figs. 40–55, the theoretical models provide descriptions of the data that are similar or improved in quality, compared to POW+PYT, with a few exceptions. For the $p_{\mathrm{T}}(\mathrm{t})$ and $p_{\mathrm{T}}(\bar{\mathrm{t}})$ distributions shown in Fig. 40, the MATRIX, STRIPPER, and MiNNLOPS models provide a good description of the data, with no discernible trend towards a distribution that is harder, as exhibited by POW+PYT. For the $a\mathrm{N^3LO}$ calculation, some wiggles are visible in the distribution of the ratio to the data, leading to a rather poor χ^2. The STRIPPER model describes the data also at the particle level reasonably well. The theoretical models also provide a reasonable description of other measured cross sections related to top quark p_{T}, such as $p_{\mathrm{T}}(\mathrm{t})/m(\mathrm{t\bar{t}})$ (Fig. 44), and $[m(\mathrm{t\bar{t}}),\, p_{\mathrm{T}}(\mathrm{t})]$ (Fig. 47), clearly improving upon POW+PYT. For observables related to the top quark rapidity and the rapidity and mass of the $\mathrm{t\bar{t}}$ system, the trends between data and theoretical calculations are mostly similar to those of POW+PYT. Exemplary cases are the rapidity spectra $y(\mathrm{t})$ and $y(\bar{\mathrm{t}})$, depicted in Fig. 41, where the models exhibit rapidity distributions that are more central than what is observed in data, and the $[m(\mathrm{t\bar{t}}),\, |y(\mathrm{t\bar{t}})|]$ cross sections (Fig. 49), where the predictions overshoot the data in the high-$m(\mathrm{t\bar{t}})$ region at large $y(\mathrm{t\bar{t}})$.

For cross sections as functions of $p_{\mathrm{T}}(\mathrm{t\bar{t}})$ and $|\Delta\phi(\mathrm{t},\bar{\mathrm{t}})|$, shown in Figs. 42 and 43, the theoretical calculations exhibit large scale uncertainties, reflecting the sensitivity to higher order QCD effects, and the central predictions overall fail to provide a good data description. Similar observations can be made for the multi-differential cross sections involving these two kinematic variables.

Summarizing, the beyond-NLO theoretical predictions provide descriptions of the data that are of similar or improved quality, compared to POW+PYT, except for some of the kinematic distributions where the theoretical scale uncertainties are large. This is also reflected by the theory-to-data χ^2 values that are often quite large when only measurement uncertainties are taken into account, but are reduced to reasonably small values when the theory scale uncertainties are also included.

For the differential cross sections as functions of lepton and b jet kinematic variables at the particle level, shown in Figs. 56–62, the STRIPPER calculation provides descriptions that are overall of similar quality compared to POW+PYT. One exception is the $m(\mathrm{b\bar{b}})$ distribution, where STRIPPER clearly predicts too many events in the lowest mass bin.

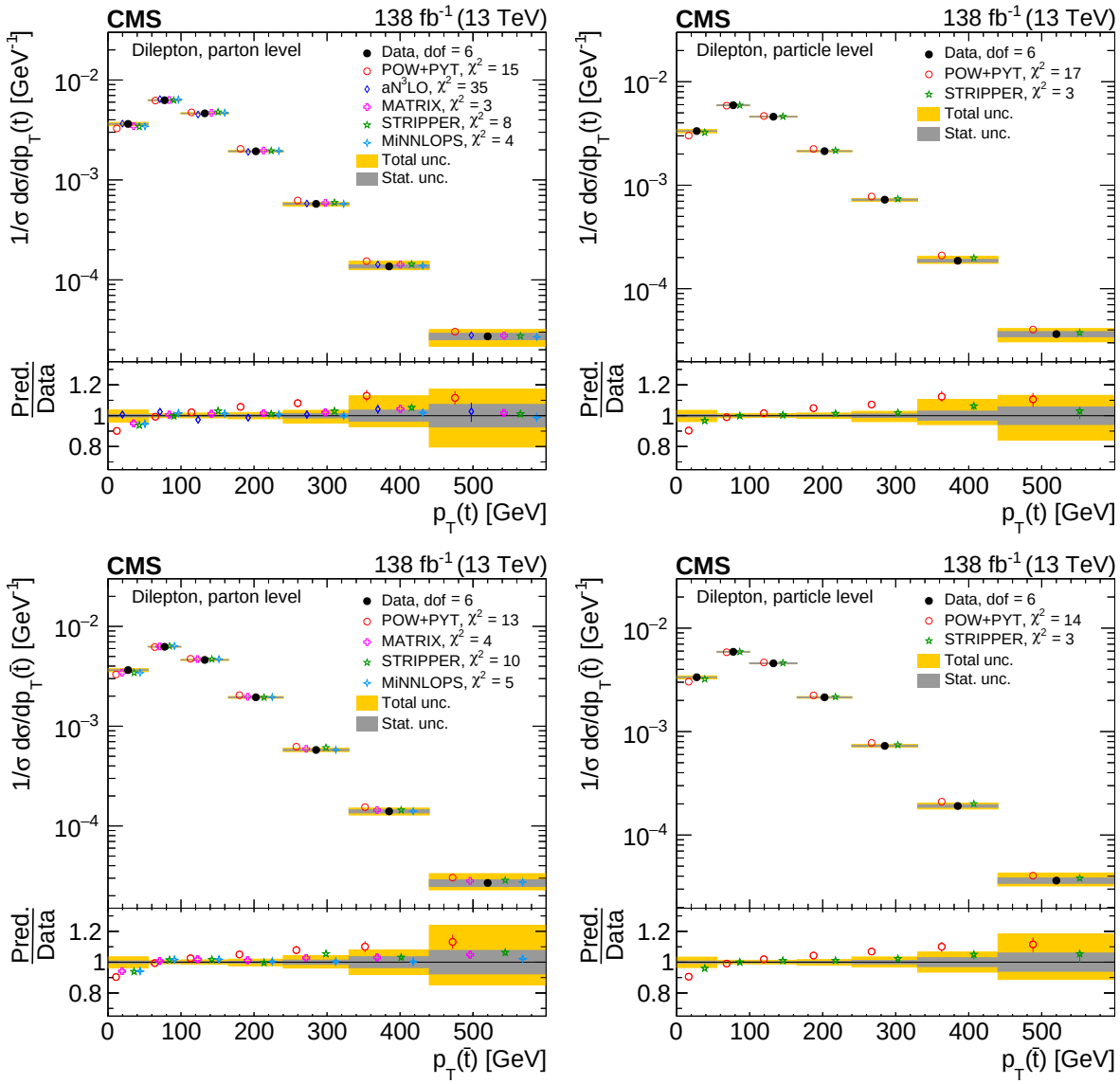

Figure 40: Normalized differential $t\bar{t}$ production cross sections as functions of $p_T(t)$ (upper) and $p_T(\bar{t})$ (lower), measured at the parton level in the full phase space (left) and at the particle level in a fiducial phase space (right). The data are shown as filled circles with grey and yellow bands indicating the statistical and total uncertainties (statistical and systematic uncertainties added in quadrature), respectively. For each distribution, the number of degrees of freedom (dof) is also provided. The cross sections are compared to predictions from the POWHEG+PYTHIA 8 ('POW-PYT', open circles) simulation and various theoretical predictions with beyond-NLO precision (other points). The estimated uncertainties in the predictions are represented by a vertical bar on the corresponding points. For each model, a value of χ^2 is reported that takes into account the measurement uncertainties. The lower panel in each plot shows the ratios of the predictions to the data.

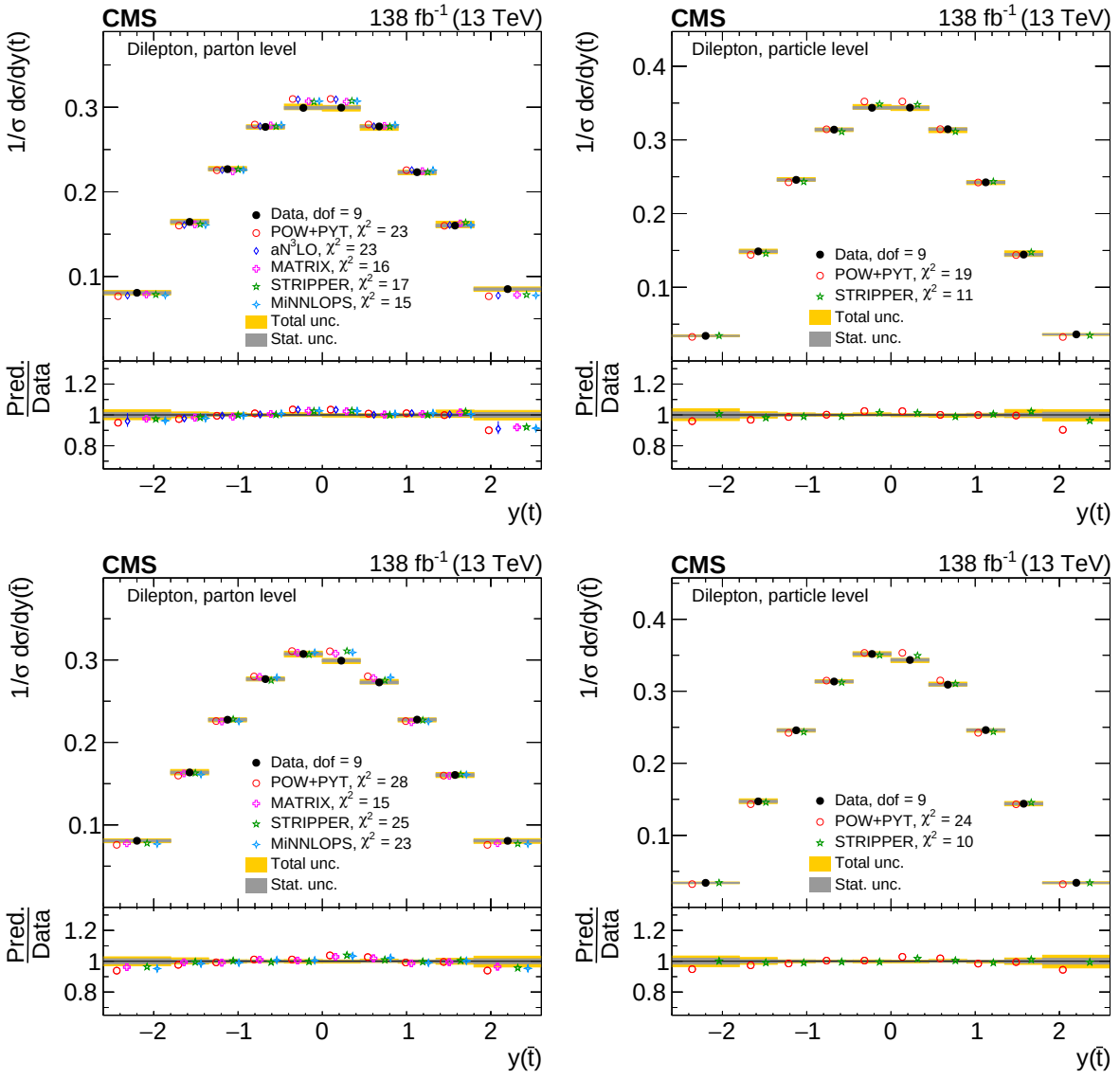

Figure 41: Normalized differential $\mathrm{t\bar{t}}$ production cross sections as functions of $y(\mathrm{t})$ (upper) and $y(\bar{\mathrm{t}})$ (lower) are shown for data (filled circles), POWHEG+PYTHIA 8 ('POW-PYT', open circles) simulation, and various theoretical predictions with beyond-NLO precision (other points). Further details can be found in the caption of Fig. 40.

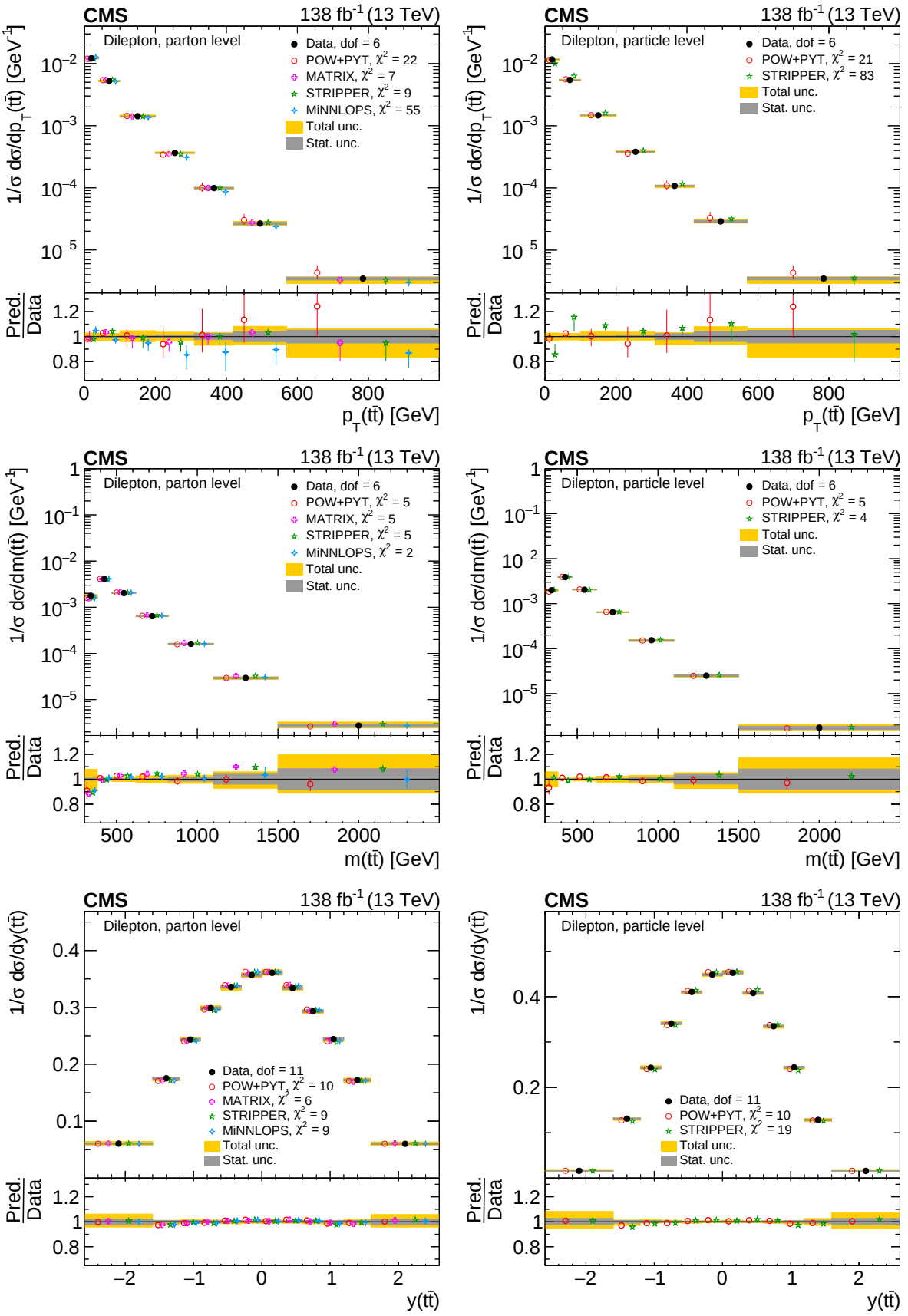

Figure 42: Normalized differential $\mathrm{t\bar{t}}$ production cross sections as functions of $p_{\mathrm{T}}(\mathrm{t\bar{t}})$ (upper), $m(\mathrm{t\bar{t}})$ (middle), and $y(\mathrm{t\bar{t}})$ (lower) are shown for data (filled circles), POWHEG+PYTHIA8 ('POW-PYT', open circles) simulation, and various theoretical predictions with beyond-NLO precision (other points). Further details can be found in the caption of Fig. 40.

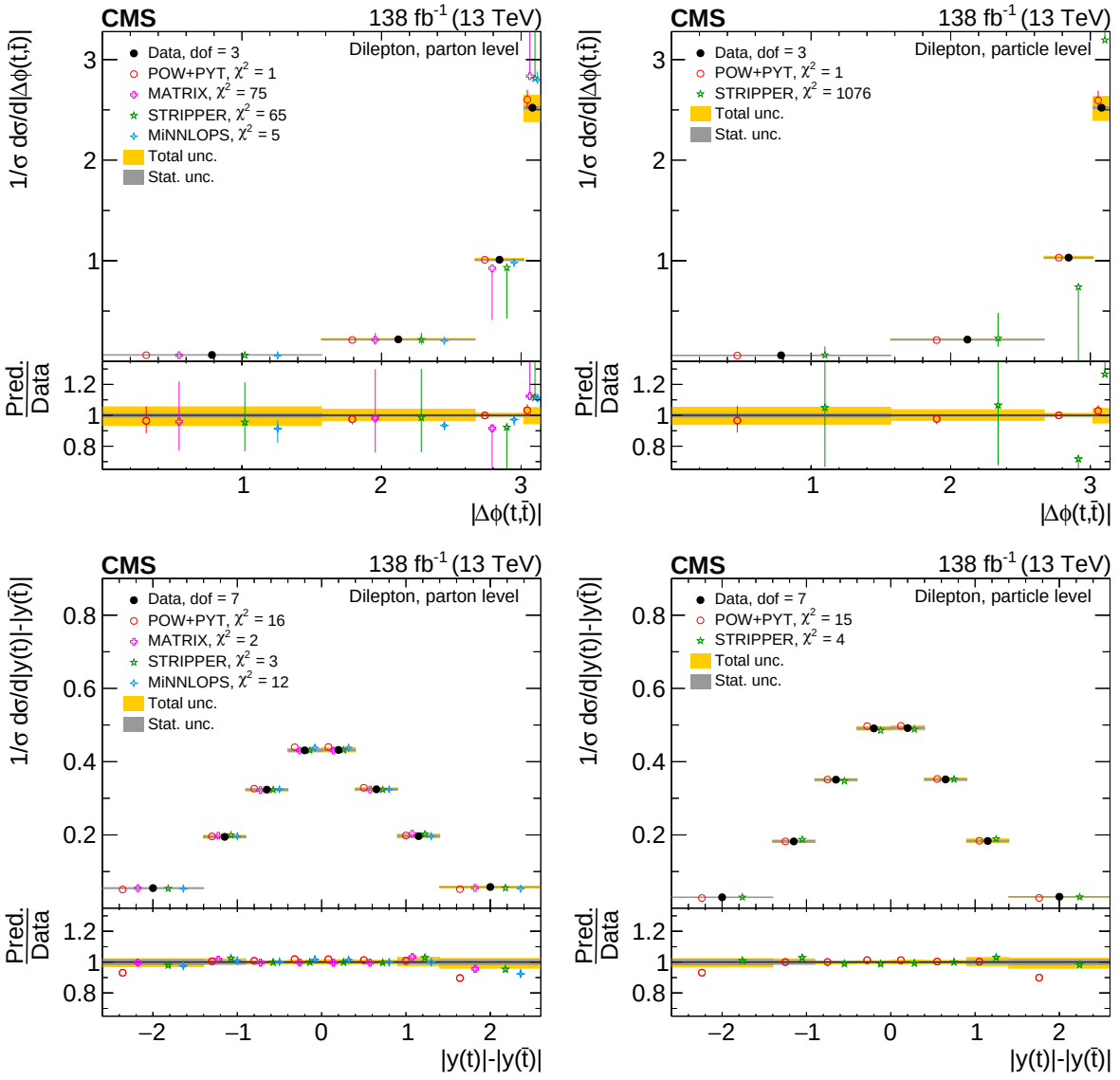

Figure 43: Normalized differential $\mathrm{t\bar{t}}$ production cross sections as functions of $|\Delta\phi(\mathrm{t},\bar{\mathrm{t}})|$ (upper) and $|y(\mathrm{t})| - |y(\bar{\mathrm{t}})|$ (lower) are shown for data (filled circles), POWHEG+PYTHIA 8 ('POW-PYT', open circles) simulation, and various theoretical predictions with beyond-NLO precision (other points). Further details can be found in the caption of Fig. 40.

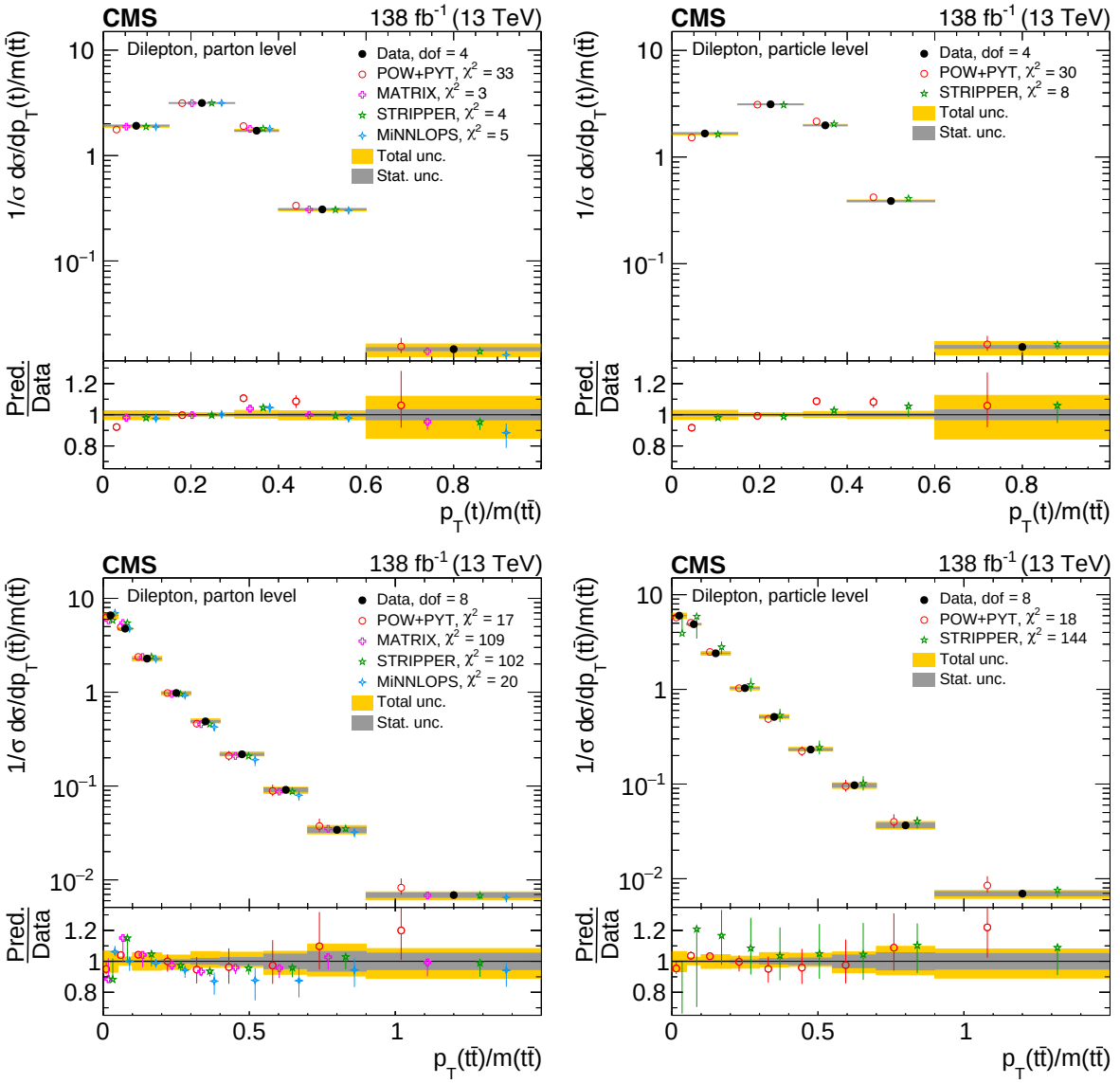

Figure 44: Normalized differential $t\bar{t}$ production cross sections as functions of $p_T(t)/m(t\bar{t})$ (upper) and $p_T(t\bar{t})/m(t\bar{t})$ (lower) are shown for data (filled circles), POWHEG+PYTHIA8 ('POW-PYT', open circles) simulation, and various theoretical predictions with beyond-NLO precision (other points). Further details can be found in the caption of Fig. 40.

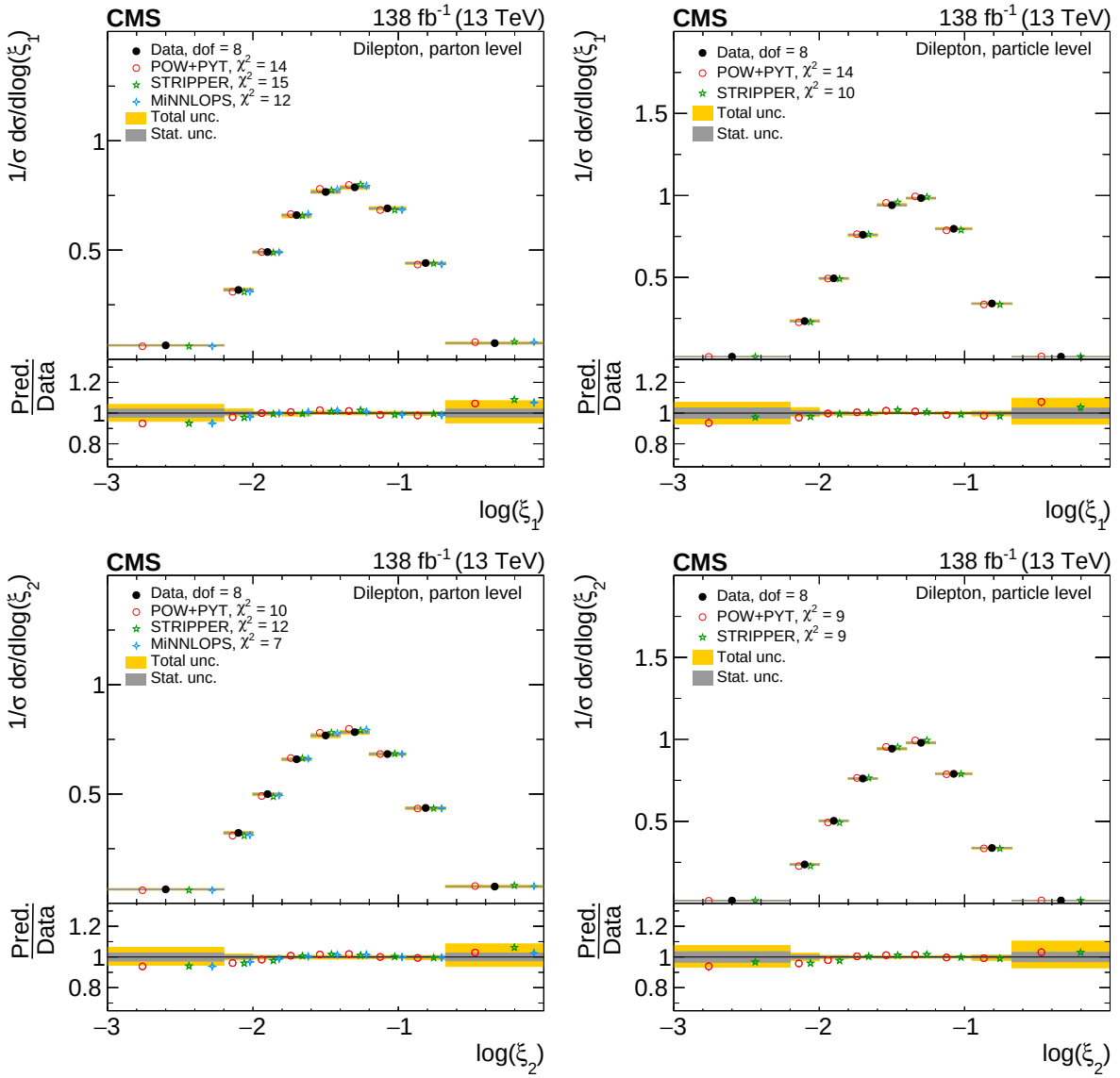

Figure 45: Normalized differential $\mathrm{t\bar{t}}$ production cross sections as functions of $\log(\xi_1)$ (upper) and $\log(\xi_2)$ (lower) are shown for data (filled circles), POWHEG+PYTHIA 8 ('POW-PYT', open circles) simulation, and STRIPPER NNLO calculation (stars). Further details can be found in the caption of Fig. 40.

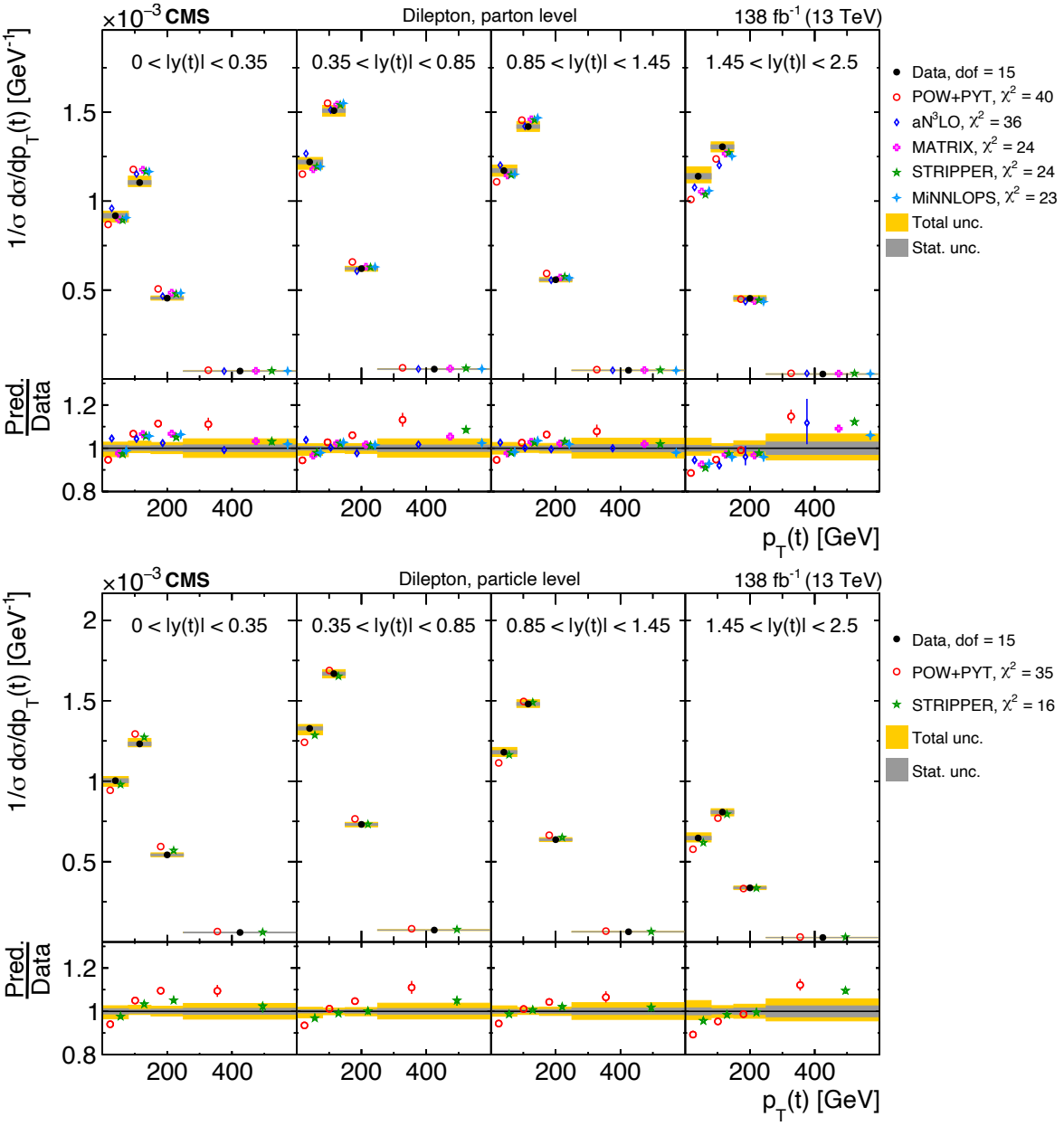

Figure 46: Normalized $[|y(t)|, p_T(t)]$ cross sections measured at the parton level in the full phase space (upper) and at the particle level in a fiducial phase space (lower). The data are shown as filled circles with grey and yellow bands indicating the statistical and total uncertainties (statistical and systematic uncertainties added in quadrature), respectively. For each distribution, the number of degrees of freedom (dof) is also provided. The cross sections are compared to predictions from the POWHEG+PYTHIA 8 ('POW-PYT', open circles) simulation and various theoretical predictions with beyond-NLO precision (other points). The estimated uncertainties in the predictions are represented by a vertical bar on the corresponding points. For each model, a value of χ^2 is reported that takes into account the measurement uncertainties. The lower panel in each plot shows the ratios of the predictions to the data.

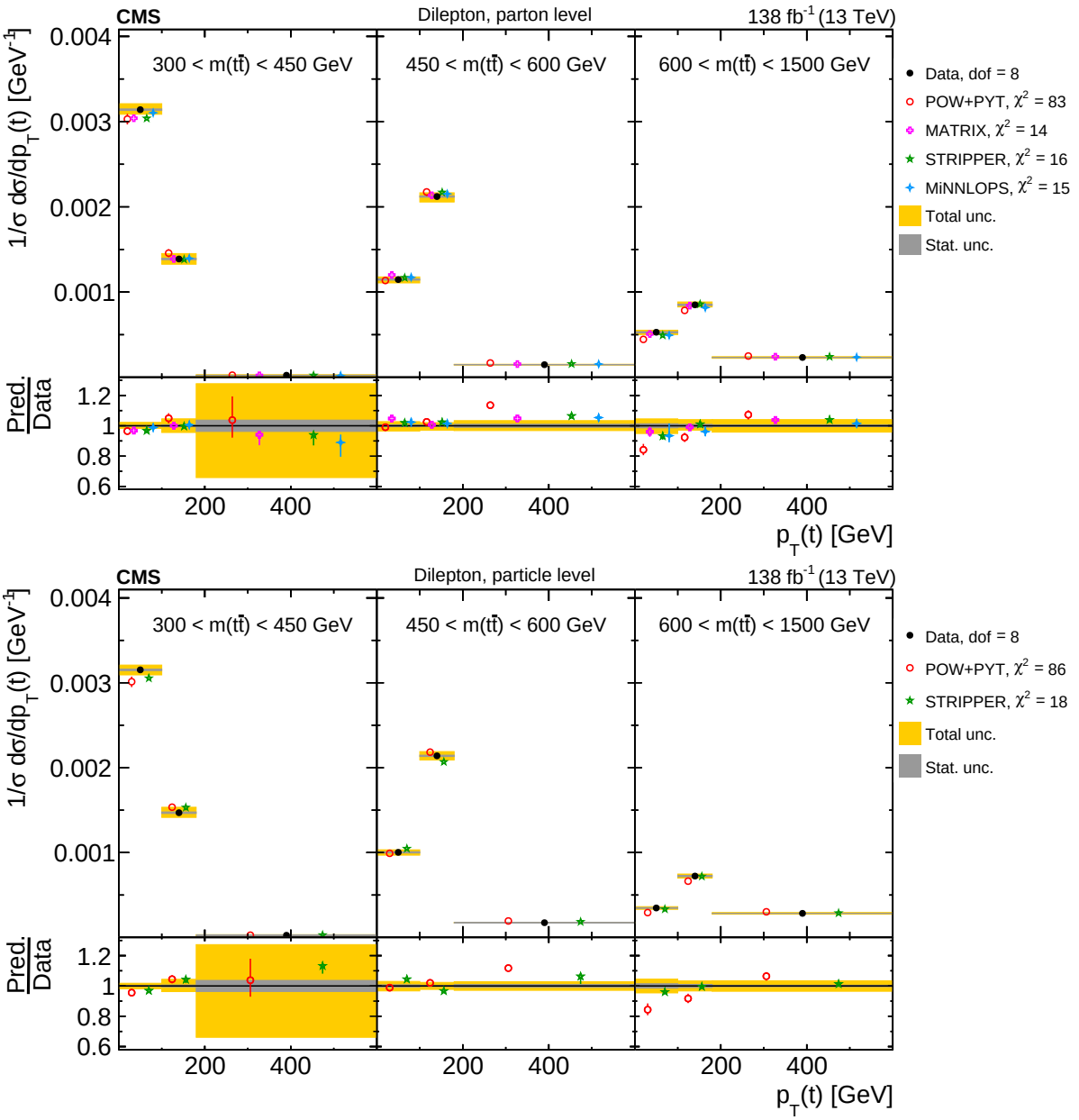

Figure 47: Normalized $[m(\mathrm{t\bar{t}}), p_{\mathrm{T}}(\mathrm{t})]$ cross sections are shown for data (filled circles), POWHEG+PYTHIA 8 ('POW-PYT', open circles) simulation, and various theoretical predictions with beyond-NLO precision (other points). Further details can be found in the caption of Fig. 46.

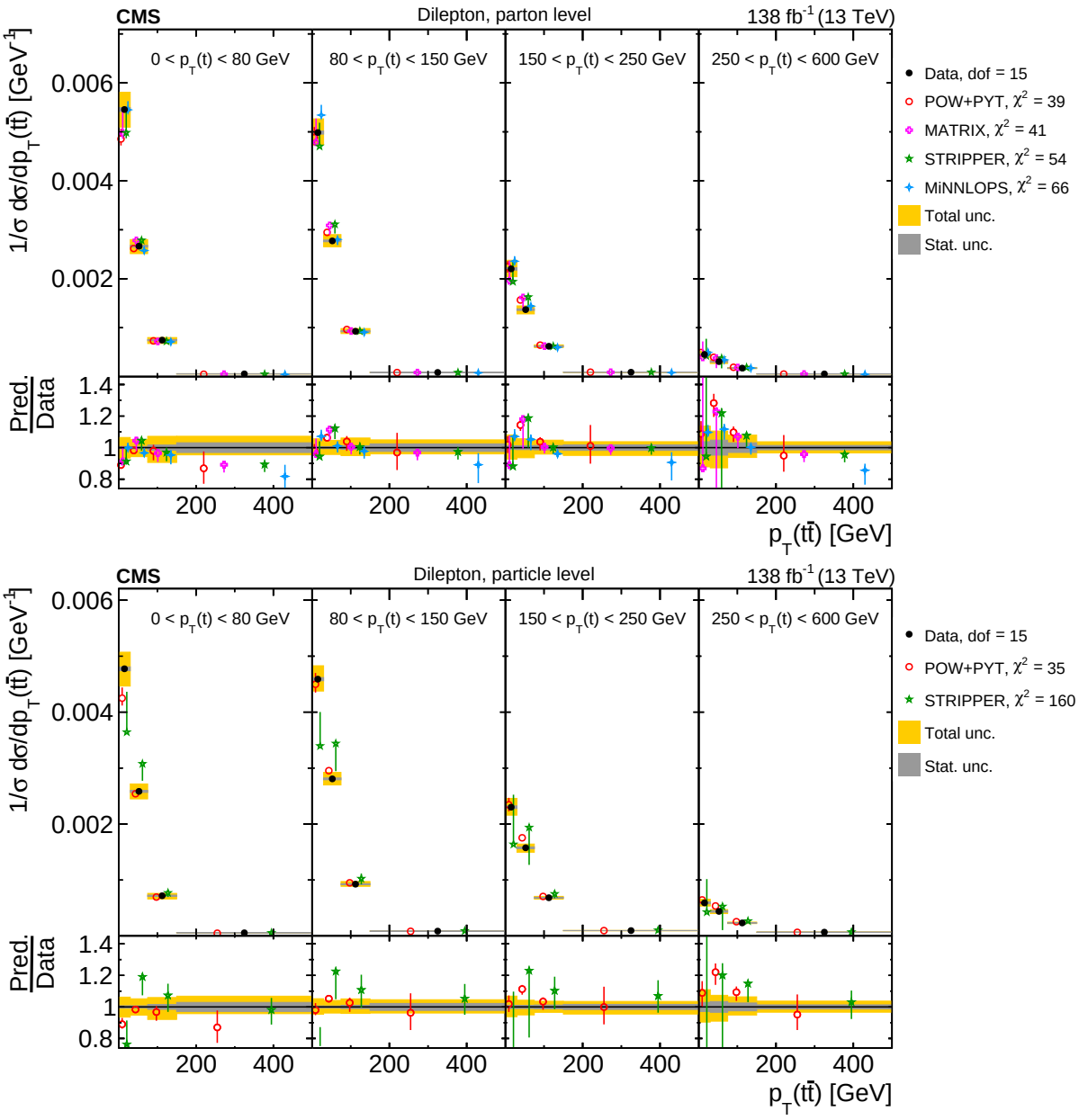

Figure 48: Normalized $[p_{\mathrm{T}}(\mathrm{t}), p_{\mathrm{T}}(\mathrm{t\bar{t}})]$ cross sections are shown for data (filled circles), POWHEG+PYTHIA 8 ('POW-PYT', open circles) simulation, and various theoretical predictions with beyond-NLO precision (other points). Further details can be found in the caption of Fig. 46.

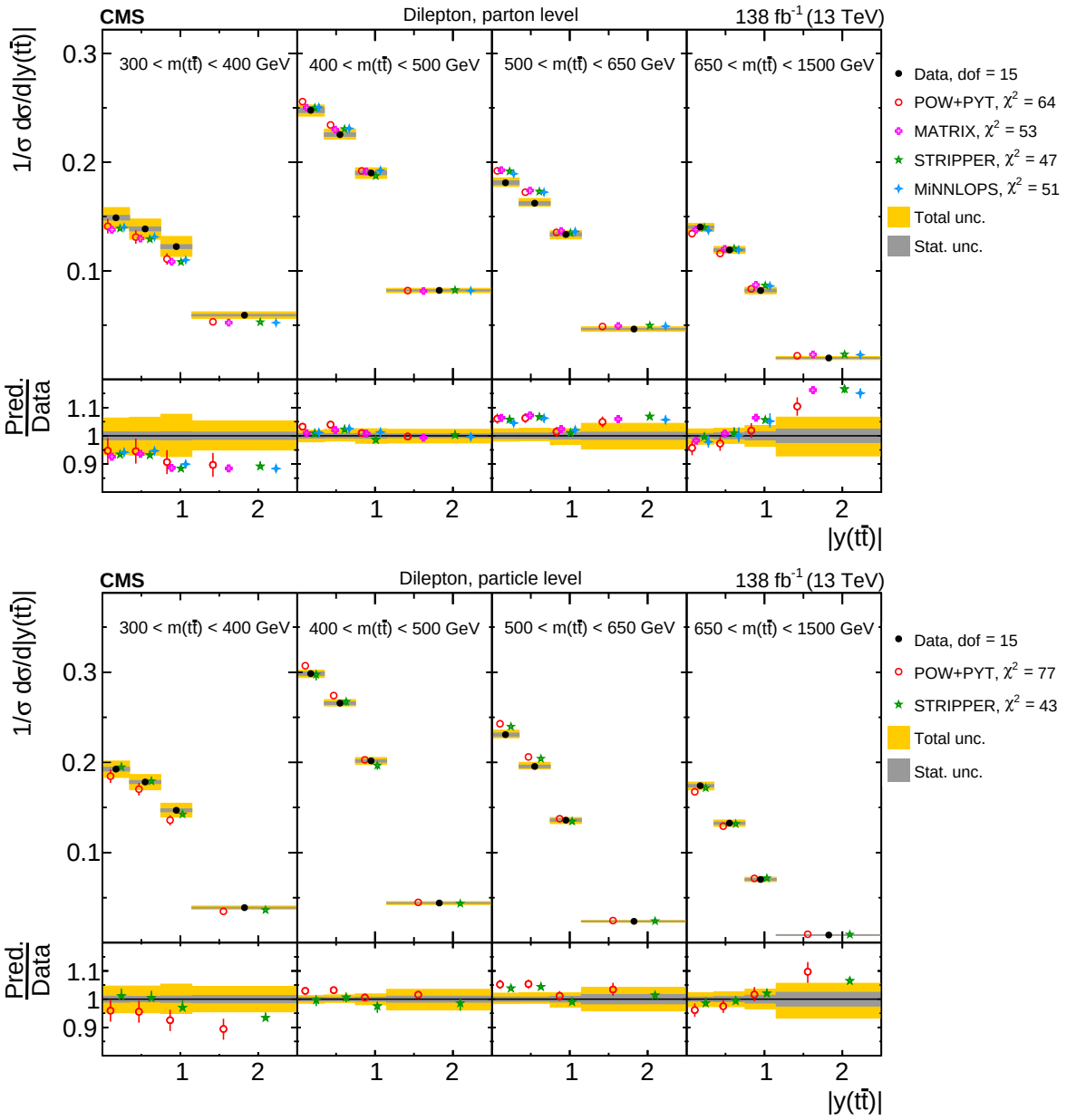

Figure 49: Normalized $[m(\mathrm{t\bar{t}}), |y(\mathrm{t\bar{t}})|]$ cross sections are shown for data (filled circles), POWHEG+PYTHIA 8 ('POW-PYT', open circles) simulation, and various theoretical predictions with beyond-NLO precision (other points). Further details can be found in the caption of Fig. 46.

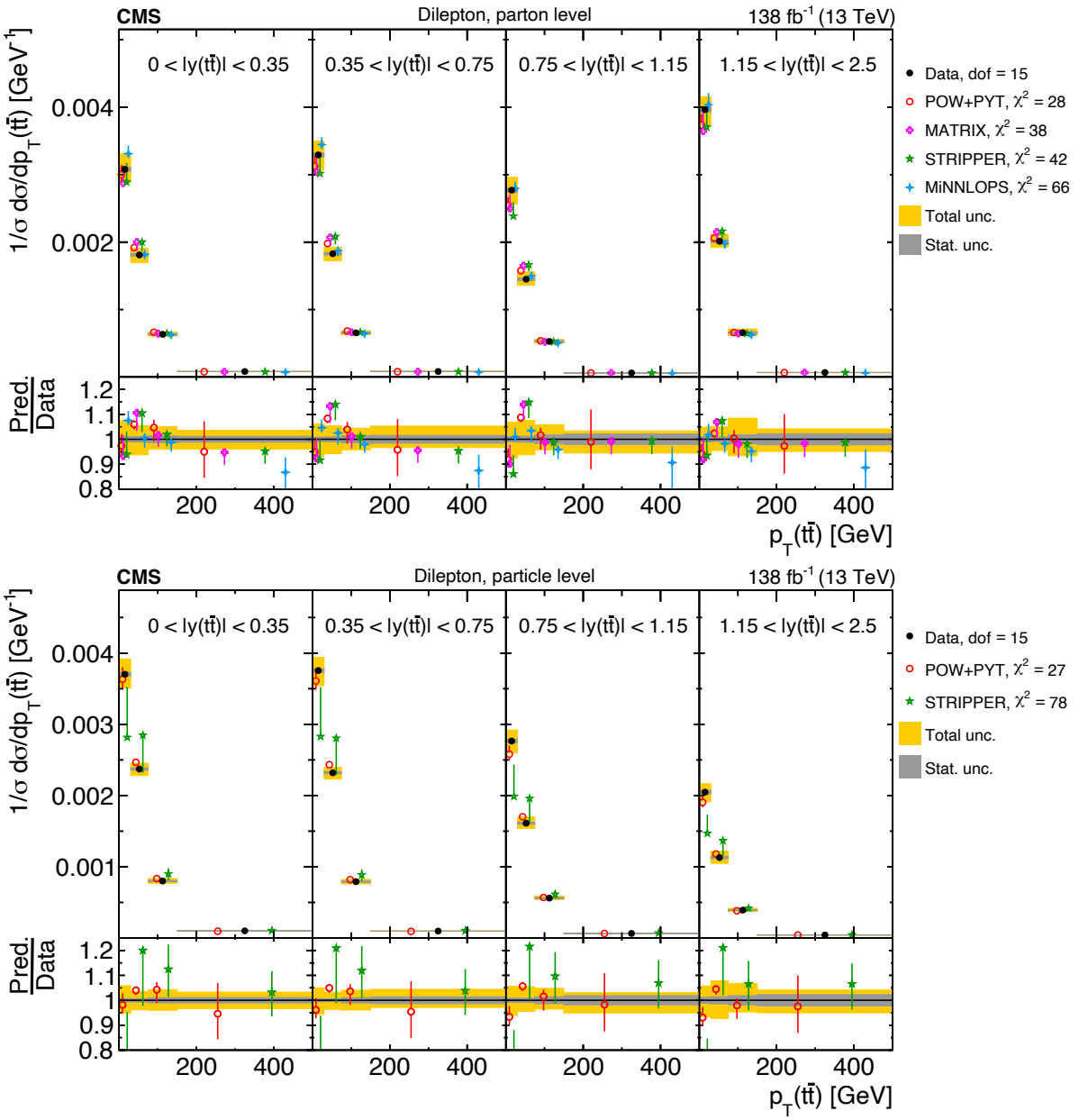

Figure 50: Normalized $[|y(t\bar{t})|, p_T(t\bar{t})]$ cross sections are shown for data (filled circles), POWHEG+PYTHIA 8 ('POW-PYT', open circles) simulation, and various theoretical predictions with beyond-NLO precision (other points). Further details can be found in the caption of Fig. 46.

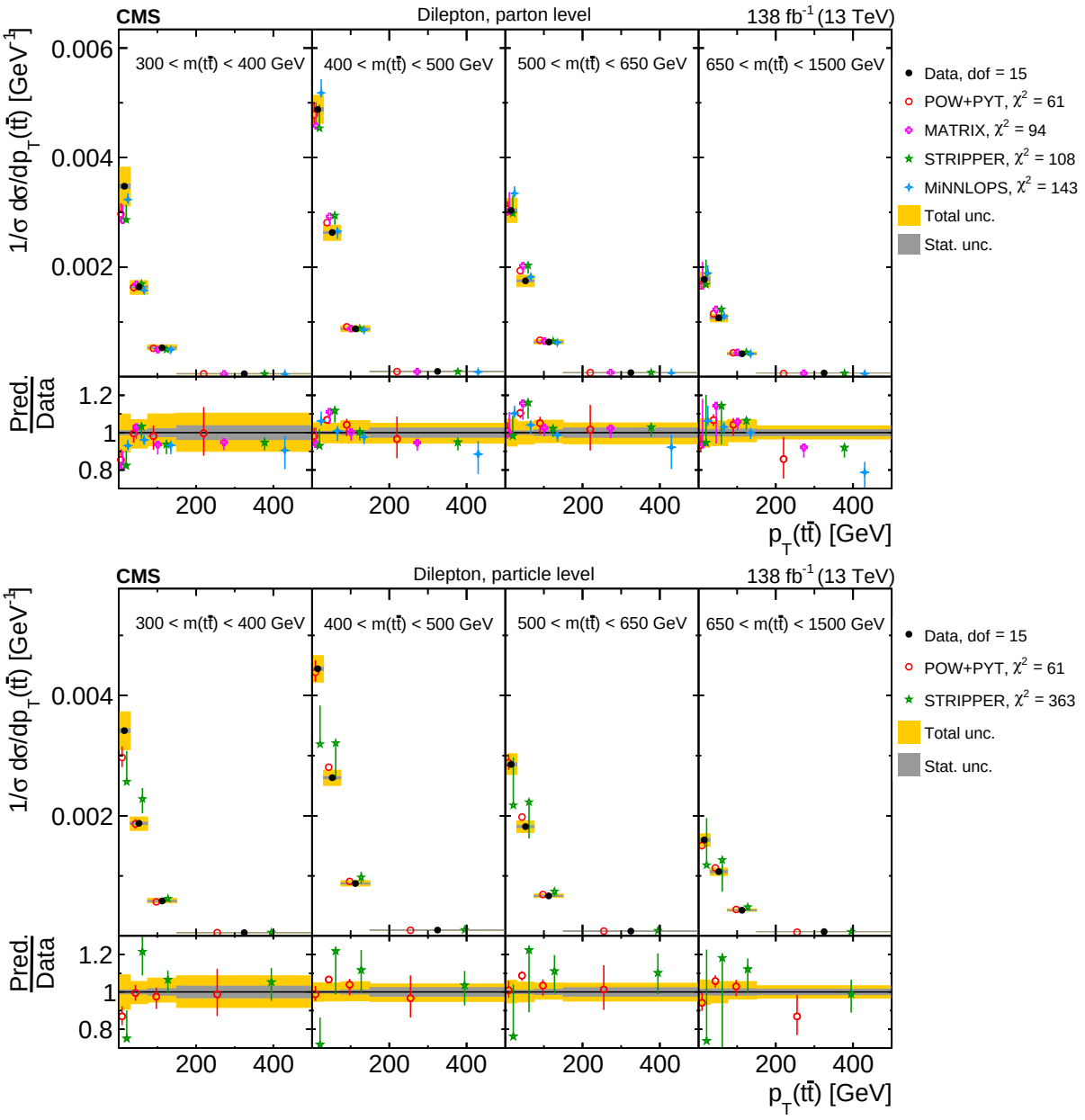

Figure 51: Normalized $[m(\mathrm{t\bar{t}}), p_{\mathrm{T}}(\mathrm{t\bar{t}})]$ cross sections are shown for data (filled circles), POWHEG+PYTHIA 8 ('POW-PYT', open circles) simulation, and various theoretical predictions with beyond-NLO precision (other points). Further details can be found in the caption of Fig. 46.

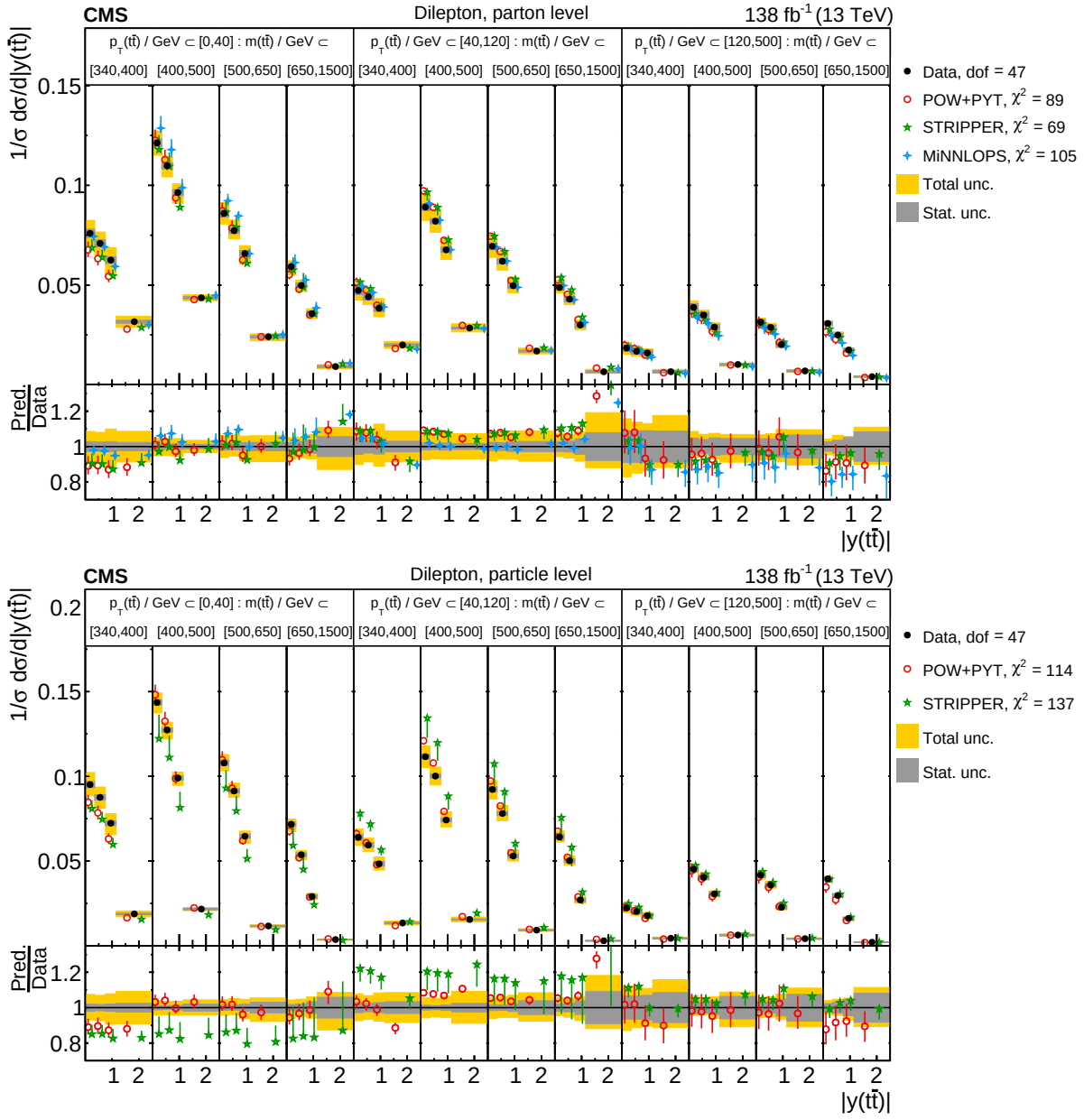

Figure 52: Normalized $[p_{\mathrm{T}}(\mathrm{t\bar{t}}), m(\mathrm{t\bar{t}}), |y(\mathrm{t\bar{t}})|]$ cross sections are shown for data (filled circles), POWHEG+PYTHIA 8 ('POW-PYT', open circles) simulation, and various theoretical predictions with beyond-NLO precision (other points). Further details can be found in the caption of Fig. 46.

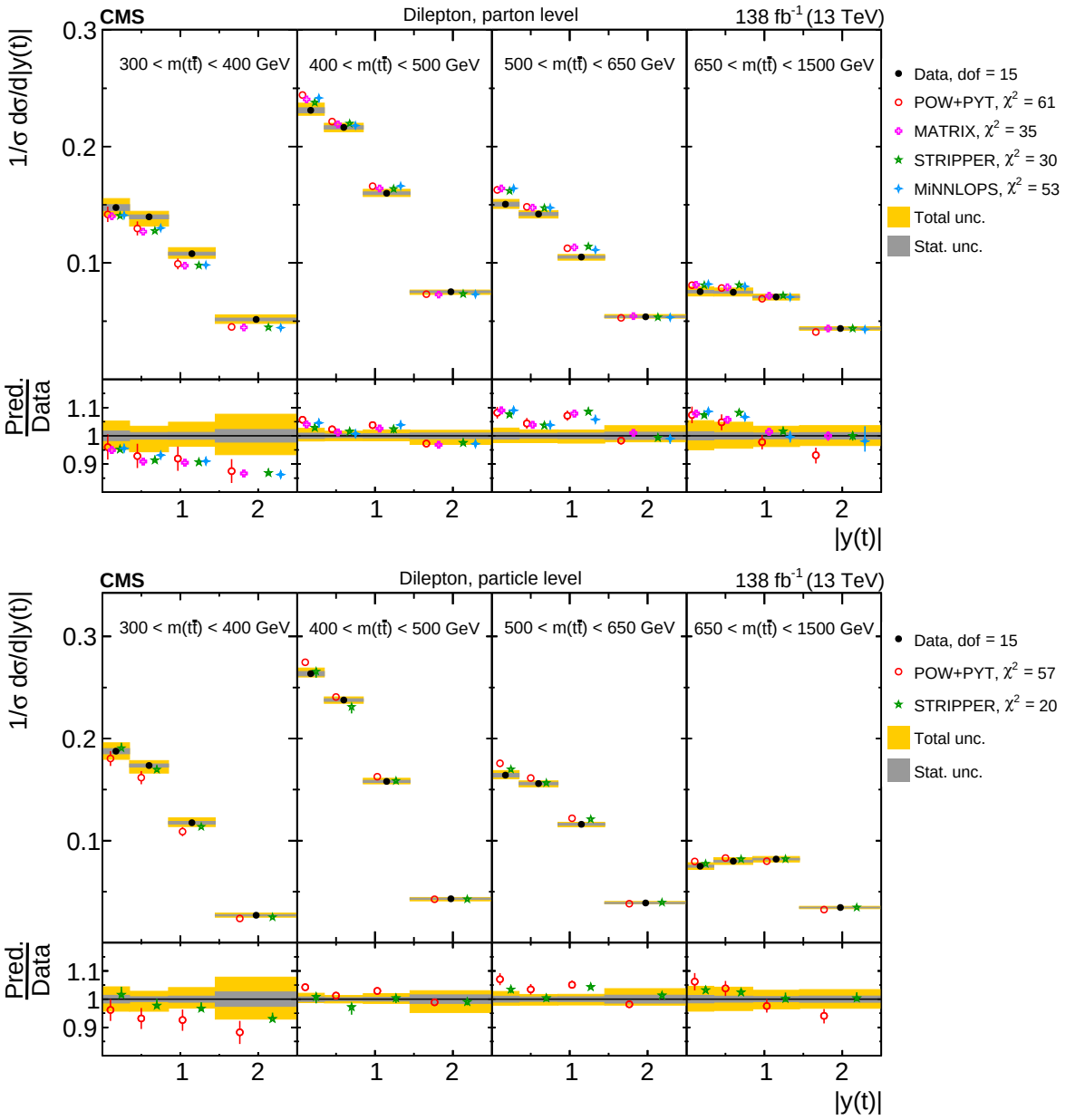

Figure 53: Normalized $[m(\mathrm{t\bar{t}}), |y(\mathrm{t})|]$ cross sections are shown for data (filled circles), POWHEG+PYTHIA 8 ('POW-PYT', open circles) simulation, and various theoretical predictions with beyond-NLO precision (other points). Further details can be found in the caption of Fig. 46.

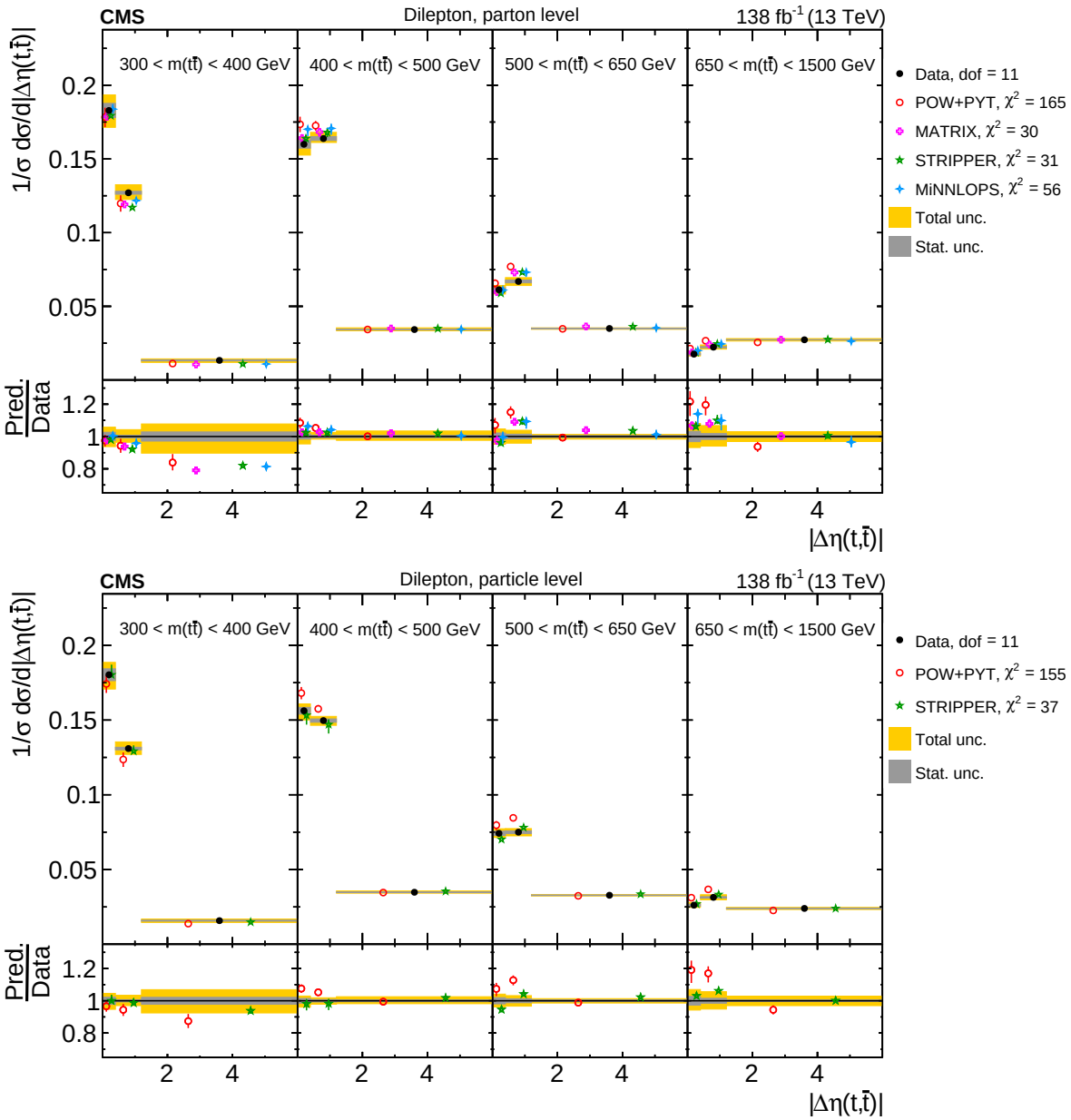

Figure 54: Normalized $[m(\mathrm{t\bar{t}}), |\Delta\eta(\mathrm{t},\bar{\mathrm{t}})|]$ cross sections are shown for data (filled circles), POWHEG+PYTHIA 8 ('POW-PYT', open circles) simulation, and various theoretical predictions with beyond-NLO precision (other points). Further details can be found in the caption of Fig. 46.

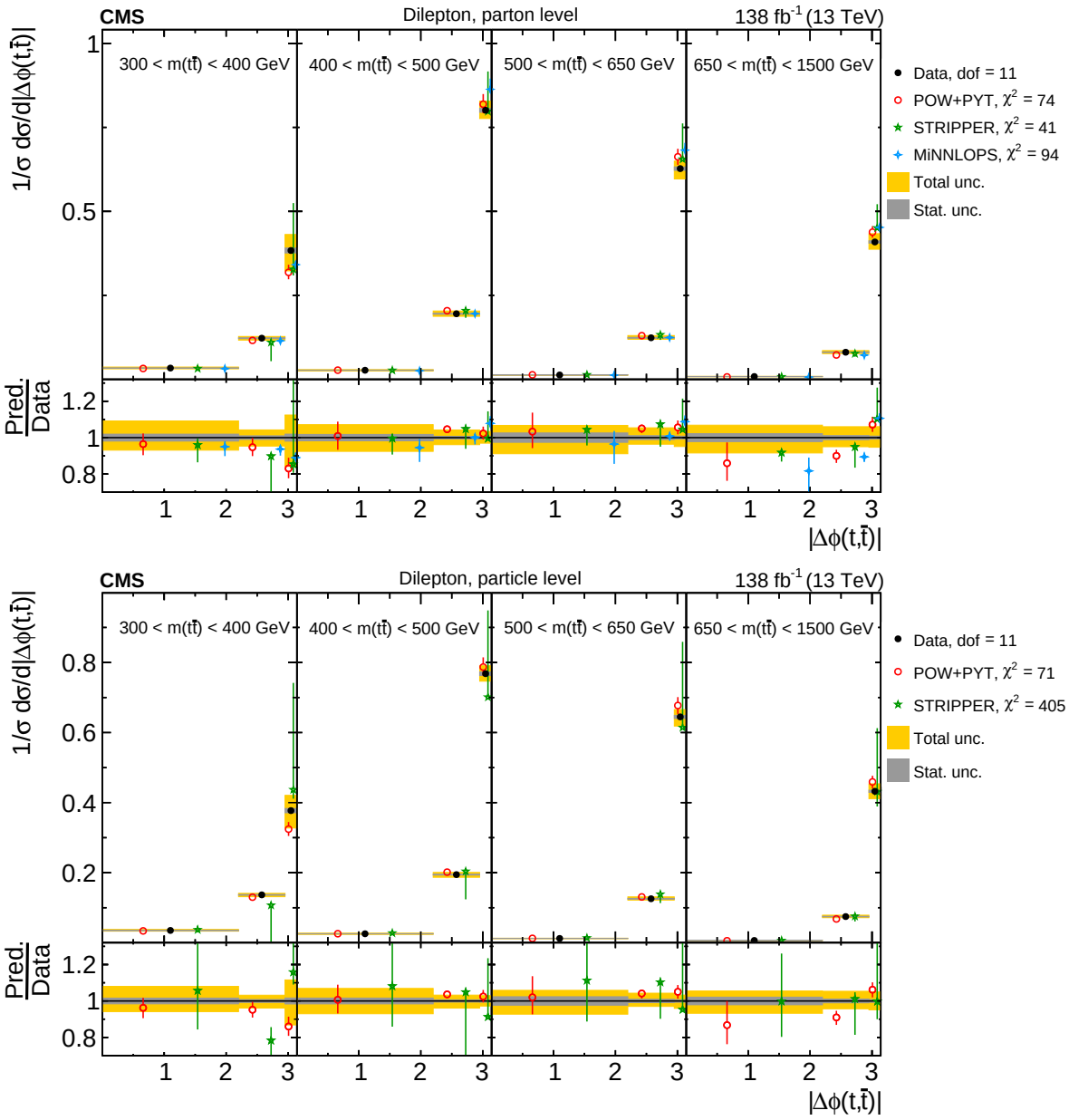

Figure 55: Normalized $[m(\mathrm{t\bar{t}}), |\Delta\phi(\mathrm{t},\bar{\mathrm{t}})|]$ cross sections are shown for data (filled circles), POWHEG+PYTHIA 8 ('POW-PYT', open circles) simulation, and various theoretical predictions with beyond-NLO precision (other points). Further details can be found in the caption of Fig. 46.

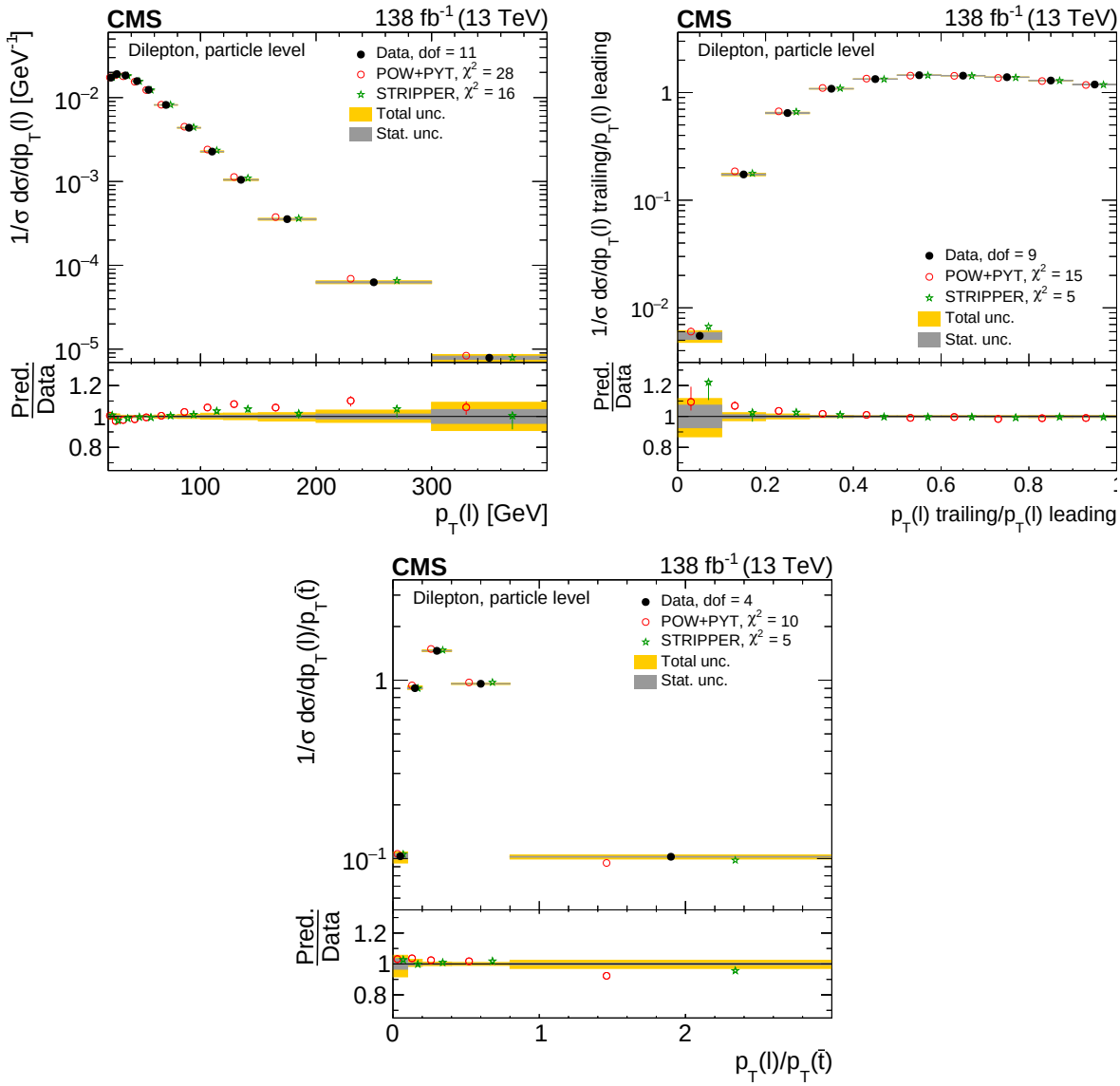

Figure 56: Normalized differential $t\bar{t}$ production cross sections as functions of p_T of the lepton (upper left), of the ratio of the trailing and leading lepton p_T (upper right), and of the ratio of lepton and top antiquark p_T (lower middle), measured at the particle level in a fiducial phase space. The data are shown as filled circles with grey and yellow bands indicating the statistical and total uncertainties (statistical and systematic uncertainties added in quadrature), respectively. For each distribution, the number of degrees of freedom (dof) is also provided. The cross sections are compared to predictions from the POWHEG+PYTHIA8 ('POW-PYT', open circles) simulation and STRIPPER NNLO calculation (stars). The estimated uncertainties in the predictions are represented by a vertical bar on the corresponding points. For each model, a value of χ^2 is reported that takes into account the measurement uncertainties. The lower panel in each plot shows the ratios of the predictions to the data.

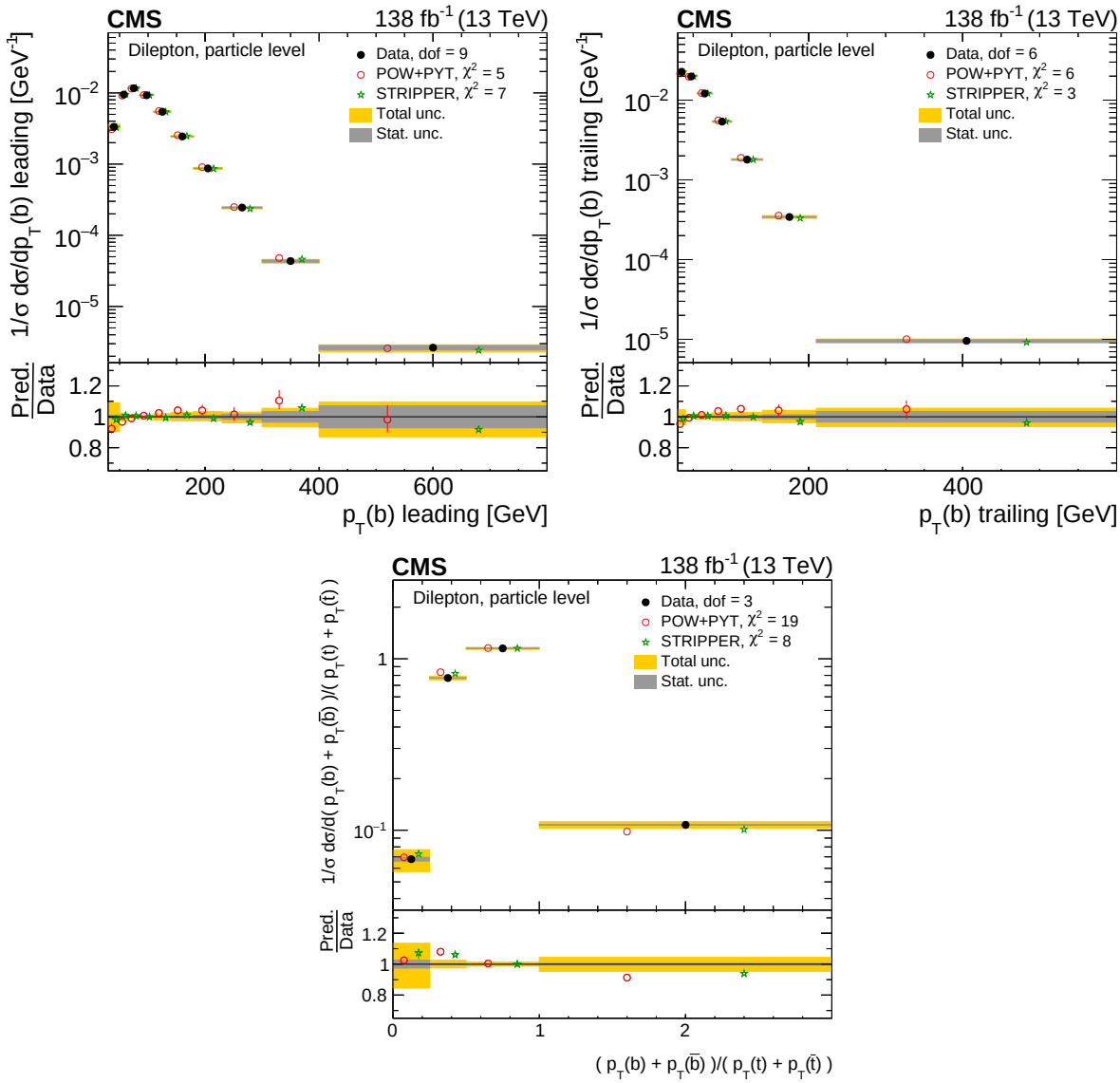

Figure 57: Normalized differential $\mathrm{t\bar{t}}$ production cross sections as functions of the p_{T} of the leading (upper left) and trailing (upper right) b jet, and $(p_{\mathrm{T}}(\mathrm{b}) + p_{\mathrm{T}}(\bar{\mathrm{b}}))/(p_{\mathrm{T}}(\mathrm{t}) + p_{\mathrm{T}}(\bar{\mathrm{t}}))$ (lower) are shown for data (filled circles), POWHEG+PYTHIA 8 ('POW-PYT', open circles) simulation, and STRIPPER NNLO calculation (stars). Further details can be found in the caption of Fig. 56.

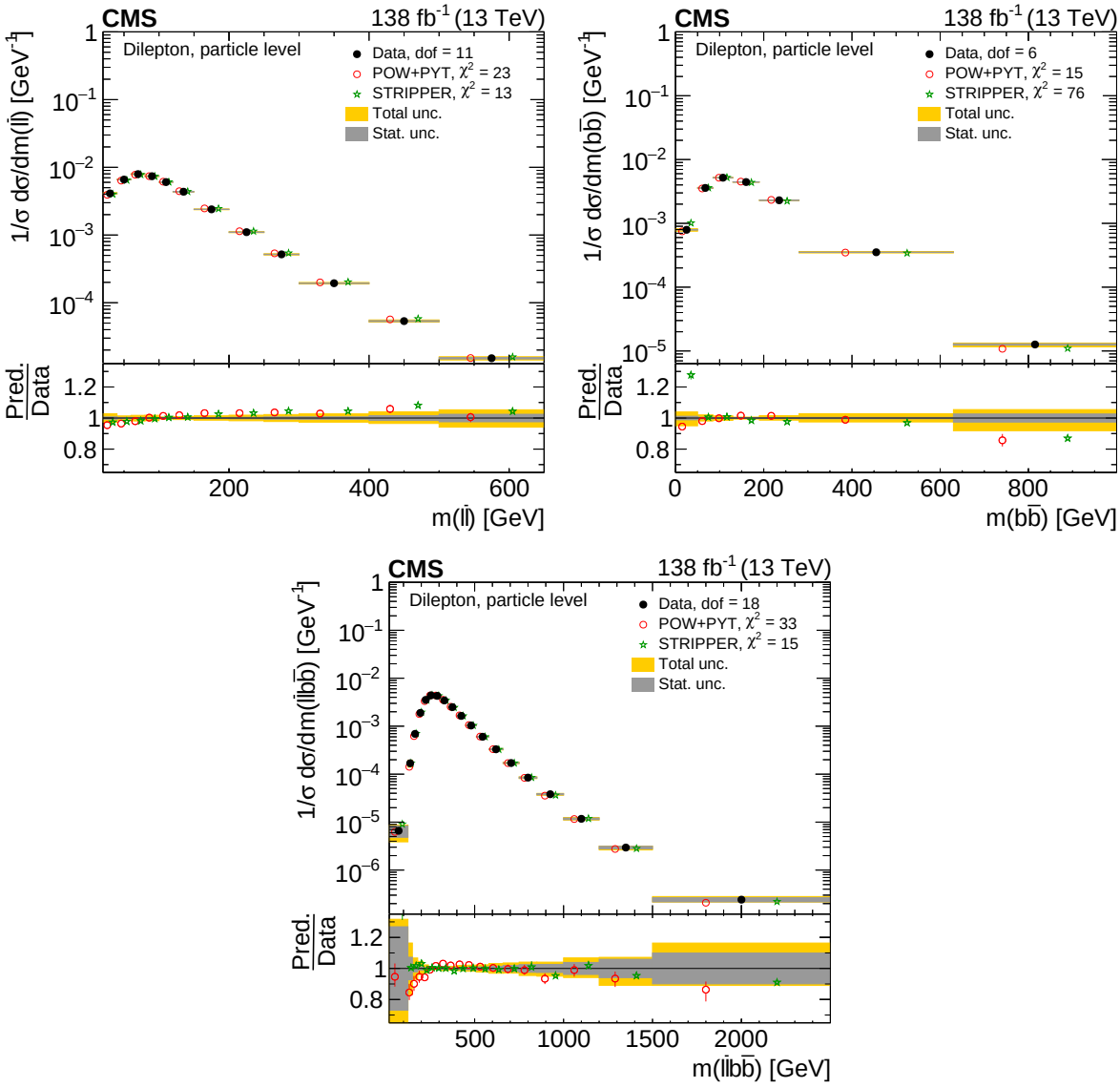

Figure 58: Normalized differential $\mathrm{t\bar{t}}$ production cross sections as functions of $m(\ell\bar{\ell})$ (upper left), $m(\mathrm{b\bar{b}})$ (upper right), and $m(\ell\bar{\ell}\mathrm{b\bar{b}})$ (lower) are shown for data (filled circles), POWHEG+PYTHIA 8 ('POW-PYT', open circles) simulation, and STRIPPER NNLO calculation (stars). Further details can be found in the caption of Fig. 56.

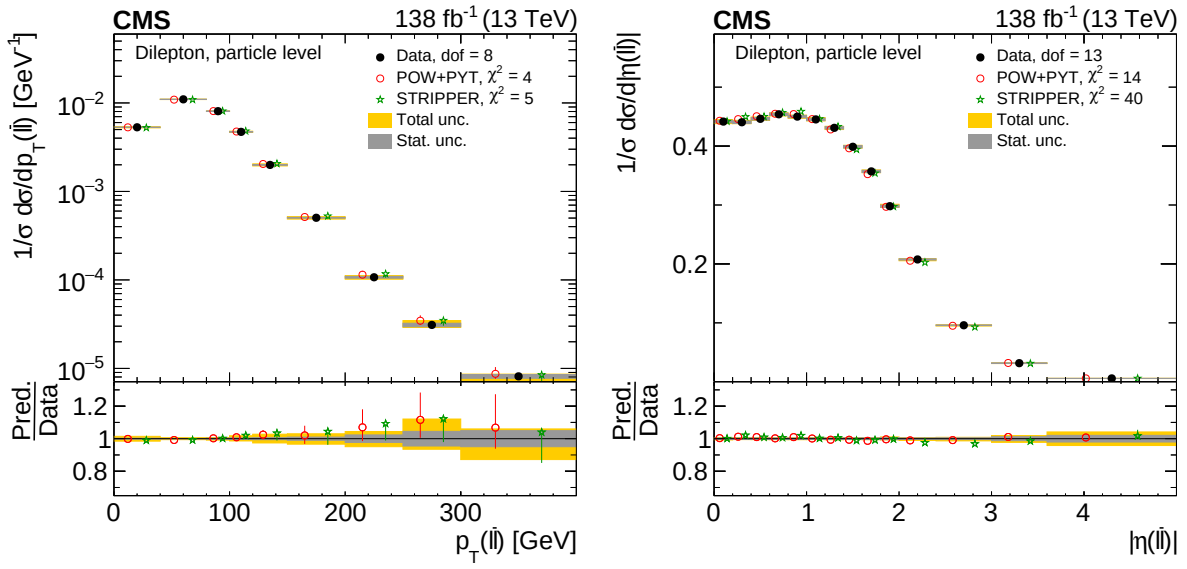

Figure 59: Normalized differential $\mathrm{t\bar{t}}$ production cross sections as functions of $p_{\mathrm{T}}(\ell\bar{\ell})$ (left) and $|\eta(\ell\bar{\ell})|$ (right) are shown for data (filled circles), POWHEG+PYTHIA 8 ('POW-PYT', open circles) simulation, and STRIPPER NNLO calculation (stars). Further details can be found in the caption of Fig. 56.

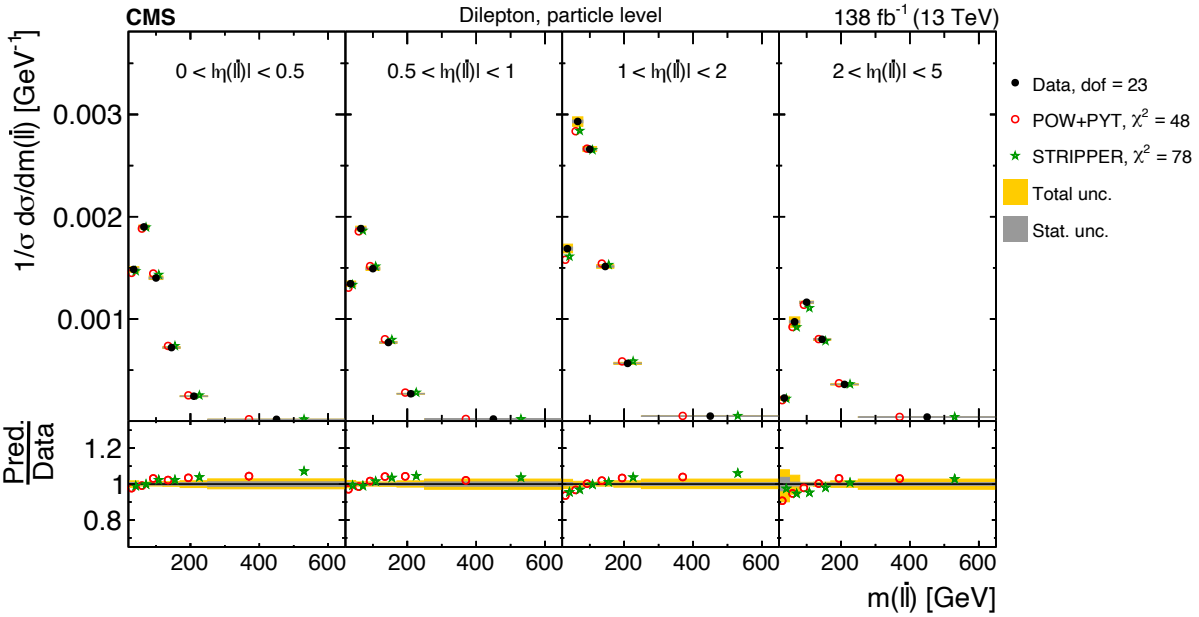

Figure 60: Normalized $[|\eta(\ell\bar{\ell})|, m(\ell\bar{\ell})]$ cross sections are shown for data (filled circles), POWHEG+PYTHIA 8 ('POW-PYT', open circles) simulation, and STRIPPER NNLO calculation (stars). Further details can be found in the caption of Fig. 56.

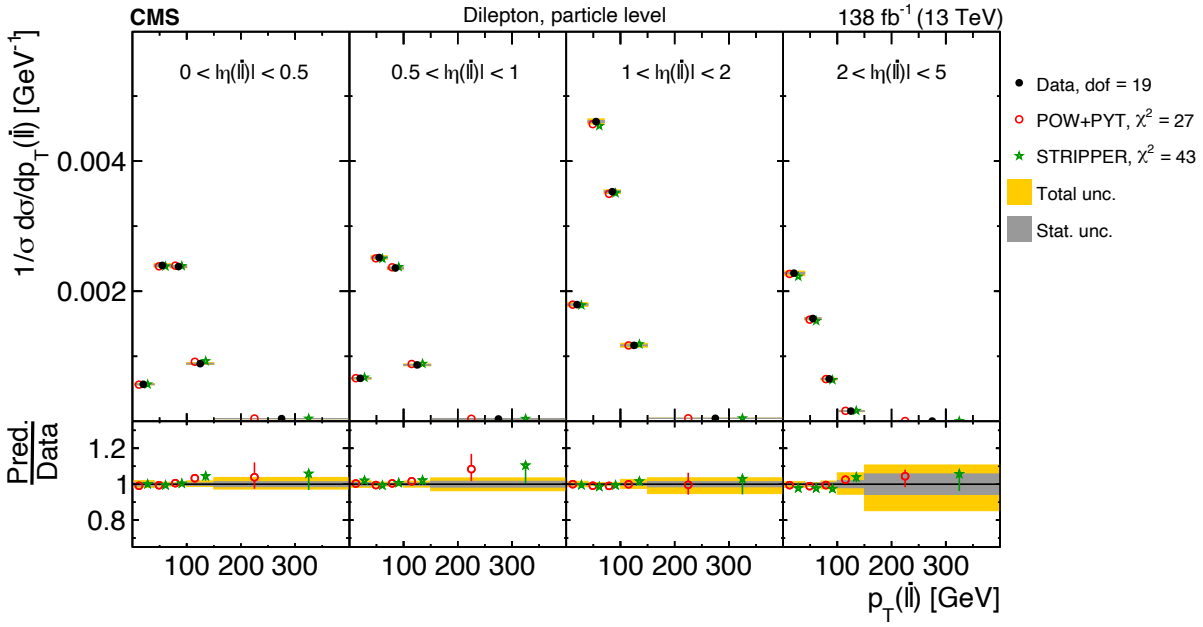

Figure 61: Normalized $[|\eta(\ell\bar{\ell})|, p_{\mathrm{T}}(\ell\bar{\ell})]$ cross sections are shown for data (filled circles), POWHEG+PYTHIA 8 ('POW-PYT', open circles) simulation, and STRIPPER NNLO calculation (stars). Further details can be found in the caption of Fig. 56.

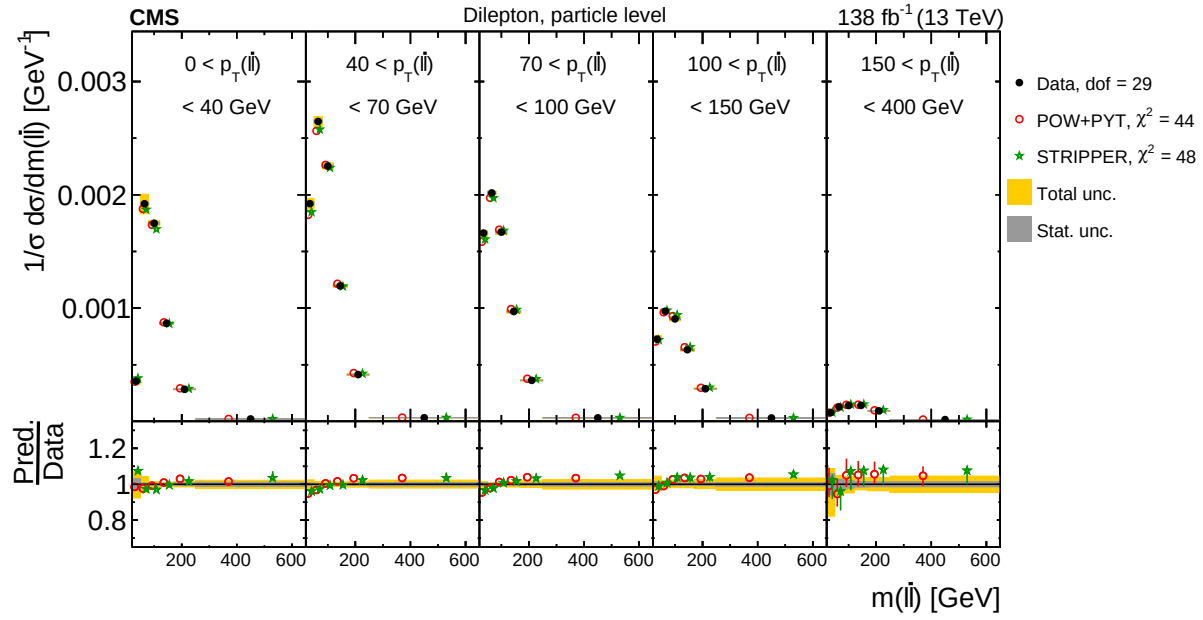

Figure 62: Normalized $[p_{\mathrm{T}}(\ell\bar{\ell}), m(\ell\bar{\ell})]$ cross sections are shown for data (filled circles), POWHEG+PYTHIA 8 ('POW-PYT', open circles) simulation, and STRIPPER NNLO calculation (stars). Further details can be found in the caption of Fig. 56.

Table 8: The χ^2 values and dof of the measured normalized single-differential cross sections for $t\bar{t}$ and top quark kinematic observables at the parton level are shown with respect to the POWHEG+PYTHIA8 ('POW-PYT') simulation and various theoretical predictions with beyond-NLO precision. The χ^2 values are calculated taking only measurement uncertainties into account and excluding theory uncertainties. The corresponding χ^2 values including theory uncertainties are indicated with the brackets (w. unc.).

Cross section variables	dof	χ^2				
		POW+PYT (w. unc.)	aN^{3}LO (w. unc.)	MATRIX (w. unc.)	STRIPPER (w. unc.)	MiNNLOPS (w. unc.)
$p_T(t)$	6	15 (11)	35 (29)	3 (3)	8 (5)	4 (4)
$p_T(\bar{t})$	6	13 (9)	—	4 (3)	10 (9)	5 (5)
$y(t)$	9	23 (20)	23 (12)	16 (16)	17 (16)	15 (13)
$y(\bar{t})$	9	28 (25)	—	15 (13)	25 (24)	23 (17)
$p_T(t\bar{t})$	6	22 (7)	—	7 (2)	9 (3)	55 (14)
$y(t\bar{t})$	11	10 (8)	—	6 (6)	9 (9)	9 (9)
$m(t\bar{t})$	6	5 (3)	—	5 (4)	5 (4)	2 (2)
$\lvert\Delta\phi(t,\bar{t})\rvert$	3	1 (0)	—	75 (0)	65 (1)	5 (4)
$\lvert y(t)\rvert - \lvert y(\bar{t})\rvert$	7	16 (9)	—	2 (2)	3 (3)	12 (9)
$p_T(t)/m(t\bar{t})$	4	33 (20)	—	3 (3)	4 (4)	5 (2)
$p_T(t\bar{t})/m(t\bar{t})$	8	17 (6)	—	109 (9)	102 (10)	20 (5)
$\log(\xi_1)$	8	14 (10)	—	—	15 (14)	12 (11)
$\log(\xi_2)$	8	10 (7)	—	—	12 (11)	7 (7)

Table 9: The χ^2 values and dof of the measured normalized single-differential cross sections for $t\bar{t}$ and top quark kinematic observables at the particle level are shown with respect to the POWHEG+PYTHIA8 ('POW-PYT') simulation and the STRIPPER NNLO calculation. The χ^2 values are calculated taking only measurement uncertainties into account and excluding theory uncertainties. The corresponding χ^2 values including theory uncertainties are indicated with the brackets (w. unc.).

Cross section variables	dof	χ^2	
		POW+PYT (w. unc.)	STRIPPER (w. unc.)
$p_T(t)$	6	17 (12)	3 (2)
$p_T(\bar{t})$	6	14 (9)	3 (2)
$y(t)$	9	19 (16)	11 (11)
$y(\bar{t})$	9	24 (20)	10 (9)
$p_T(t\bar{t})$	6	21 (7)	83 (8)
$y(t\bar{t})$	11	10 (7)	19 (14)
$m(t\bar{t})$	6	5 (3)	4 (2)
$\lvert\Delta\phi(t,\bar{t})\rvert$	3	1 (0)	1076 (2)
$\lvert y(t)\rvert - \lvert y(\bar{t})\rvert$	7	15 (10)	4 (3)
$p_T(t)/m(t\bar{t})$	4	30 (20)	8 (4)
$p_T(t\bar{t})/m(t\bar{t})$	8	18 (7)	144 (7)
$\log(\xi_1)$	8	14 (9)	10 (10)
$\log(\xi_2)$	8	9 (6)	9 (9)

Table 10: The χ^2 values and dof of the measured normalized multi-differential cross sections for $t\bar{t}$ and top quark kinematic observables at the parton level are shown with respect to the POWHEG+PYTHIA8 ('POW-PYT') simulation and various theoretical predictions with beyond-NLO precision. The χ^2 values are calculated taking only measurement uncertainties into account and excluding theory uncertainties. The corresponding χ^2 values including theory uncertainties are indicated with the brackets (w. unc.).

Cross section variables	dof	χ^2				
		POW+PYT (w. unc.)	aN^{3}LO (w. unc.)	MATRIX (w. unc.)	STRIPPER (w. unc.)	MiNNLOPS (w. unc.)
$[\lvert y(t)\rvert,\ p_T(t)]$	15	40 (31)	36 (36)	24 (24)	24 (24)	23 (22)
$[m(t\bar{t}),\ p_T(t)]$	8	83 (35)	—	14 (12)	16 (13)	15 (8)
$[p_T(t),\ p_T(t\bar{t})]$	15	39 (21)	—	41 (36)	54 (53)	66 (29)
$[m(t\bar{t}),\ \lvert y(t\bar{t})\rvert]$	15	64 (42)	—	53 (52)	47 (46)	51 (40)
$[\lvert y(t\bar{t})\rvert,\ p_T(t\bar{t})]$	15	28 (15)	—	38 (36)	42 (41)	66 (25)
$[m(t\bar{t}),\ p_T(t\bar{t})]$	15	61 (43)	—	94 (83)	108 (95)	143 (34)
$[p_T(t\bar{t}),\ m(t\bar{t}),\ \lvert y(t\bar{t})\rvert]$	47	89 (64)	—	—	69 (68)	105 (77)
$[m(t\bar{t}),\ \lvert y(t)\rvert]$	15	61 (37)	—	35 (34)	30 (29)	53 (45)
$[m(t\bar{t}),\ \lvert \Delta\eta(t,\bar{t})\rvert]$	11	165 (31)	—	30 (29)	31 (30)	56 (17)
$[m(t\bar{t}),\ \lvert \Delta\phi(t,\bar{t})\rvert]$	11	74 (47)	—	—	41 (18)	94 (67)

Table 11: The χ^2 values and dof of the measured normalized multi-differential cross sections for $t\bar{t}$ and top quark kinematic observables at the particle level are shown with respect to the POWHEG+PYTHIA 8 ('POW-PYT') simulation and the STRIPPER NNLO calculation. The χ^2 values are calculated taking only measurement uncertainties into account and excluding theory uncertainties. The corresponding χ^2 values including theory uncertainties are indicated with the brackets (w. unc.).

Cross section variables	dof	χ^2	
		POW+PYT (w. unc.)	STRIPPER (w. unc.)
$[\lvert y(t)\rvert,\ p_T(t)]$	15	35 (25)	16 (16)
$[m(t\bar{t}),\ p_T(t)]$	8	86 (36)	18 (9)
$[p_T(t),\ p_T(t\bar{t})]$	15	35 (19)	160 (109)
$[m(t\bar{t}),\ \lvert y(t\bar{t})\rvert]$	15	77 (40)	43 (42)
$[\lvert y(t\bar{t})\rvert,\ p_T(t\bar{t})]$	15	27 (18)	78 (40)
$[m(t\bar{t}),\ p_T(t\bar{t})]$	15	61 (36)	363 (146)
$[p_T(t\bar{t}),\ m(t\bar{t}),\ \lvert y(t\bar{t})\rvert]$	47	114 (68)	137 (82)
$[m(t\bar{t}),\ \lvert y(t)\rvert]$	15	57 (26)	20 (18)
$[m(t\bar{t}),\ \lvert \Delta\eta(t,\bar{t})\rvert]$	11	155 (30)	37 (21)
$[m(t\bar{t}),\ \lvert \Delta\phi(t,\bar{t})\rvert]$	11	71 (42)	405 (334)

Table 12: The χ^2 values and dof of the measured normalized single-differential cross sections for lepton and b-jet kinematic observables at the particle level are shown with respect to the POWHEG+PYTHIA8 ('POW-PYT') simulation and the STRIPPER NNLO calculation. The χ^2 values are calculated taking only measurement uncertainties into account and excluding theory uncertainties. The corresponding χ^2 values including theory uncertainties are indicated with the brackets (w. unc.).

Cross section variables	dof	χ^2	
		POW+PYT (w. unc.)	STRIPPER (w. unc.)
$p_{\mathrm{T}}(\ell)$	11	28 (18)	16 (16)
$p_{\mathrm{T}}(\ell)$ trailing/$p_{\mathrm{T}}(\ell)$ leading	9	15 (11)	5 (5)
$p_{\mathrm{T}}(\ell)/p_{\mathrm{T}}(\bar{\mathrm{t}})$	4	10 (9)	5 (5)
$p_{\mathrm{T}}(\mathrm{b})$ leading	9	5 (4)	7 (6)
$p_{\mathrm{T}}(\mathrm{b})$ trailing	6	6 (4)	3 (1)
$(p_{\mathrm{T}}(\mathrm{b}) + p_{\mathrm{T}}(\bar{\mathrm{b}}))/(p_{\mathrm{T}}(\mathrm{t}) + p_{\mathrm{T}}(\bar{\mathrm{t}}))$	3	19 (15)	8 (8)
$m(\ell\bar{\ell})$	11	23 (20)	13 (12)
$m(\mathrm{b}\bar{\mathrm{b}})$	6	15 (12)	76 (71)
$m(\ell\bar{\ell}\mathrm{b}\bar{\mathrm{b}})$	18	33 (18)	15 (14)
$p_{\mathrm{T}}(\ell\bar{\ell})$	8	4 (3)	5 (3)
$\lvert\eta(\ell\bar{\ell})\rvert$	13	14 (9)	40 (21)
$[\lvert\eta(\ell\bar{\ell})\rvert, m(\ell\bar{\ell})]$	23	48 (28)	78 (59)
$[\lvert\eta(\ell\bar{\ell})\rvert, p_{\mathrm{T}}(\ell\bar{\ell})]$	19	27 (14)	43 (27)
$[p_{\mathrm{T}}(\ell\bar{\ell}), m(\ell\bar{\ell})]$	29	44 (37)	48 (48)

9.5 Comparisons to POWHEG+PYTHIA 8 predictions using different PDFs

In this subsection the sensitivity of the measured differential $\mathrm{t\bar{t}}$ production cross sections to the PDFs is assessed. The $\mathrm{t\bar{t}}$ production at the LHC is known to be particularly sensitive to the gluon density at higher proton momentum fractions x. In the previous CMS analyses [19, 27], systematic investigations were performed in which different sets of $\mathrm{t\bar{t}}$ kinematic spectra were included in PDF fits and their impact evaluated. A particularly large sensitivity was observed in Ref. [19] for the $[m(\mathrm{t\bar{t}}), |y(\mathrm{t\bar{t}})|]$ cross sections measured at $\sqrt{s} = 8\,\mathrm{TeV}$, leading to a strong constraint on the gluon density at x values around 0.3. In the present analysis, the PDF sensitivity is assessed by comparing kinematic spectra of the top quark or the $\mathrm{t\bar{t}}$ system with the POWHEG+PYTHIA8 predictions, evaluated with a number of different PDF sets: NNPDF3.1 [36], CT14 [116], ABMP16 [117], MMHT2014 [118], and HERAPDF2.0 [119]. For the NNPDF3.1 PDFs, both the NNLO (used in the nominal simulation) and NLO variants are studied, while only the NLO versions are taken for all other sets. The PDFs differ in the input data and methodologies that were used to extract them, as discussed elsewhere [120, 121].

Figure 63 shows the measured normalized single-differential cross sections, defined at the parton level, as functions of $p_{\mathrm{T}}(\mathrm{t})$, $y(\mathrm{t})$, $m(\mathrm{t\bar{t}})$, and $y(\mathrm{t\bar{t}})$, and compared to the predictions obtained with different PDF sets. Most of the PDFs provide a similar description of the data, except HERAPDF2.0 NLO that describes the $p_{\mathrm{T}}(\mathrm{t})$ distribution well but exhibits clear shape deviations for the other spectra, leading to large χ^2 values. In Fig. 64, the $\log(\xi_1)$, $\log(\xi_2)$, and $[m(\mathrm{t\bar{t}}), |y(\mathrm{t\bar{t}})|]$ cross section distributions are shown. As discussed above, in the LO QCD picture the $\log(\xi_1)$ and $\log(\xi_2)$ variables represent the proton momentum fractions carried by the two partons entering the hard interaction. The HERAPDF2.0 NLO prediction undershoots the data near the smallest and largest values of these observables, which may give a hint of a possibly wrong x dependence of the gluon density in this PDF set. For $[m(\mathrm{t\bar{t}}), |y(\mathrm{t\bar{t}})|]$, all PDFs again provide data descriptions of similar quality, except HERAPDF2.0 NLO, that predicts too few events towards large $m(\mathrm{t\bar{t}})$ and $y(\mathrm{t\bar{t}})$ values. The particularly large χ^2 for HERAPDF2.0 NLO for this distribution indicates an enhanced PDF sensitivity for this double-differential cross section. Summarizing, the differential spectra of the top quark and the $\mathrm{t\bar{t}}$ system clearly show sensitivity to the PDFs and, therefore, it will be useful to include the corresponding data in future global PDF fits.

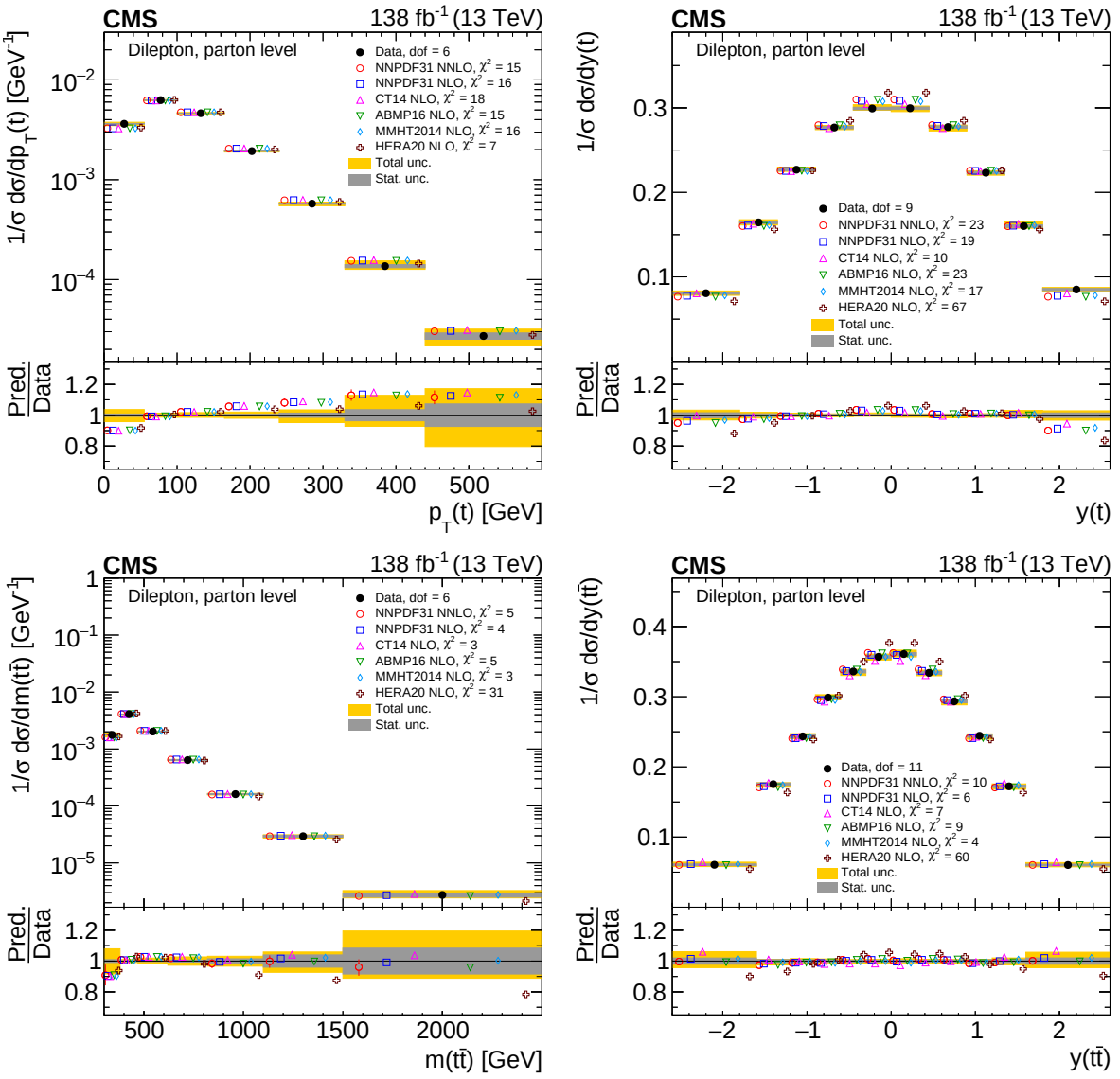

Figure 63: Normalized differential $\mathrm{t\bar{t}}$ production cross sections as functions of $p_{\mathrm{T}}(\mathrm{t})$ (upper left), $y(\mathrm{t})$ (upper right), $m(\mathrm{t\bar{t}})$ (lower left), and $y(\mathrm{t\bar{t}})$ (lower right), measured at the parton level in the full phase space. The data are shown as filled circles with grey and yellow bands indicating the statistical and total uncertainties (statistical and systematic uncertainties added in quadrature), respectively. For each distribution, the number of degrees of freedom (dof) is also provided. The cross sections are compared to predictions from the POWHEG+PYTHIA 8 ('POW-PYT') simulation with various PDF sets. The nominal prediction (open circles) uses the PDF set NNPDF3.1 at NNLO accuracy, assuming a top quark mass value of 172.5 GeV and $\alpha_{\mathrm{S}} = 0.118$. The alternative PDF sets (other points) constitute NNPDF3.1, CT14, ABMP16, MMHT2014, and HERAPDF2.0 at NLO accuracy and assume the same values for the top quark mass and α_{S} as the nominal NNPDF3.1 NNLO PDF set. The estimated uncertainties in the nominal prediction are represented by a vertical bar on the corresponding points. For each PDF set, a value of χ^2 is reported that takes into account the measurement uncertainties. The lower panel in each plot shows the ratios of the predictions to the data.

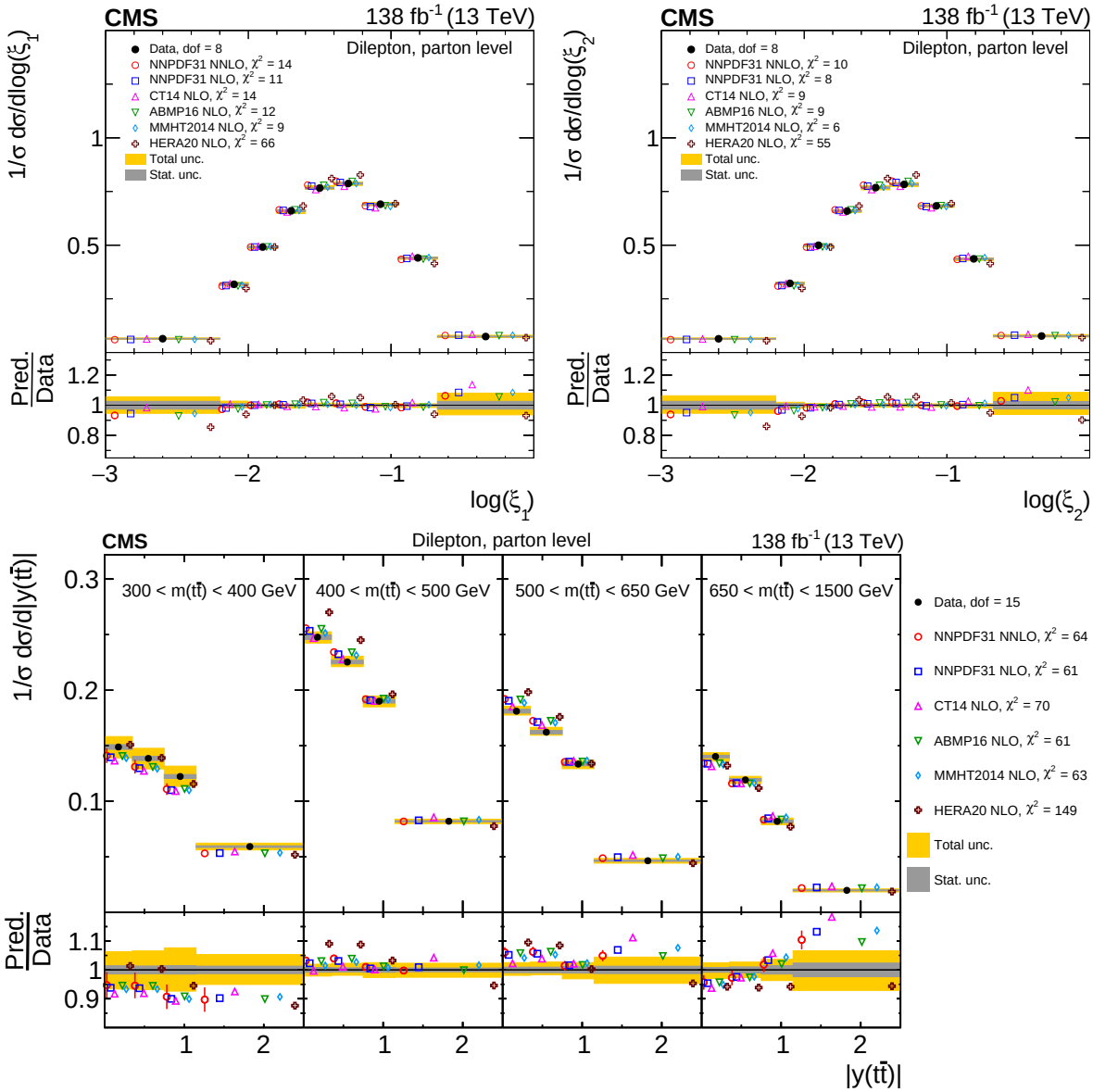

Figure 64: Normalized $\log(\xi_1)$ (upper left), $\log(\xi_2)$ (upper right), and $[m(\mathrm{t\bar{t}}), |y(\mathrm{t\bar{t}})|]$ (lower) cross sections are shown for data (filled circles) and predictions from the POWHEG+PYTHIA 8 ('POW-PYT') simulation with various PDF sets (other points). Further details can be found in the caption of Fig. 63.

10 Summary

A measurement of differential top quark pair ($\mathrm{t\bar{t}}$) production cross sections in proton-proton collisions at $\sqrt{s} = 13\,\mathrm{TeV}$ was presented, performed with events containing two oppositely charged leptons (electrons or muons). The data used in this analysis were recorded in the years 2016 through 2018 with the CMS detector at the LHC and correspond to an integrated luminosity of 138 fb^{-1}. Differential cross sections are measured as functions of kinematical observables of the $\mathrm{t\bar{t}}$ system, the top quark and antiquark and their decay products, and the total number of additional jets in the event not originating from the $\mathrm{t\bar{t}}$ decay. The measurements are performed as functions of single observables, or simultaneously as functions of two or three kinematic variables. The differential cross sections are defined both with particle-level objects in a fiducial phase space close to that of the detector acceptance and with parton-level top quarks in the full phase space. Overall, both the statistical and the systematic uncertainties in the measurements are improved by a factor of about two compared to the previous analyses [26, 27] which are based on the 2016 data set.

Predictions of several next-to-leading-order (NLO) Monte Carlo (MC) event generators that differ in the hard matrix element, parton shower, and hadronization models were compared to the data. The predictions of these MC models, without taking theoretical uncertainties into account, generally fail to describe many of the measured cross sections in their full kinematic range. The predicted transverse momentum p_{T} distributions of the top quark and antiquark are harder than observed in the data, and the rapidity distributions are more central. The invariant mass and rapidity distributions of the $\mathrm{t\bar{t}}$ system are reasonably well described by the models overall. The predictions for the $\mathrm{t\bar{t}}$ transverse momentum distribution differ from the data even more than the top quark and antiquark distributions do; none of them provides a good description of the data. Double- and triple-differential cross sections show large model-to-data discrepancies, for instance the effect of a harder top quark p_{T} spectrum $p_{\mathrm{T}}(\mathrm{t})$ in the models is pronounced at high $m(\mathrm{t\bar{t}})$. Differential cross sections as functions of kinematic observables of the leptons and b jets originating from the decay of the top quark and antiquark are measured with high precision. Overall, the observed trends for these objects follow those for the top quarks and antiquarks, with the models predicting harder p_{T} spectra than seen in the data. For the leptons, this effect is somewhat enhanced and furthermore the dilepton invariant mass spectrum is harder in the models than in the data. The distribution of the multiplicity of additional jets in $\mathrm{t\bar{t}}$ events shows varying level of agreement between data and the models. When considered as a function of jet multiplicity, the evolution of the shapes of $\mathrm{t\bar{t}}$, top quark and antiquark kinematic distributions is different for the models and for data. There is an indication that the trend of harder $p_{\mathrm{T}}(\mathrm{t})$ distributions in the models is localized at small jet multiplicities.

Selected kinematic distributions were also compared to a variety of theoretical predictions beyond NLO precision. For observables of the top quark and the $\mathrm{t\bar{t}}$ system, these predictions provide descriptions of the data that are of similar or improved quality, compared to the MC model best describing each variable, except for some of the kinematic spectra for which the theory scale uncertainties are large. For observables associated with the leptons and b jets, the quality of the tested next-to-NLO model is on average comparable to but not better than that of the NLO MC models. Comparing several kinematic distributions of the top quark and the $\mathrm{t\bar{t}}$ system to NLO MC models using various parton distribution function (PDF) sets, clear differences are observed which indicate a sensitivity to PDFs that could be exploited in future PDF fits.

For each distribution, the quality of the description of the data by the models has been assessed with a χ^2 test statistic. When only the measurement uncertainties are taken into account in the

calculation (i.e. neglecting the uncertainties on the predictions), the p-values obtained from the χ^2 tests are in general close to zero, pointing to a poor description of the data by the nominal models. The inclusion of the uncertainties on the predictions leads, in many cases, to substantially reduced χ^2 values with reasonable p-values. However, for several distributions, and in particular for a larger fraction of the multi-differential distributions, the observed differences between data and simulation still remain significant, providing important input for future theoretical predictions.

Acknowledgments

We congratulate our colleagues in the CERN accelerator departments for the excellent performance of the LHC and thank the technical and administrative staffs at CERN and at other CMS institutes for their contributions to the success of the CMS effort. In addition, we gratefully acknowledge the computing centers and personnel of the Worldwide LHC Computing Grid and other centers for delivering so effectively the computing infrastructure essential to our analyses. Finally, we acknowledge the enduring support for the construction and operation of the LHC, the CMS detector, and the supporting computing infrastructure provided by the following funding agencies: SC (Armenia), BMBWF and FWF (Austria); FNRS and FWO (Belgium); CNPq, CAPES, FAPERJ, FAPERGS, and FAPESP (Brazil); MES and BNSF (Bulgaria); CERN; CAS, MoST, and NSFC (China); MINCIENCIAS (Colombia); MSES and CSF (Croatia); RIF (Cyprus); SENESCYT (Ecuador); ERC PRG, RVTT3 and TK202 (Estonia); Academy of Finland, MEC, and HIP (Finland); CEA and CNRS/IN2P3 (France); SRNSF (Georgia); BMBF, DFG, and HGF (Germany); GSRI (Greece); NKFIH (Hungary); DAE and DST (India); IPM (Iran); SFI (Ireland); INFN (Italy); MSIP and NRF (Republic of Korea); MES (Latvia); LAS (Lithuania); MOE and UM (Malaysia); BUAP, CINVESTAV, CONACYT, LNS, SEP, and UASLP-FAI (Mexico); MOS (Montenegro); MBIE (New Zealand); PAEC (Pakistan); MES and NSC (Poland); FCT (Portugal); MESTD (Serbia); MCIN/AEI and PCTI (Spain); MOSTR (Sri Lanka); Swiss Funding Agencies (Switzerland); MST (Taipei); MHESI and NSTDA (Thailand); TUBITAK and TENMAK (Turkey); NASU (Ukraine); STFC (United Kingdom); DOE and NSF (USA).

Individuals have received support from the Marie-Curie program and the European Research Council and Horizon 2020 Grant, contract Nos. 675440, 724704, 752730, 758316, 765710, 824093, and COST Action CA16108 (European Union); the Leventis Foundation; the Alfred P. Sloan Foundation; the Alexander von Humboldt Foundation; the Science Committee, project no. 22rl-037 (Armenia); the Belgian Federal Science Policy Office; the Fonds pour la Formation à la Recherche dans l'Industrie et dans l'Agriculture (FRIA-Belgium); the Agentschap voor Innovatie door Wetenschap en Technologie (IWT-Belgium); the F.R.S.-FNRS and FWO (Belgium) under the "Excellence of Science – EOS" – be.h project n. 30820817; the Beijing Municipal Science & Technology Commission, No. Z191100007219010 and Fundamental Research Funds for the Central Universities (China); the Ministry of Education, Youth and Sports (MEYS) of the Czech Republic; the Shota Rustaveli National Science Foundation, grant FR-22-985 (Georgia); the Deutsche Forschungsgemeinschaft (DFG), under Germany's Excellence Strategy – EXC 2121 "Quantum Universe" – 390833306, and under project number 400140256 - GRK2497; the Hellenic Foundation for Research and Innovation (HFRI), Project Number 2288 (Greece); the Hungarian Academy of Sciences, the New National Excellence Program - ÚNKP, the NKFIH research grants K 124845, K 124850, K 128713, K 128786, K 129058, K 131991, K 133046, K 138136, K 143460, K 143477, 2020-2.2.1-ED-2021-00181, and TKP2021-NKTA-64 (Hungary); the Council of Science and Industrial Research, India; ICSC – National Research Center for High Performance Computing, Big Data and Quantum Computing, funded by the EU NexGeneration program (Italy); the Latvian Council of Science; the Ministry of Educa-

tion and Science, project no. 2022/WK/14, and the National Science Center, contracts Opus 2021/41/B/ST2/01369 and 2021/43/B/ST2/01552 (Poland); the Fundação para a Ciência e a Tecnologia, grant CEECIND/01334/2018 (Portugal); the National Priorities Research Program by Qatar National Research Fund; MCIN/AEI/10.13039/501100011033, ERDF "a way of making Europe", and the Programa Estatal de Fomento de la Investigación Científica y Técnica de Excelencia María de Maeztu, grant MDM-2017-0765 and Programa Severo Ochoa del Principado de Asturias (Spain); the Chulalongkorn Academic into Its 2nd Century Project Advancement Project, and the National Science, Research and Innovation Fund via the Program Management Unit for Human Resources & Institutional Development, Research and Innovation, grant B37G660013 (Thailand); the Kavli Foundation; the Nvidia Corporation; the SuperMicro Corporation; the Welch Foundation, contract C-1845; and the Weston Havens Foundation (USA).

References

[1] Particle Data Group Collaboration, "Review of Particle Physics", *PTEP* **2022** (2022) 083C01, doi:10.1093/ptep/ptac097.

[2] N. Kidonakis, "NNNLO soft-gluon corrections for the top-quark p_T and rapidity distributions", *Phys. Rev. D* **91** (2015) 031501, doi:10.1103/PhysRevD.91.031501, arXiv:1411.2633.

[3] N. Kidonakis, "Top-quark double-differential distributions at approximate N^{3}LO", *Phys. Rev. D* **101** (2020) 074006, doi:10.1103/PhysRevD.101.074006, arXiv:1912.10362.

[4] M. Czakon, D. Heymes, and A. Mitov, "High-precision differential predictions for top-quark pairs at the LHC", *Phys. Rev. Lett.* **116** (2016) 082003, doi:10.1103/PhysRevLett.116.082003, arXiv:1511.00549.

[5] M. Czakon et al., "Top-pair production at the LHC through NNLO QCD and NLO EW", *JHEP* **10** (2017) 186, doi:10.1007/JHEP10(2017)186, arXiv:1705.04105.

[6] M. Czakon et al., "Resummation for (boosted) top-quark pair production at NNLO+NNLL' in QCD", *JHEP* **05** (2018) 149, doi:10.1007/JHEP05(2018)149, arXiv:1803.07623.

[7] S. Catani et al., "Top-quark pair production at the LHC: Fully differential QCD predictions at NNLO", *JHEP* **07** (2019) 100, doi:10.1007/JHEP07(2019)100, arXiv:1906.06535.

[8] M. Czakon, A. Mitov, and R. Poncelet, "NNLO QCD corrections to leptonic observables in top-quark pair production and decay", *JHEP* **05** (2021) 212, doi:10.1007/JHEP05(2021)212, arXiv:2008.11133.

[9] ATLAS Collaboration, "Measurements of top quark pair relative differential cross sections with ATLAS in pp collisions at $\sqrt{s} = 7$ TeV", *Eur. Phys. J. C* **73** (2013) 2261, doi:10.1140/epjc/s10052-012-2261-1, arXiv:1207.5644.

[10] CMS Collaboration, "Measurement of differential top-quark pair production cross sections in pp collisions at $\sqrt{s} = 7$ TeV", *Eur. Phys. J. C* **73** (2013) 2339, doi:10.1140/epjc/s10052-013-2339-4, arXiv:1211.2220.

[11] ATLAS Collaboration, "Measurements of normalized differential cross sections for $t\bar{t}$ production in pp collisions at $\sqrt{s} = 7$ TeV using the ATLAS detector", *Phys. Rev. D* **90** (2014) 072004, doi:10.1103/PhysRevD.90.072004, arXiv:1407.0371.

[12] ATLAS Collaboration, "Differential top-antitop cross section measurements as a function of observables constructed from final-state particles using pp collisions at $\sqrt{s} = 7$ TeV in the ATLAS detector", *JHEP* **06** (2015) 100, doi:10.1007/JHEP06(2015)100, arXiv:1502.05923.

[13] ATLAS Collaboration, "Measurement of top quark pair differential cross sections in the dilepton channel in pp collisions at $\sqrt{s} = 7$ and 8 TeV with ATLAS", *Phys. Rev. D* **94** (2016) 092003, doi:10.1103/PhysRevD.94.092003, arXiv:1607.07281.

[14] CMS Collaboration, "Measurement of the differential cross section for top quark pair production in pp collisions at $\sqrt{s} = 8$ TeV", *Eur. Phys. J. C* **75** (2015) 542, doi:10.1140/epjc/s10052-015-3709-x, arXiv:1505.04480.

[15] ATLAS Collaboration, "Measurements of top-quark pair differential cross sections in the lepton+jets channel in pp collisions at $\sqrt{s} = 8$ TeV using the ATLAS detector", *Eur. Phys. J. C* **76** (2016) 538, doi:10.1140/epjc/s10052-016-4366-4, arXiv:1511.04716.

[16] ATLAS Collaboration, "Measurement of the differential cross section of highly boosted top quarks as a function of their transverse momentum in $\sqrt{s} = 8$ TeV proton-proton collisions using the ATLAS detector", *Phys. Rev. D* **93** (2016) 032009, doi:10.1103/PhysRevD.93.032009, arXiv:1510.03818.

[17] CMS Collaboration, "Measurement of the $t\bar{t}$ production cross section in the all-jets final state in pp collisions at $\sqrt{s} = 8$ TeV", *Eur. Phys. J. C* **76** (2016) 128, doi:10.1140/epjc/s10052-016-3956-5, arXiv:1509.06076.

[18] CMS Collaboration, "Measurement of the integrated and differential $t\bar{t}$ production cross sections for high-p_T top quarks in pp collisions at $\sqrt{s} = 8$ TeV", *Phys. Rev. D* **94** (2016) 072002, doi:10.1103/PhysRevD.94.072002, arXiv:1605.00116.

[19] CMS Collaboration, "Measurement of double-differential cross sections for top quark pair production in pp collisions at $\sqrt{s} = 8$ TeV and impact on parton distribution functions", *Eur. Phys. J. C* **77** (2017) 459, doi:10.1140/epjc/s10052-017-4984-5, arXiv:1703.01630.

[20] ATLAS Collaboration, "Measurement of the top-quark mass in $t\bar{t}$ + 1-jet events collected with the ATLAS detector in pp collisions at $\sqrt{s} = 8$ TeV", *JHEP* **11** (2019) 150, doi:10.1007/JHEP11(2019)150, arXiv:1905.02302.

[21] CMS Collaboration, "Measurement of differential cross sections for top quark pair production using the lepton+jets final state in proton-proton collisions at 13 TeV", *Phys. Rev. D* **95** (2017) 092001, doi:10.1103/PhysRevD.95.092001, arXiv:1610.04191.

[22] ATLAS Collaboration, "Measurement of jet activity produced in top-quark events with an electron, a muon and two b-tagged jets in the final state in pp collisions at $\sqrt{s} =$ 13 TeV with the ATLAS detector", *Eur. Phys. J. C* **77** (2017) 220, doi:10.1140/epjc/s10052-017-4766-0, arXiv:1610.09978.

[23] ATLAS Collaboration, "Measurements of top-quark pair differential cross sections in the eμ channel in pp collisions at $\sqrt{s} = 13$ TeV using the ATLAS detector", *Eur. Phys. J. C* **77** (2017) 292, doi:10.1140/epjc/s10052-017-4821-x, arXiv:1612.05220.

[24] CMS Collaboration, "Measurement of normalized differential $\mathrm{t\bar{t}}$ cross sections in the dilepton channel from pp collisions at $\sqrt{s} = 13$ TeV", *JHEP* **04** (2018) 060, doi:10.1007/JHEP04(2018)060, arXiv:1708.07638.

[25] CMS Collaboration, "Measurement of differential cross sections for the production of top quark pairs and of additional jets in lepton+jets events from pp collisions at $\sqrt{s} = 13$ TeV", *Phys. Rev. D* **97** (2018) 112003, doi:10.1103/PhysRevD.97.112003, arXiv:1803.08856.

[26] CMS Collaboration, "Measurements of $\mathrm{t\bar{t}}$ differential cross sections in proton-proton collisions at $\sqrt{s} = 13$ TeV using events containing two leptons", *JHEP* **02** (2019) 149, doi:10.1007/JHEP02(2019)149, arXiv:1811.06625.

[27] CMS Collaboration, "Measurement of $\mathrm{t\bar{t}}$ normalised multi-differential cross sections in pp collisions at $\sqrt{s} = 13$ TeV, and simultaneous determination of the strong coupling strength, top quark pole mass, and parton distribution functions", *Eur. Phys. J. C* **80** (2020) 658, doi:10.1140/epjc/s10052-020-7917-7, arXiv:1904.05237.

[28] ATLAS Collaboration, "Measurements of top-quark pair differential and double-differential cross sections in the ℓ+jets channel with pp collisions at $\sqrt{s} = 13$ TeV using the ATLAS detector", *Eur. Phys. J. C* **79** (2019) 1028, doi:10.1140/epjc/s10052-019-7525-6, arXiv:1908.07305. [Erratum: doi:10.1140/epjc/s10052-020-08541-3].

[29] ATLAS Collaboration, "Measurement of the $\mathrm{t\bar{t}}$ production cross section and lepton differential distributions in eμ dilepton events from pp collisions at $\sqrt{s} = 13$ TeV with the ATLAS detector", *Eur. Phys. J. C* **80** (2020) 528, doi:10.1140/epjc/s10052-020-7907-9, arXiv:1910.08819.

[30] ATLAS Collaboration, "Measurements of top-quark pair single- and double-differential cross sections in the all-hadronic channel in pp collisions at $\sqrt{s} = 13$ TeV using the ATLAS detector", *JHEP* **01** (2021) 033, doi:10.1007/JHEP01(2021)033, arXiv:2006.09274.

[31] CMS Collaboration, "Measurement of differential $\mathrm{t\bar{t}}$ production cross sections in the full kinematic range using lepton+jets events from proton-proton collisions at $\sqrt{s} = 13$ TeV", *Phys. Rev. D* **104** (2021) 092013, doi:10.1103/PhysRevD.104.092013, arXiv:2108.02803.

[32] "HEPData record for this analysis", 2023. doi:10.17182/hepdata.127702.

[33] CMS Collaboration, "The CMS trigger system", *JINST* **12** (2017) P01020, doi:10.1088/1748-0221/12/01/P01020, arXiv:1609.02366.

[34] CMS Collaboration, "The CMS experiment at the CERN LHC", *JINST* **3** (2008) S08004, doi:10.1088/1748-0221/3/08/S08004.

[35] NNPDF Collaboration, "Unbiased global determination of parton distributions and their uncertainties at NNLO and LO", *Nucl. Phys. B* **855** (2012) 153, doi:10.1016/j.nuclphysb.2011.09.024, arXiv:1107.2652.

[36] NNPDF Collaboration, "Parton distributions from high-precision collider data", *Eur. Phys. J. C* **77** (2017) 663, doi:10.1140/epjc/s10052-017-5199-5, arXiv:1706.00428.

[37] P. Nason, "A new method for combining NLO QCD with shower Monte Carlo algorithms", *JHEP* **11** (2004) 040, doi:10.1088/1126-6708/2004/11/040, arXiv:hep-ph/0409146.

[38] S. Frixione, P. Nason, and C. Oleari, "Matching NLO QCD computations with parton shower simulations: the POWHEG method", *JHEP* **11** (2007) 070, doi:10.1088/1126-6708/2007/11/070, arXiv:0709.2092.

[39] S. Alioli, P. Nason, C. Oleari, and E. Re, "A general framework for implementing NLO calculations in shower Monte Carlo programs: the POWHEG BOX", *JHEP* **06** (2010) 043, doi:10.1007/JHEP06(2010)043, arXiv:1002.2581.

[40] S. Frixione, P. Nason, and G. Ridolfi, "A positive-weight next-to-leading-order Monte Carlo for heavy flavour hadroproduction", *JHEP* **09** (2007) 126, doi:10.1088/1126-6708/2007/09/126, arXiv:0707.3088.

[41] CMS Collaboration, "Extraction and validation of a new set of CMS PYTHIA8 tunes from underlying-event measurements", *Eur. Phys. J. C* **80** (2020) 4, doi:10.1140/epjc/s10052-019-7499-4, arXiv:1903.12179.

[42] T. Sjöstrand et al., "An introduction to PYTHIA 8.2", *Comput. Phys. Commun.* **191** (2015) 159, doi:10.1016/j.cpc.2015.01.024, arXiv:1410.3012.

[43] J. Alwall et al., "The automated computation of tree-level and next-to-leading order differential cross sections, and their matching to parton shower simulations", *JHEP* **07** (2014) 079, doi:10.1007/JHEP07(2014)079, arXiv:1405.0301.

[44] R. Frederix and S. Frixione, "Merging meets matching in MC@NLO", *JHEP* **12** (2012) 061, doi:10.1007/JHEP12(2012)061, arXiv:1209.6215.

[45] P. Artoisenet, R. Frederix, O. Mattelaer, and R. Rietkerk, "Automatic spin-entangled decays of heavy resonances in Monte Carlo simulations", *JHEP* **03** (2013) 015, doi:10.1007/JHEP03(2013)015, arXiv:1212.3460.

[46] J. Bellm et al., "HERWIG 7.0/HERWIG++ 3.0 release note", *Eur. Phys. J. C* **76** (2016) 196, doi:10.1140/epjc/s10052-016-4018-8, arXiv:1512.01178.

[47] CMS Collaboration, "Development and validation of HERWIG 7 tunes from CMS underlying-event measurements", *Eur. Phys. J. C* **81** (2021) 312, doi:10.1140/epjc/s10052-021-08949-5, arXiv:2011.03422.

[48] S. Alioli, P. Nason, C. Oleari, and E. Re, "NLO single-top production matched with shower in POWHEG: s- and t-channel contributions", *JHEP* **09** (2009) 111, doi:10.1088/1126-6708/2009/09/111, arXiv:0907.4076. [Erratum: doi:10.1007/JHEP02(2010)011].

[49] R. Frederix, E. Re, and P. Torrielli, "Single-top t-channel hadroproduction in the four-flavour scheme with POWHEG and aMC@NLO", *JHEP* **09** (2012) 130, doi:10.1007/JHEP09(2012)130, arXiv:1207.5391.

[50] E. Re, "Single-top Wt-channel production matched with parton showers using the POWHEG method", *Eur. Phys. J. C* **71** (2011) 1547, doi:10.1140/epjc/s10052-011-1547-z, arXiv:1009.2450.

[51] CMS Collaboration, "Investigations of the impact of the parton shower tuning in PYTHIA in the modelling of $t\bar{t}$ at $\sqrt{s} = 8$ and 13 TeV", CMS Physics Analysis Summary CMS-PAS-TOP-16-021, 2016.

[52] CMS Collaboration, "Event generator tunes obtained from underlying event and multiparton scattering measurements", *Eur. Phys. J. C* **76** (2016) 155, doi:10.1140/epjc/s10052-016-3988-x, arXiv:1512.00815.

[53] P. Skands, S. Carrazza, and J. Rojo, "Tuning PYTHIA 8.1: the Monash 2013 Tune", *Eur. Phys. J. C* **74** (2014) 3024, doi:10.1140/epjc/s10052-014-3024-y, arXiv:1404.5630.

[54] NNPDF Collaboration, "Parton distributions for the LHC Run II", *JHEP* **04** (2015) 040, doi:10.1007/JHEP04(2015)040, arXiv:1410.8849.

[55] M. L. Mangano, M. Moretti, F. Piccinini, and M. Treccani, "Matching matrix elements and shower evolution for top-quark production in hadronic collisions", *JHEP* **01** (2007) 013, doi:10.1088/1126-6708/2007/01/013, arXiv:hep-ex/0611129.

[56] S. Mrenna and P. Richardson, "Matching matrix elements and parton showers with HERWIG and PYTHIA", *JHEP* **05** (2004) 040, doi:10.1088/1126-6708/2004/05/040, arXiv:hep-ph/0312274.

[57] P. Kant et al., "HatHor for single top-quark production: Updated predictions and uncertainty estimates for single top-quark production in hadronic collisions", *Comput. Phys. Commun.* **191** (2015) 74, doi:10.1016/j.cpc.2015.02.001, arXiv:1406.4403.

[58] N. Kidonakis, "Two-loop soft anomalous dimensions for single top quark associated production with W^- or H^-", *Phys. Rev. D* **82** (2010) 054018, doi:10.1103/PhysRevD.82.054018, arXiv:hep-ph/1005.4451.

[59] Y. Li and F. Petriello, "Combining QCD and electroweak corrections to dilepton production in FEWZ", *Phys. Rev. D* **86** (2012) 094034, doi:10.1103/PhysRevD.86.094034, arXiv:1208.5967.

[60] J. M. Campbell, R. K. Ellis, and C. Williams, "Vector boson pair production at the LHC", *JHEP* **07** (2011) 018, doi:10.1007/JHEP07(2011)018, arXiv:1105.0020.

[61] M. Czakon and A. Mitov, "TOP++: a program for the calculation of the top-pair cross section at hadron colliders", *Comput. Phys. Commun.* **185** (2014) 2930, doi:10.1016/j.cpc.2014.06.021, arXiv:1112.5675.

[62] M. Cacciari et al., "Top-pair production at hadron colliders with next-to-next-to-leading logarithmic soft-gluon resummation", *Phys. Lett. B* **710** (2012) 612, doi:10.1016/j.physletb.2012.03.013, arXiv:1111.5869.

[63] P. Bärnreuther, M. Czakon, and A. Mitov, "Percent level precision physics at the Tevatron: first genuine NNLO QCD corrections to $q\bar{q} \to t\bar{t} + X$", *Phys. Rev. Lett.* **109** (2012) 132001, doi:10.1103/PhysRevLett.109.132001, arXiv:1204.5201.

[64] M. Czakon and A. Mitov, "NNLO corrections to top-pair production at hadron colliders: the all-fermionic scattering channels", *JHEP* **12** (2012) 054, doi:10.1007/JHEP12(2012)054, arXiv:1207.0236.

[65] M. Czakon and A. Mitov, "NNLO corrections to top-pair production at hadron colliders: the quark-gluon reaction", *JHEP* **01** (2013) 080, doi:10.1007/JHEP01(2013)080, arXiv:1210.6832.

[66] M. Beneke, P. Falgari, S. Klein, and C. Schwinn, "Hadronic top-quark pair production with NNLL threshold resummation", *Nucl. Phys. B* **855** (2012) 695, doi:10.1016/j.nuclphysb.2011.10.021, arXiv:1109.1536.

[67] M. Czakon, P. Fiedler, and A. Mitov, "Total top-quark pair-production cross section at hadron colliders through $\mathcal{O}(\alpha_s^4)$", *Phys. Rev. Lett.* **110** (2013) 252004, doi:10.1103/PhysRevLett.110.252004, arXiv:1303.6254.

[68] GEANT4 Collaboration, "GEANT4—a simulation toolkit", *Nucl. Instrum. Meth. A* **506** (2003) 250, doi:10.1016/S0168-9002(03)01368-8.

[69] ATLAS Collaboration, "Measurement of the inelastic proton-proton cross section at $\sqrt{s} = 13\,\text{TeV}$ with the ATLAS detector at the LHC", *Phys. Rev. Lett.* **117** (2016) 182002, doi:10.1103/PhysRevLett.117.182002, arXiv:1606.02625.

[70] CMS Collaboration, "Particle-flow reconstruction and global event description with the CMS detector", *JINST* **12** (2017) P10003, doi:10.1088/1748-0221/12/10/P10003, arXiv:1706.04965.

[71] CMS Collaboration, "Technical proposal for the Phase-II upgrade of the Compact Muon Solenoid", CMS Technical Proposal CERN-LHCC-2015-010, CMS-TDR-15-02, 2015.

[72] CMS Collaboration, "Electron and photon reconstruction and identification with the CMS experiment at the CERN LHC", *JINST* **16** (2021) P05014, doi:10.1088/1748-0221/16/05/P05014, arXiv:2012.06888.

[73] CMS Collaboration, "Performance of the CMS muon detector and muon reconstruction with proton-proton collisions at $\sqrt{s} = 13\,\text{TeV}$", *JINST* **13** (2018) P06015, doi:10.1088/1748-0221/13/06/P06015, arXiv:1804.04528.

[74] M. Cacciari, G. P. Salam, and G. Soyez, "The anti-k_T jet clustering algorithm", *JHEP* **04** (2008) 063, doi:10.1088/1126-6708/2008/04/063, arXiv:0802.1189.

[75] M. Cacciari, G. P. Salam, and G. Soyez, "FastJet user manual", *Eur. Phys. J. C* **72** (2012) 1896, doi:10.1140/epjc/s10052-012-1896-2, arXiv:1111.6097.

[76] CMS Collaboration, "Jet energy scale and resolution in the CMS experiment in pp collisions at 8 TeV", *JINST* **12** (2017) P02014, doi:10.1088/1748-0221/12/02/P02014, arXiv:1607.03663.

[77] CMS Collaboration, "Identification of heavy-flavour jets with the CMS detector in pp collisions at 13 TeV", *JINST* **13** (2018) P05011, doi:10.1088/1748-0221/13/05/P05011, arXiv:1712.07158.

[78] CMS Collaboration, "A Deep Neural Network for simultaneous estimation of b jet energy and resolution", *Comput. Softw. Big Sci.* **4** (2020) 10, doi:10.1007/s41781-020-00041-z, arXiv:1912.06046.

[79] CMS Collaboration, "Performance of missing transverse momentum reconstruction in proton-proton collisions at $\sqrt{s} = 13$ TeV using the CMS detector", *JINST* **14** (2019) P07004, doi:10.1088/1748-0221/14/07/P07004, arXiv:1903.06078.

[80] D. Bertolini, P. Harris, M. Low, and N. Tran, "Pileup per particle identification", *JHEP* **10** (2014) 59, doi:10.1007/JHEP10(2014)059, arXiv:1407.6013.

[81] I. Korol, "Measurement of Double Differential $\mathrm{t\bar{t}}$ Production Cross Sections with the CMS Detector". PhD thesis, Universität Hamburg, 2016. doi:10.3204/DESY-THESIS-2016-011.

[82] R. J. Barlow and C. Beeston, "Fitting using finite Monte Carlo samples", *Comput. Phys. Commun.* **77** (1993) 219, doi:10.1016/0010-4655(93)90005-W.

[83] R. Brun and F. Rademakers, "ROOT: An object oriented data analysis framework", *Nucl. Instrum. Meth. A* **389** (1997) 81, doi:10.1016/S0168-9002(97)00048-X.

[84] S. Schmitt, "TUnfold: an algorithm for correcting migration effects in high energy physics", *JINST* **7** (2012) T10003, doi:10.1088/1748-0221/7/10/T10003, arXiv:1205.6201.

[85] A. N. Tikhonov, "Solution of incorrectly formulated problems and the regularization method", *Sov. Math. Dokl.* **4** (1963) 1035.

[86] S. Schmitt, "Data unfolding methods in high energy physics", *Eur. Phys. J. Web Conf.* **137** (2017) 11008, doi:10.1051/epjconf/201713711008, arXiv:1611.01927.

[87] CMS Collaboration, "Object definitions for top quark analyses at the particle level", CMS Note CERN-CMS-NOTE-2017-004, 2017.

[88] M. Cacciari, G. P. Salam, and G. Soyez, "The catchment area of jets", *JHEP* **04** (2008) 005, doi:10.1088/1126-6708/2008/04/005, arXiv:0802.1188.

[89] CMS Collaboration, "Precision luminosity measurement in proton-proton collisions at $\sqrt{s} = 13$ TeV in 2015 and 2016 at CMS", *Eur. Phys. J. C* **81** (2021) 800, doi:10.1140/epjc/s10052-021-09538-2, arXiv:2104.01927.

[90] CMS Collaboration, "CMS Luminosity measurement for the 2017 data-taking period at $\sqrt{s} = 13$ TeV", CMS Physics Analysis Summary CMS-PAS-LUM-17-004, 2018.

[91] CMS Collaboration, "CMS Luminosity measurement for the 2018 data-taking period at $\sqrt{s} = 13$ TeV", CMS Physics Analysis Summary CMS-PAS-LUM-18-002, 2019.

[92] CMS Collaboration, "Measurement of the Drell-Yan cross section in pp collisions at $\sqrt{s} = 7$ TeV", *JHEP* **10** (2011) 007, doi:10.1007/JHEP10(2011)007, arXiv:1108.0566.

[93] CMS Collaboration, "Measurement of the top quark pair production cross section in proton-proton collisions at $\sqrt{s} = 13$ TeV", *Phys. Rev. Lett.* **116** (2016) 052002, doi:10.1103/PhysRevLett.116.052002, arXiv:1510.05302.

[94] CMS Collaboration, "Measurement of the Higgs boson production rate in association with top quarks in final states with electrons, muons, and hadronically decaying tau leptons at $\sqrt{s} = 13$ TeV", *Eur. Phys. J. C* **81** (2021) 378, doi:10.1140/epjc/s10052-021-09014-x, arXiv:2011.03652.

[95] S. Argyropoulos and T. Sjöstrand, "Effects of color reconnection on $t\bar{t}$ final states at the LHC", *JHEP* **11** (2014) 043, doi:10.1007/JHEP11(2014)043, arXiv:1407.6653.

[96] J. R. Christiansen and P. Z. Skands, "String formation beyond leading colour", *JHEP* **08** (2015) 003, doi:10.1007/JHEP08(2015)003, arXiv:1505.01681.

[97] M. Bähr et al., "HERWIG++ physics and manual", *Eur. Phys. J. C* **58** (2008) 639, doi:10.1140/epjc/s10052-008-0798-9, arXiv:0803.0883.

[98] CMS Collaboration, "Running of the top quark mass from proton-proton collisions at $\sqrt{s} = 13$TeV", *Phys. Lett. B* **803** (2020) 135263, doi:10.1016/j.physletb.2020.135263, arXiv:1909.09193.

[99] T. Chwalek and F. Déliot, "Top quark asymmetries", *Universe* **8** (2022) 622, doi:10.3390/universe8120622.

[100] M. Diehl.

[101] M. Grazzini, S. Kallweit, and M. Wiesemann, "Fully differential NNLO computations with MATRIX", *Eur. Phys. J. C* **78** (2018) 537, doi:10.1140/epjc/s10052-018-5771-7, arXiv:1711.06631.

[102] S. Catani et al., "Top-quark pair hadroproduction at next-to-next-to-leading order in QCD", *Phys. Rev. D* **99** (2019) 051501, doi:10.1103/PhysRevD.99.051501, arXiv:1901.04005.

[103] F. Buccioni et al., "OpenLoops 2", *Eur. Phys. J. C* **79** (2019) 866, doi:10.1140/epjc/s10052-019-7306-2, arXiv:1907.13071.

[104] F. Cascioli, P. Maierhofer, and S. Pozzorini, "Scattering amplitudes with Open Loops", *Phys. Rev. Lett.* **108** (2012) 111601, doi:10.1103/PhysRevLett.108.111601, arXiv:1111.5206.

[105] A. Denner, S. Dittmaier, and L. Hofer, "Collier: a fortran-based Complex One-Loop LIbrary in Extended Regularizations", *Comput. Phys. Commun.* **212** (2017) 220, doi:10.1016/j.cpc.2016.10.013, arXiv:1604.06792.

[106] S. Catani et al., "Vector boson production at hadron colliders: hard-collinear coefficients at the NNLO", *Eur. Phys. J. C* **72** (2012) 2195, doi:10.1140/epjc/s10052-012-2195-7, arXiv:1209.0158.

[107] S. Catani and M. Grazzini, "An NNLO subtraction formalism in hadron collisions and its application to Higgs boson production at the LHC", *Phys. Rev. Lett.* **98** (2007) 222002, doi:10.1103/PhysRevLett.98.222002, arXiv:hep-ph/0703012.

[108] M. Czakon, "A novel subtraction scheme for double-real radiation at NNLO", *Phys. Lett. B* **693** (2010) 259, doi:10.1016/j.physletb.2010.08.036, arXiv:1005.0274.

[109] M. Czakon and D. Heymes, "Four-dimensional formulation of the sector-improved residue subtraction scheme", *Nucl. Phys. B* **890** (2014) 152, doi:10.1016/j.nuclphysb.2014.11.006, arXiv:1408.2500.

[110] M. Czakon, "Double-real radiation in hadronic top quark pair production as a proof of a certain concept", *Nucl. Phys. B* **849** (2011) 250, doi:10.1016/j.nuclphysb.2011.03.020, arXiv:1101.0642.

[111] P. F. Monni et al., "MiNNLO$_{\text{PS}}$: a new method to match NNLO QCD to parton showers", *JHEP* **05** (2020) 143, doi:10.1007/JHEP05(2020)143, arXiv:1908.06987.

[112] P. F. Monni, E. Re, and M. Wiesemann, "MiNNLO$_{\text{PS}}$: optimizing $2 \to 1$ hadronic processes", *Eur. Phys. J. C* **80** (2020) 1075, doi:10.1140/epjc/s10052-020-08658-5, arXiv:2006.04133.

[113] J. Mazzitelli et al., "Top-pair production at the LHC with MINNLO$_{PS}$", *JHEP* **04** (2022) 079, doi:10.1007/JHEP04(2022)079, arXiv:2112.12135.

[114] K. Hamilton, P. Nason, and G. Zanderighi, "MINLO: Multi-scale improved NLO", *JHEP* **10** (2012) 155, doi:10.1007/JHEP10(2012)155, arXiv:1206.3572.

[115] K. Hamilton, P. Nason, C. Oleari, and G. Zanderighi, "Merging H/W/Z + 0 and 1 jet at NLO with no merging scale: a path to parton shower + NNLO matching", *JHEP* **05** (2013) 082, doi:10.1007/JHEP05(2013)082, arXiv:1212.4504.

[116] S. Dulat et al., "New parton distribution functions from a global analysis of quantum chromodynamics", *Phys. Rev. D* **93** (2016) 033006, doi:10.1103/PhysRevD.93.033006, arXiv:1506.07443.

[117] S. Alekhin, J. Blümlein, and S. Moch, "NLO PDFs from the ABMP16 fit", *Eur. Phys. J. C* **78** (2018) 477, doi:10.1140/epjc/s10052-018-5947-1, arXiv:1803.07537.

[118] L. A. Harland-Lang, A. D. Martin, P. Motylinski, and R. S. Thorne, "Parton distributions in the LHC era: MMHT 2014 PDFs", *Eur. Phys. J. C* **75** (2015) 204, doi:10.1140/epjc/s10052-015-3397-6, arXiv:1412.3989.

[119] H1 and ZEUS Collaborations, "Combination of measurements of inclusive deep inelastic $e^{\pm}p$ scattering cross sections and QCD analysis of HERA data", *Eur. Phys. J. C* **75** (2015) 580, doi:10.1140/epjc/s10052-015-3710-4, arXiv:1506.06042.

[120] J. Butterworth et al., "PDF4LHC recommendations for LHC Run II", *J. Phys. G* **43** (2016) 023001, doi:10.1088/0954-3899/43/2/023001, arXiv:1510.03865.

[121] A. Accardi et al., "A critical appraisal and evaluation of modern PDFs", *Eur. Phys. J. C* **76** (2016) 471, doi:10.1140/epjc/s10052-016-4285-4, arXiv:1603.08906.

A Definition of χ^2 for theory-to-data comparisons

We define here the χ^2 values for the theory-to-data comparisons shown in Section 9 and Appendix B. The standard χ^2 values are calculated taking the measurement uncertainties into account, but ignoring the uncertainties in the predictions:

$$\chi^2 = \mathbf{R}_N^T \mathbf{Cov}_N^{-1} \mathbf{R}_N, \tag{2}$$

where N denotes the number of bins of the respective cross section distribution and $\mathbf{R}_N$ the vector of differences of the measured cross sections and the corresponding predictions. The covariance matrix **Cov** is calculated as:

$$\mathbf{Cov} = \mathbf{Cov}^{\text{unf}} + \mathbf{Cov}^{\text{syst}}, \tag{3}$$

where $\mathbf{Cov}^{\text{unf}}$ and $\mathbf{Cov}^{\text{syst}}$ are the covariance matrices representing the statistical uncertainties from the unfolding, and the systematic uncertainties, respectively. The systematic covariance matrix $\mathbf{Cov}^{\text{syst}}$ is calculated as

$$\mathbf{Cov}_{ij}^{\text{syst}} = \sum_{k,l} \frac{1}{N_k} C_{j,k,l} C_{i,k,l}, \quad 1 \leq i \leq N, \quad 1 \leq j \leq N. \tag{4}$$

Here, $C_{i,k,l}$ denotes the systematic uncertainty from variation l of source k in the ith bin, and N_k is the number of variations for source k. The sums run over all sources of systematic uncertainties and all their corresponding variations. Most of the systematic uncertainty sources in this analysis consist of positive and negative variations and thus have $N_k = 2$, though one model uncertainty (namely, the model of color reconnection) consists of more than two variations, a property that is accounted for in Eq. (4). For a subset of the models, χ^2 values are provided including the uncertainties in the predictions. This is achieved by adding the covariance matrix of these predictions, $\mathbf{Cov}^{\text{pred}}$, calculated analogously to Eq. (4), to $\mathbf{Cov}$.

For normalized cross sections the χ^2 values are calculated as

$$\chi^2 = \mathbf{R}_{N-1}^T \mathbf{Cov}_{N-1}^{-1} \mathbf{R}_{N-1}, \tag{5}$$

where $\mathbf{R}_{N-1}$ is the column vector of the residuals calculated as the difference of the measured normalized cross sections and the corresponding predictions and discarding one of the N bins, and $\mathbf{Cov}_{N-1}$ is the $(N-1) \times (N-1)$ submatrix obtained from the full covariance matrix by discarding the corresponding row and column. The matrix $\mathbf{Cov}_{N-1}$ obtained in this way is invertible, while the original covariance matrix $\mathbf{Cov}$ is singular because for normalized cross sections one degree of freedom is lost.

B Results for absolute cross sections

Absolute differential cross sections corresponding to the normalized ones discussed in Section 9 are presented in the following, together with tables listing χ^2 values of all prediction-to-data comparisons.

B.1 Comparisons to MC simulations

The absolute differential cross sections comparing data to predictions based on MC simulations are shown in Figs. 65–97, and the corresponding χ^2 values are presented in Tables 13–19. The p-values of the χ^2 tests are provided in Tables 37–43. The measurements are compared to the three MC simulations introduced in Section 3: POWHEG+PYTHIA 8 (POW+PYT), MG5_aMC@NLO[FxFx]+PYTHIA8 (FxFx+PYT), and POWHEG+HERWIG7 (POW+HER). Comparing the absolute cross sections to the normalized ones presented in Section 9, two effects are visible. Firstly, the uncertainties in the measured and also the predicted absolute cross sections are considerably larger than those of the corresponding normalized ones, which can be attributed to bin-to-bin correlated global normalization uncertainties. Secondly, the absolute total cross section obtained by integrating over the spectra of the three MC models is within 5% of that calculated from the data, indicating a reasonable agreement.

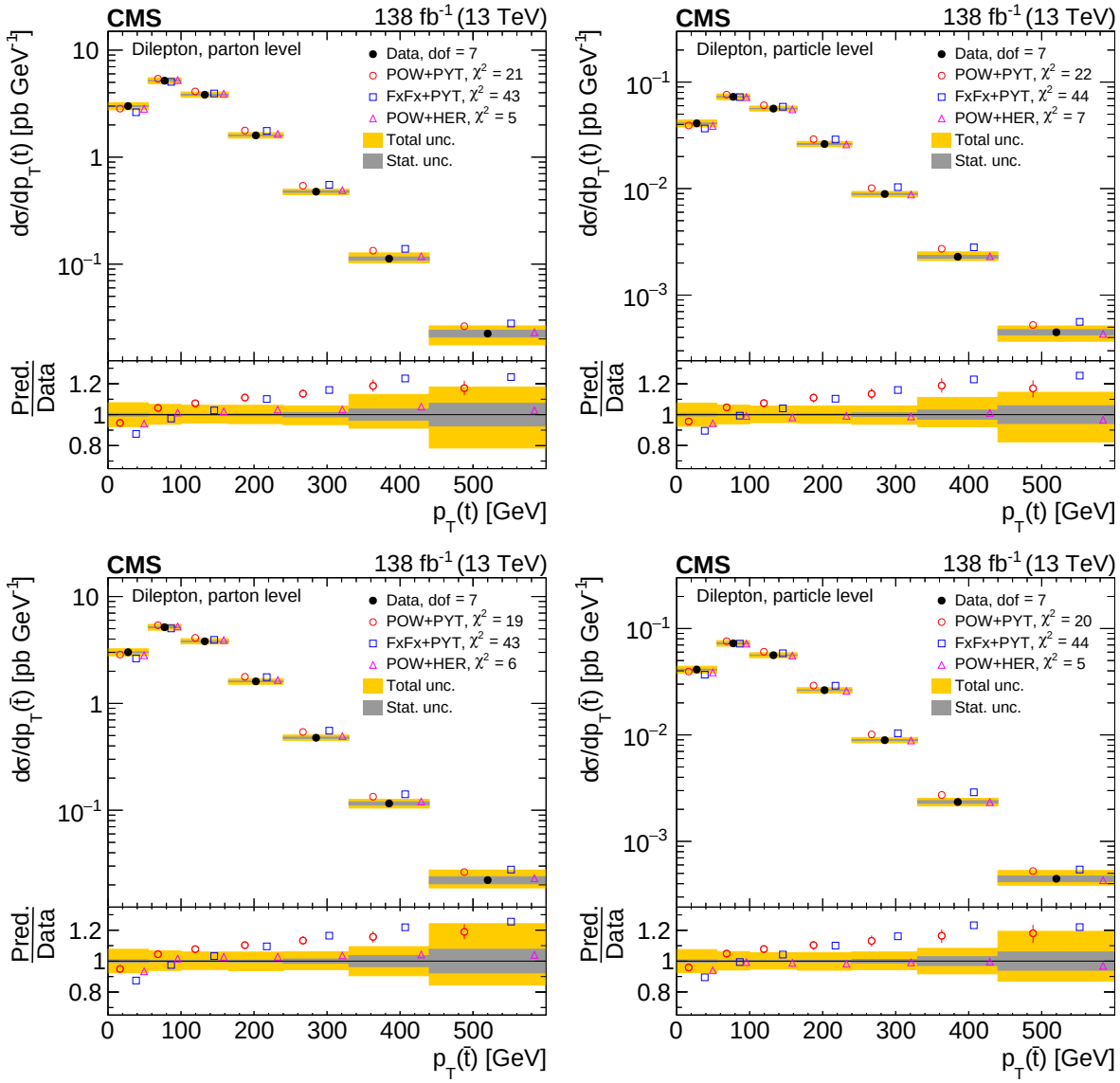

Figure 65: Absolute differential $t\bar{t}$ production cross sections as functions of $p_T(t)$ (upper) and $p_T(\bar{t})$ (lower), measured at the parton level in the full phase space (left) and at the particle level in a fiducial phase space (right). The data are shown as filled circles with grey and yellow bands indicating the statistical and total uncertainties (statistical and systematic uncertainties added in quadrature), respectively. For each distribution, the number of degrees of freedom (dof) is also provided. The cross sections are compared to various MC predictions (other points). The estimated uncertainties in the POWHEG+PYTHIA 8 ('POW-PYT') simulation are represented by a vertical bar on the corresponding points. For each MC model, a value of χ^2 is reported that takes into account the measurement uncertainties. The lower panel in each plot shows the ratios of the predictions to the data.

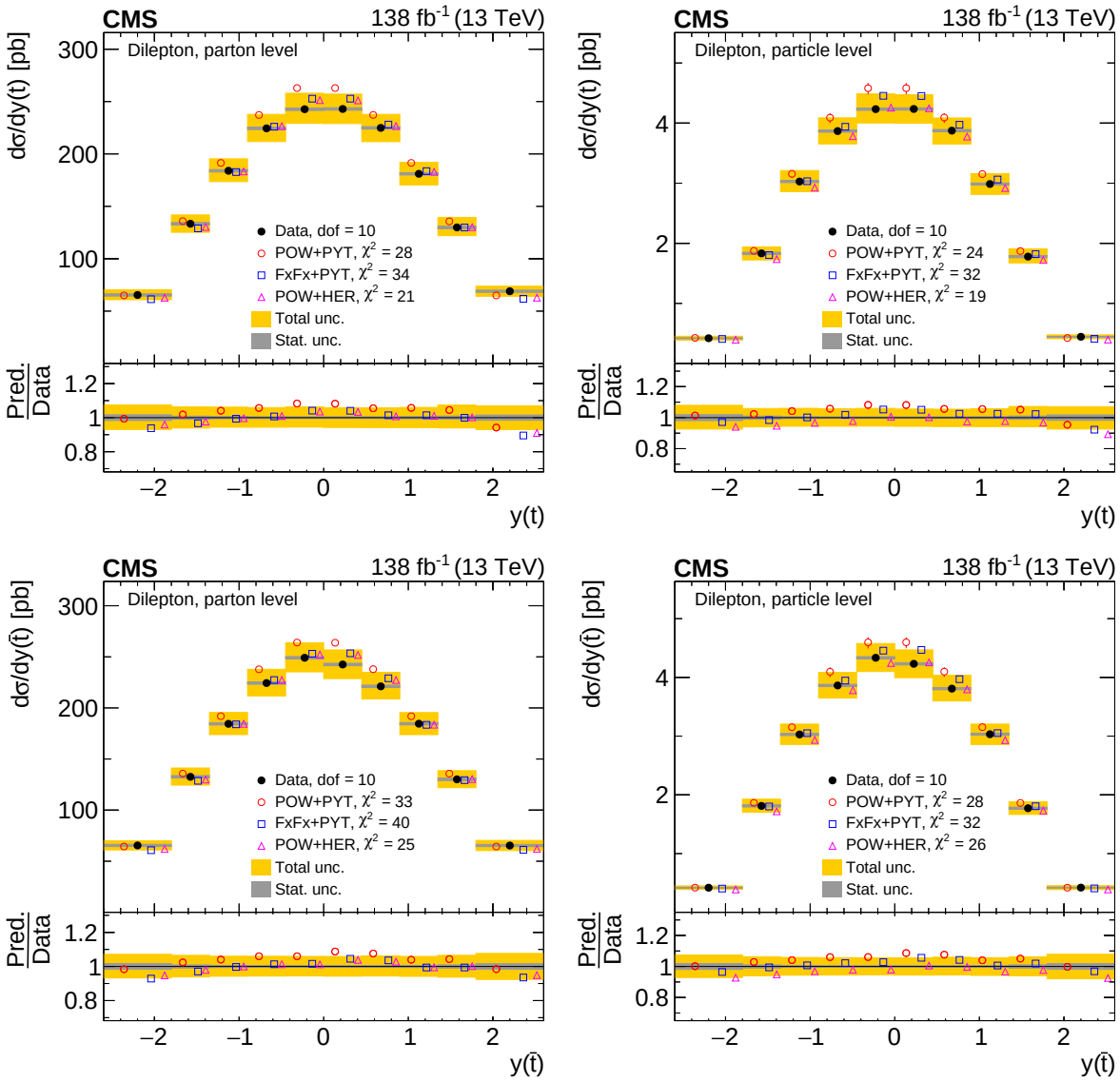

Figure 66: Absolute differential $\mathrm{t\bar{t}}$ production cross sections as functions of $y(\mathrm{t})$ (upper) and $y(\bar{\mathrm{t}})$ (lower) are shown for data (filled circles) and various MC predictions (other points). Further details can be found in the caption of Fig. 65.

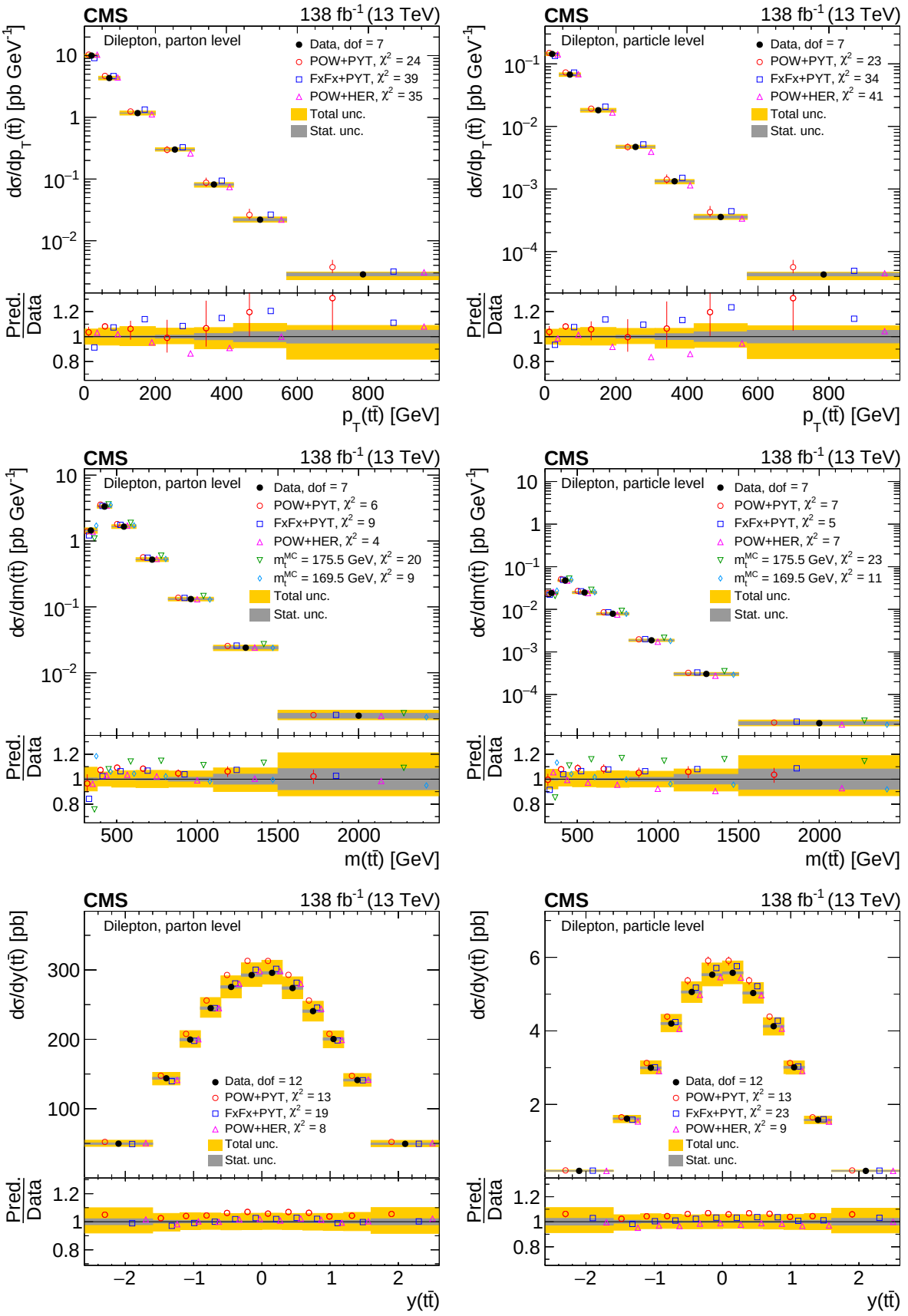

Figure 67: Absolute differential $t\bar{t}$ production cross sections as functions of $p_T(t\bar{t})$ (upper), $m(t\bar{t})$ (middle) and $y(t\bar{t})$ (lower) are shown for data (filled circles) and various MC predictions (other points). Further details can be found in the caption of Fig. 65.

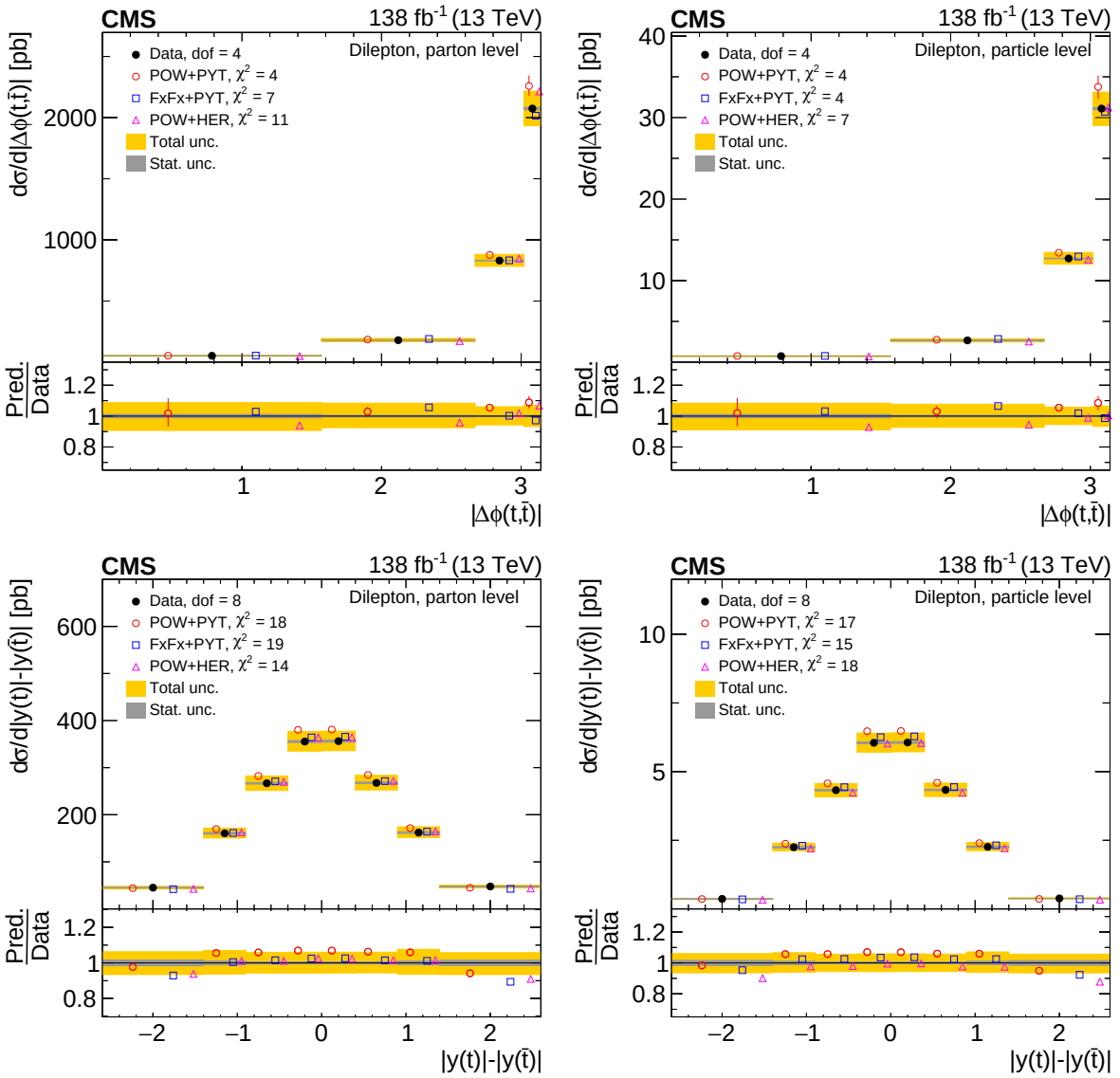

Figure 68: Absolute differential $\mathrm{t\bar{t}}$ production cross sections as functions of $|\Delta\phi(\mathrm{t},\bar{\mathrm{t}})|$ (upper) and $|y(\mathrm{t})| - |y(\bar{\mathrm{t}})|$ (lower) are shown for the data (filled circles) and various MC predictions (other points). Further details can be found in the caption of Fig. 65.

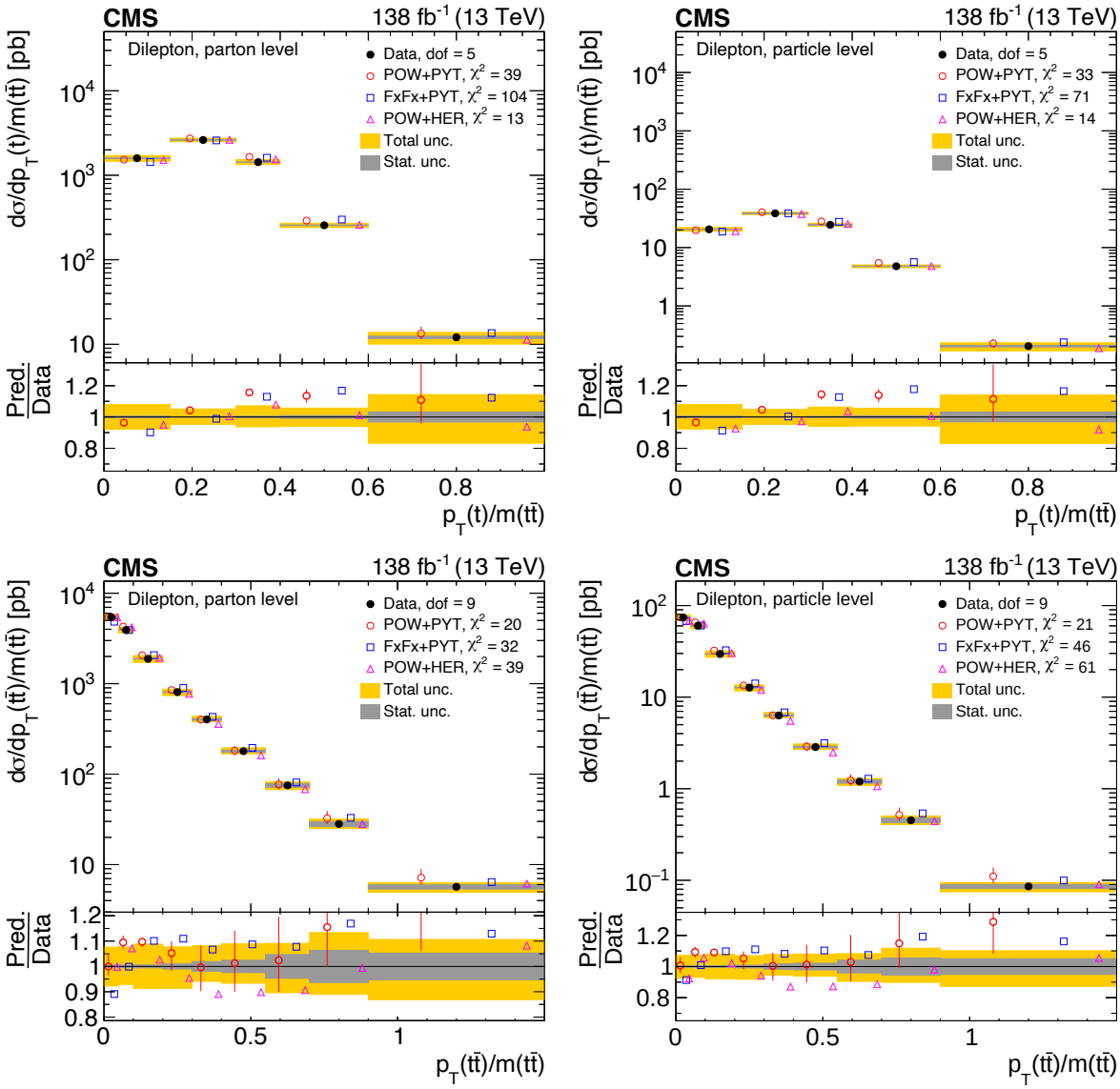

Figure 69: Absolute differential $\mathrm{t\bar{t}}$ production cross sections as functions of $p_{\mathrm{T}}(\mathrm{t})/m(\mathrm{t\bar{t}})$ (upper) and $p_{\mathrm{T}}(\mathrm{t\bar{t}})/m(\mathrm{t\bar{t}})$ (lower) are shown for the data (filled circles) and various MC predictions (other points). Further details can be found in the caption of Fig. 65.

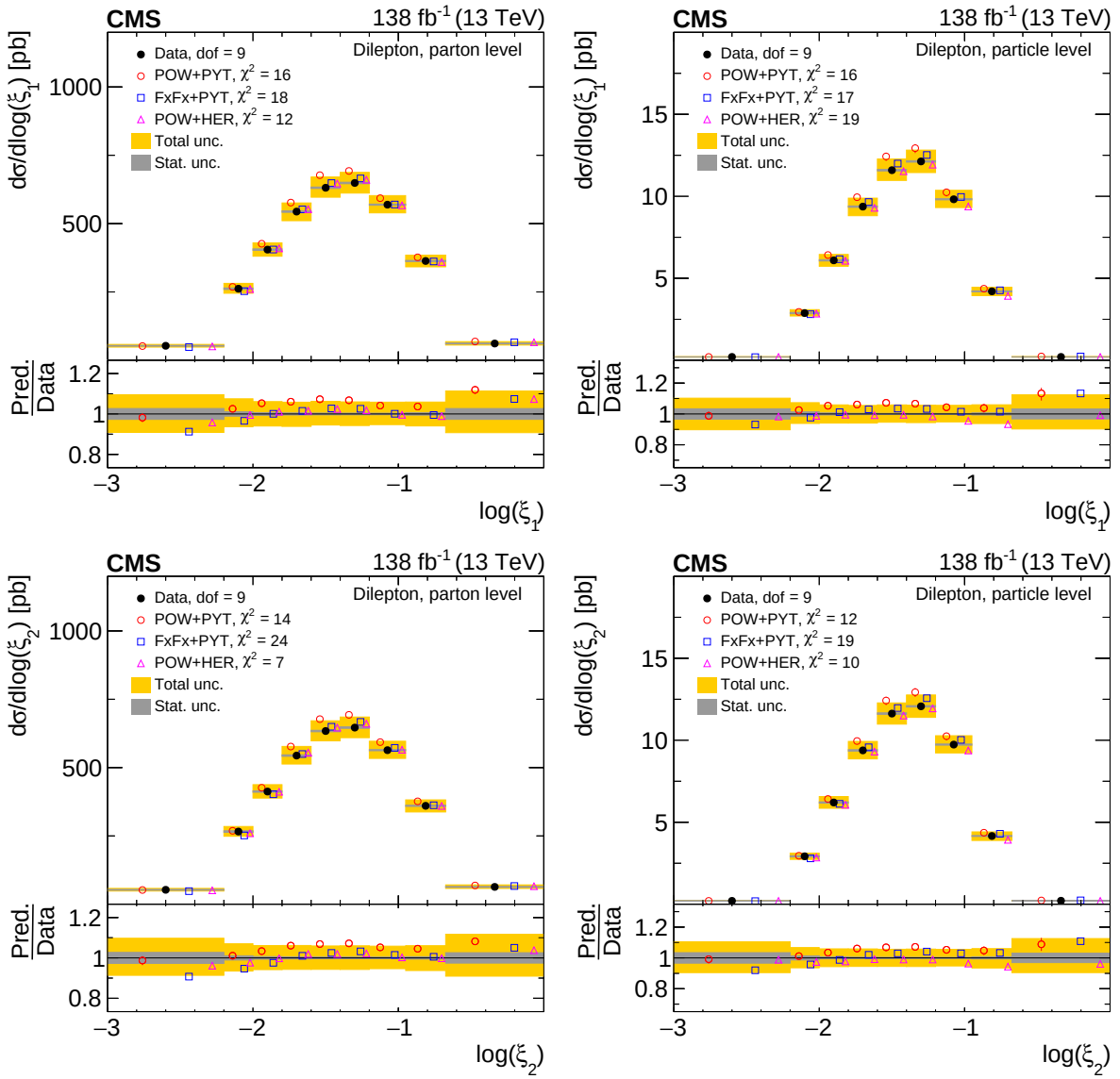

Figure 70: Absolute differential $\mathrm{t\bar{t}}$ production cross sections as functions of $\log(\xi_1)$ (upper) and $\log(\xi_2)$ (lower) are shown for the data (filled circles) and various MC predictions (other points). Further details can be found in the caption of Fig. 65.

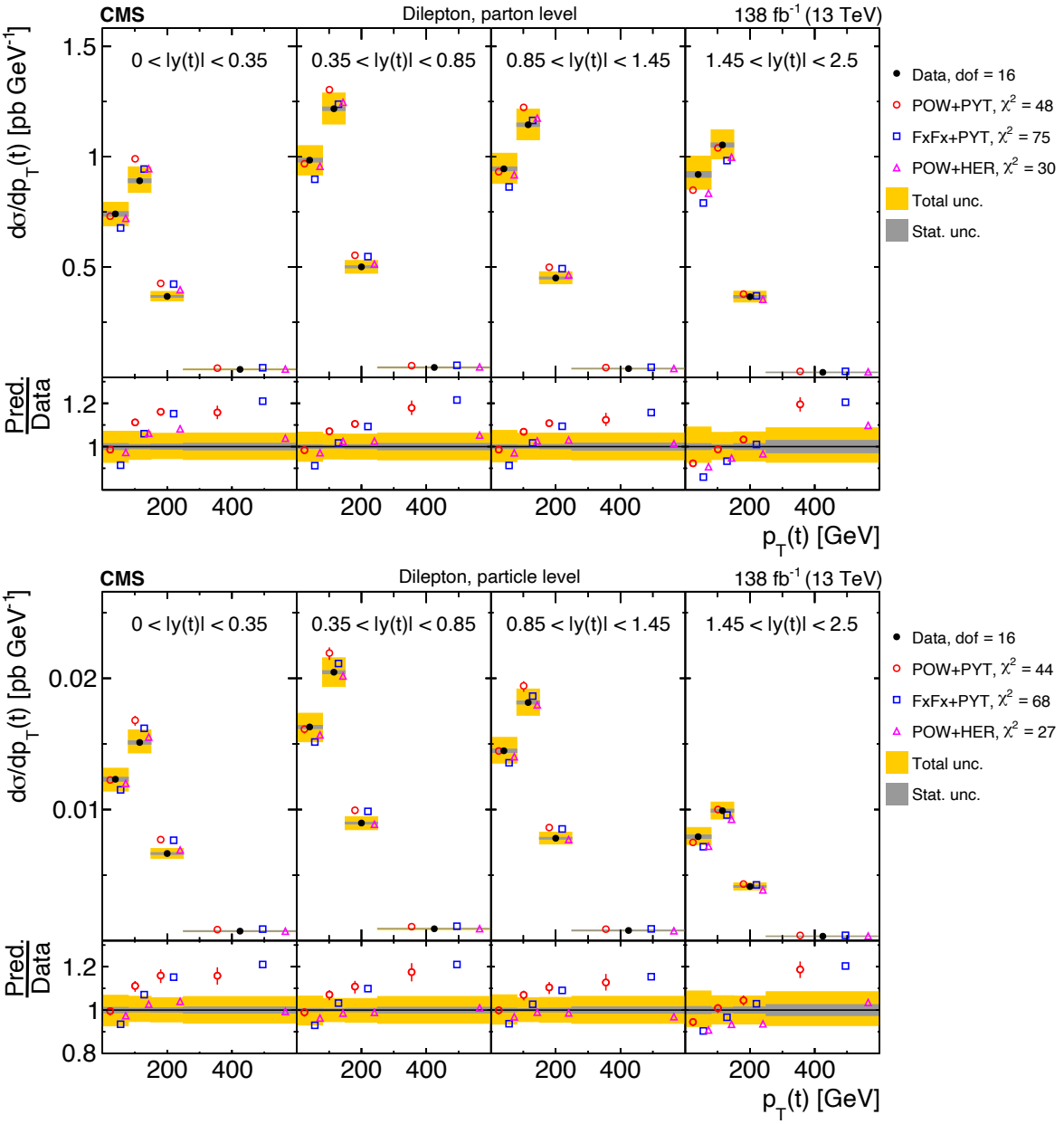

Figure 71: Absolute $[|y(t)|, p_T(t)]$ cross sections measured at the parton level in the full phase space (upper) and at the particle level in a fiducial phase space (lower). The data are shown as filled circles with grey and yellow bands indicating the statistical and total uncertainties (statistical and systematic uncertainties added in quadrature), respectively. For each distribution, the number of degrees of freedom (dof) is also provided. The cross sections are compared to various MC predictions (other points). The estimated uncertainties in the POWHEG+PYTHIA 8 ('POW-PYT') simulation are represented by a vertical bar on the corresponding points. For each MC model, a value of χ^2 is reported that takes into account the measurement uncertainties. The lower panel in each plot shows the ratios of the predictions to the data.

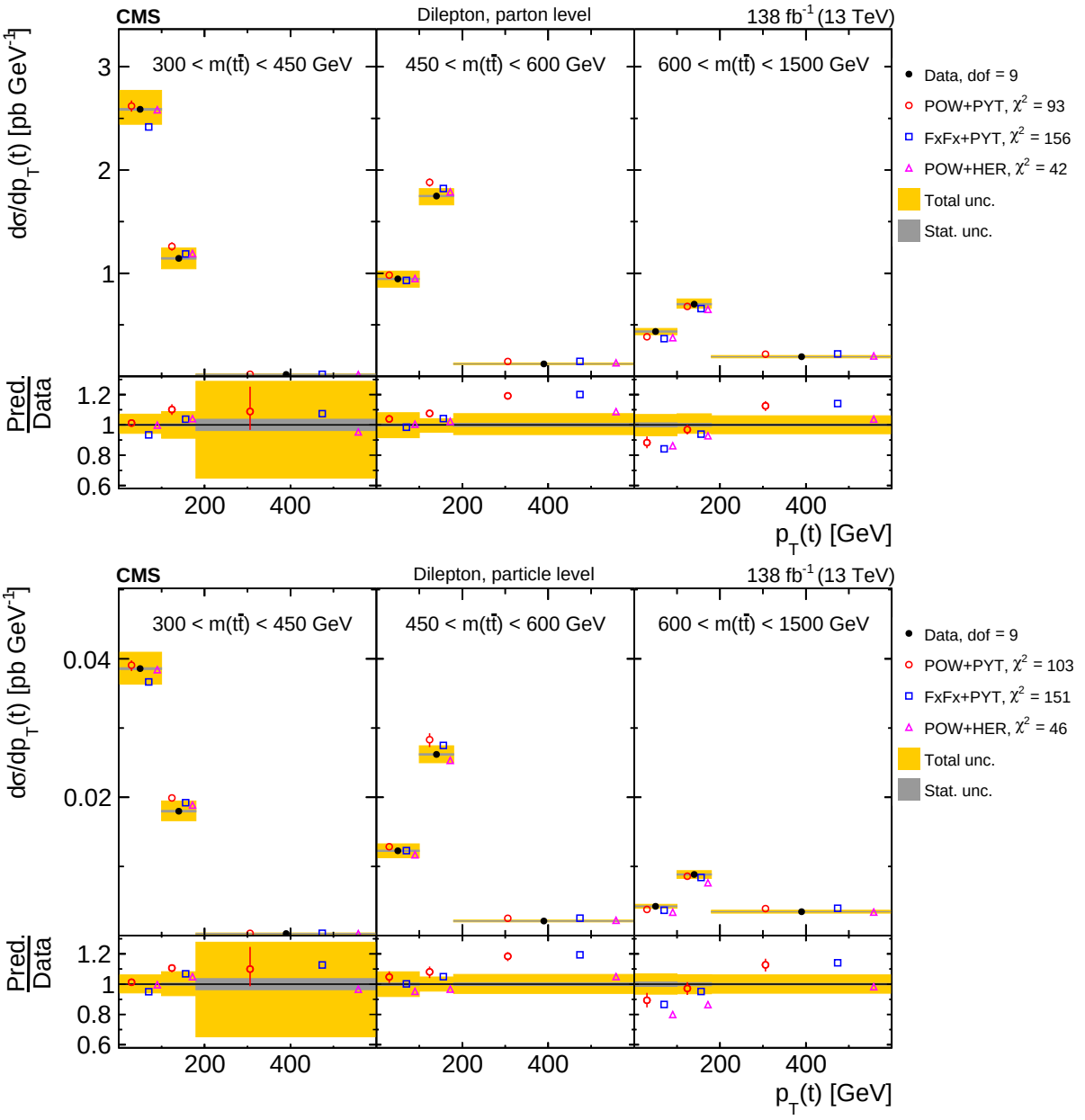

Figure 72: Absolute $[m(t\bar{t}),\ p_T(t)]$ cross sections are shown for data (filled circles) and various MC predictions (other points). Further details can be found in the caption of Fig. 71.

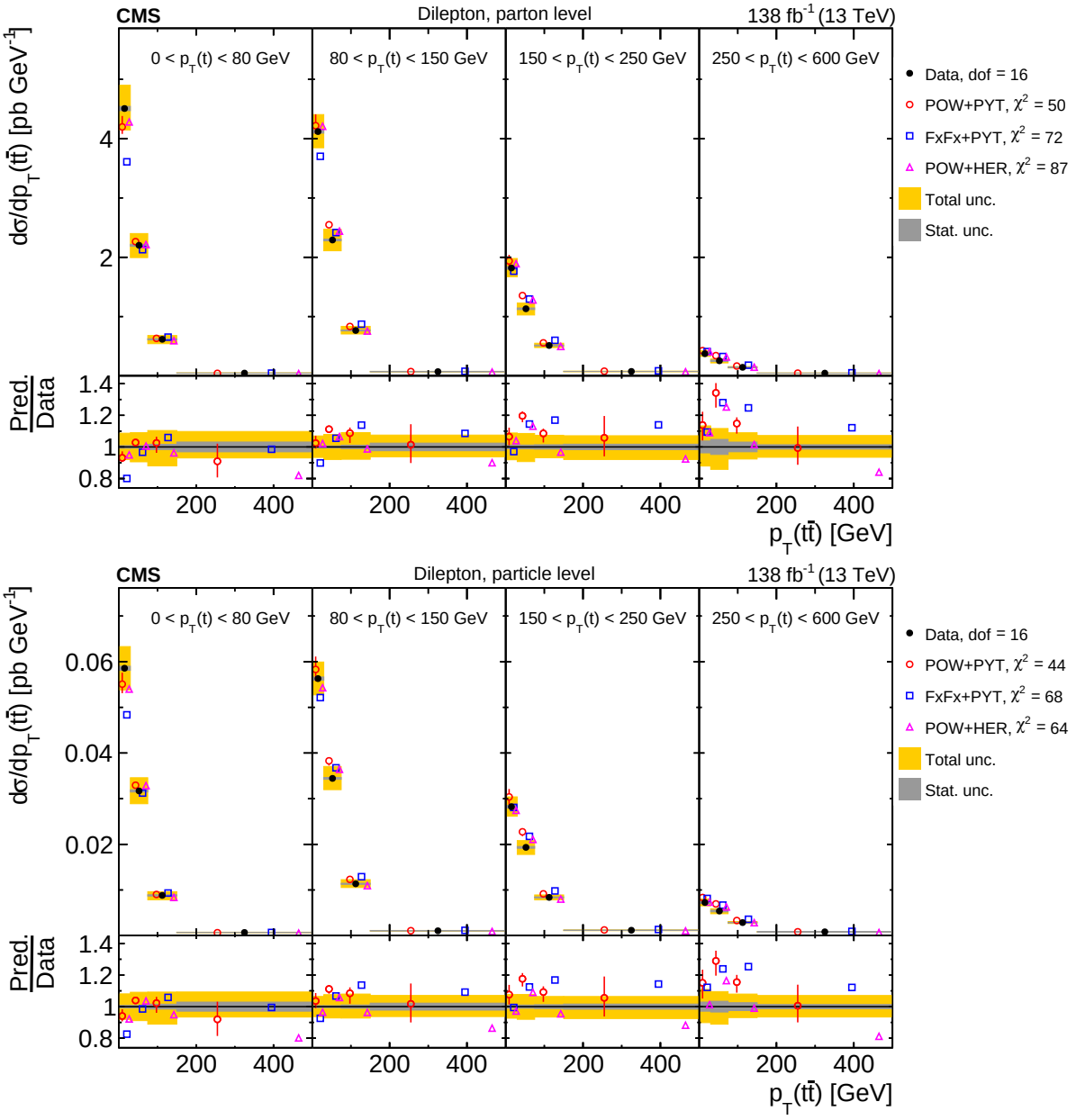

Figure 73: Absolute $[p_T(t),\ p_T(t\bar{t})]$ cross sections are shown for data (filled circles) and various MC predictions (other points). Further details can be found in the caption of Fig. 71.

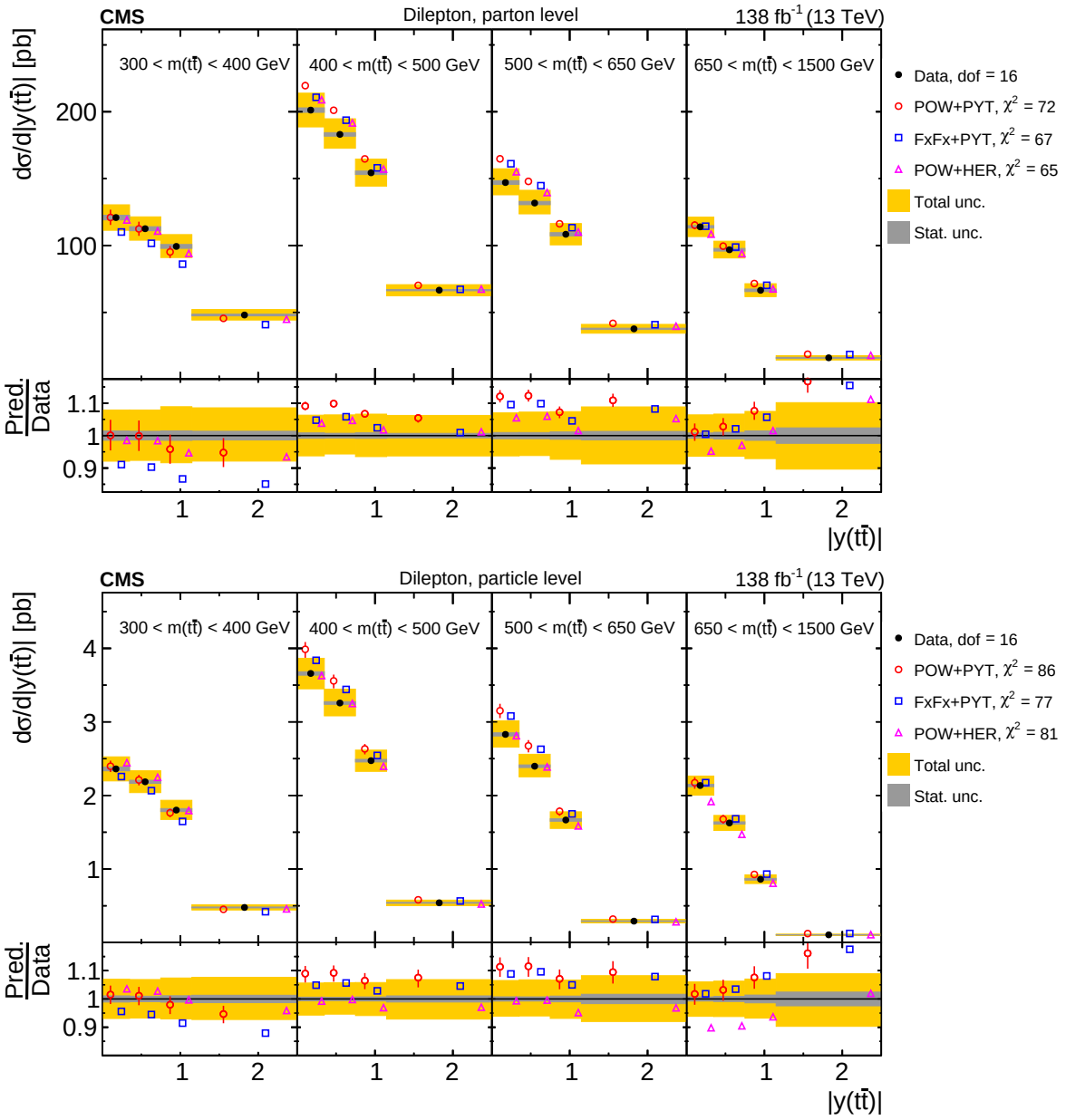

Figure 74: Absolute $[m(\mathrm{t\bar{t}}), |y(\mathrm{t\bar{t}})|]$ cross sections are shown for data (filled circles) and various MC predictions (other points). Further details can be found in the caption of Fig. 71.

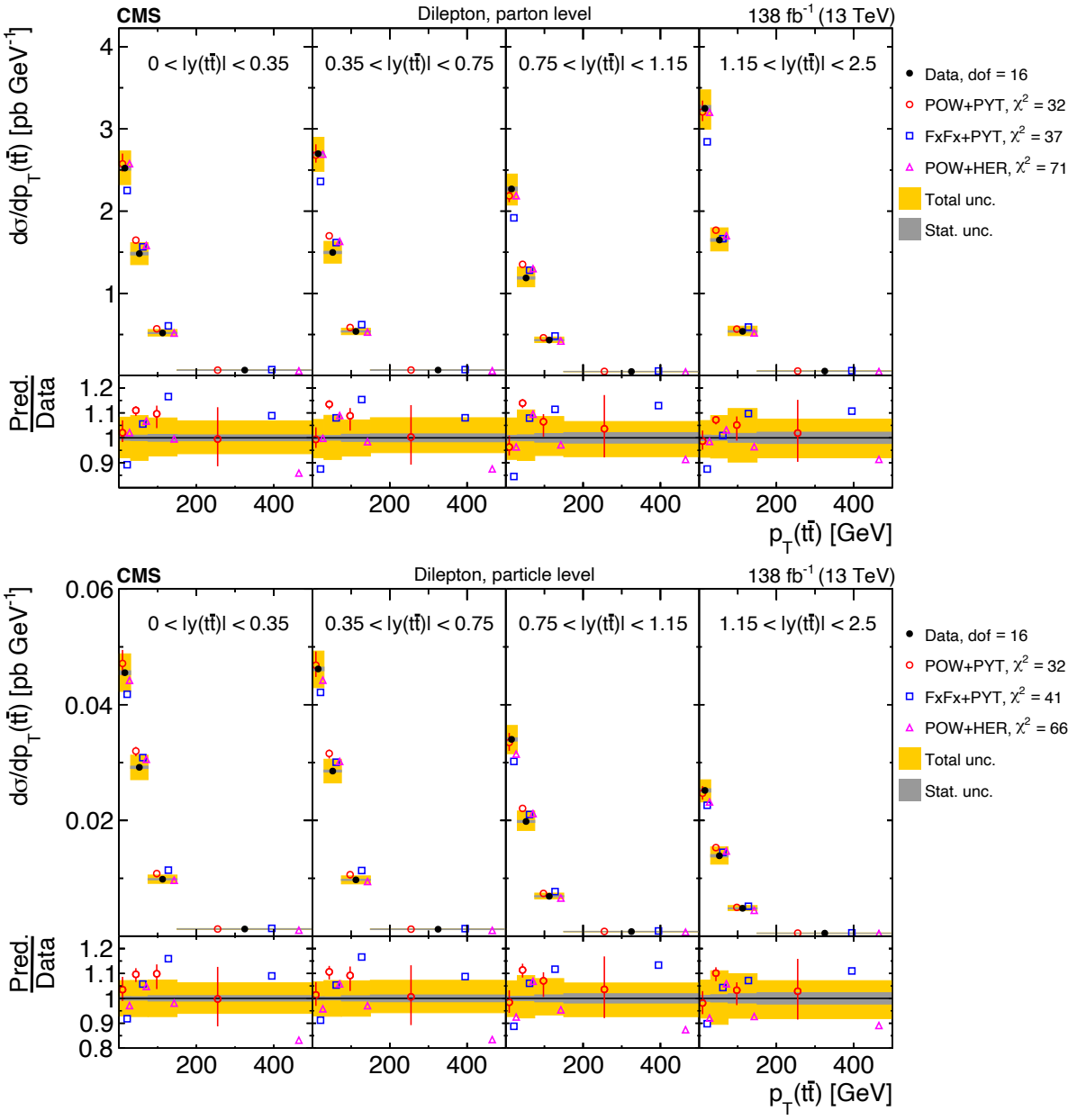

Figure 75: Absolute $[|y(\mathrm{t\bar{t}})|,\ p_{\mathrm{T}}(\mathrm{t\bar{t}})]$ cross sections are shown for data (filled circles) and various MC predictions (other points). Further details can be found in the caption of Fig. 71.

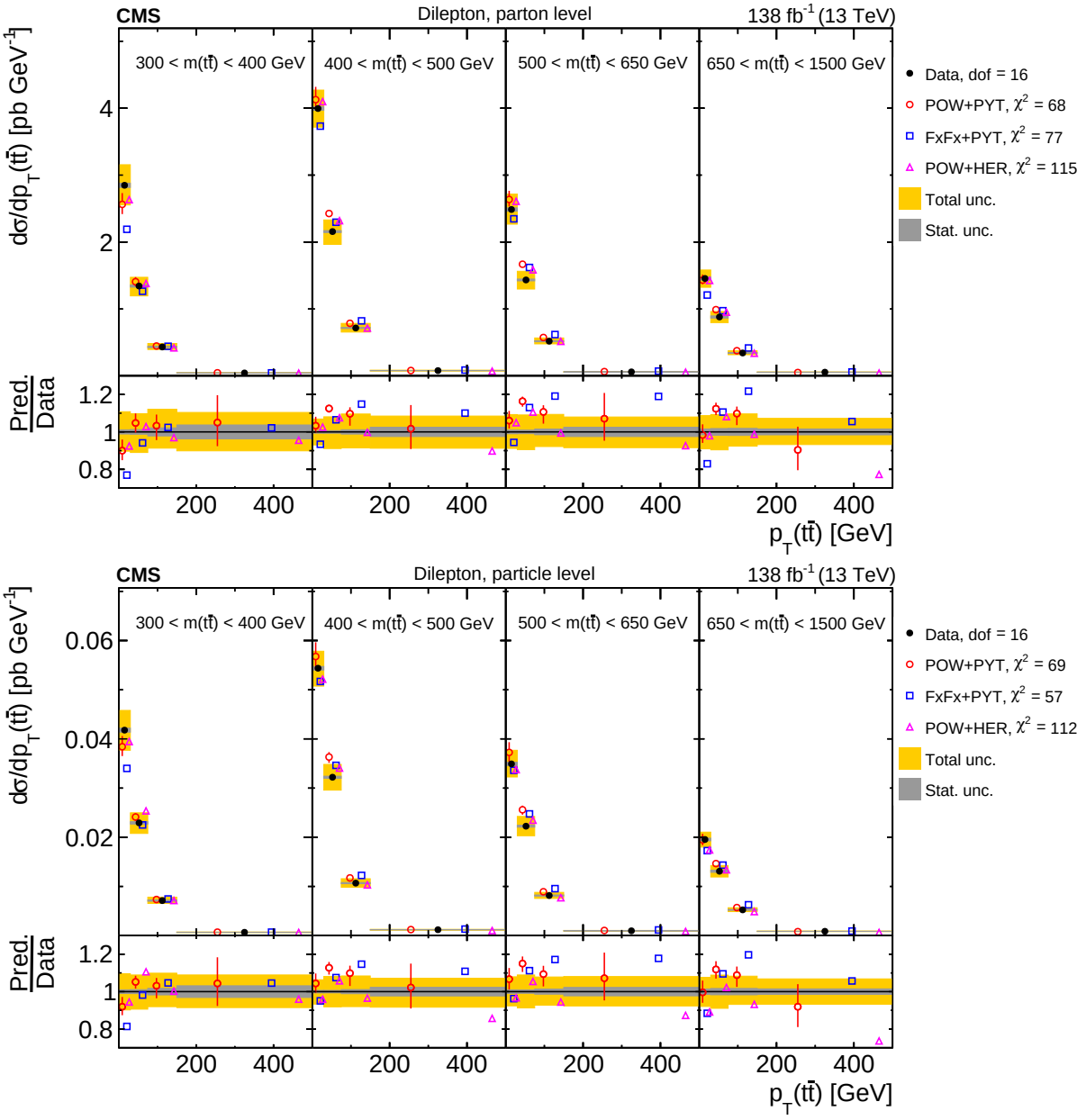

Figure 76: Absolute $[m(\mathrm{t\bar{t}}),\ p_{\mathrm{T}}(\mathrm{t\bar{t}})]$ cross sections are shown for data (filled circles) and various MC predictions (other points). Further details can be found in the caption of Fig. 71.

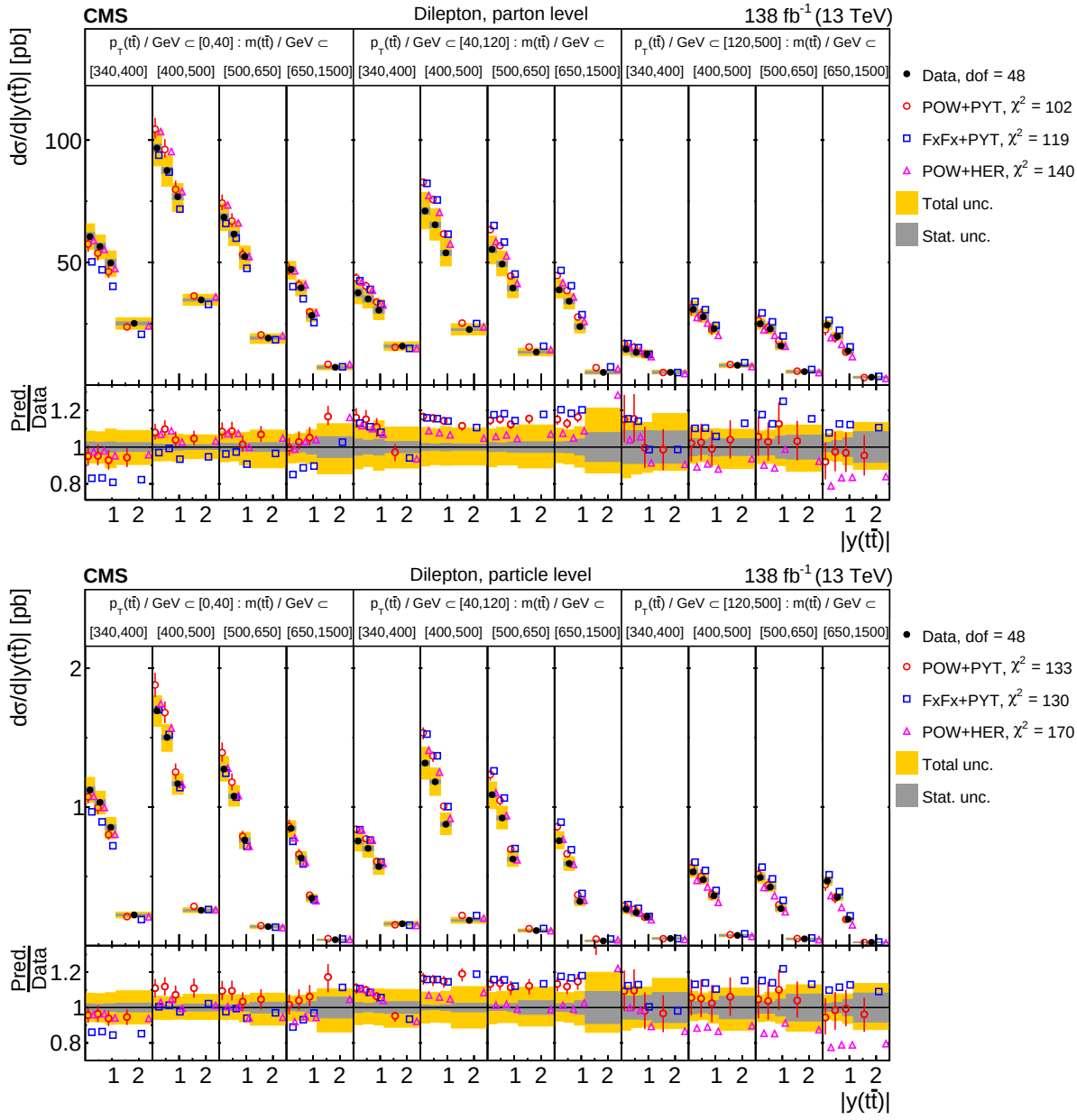

Figure 77: Absolute $[p_{\mathrm{T}}(\mathrm{t\bar{t}}), m(\mathrm{t\bar{t}}), |y(\mathrm{t\bar{t}})|]$ cross sections are shown for data (filled circles) and various MC predictions (other points). Further details can be found in the caption of Fig. 71.

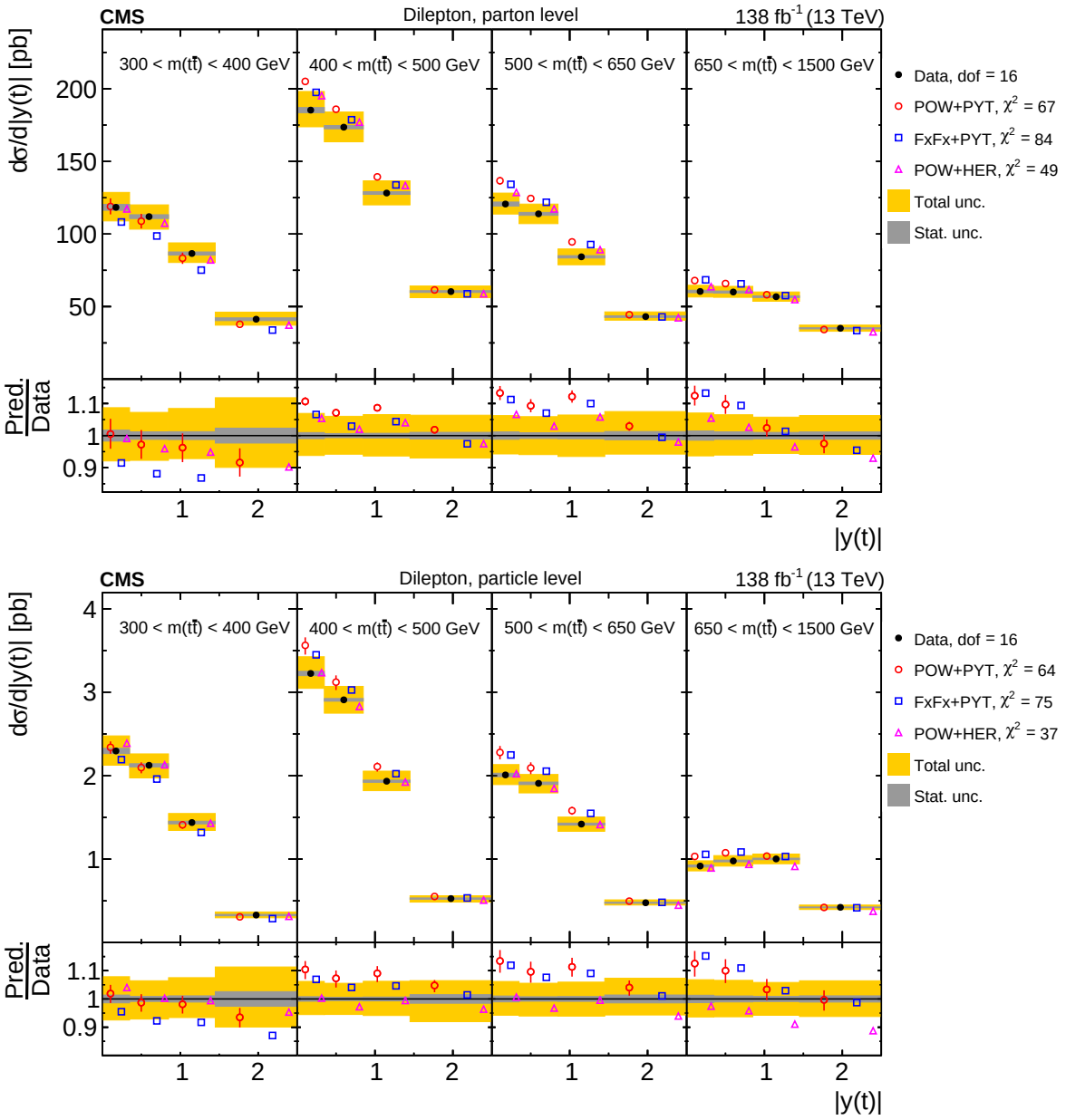

Figure 78: Absolute $[m(\mathrm{t\bar{t}}), |y(\mathrm{t})|]$ cross sections are shown for data (filled circles) and various MC predictions (other points). Further details can be found in the caption of Fig. 71.

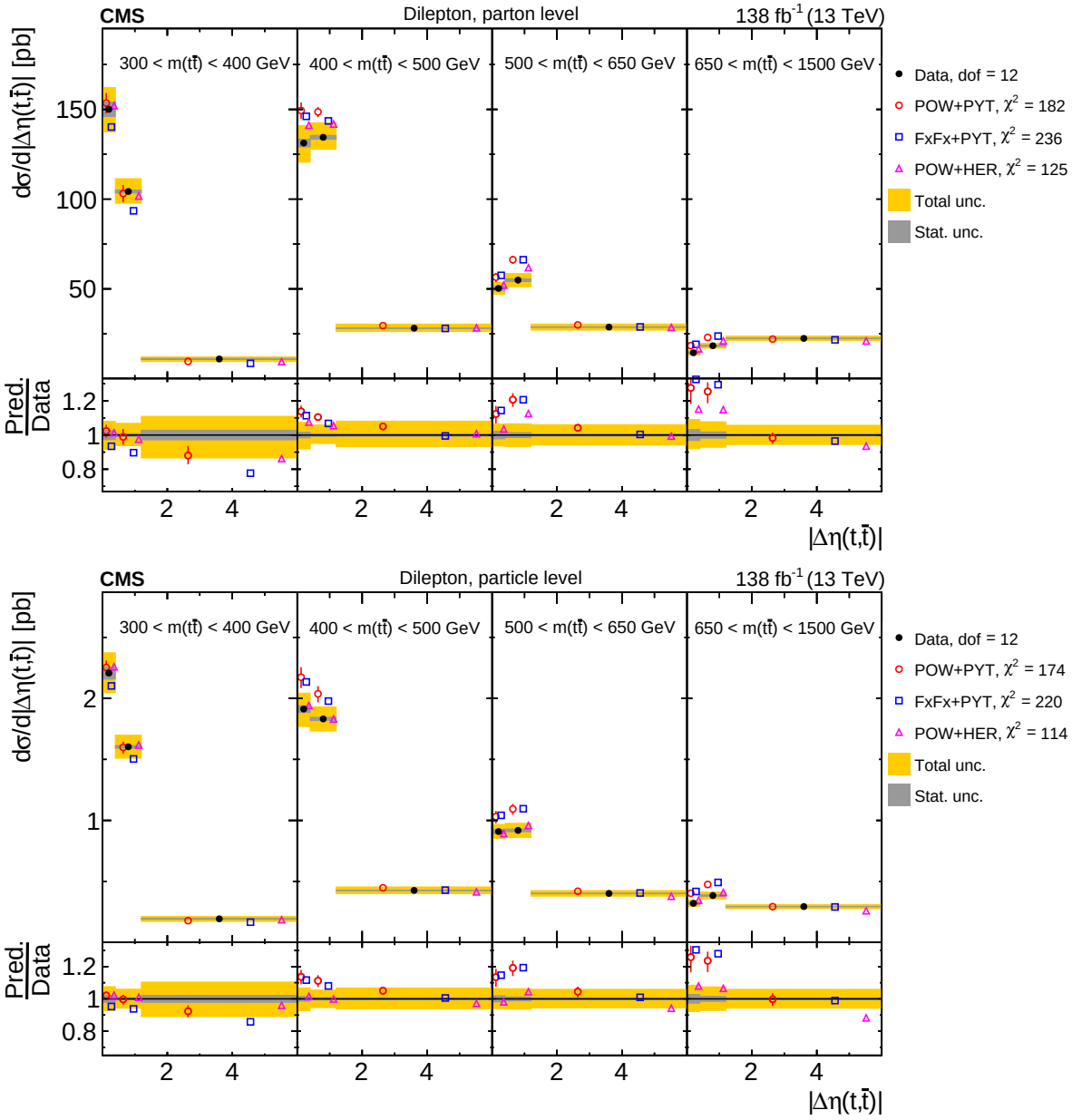

Figure 79: Absolute $[m(t\bar{t}), |\Delta\eta(t,\bar{t})|]$ cross sections are shown for data (filled circles) and various MC predictions (other points). Further details can be found in the caption of Fig. 71.

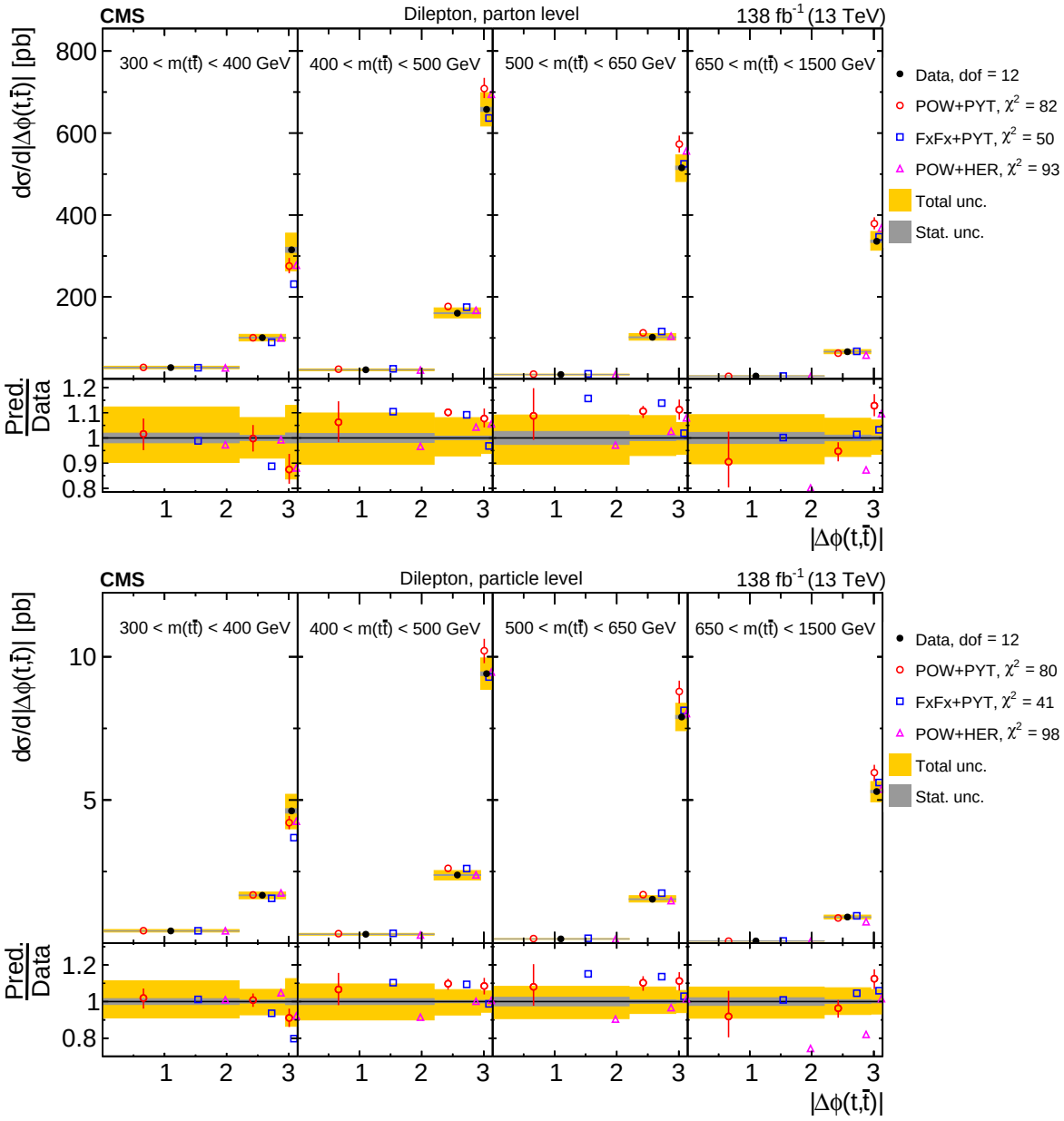

Figure 80: Absolute $[m(t\bar{t}), |\Delta\phi(t,\bar{t})|]$ cross sections are shown for data (filled circles) and various MC predictions (other points). Further details can be found in the caption of Fig. 71.

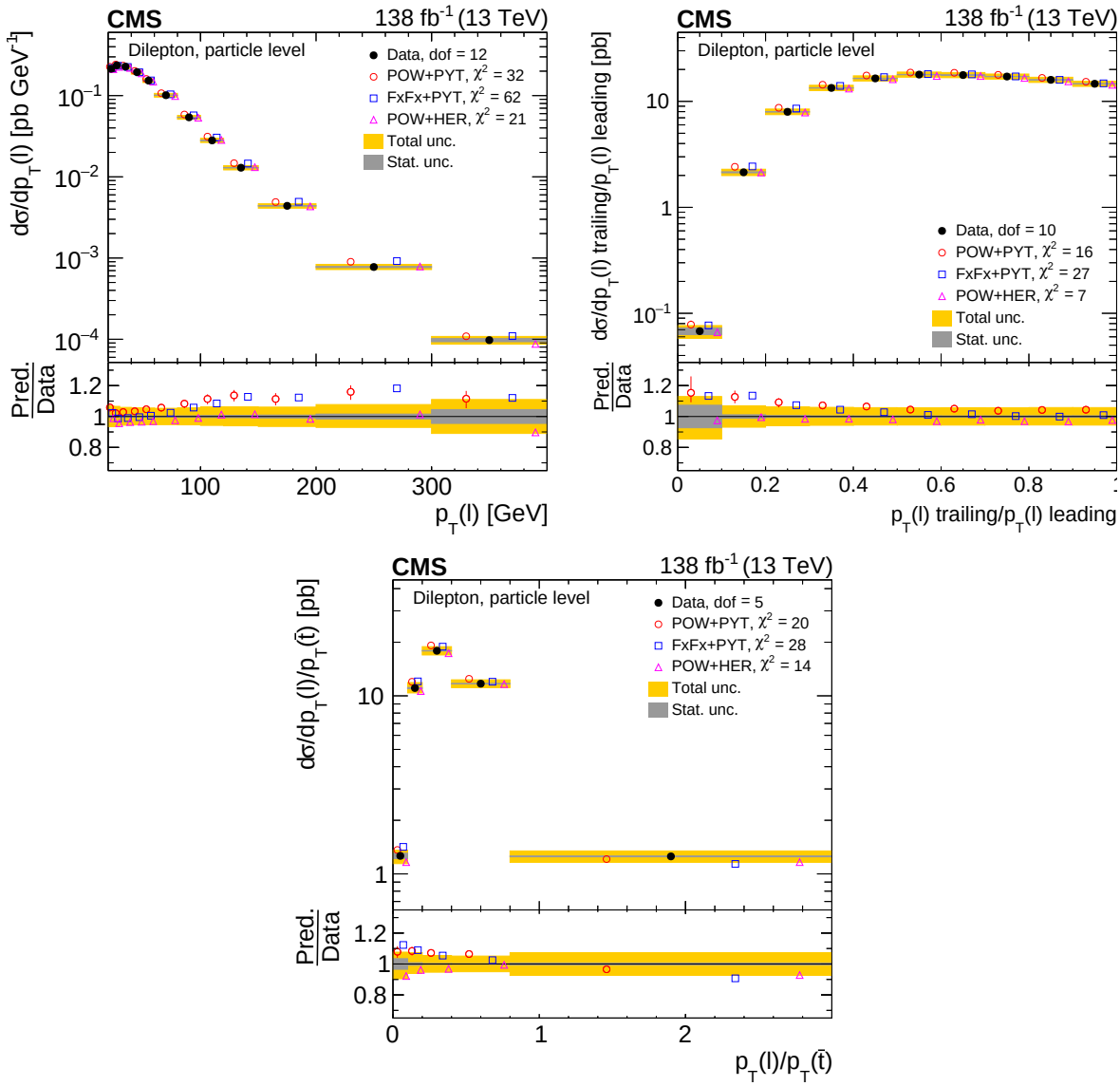

Figure 81: Absolute differential $t\bar{t}$ production cross sections as a function of p_T of the lepton (upper left), of the ratio of the trailing and leading lepton p_T (upper right), and of the ratio of lepton and top antiquark p_T (lower middle), measured at the particle level in a fiducial phase space. The data are shown as filled circles with grey and yellow bands indicating the statistical and total uncertainties (statistical and systematic uncertainties added in quadrature), respectively. For each distribution, the number of degrees of freedom (dof) is also provided. The cross sections are compared to various MC predictions (other points). The estimated uncertainties in the POWHEG+PYTHIA8 ('POW-PYT') simulation are represented by a vertical bar on the corresponding points. For each MC model, a value of χ^2 is reported that takes into account the measurement uncertainties. The lower panel in each plot shows the ratios of the predictions to the data.

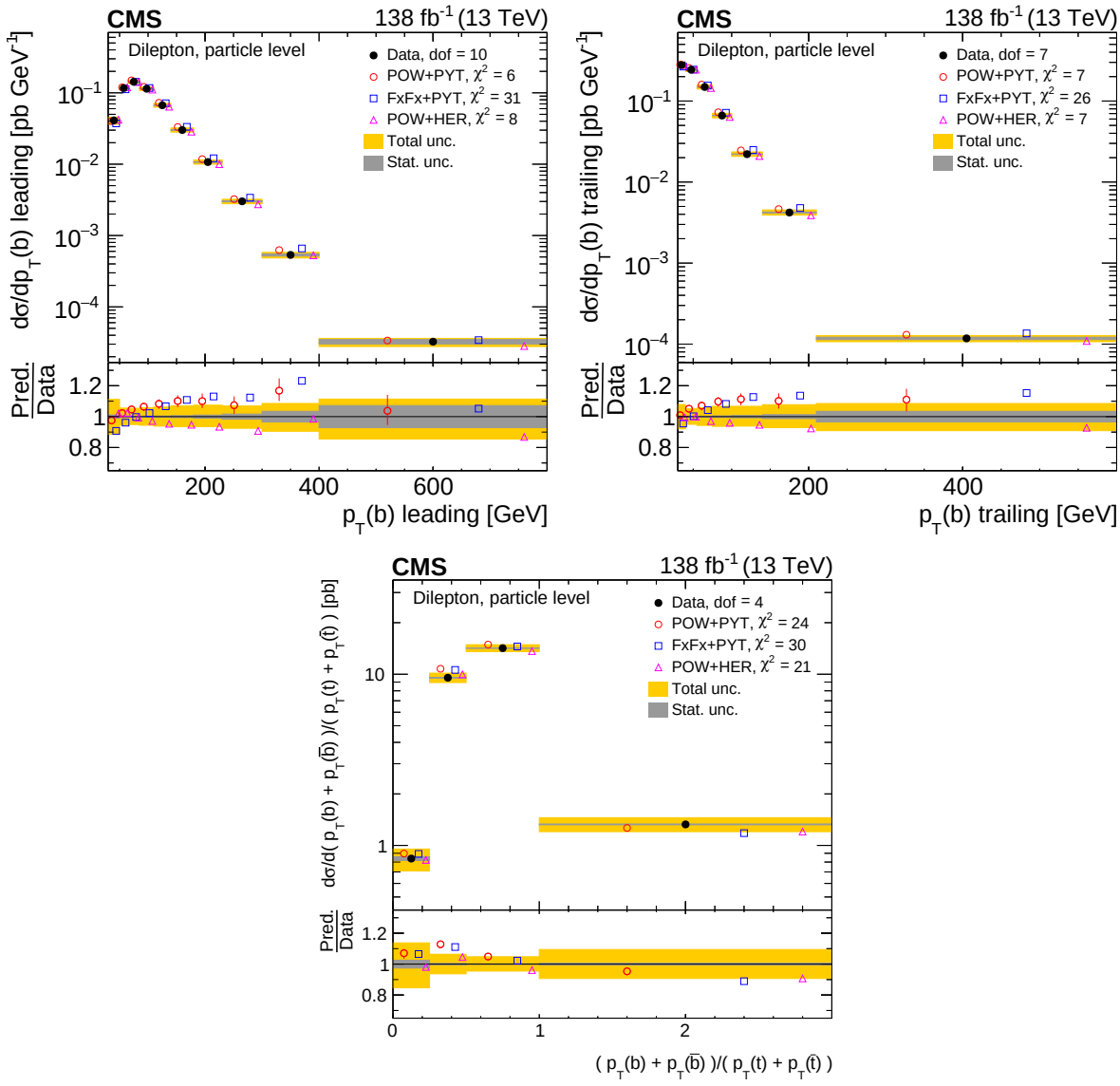

Figure 82: Absolute differential $\mathrm{t\bar{t}}$ production cross sections as functions of the p_{T} of the leading (upper left) and trailing (upper right) b jet, and $(p_{\mathrm{T}}(\mathrm{b}) + p_{\mathrm{T}}(\bar{\mathrm{b}}))/(p_{\mathrm{T}}(\mathrm{t}) + p_{\mathrm{T}}(\bar{\mathrm{t}}))$ (lower). Further details can be found in the caption of Fig. 81.

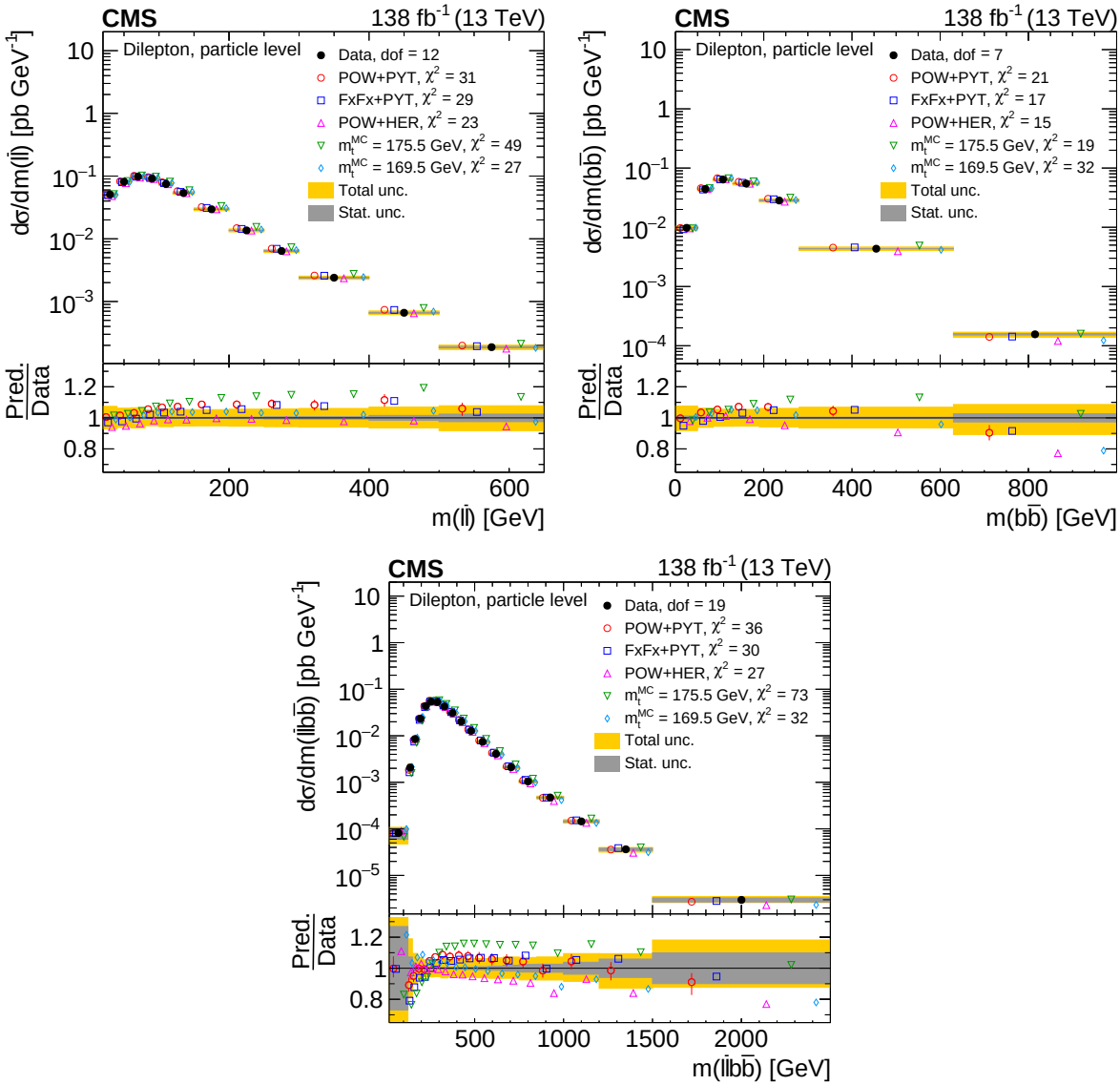

Figure 83: Absolute differential $\mathrm{t\bar{t}}$ production cross sections as functions of $m(\ell\bar{\ell})$ (upper left), $m(\mathrm{b\bar{b}})$ (upper right) and $m(\ell\bar{\ell}\mathrm{b\bar{b}})$ (lower) are shown for data (filled circles) and various MC predictions (other points). Further details can be found in the caption of Fig. 81.

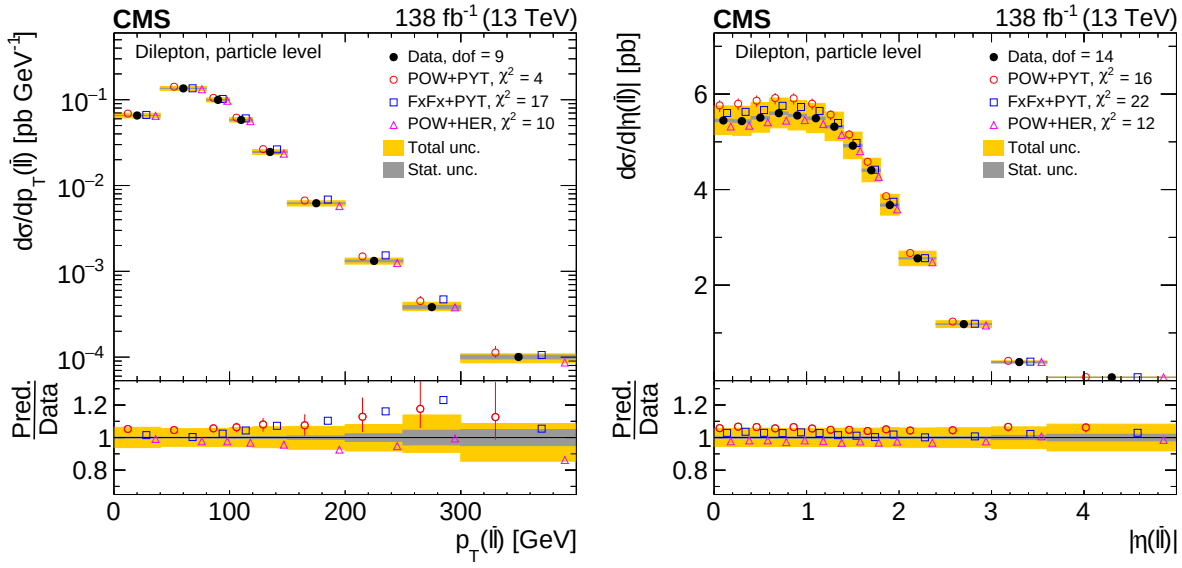

Figure 84: Absolute differential $t\bar{t}$ production cross sections as functions of $p_T(\ell\bar{\ell})$ (left) and $|\eta(\ell\bar{\ell})|$ (right) are shown for data (filled circles) and various MC predictions (other points). Further details can be found in the caption of Fig. 81.

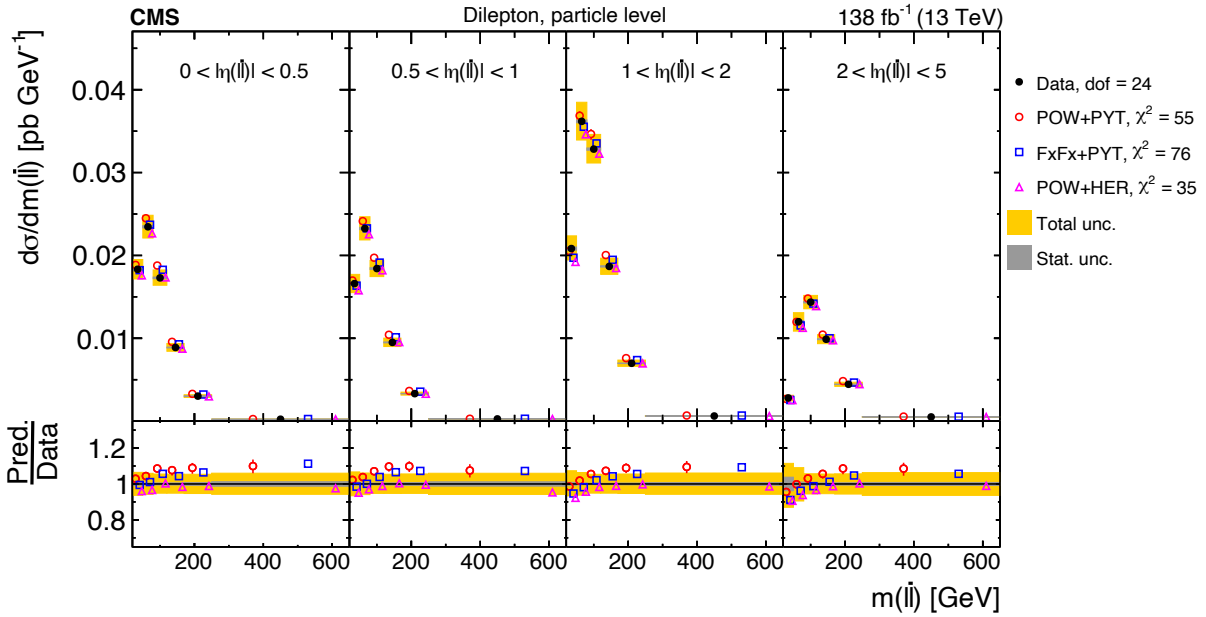

Figure 85: Absolute $[|\eta(\ell\bar{\ell})|, m(\ell\bar{\ell})]$ cross sections are shown for data (filled circles) and various MC predictions (other points). Further details can be found in the caption of Fig. 81.

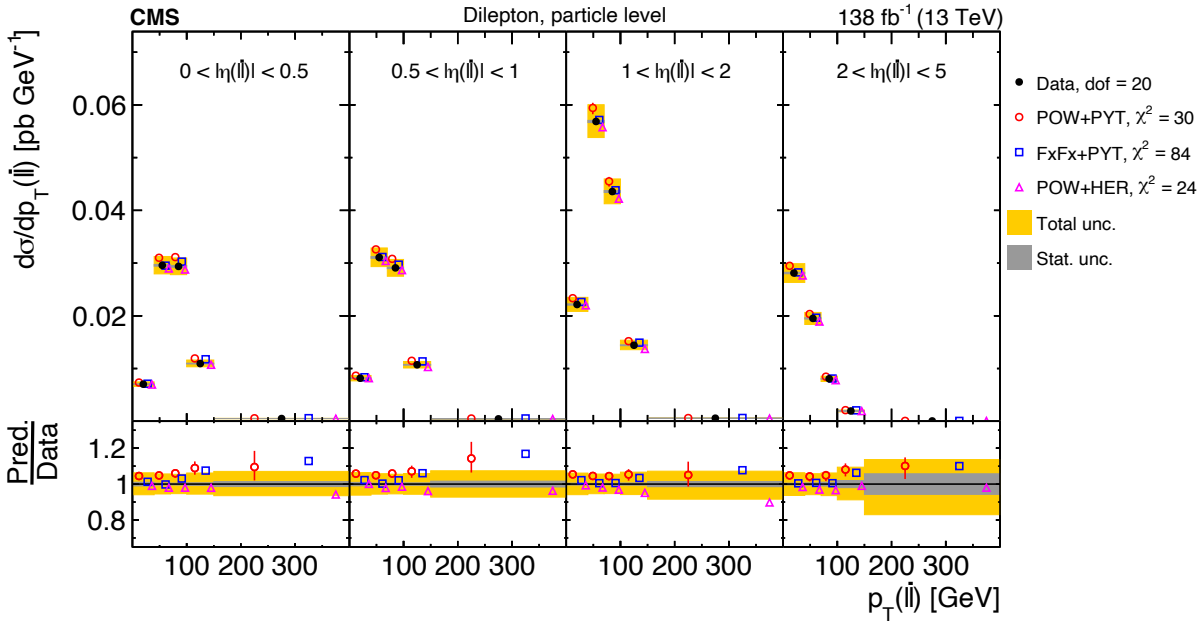

Figure 86: Absolute $[|\eta(\ell\bar{\ell})|,\ p_{\mathrm{T}}(\ell\bar{\ell})]$ cross sections are shown for data (filled circles) and various MC predictions (other points). Further details can be found in the caption of Fig. 81.

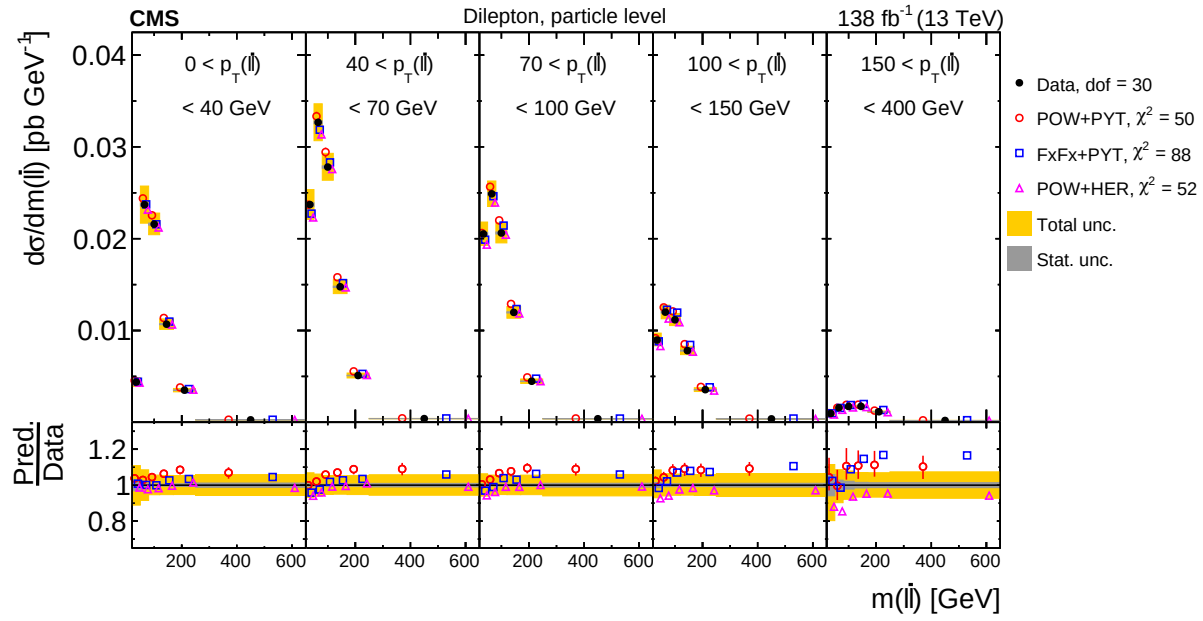

Figure 87: Absolute $[p_{\mathrm{T}}(\ell\bar{\ell}),\ m(\ell\bar{\ell})]$ cross sections are shown for data (filled circles) and various MC predictions (other points). Further details can be found in the caption of Fig. 81.

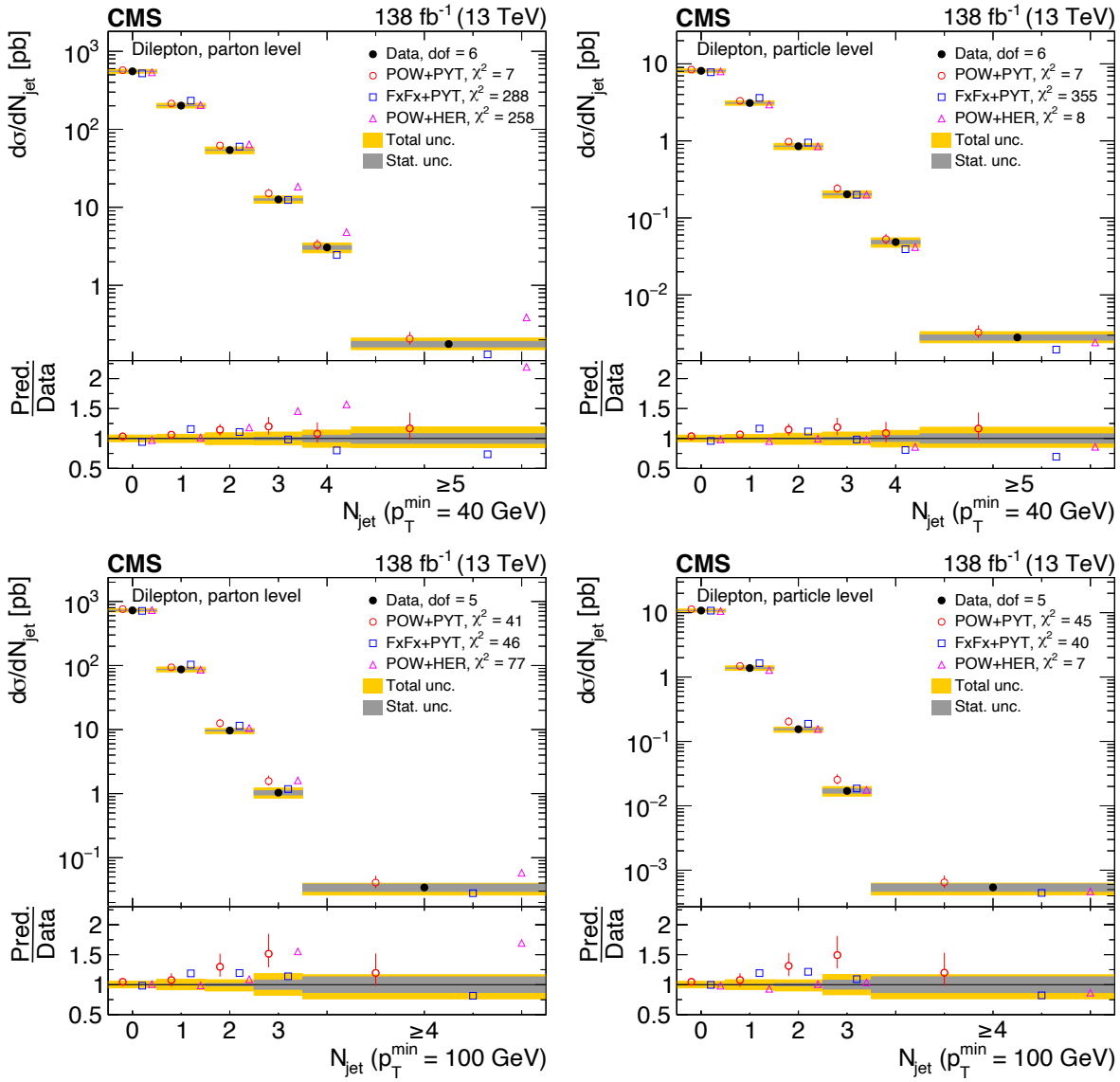

Figure 88: Absolute differential $\mathrm{t\bar{t}}$ production cross sections as a function of N_{jet}, for a minimum jet p_{T} of 40 GeV (upper) and 100 GeV (lower), measured at the parton level in the full phase space (left) and at the particle level in a fiducial phase space (right). The data are shown as filled circles with grey and yellow bands indicating the statistical and total uncertainties (statistical and systematic uncertainties added in quadrature), respectively. For each distribution, the number of degrees of freedom (dof) is also provided. The cross sections are compared to various MC predictions (other points). The estimated uncertainties in the POWHEG+PYTHIA 8 ('POW-PYT') simulation are represented by a vertical bar on the corresponding points. For each MC model, a value of χ^2 is reported that takes into account the measurement uncertainties. The lower panel in each plot shows the ratios of the predictions to the data.

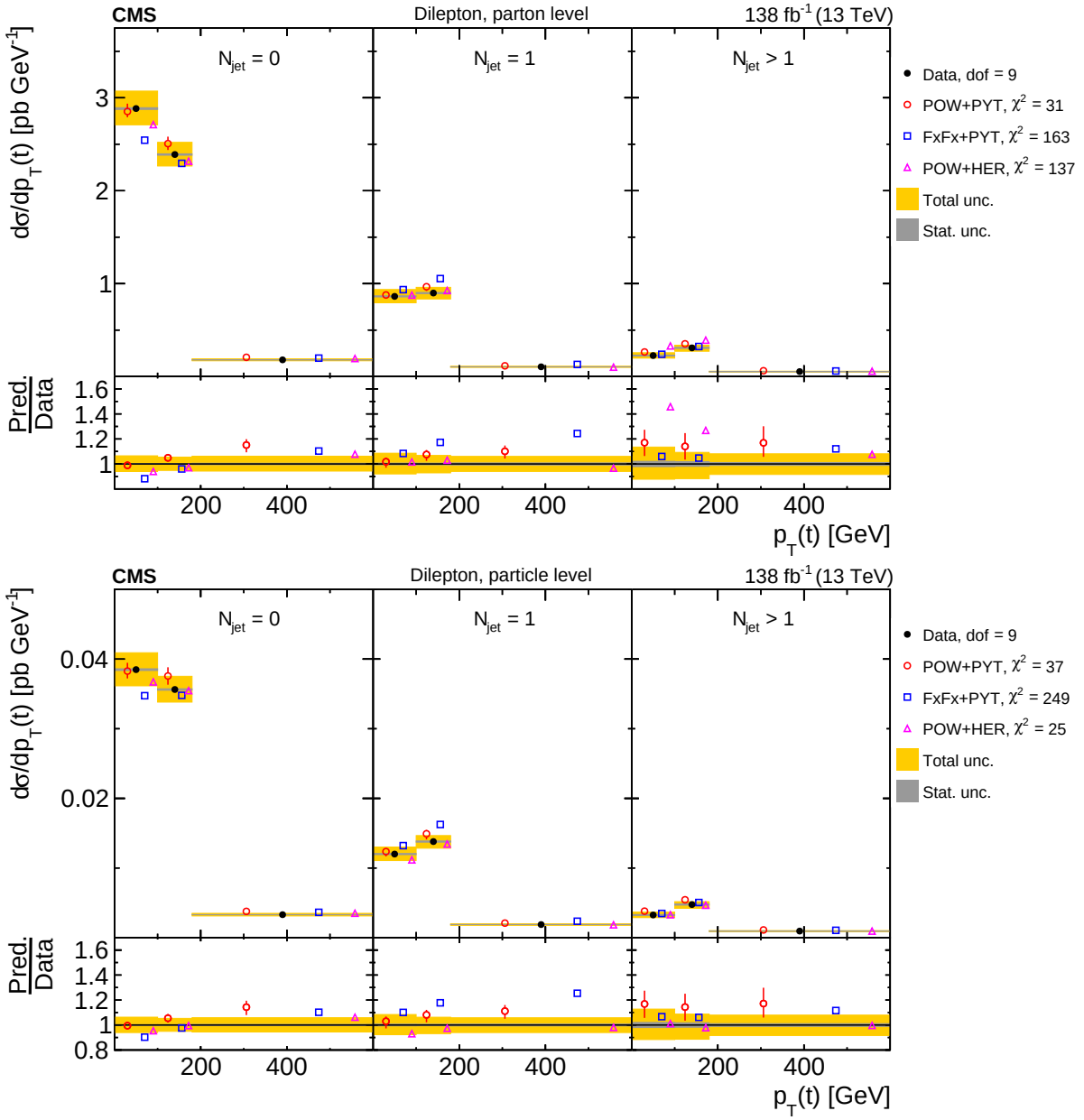

Figure 89: Absolute $[N_{\text{jet}}, p_{\text{T}}(\text{t})]$ cross sections measured at the parton level in the full phase space (upper) and at the particle level in a fiducial phase space (lower). The data are shown as filled circles with grey and yellow bands indicating the statistical and total (sum in quadrature of statistical and systematic) uncertainties, respectively. For each distribution, the number of degrees of freedom (dof) is also provided. The cross sections are compared to various MC predictions (other points). The estimated uncertainties in the POWHEG+PYTHIA 8 ('POW-PYT') simulation are represented by a vertical bar on the corresponding points. For each MC model, a value of χ^2 is reported that takes into account the measurement uncertainties. The lower panel in each plot shows the ratios of the predictions to the data.

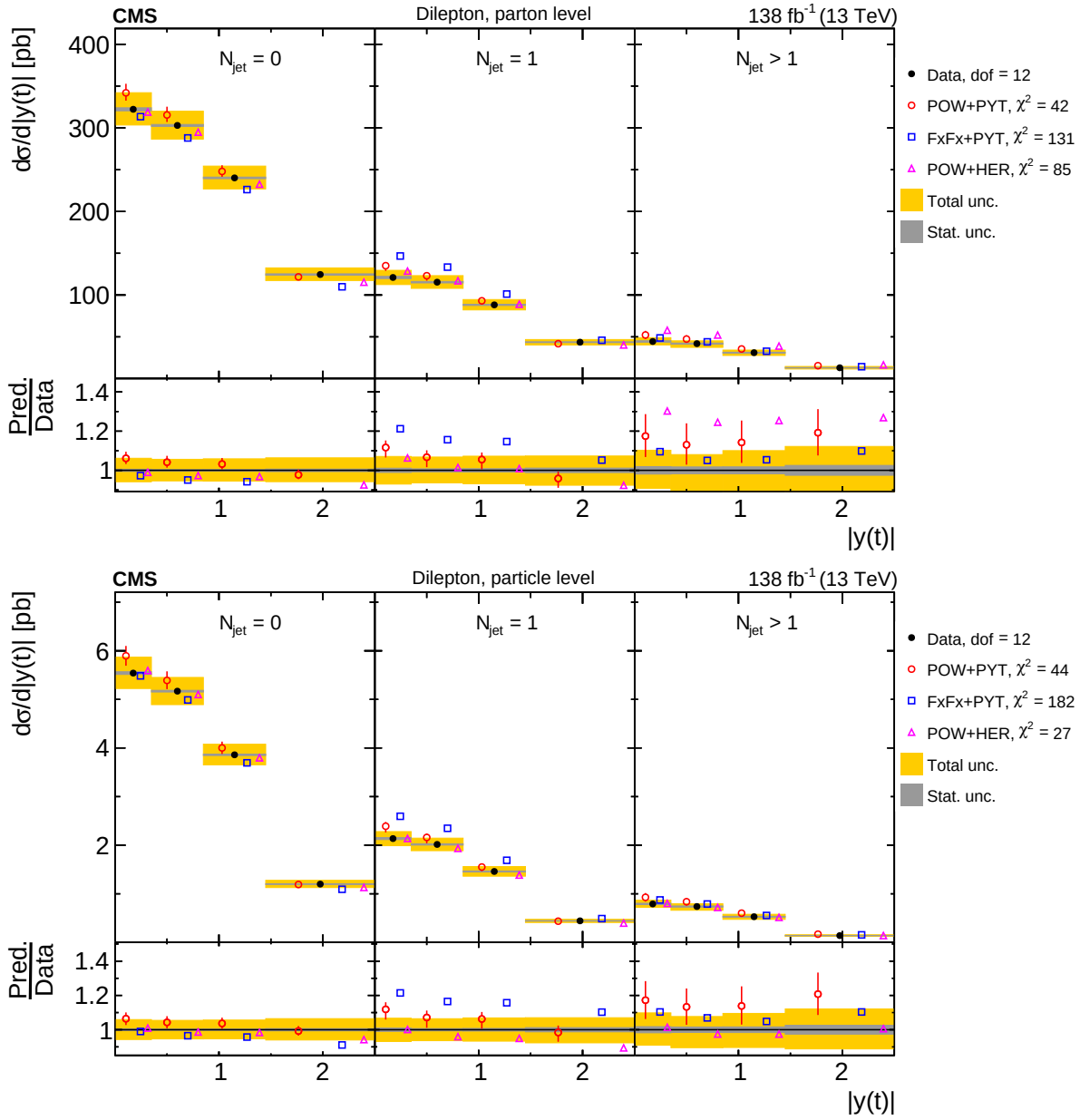

Figure 90: Absolute $[N_{\text{jet}}, |y(t)|]$ cross sections are shown for data (filled circles) and various MC predictions (other points). Further details can be found in the caption of Fig. 89.

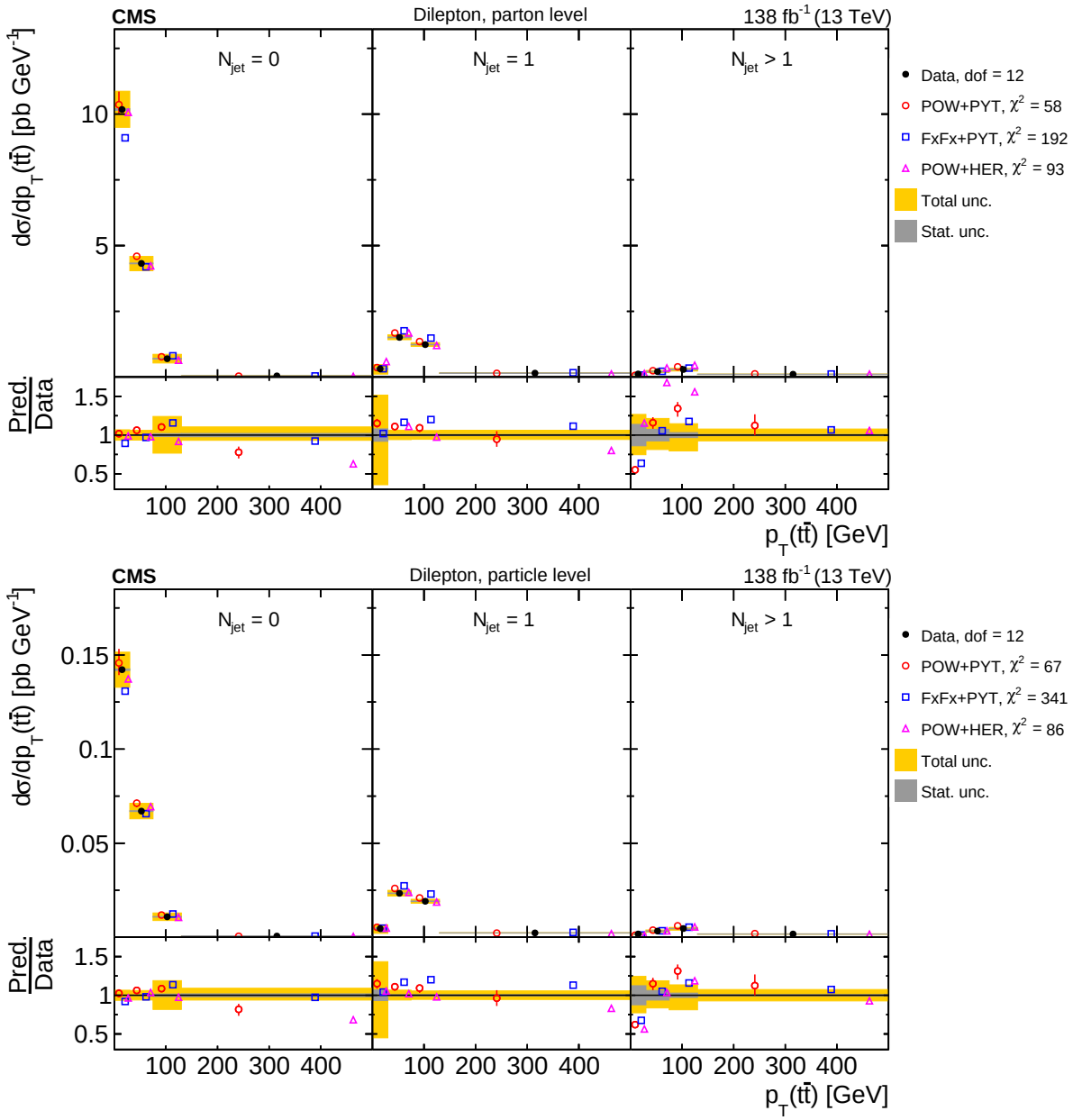

Figure 91: Absolute $[N_{\text{jet}}, p_{\text{T}}(\text{t}\bar{\text{t}})]$ cross sections are shown for data (filled circles) and various MC predictions (other points). Further details can be found in the caption of Fig. 89.

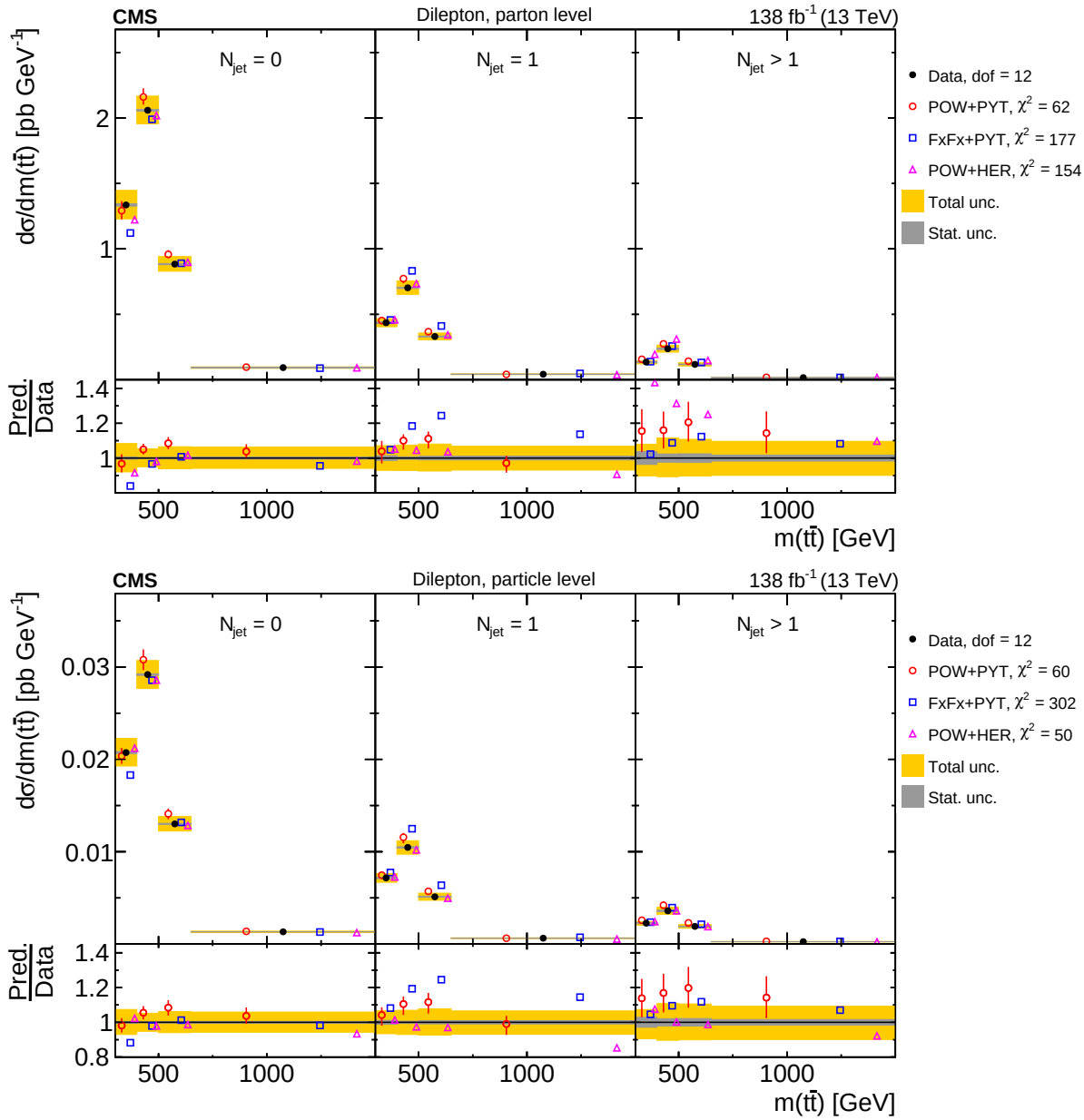

Figure 92: Absolute $[N_{\text{jet}}, m(\text{t}\bar{\text{t}})]$ cross sections are shown for data (filled circles) and various MC predictions (other points). Further details can be found in the caption of Fig. 89.

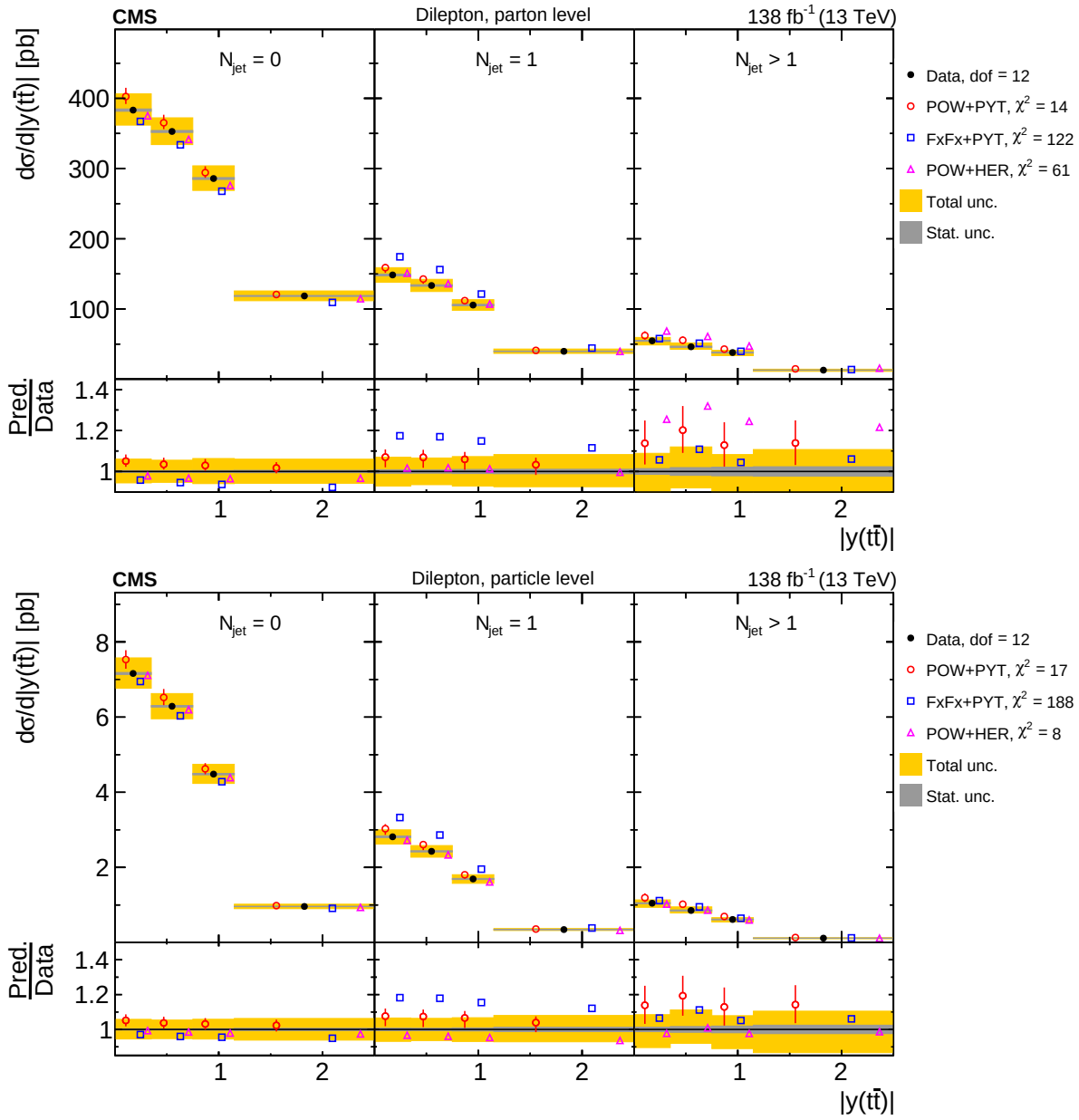

Figure 93: Absolute $[N_{\text{jet}}, |y(\text{t}\bar{\text{t}})|]$ cross sections are shown for data (filled circles) and various MC predictions (other points). Further details can be found in the caption of Fig. 89.

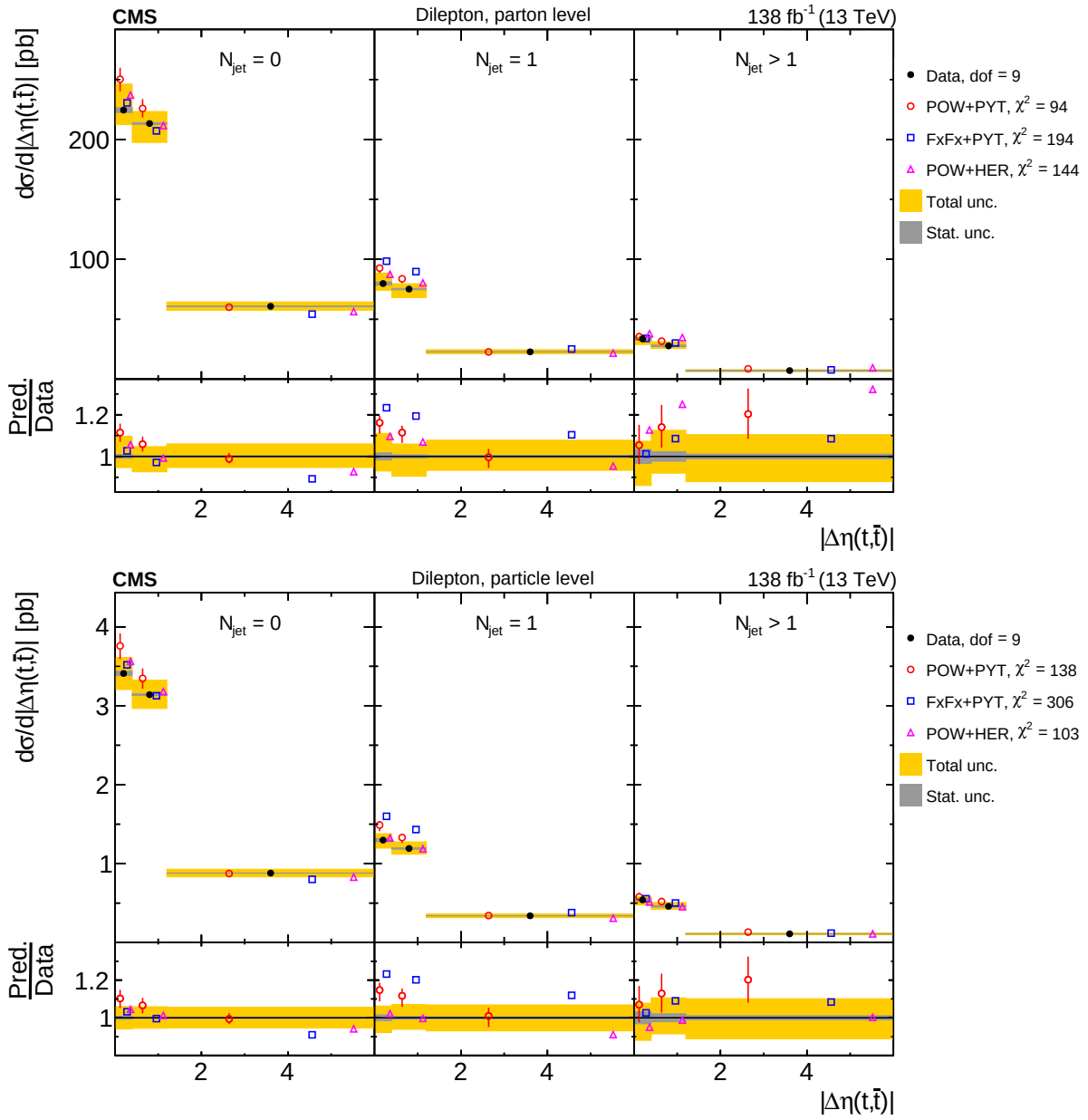

Figure 94: Absolute $[N_{\text{jet}}, |\Delta\eta(\text{t},\bar{\text{t}})|]$ cross sections are shown for data (filled circles) and various MC predictions (other points). Further details can be found in the caption of Fig. 89.

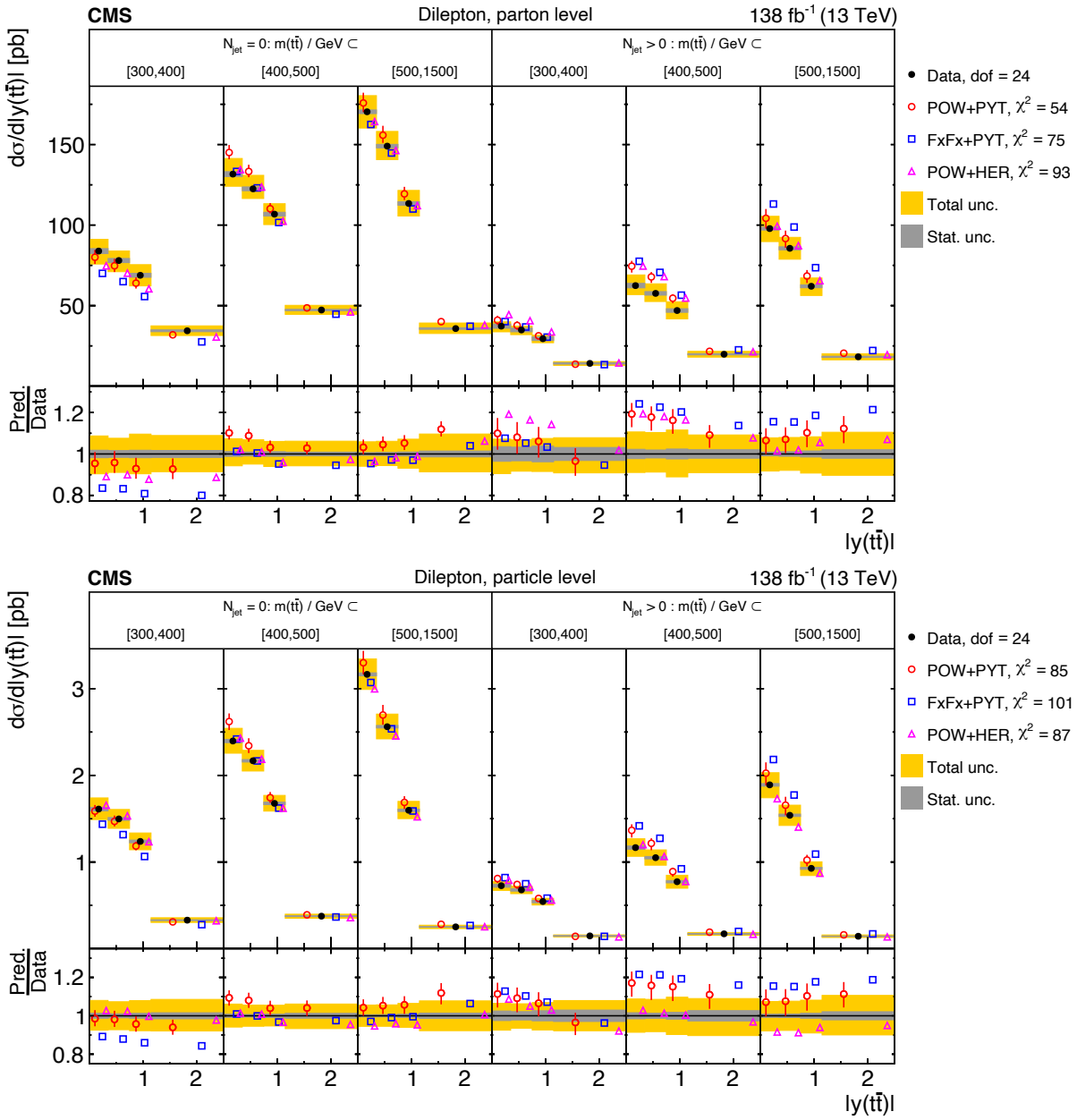

Figure 95: Absolute $[N_{\text{jet}}^{0,1+}, m(\text{t}\bar{\text{t}}), |y(\text{t}\bar{\text{t}})|]$ cross sections are shown for data (filled circles) and various MC predictions (other points). Further details can be found in the caption of Fig. 89.

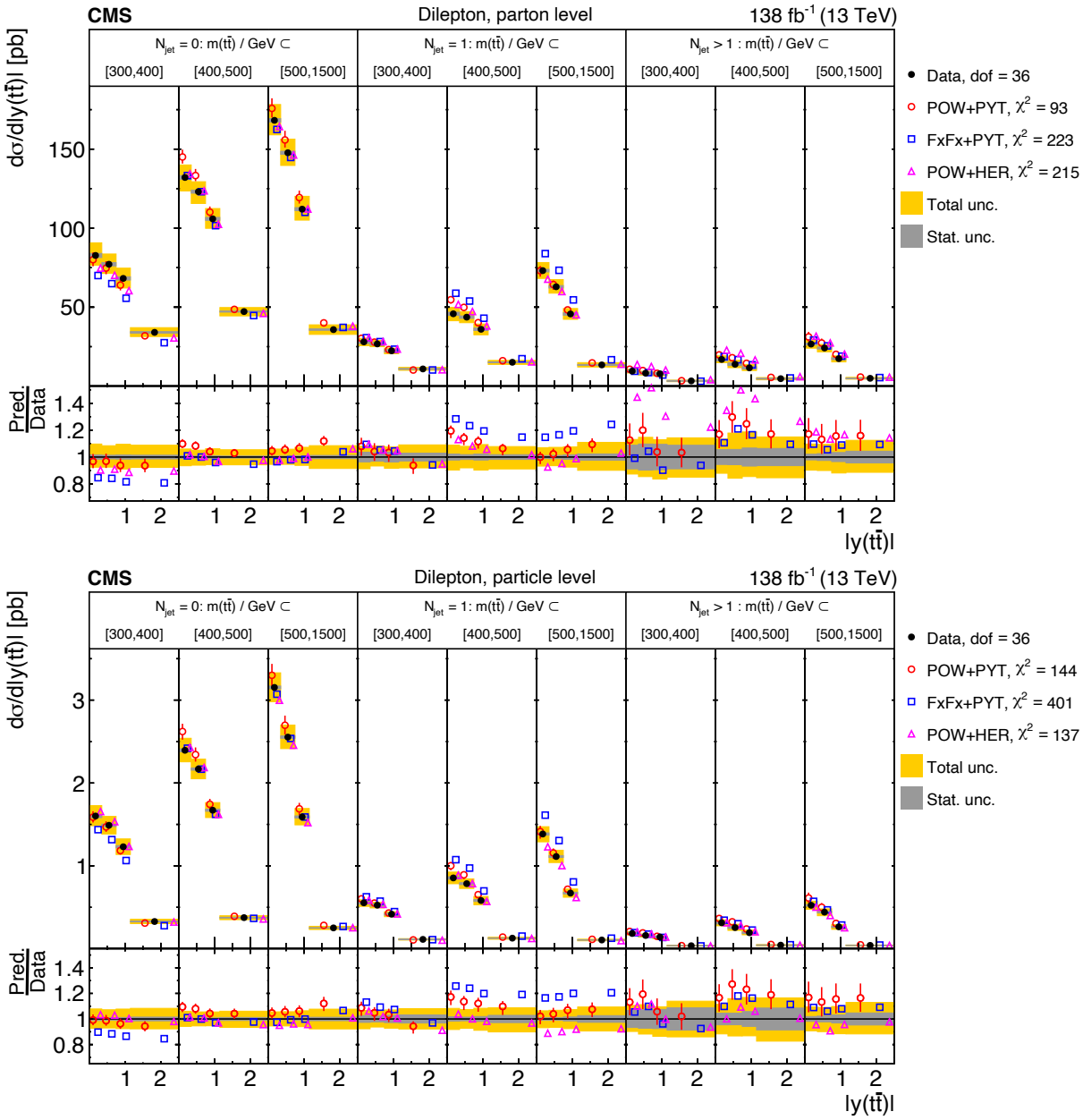

Figure 96: Absolute $[N_{\text{jet}}^{0,1,2+}, m(\text{t}\bar{\text{t}}), |y(\text{t}\bar{\text{t}})|]$ cross sections are shown for data (filled circles) and various MC predictions (other points). Further details can be found in the caption of Fig. 89.

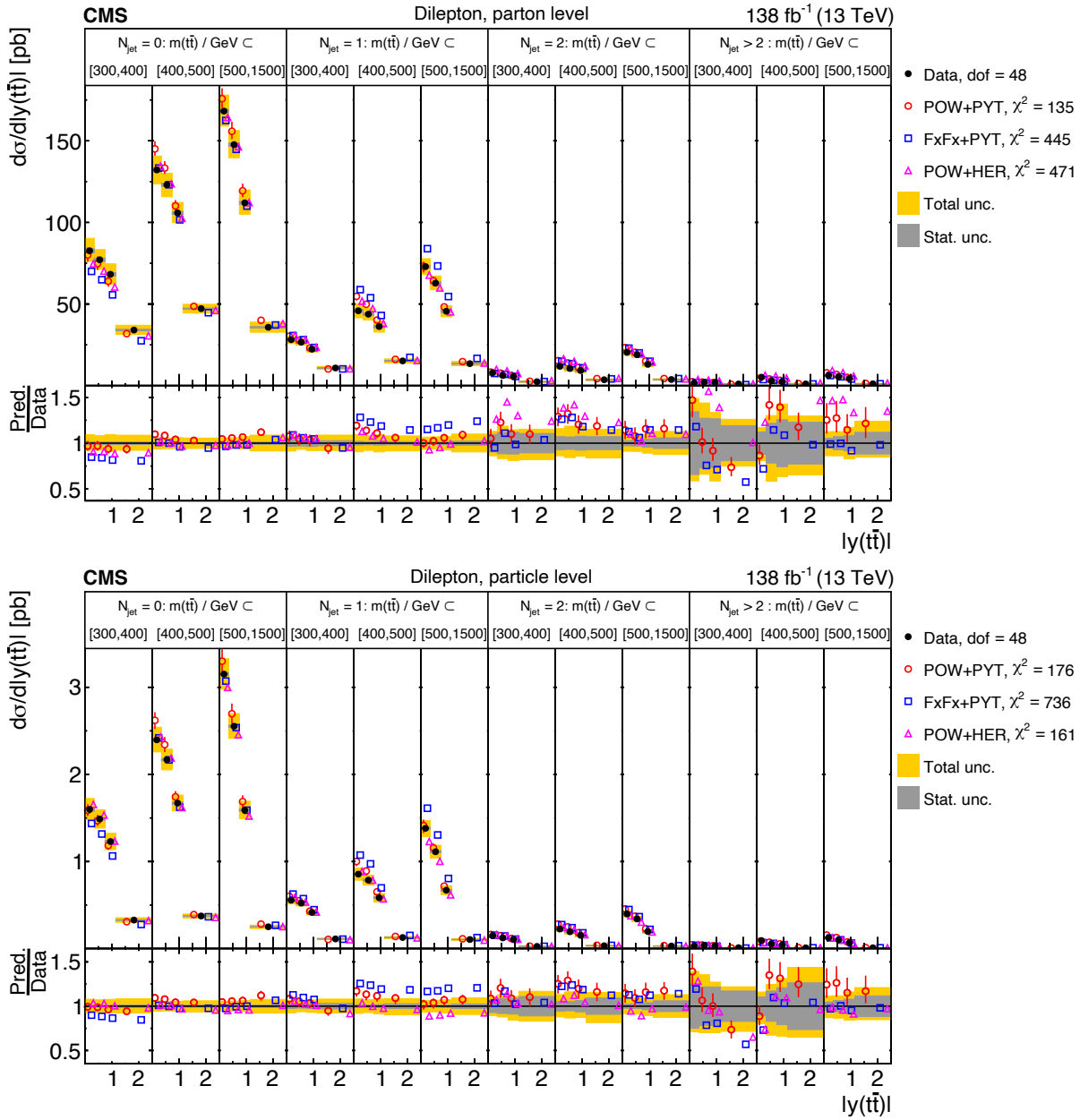

Figure 97: Absolute $[N_{\text{jet}}^{0,1,2,3+}, m(\text{t}\bar{\text{t}}), |y(\text{t}\bar{\text{t}})|]$ cross sections are shown for data (filled circles) and various MC predictions (other points). Further details can be found in the caption of Fig. 89.

Table 13: The χ^2 values and dof of the measured absolute single-differential cross sections for $t\bar{t}$ and top quark kinematic observables at the parton level are shown with respect to the predictions of various MC generators. The χ^2 values are calculated taking only measurement uncertainties into account and excluding theory uncertainties. For POW+PYT, the χ^2 values including theory uncertainties are indicated with the brackets (w. unc.).

Cross section variables	dof	χ^2		
		POW+PYT (w. unc.)	FxFx+PYT	POW+HER
$p_T(t)$	7	21 (13)	43	5
$p_T(\bar{t})$	7	19 (12)	43	6
$y(t)$	10	28 (24)	34	21
$y(\bar{t})$	10	33 (28)	40	25
$p_T(t\bar{t})$	7	24 (8)	39	35
$y(t\bar{t})$	12	13 (9)	19	8
$m(t\bar{t})$	7	6 (4)	9	4
$\lvert\Delta\phi(t,\bar{t})\rvert$	4	4 (2)	7	11
$\lvert y(t)\rvert - \lvert y(\bar{t})\rvert$	8	18 (10)	19	14
$p_T(t)/m(t\bar{t})$	5	39 (21)	104	13
$p_T(t\bar{t})/m(t\bar{t})$	9	20 (7)	32	39
$\log(\xi_1)$	9	16 (12)	18	12
$\log(\xi_2)$	9	14 (9)	24	7

Table 14: The χ^2 values and dof of the measured absolute single-differential cross sections for $t\bar{t}$ and top quark kinematic observables at the particle level are shown with respect to the predictions of various MC generators. The χ^2 values are calculated taking only measurement uncertainties into account and excluding theory uncertainties. For POW+PYT, the χ^2 values including theory uncertainties are indicated with the brackets (w. unc.).

Cross section variables	dof	χ^2		
		POW+PYT (w. unc.)	FxFx+PYT	POW+HER
$p_T(t)$	7	22 (13)	44	7
$p_T(\bar{t})$	7	20 (12)	44	5
$y(t)$	10	24 (18)	32	19
$y(\bar{t})$	10	28 (23)	32	26
$p_T(t\bar{t})$	7	23 (8)	34	41
$y(t\bar{t})$	12	13 (8)	23	9
$m(t\bar{t})$	7	7 (4)	5	7
$\lvert\Delta\phi(t,\bar{t})\rvert$	4	4 (1)	4	7
$\lvert y(t)\rvert - \lvert y(\bar{t})\rvert$	8	17 (11)	15	18
$p_T(t)/m(t\bar{t})$	5	33 (23)	71	14
$p_T(t\bar{t})/m(t\bar{t})$	9	21 (7)	46	61
$\log(\xi_1)$	9	16 (10)	17	19
$\log(\xi_2)$	9	12 (7)	19	10

Table 15: The χ^2 values and dof of the measured absolute multi-differential cross sections for $t\bar{t}$ and top quark kinematic observables at the parton level are shown with respect to the predictions of various MC generators. The χ^2 values are calculated taking only measurement uncertainties into account and excluding theory uncertainties. For POW+PYT, the χ^2 values including theory uncertainties are indicated with the brackets (w. unc.).

Cross section variables	dof	χ^2		
		POW+PYT (w. unc.)	FxFx+PYT	POW+HER
$[\lvert y(t)\rvert,\ p_T(t)]$	16	48 (36)	75	30
$[m(t\bar{t}),\ p_T(t)]$	9	93 (36)	156	42
$[p_T(t),\ p_T(t\bar{t})]$	16	50 (25)	72	87
$[m(t\bar{t}),\ \lvert y(t\bar{t})\rvert]$	16	72 (46)	67	65
$[\lvert y(t\bar{t})\rvert,\ p_T(t\bar{t})]$	16	32 (17)	37	71
$[m(t\bar{t}),\ p_T(t\bar{t})]$	16	68 (47)	77	115
$[p_T(t\bar{t}),\ m(t\bar{t}),\ \lvert y(t\bar{t})\rvert]$	48	102 (71)	119	140
$[m(t\bar{t}),\ \lvert y(t)\rvert]$	16	67 (39)	84	49
$[m(t\bar{t}),\ \lvert\Delta\eta(t,\bar{t})\rvert]$	12	182 (34)	236	125
$[m(t\bar{t}),\ \lvert\Delta\phi(t,\bar{t})\rvert]$	12	82 (51)	50	93

Table 16: The χ^2 values and dof of the measured absolute multi-differential cross sections for $t\bar{t}$ and top quark kinematic observables at the particle level are shown with respect to the predictions of various MC generators. The χ^2 values are calculated taking only measurement uncertainties into account and excluding theory uncertainties. For POW+PYT, the χ^2 values including theory uncertainties are indicated with the brackets (w. unc.).

Cross section variables	dof	χ^2		
		POW+PYT (w. unc.)	FxFx+PYT	POW+HER
$[\lvert y(t)\rvert,\ p_T(t)]$	16	44 (28)	68	27
$[m(t\bar{t}),\ p_T(t)]$	9	103 (37)	151	46
$[p_T(t),\ p_T(t\bar{t})]$	16	44 (21)	68	64
$[m(t\bar{t}),\ \lvert y(t\bar{t})\rvert]$	16	86 (41)	77	81
$[\lvert y(t\bar{t})\rvert,\ p_T(t\bar{t})]$	16	32 (19)	41	66
$[m(t\bar{t}),\ p_T(t\bar{t})]$	16	69 (37)	57	112
$[p_T(t\bar{t}),\ m(t\bar{t}),\ \lvert y(t\bar{t})\rvert]$	48	133 (69)	130	170
$[m(t\bar{t}),\ \lvert y(t)\rvert]$	16	64 (27)	75	37
$[m(t\bar{t}),\ \lvert\Delta\eta(t,\bar{t})\rvert]$	12	174 (32)	220	114
$[m(t\bar{t}),\ \lvert\Delta\phi(t,\bar{t})\rvert]$	12	80 (44)	41	98

Table 17: The χ^2 values and dof of the measured absolute single-differential cross sections for lepton and b-jet kinematic observables at the particle level are shown with respect to the predictions of various MC generators. The χ^2 values are calculated taking only measurement uncertainties into account and excluding theory uncertainties. For POW+PYT, the χ^2 values including theory uncertainties are indicated with the brackets (w. unc.).

Cross section variables	dof	χ^2		
		POW+PYT (w. unc.)	FxFx+PYT	POW+HER
$p_{\mathrm{T}}(\ell)$	12	32 (19)	62	21
$p_{\mathrm{T}}(\ell)$ trailing/$p_{\mathrm{T}}(\ell)$ leading	10	16 (11)	27	7
$p_{\mathrm{T}}(\ell)/p_{\mathrm{T}}(\bar{\mathrm{t}})$	5	20 (17)	28	14
$p_{\mathrm{T}}(\mathrm{b})$ leading	10	6 (5)	31	8
$p_{\mathrm{T}}(\mathrm{b})$ trailing	7	7 (5)	26	7
$(p_{\mathrm{T}}(\mathrm{b}) + p_{\mathrm{T}}(\bar{\mathrm{b}}))/(p_{\mathrm{T}}(\mathrm{t}) + p_{\mathrm{T}}(\bar{\mathrm{t}}))$	4	24 (19)	30	21
$m(\ell\bar{\ell})$	12	31 (25)	29	23
$m(\mathrm{b}\bar{\mathrm{b}})$	7	21 (16)	17	15
$m(\ell\bar{\ell}\mathrm{b}\bar{\mathrm{b}})$	19	36 (19)	30	27
$p_{\mathrm{T}}(\ell\bar{\ell})$	9	4 (3)	17	10
$\lvert\eta(\ell\bar{\ell})\rvert$	14	16 (10)	22	12
$[\lvert\eta(\ell\bar{\ell})\rvert, m(\ell\bar{\ell})]$	24	55 (29)	76	35
$[\lvert\eta(\ell\bar{\ell})\rvert, p_{\mathrm{T}}(\ell\bar{\ell})]$	20	30 (15)	84	24
$[p_{\mathrm{T}}(\ell\bar{\ell}), m(\ell\bar{\ell})]$	30	50 (39)	88	52

Table 18: The χ^2 values and dof of the measured absolute differential cross sections as a function of the additional-jet multiplicity in the events, at the parton level of the top quark and antiquark, are shown with respect to the predictions of various MC generators. The χ^2 values are calculated taking only measurement uncertainties into account and excluding theory uncertainties. For POW+PYT, the χ^2 values including theory uncertainties are indicated with the brackets (w. unc.).

Cross section variables	dof	χ^2		
		POW+PYT (w. unc.)	FxFx+PYT	POW+HER
$N_{\text{jet}}(p_{\text{T}} > 40\,\text{GeV})$	6	7 (5)	288	258
$N_{\text{jet}}(p_{\text{T}} > 100\,\text{GeV})$	5	41 (11)	46	77
$[N_{\text{jet}},\, p_{\text{T}}(\text{t})]$	9	31 (17)	163	137
$[N_{\text{jet}},\, \lvert y(\text{t})\rvert]$	12	42 (32)	131	85
$[N_{\text{jet}},\, p_{\text{T}}(\text{t}\bar{\text{t}})]$	12	58 (43)	192	93
$[N_{\text{jet}},\, m(\text{t}\bar{\text{t}})]$	12	62 (48)	177	154
$[N_{\text{jet}},\, \lvert y(\text{t}\bar{\text{t}})\rvert]$	12	14 (7)	122	61
$[N_{\text{jet}},\, \lvert \Delta\eta(\text{t},\bar{\text{t}})\rvert]$	9	94 (40)	194	144
$[N_{\text{jet}}^{0,1+},\, m(\text{t}\bar{\text{t}}),\, \lvert y(\text{t}\bar{\text{t}})\rvert]$	24	54 (39)	75	93
$[N_{\text{jet}}^{0,1,2+},\, m(\text{t}\bar{\text{t}}),\, \lvert y(\text{t}\bar{\text{t}})\rvert]$	36	93 (63)	223	215
$[N_{\text{jet}}^{0,1,2,3+},\, m(\text{t}\bar{\text{t}}),\, \lvert y(\text{t}\bar{\text{t}})\rvert]$	48	135 (92)	445	471

Table 19: The χ^2 values and dof of the measured absolute differential cross sections as a function of the additional-jet multiplicity in the events, at the particle level of the top quark and antiquark, are shown with respect to the predictions of various MC generators. The χ^2 values are calculated taking only measurement uncertainties into account and excluding theory uncertainties. For POW+PYT, the χ^2 values including theory uncertainties are indicated with the brackets (w. unc.).

Cross section variables	dof	χ^2		
		POW+PYT (w. unc.)	FxFx+PYT	POW+HER
$N_{\text{jet}}(p_{\text{T}} > 40\,\text{GeV})$	6	7 (4)	355	8
$N_{\text{jet}}(p_{\text{T}} > 100\,\text{GeV})$	5	45 (11)	40	7
$[N_{\text{jet}},\, p_{\text{T}}(\text{t})]$	9	37 (15)	249	25
$[N_{\text{jet}},\, \lvert y(\text{t})\rvert]$	12	44 (26)	182	27
$[N_{\text{jet}},\, p_{\text{T}}(\text{t}\bar{\text{t}})]$	12	67 (41)	341	86
$[N_{\text{jet}},\, m(\text{t}\bar{\text{t}})]$	12	60 (40)	302	50
$[N_{\text{jet}},\, \lvert y(\text{t}\bar{\text{t}})\rvert]$	12	17 (6)	188	8
$[N_{\text{jet}},\, \lvert \Delta\eta(\text{t},\bar{\text{t}})\rvert]$	9	138 (43)	306	103
$[N_{\text{jet}}^{0,1+},\, m(\text{t}\bar{\text{t}}),\, \lvert y(\text{t}\bar{\text{t}})\rvert]$	24	85 (46)	101	87
$[N_{\text{jet}}^{0,1,2+},\, m(\text{t}\bar{\text{t}}),\, \lvert y(\text{t}\bar{\text{t}})\rvert]$	36	144 (71)	401	137
$[N_{\text{jet}}^{0,1,2,3+},\, m(\text{t}\bar{\text{t}}),\, \lvert y(\text{t}\bar{\text{t}})\rvert]$	48	176 (97)	736	161

B.2 Comparisons to higher-order theoretical predictions

The absolute differential cross sections comparing data to theoretical predictions of beyond-NLO precision are shown in Figs. 98–120, and the corresponding χ^2 values are given in Tables 20–24. The p-values of the χ^2 tests are presented in Tables 44–48. The theoretical calculations are those discussed in Section 9.4: aN^{3}LO, STRIPPER (NNLO), MATRIX (NNLO), and MINNLOPS (NNLOPS). Comparing the absolute cross sections to the normalized ones in Section 9.4, one can see a similar level of agreement between data and predictions. We conclude that the calculations provide overall reasonable predictions of the total normalization of the data.

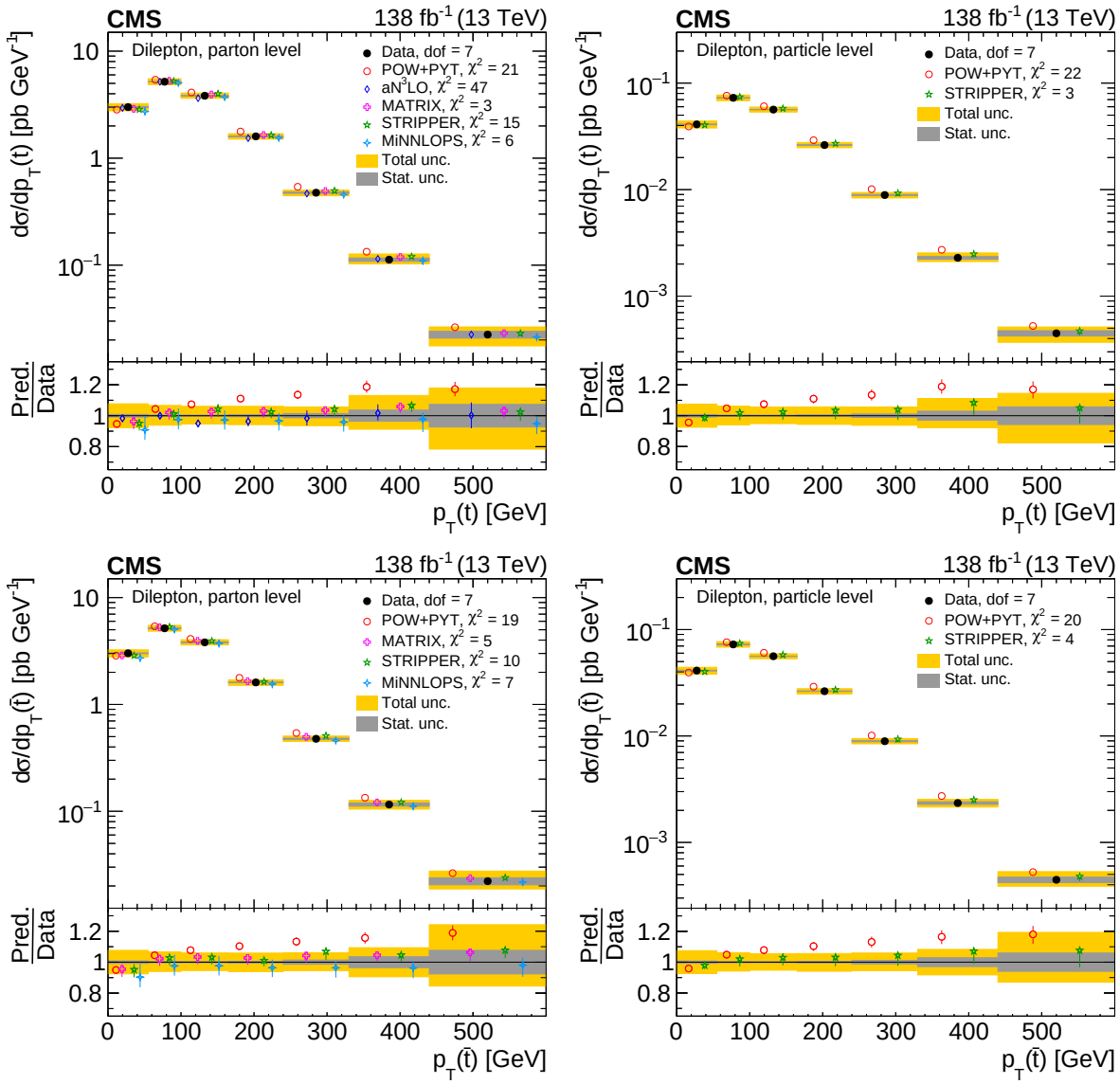

Figure 98: Absolute differential $t\bar{t}$ production cross sections as functions of $p_T(t)$ (upper) and $p_T(\bar{t})$ (lower), measured at the parton level in the full phase space (left) and at the particle level in a fiducial phase space (right). The data are shown as filled circles with grey and yellow bands indicating the statistical and total uncertainties (statistical and systematic uncertainties added in quadrature), respectively. For each distribution, the number of degrees of freedom (dof) is also provided. The cross sections are compared to predictions from the POWHEG+PYTHIA 8 ('POW-PYT', open circles) simulation and various theoretical predictions with beyond-NLO precision (other points). The estimated uncertainties in the predictions are represented by a vertical bar on the corresponding points. For each model, a value of χ^2 is reported that takes into account the measurement uncertainties. The lower panel in each plot shows the ratios of the predictions to the data.

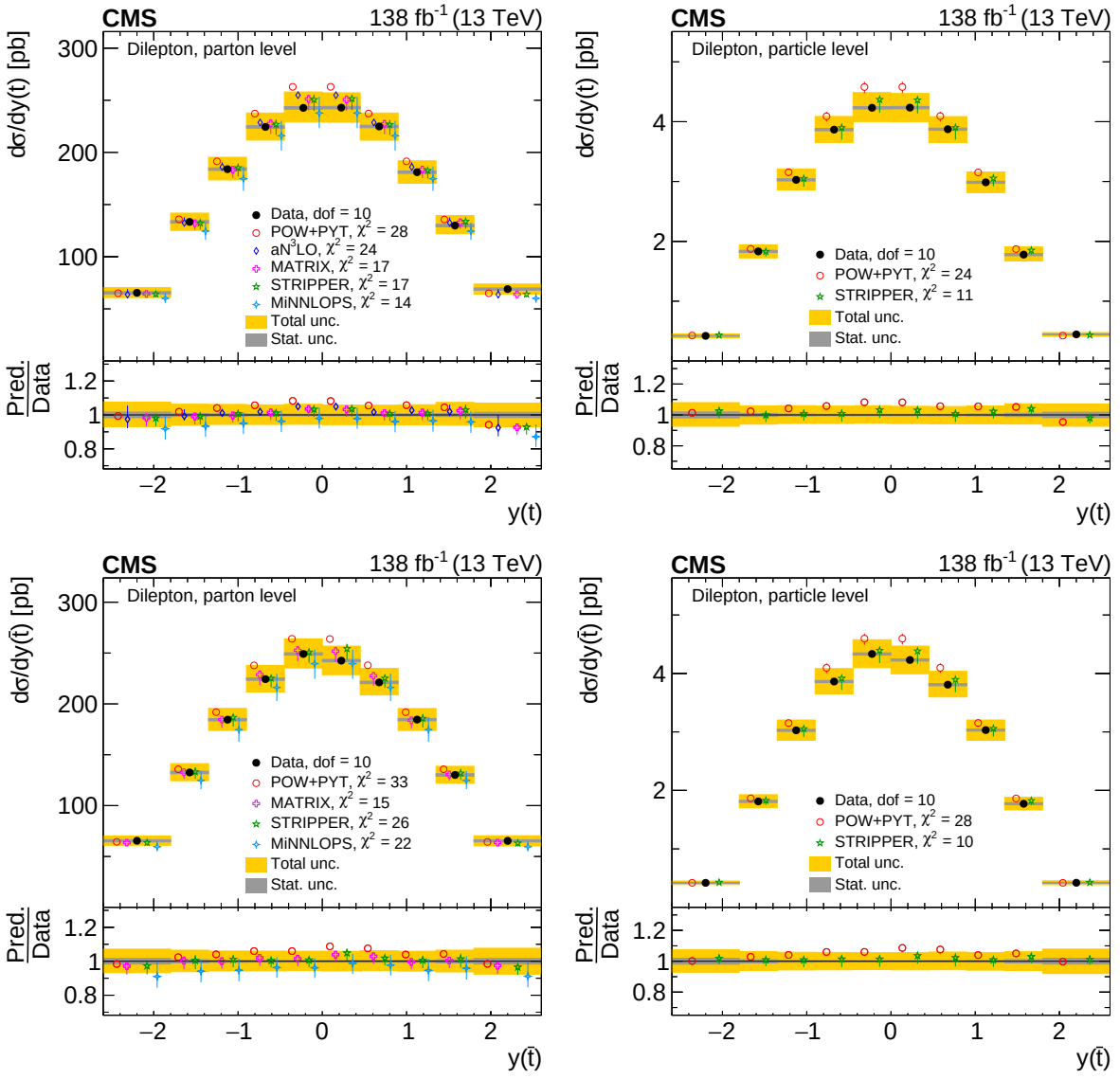

Figure 99: Absolute differential $t\bar{t}$ production cross sections as functions of $y(t)$ (upper) and $y(\bar{t})$ (lower) are shown for data (filled circles), POWHEG+PYTHIA 8 ('POW-PYT', open circles) simulation, and various theoretical predictions with beyond-NLO precision (other points). Further details can be found in the caption of Fig. 98.

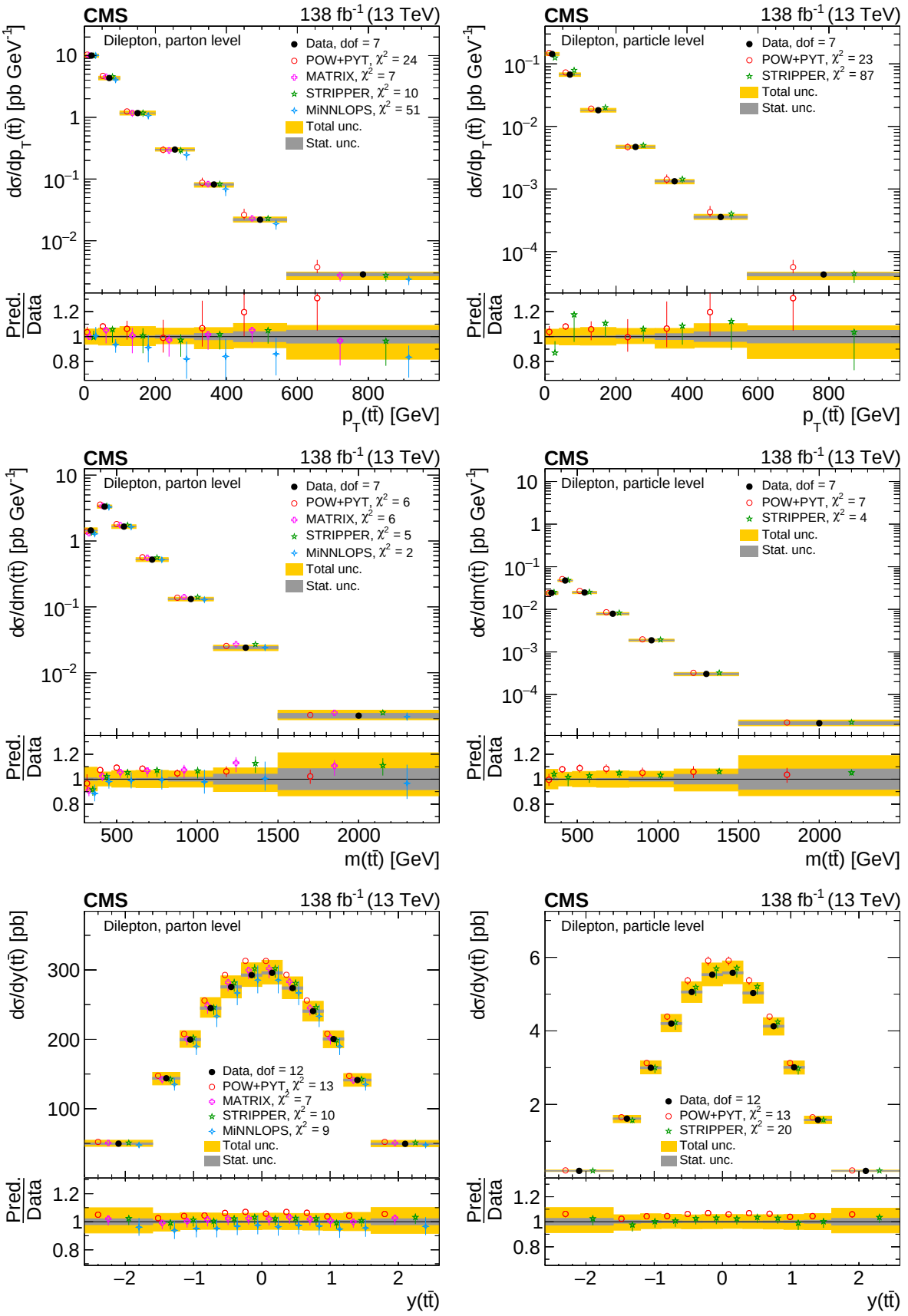

Figure 100: Absolute differential $t\bar{t}$ production cross sections as functions of $p_T(t\bar{t})$ (upper), $m(t\bar{t})$ (middle), and $y(t\bar{t})$ (lower) are shown for data (filled circles), POWHEG+PYTHIA8 ('POW-PYT', open circles) simulation, and various theoretical predictions with beyond-NLO precision (other points). Further details can be found in the caption of Fig. 98.

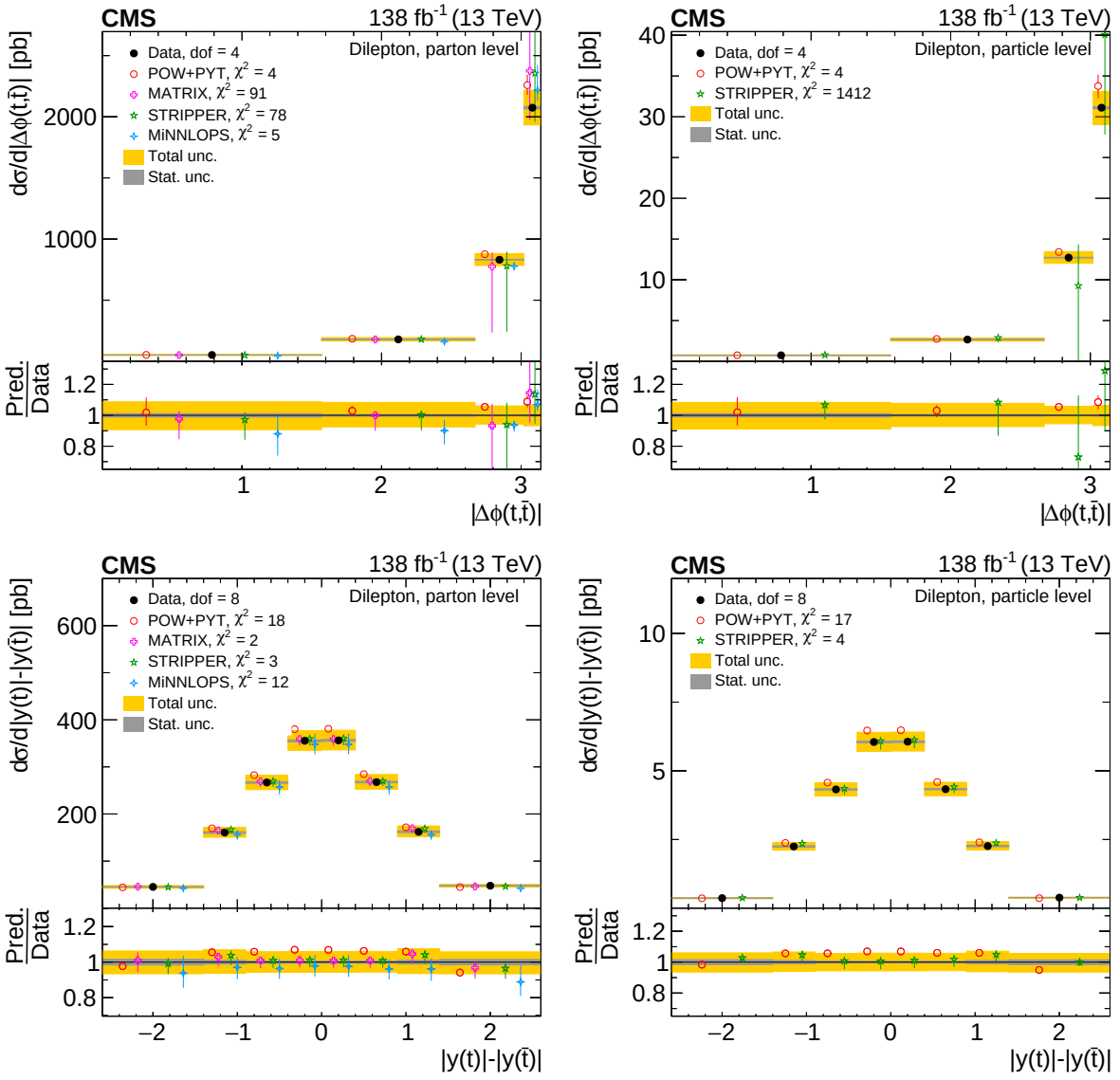

Figure 101: Absolute differential $\mathrm{t\bar{t}}$ production cross sections as functions of $|\Delta\phi(\mathrm{t},\bar{\mathrm{t}})|$ (upper) and $|y(\mathrm{t})| - |y(\bar{\mathrm{t}})|$ (lower) are shown for data (filled circles), POWHEG+PYTHIA 8 ('POW-PYT', open circles) simulation, and various theoretical predictions with beyond-NLO precision (other points). Further details can be found in the caption of Fig. 98.

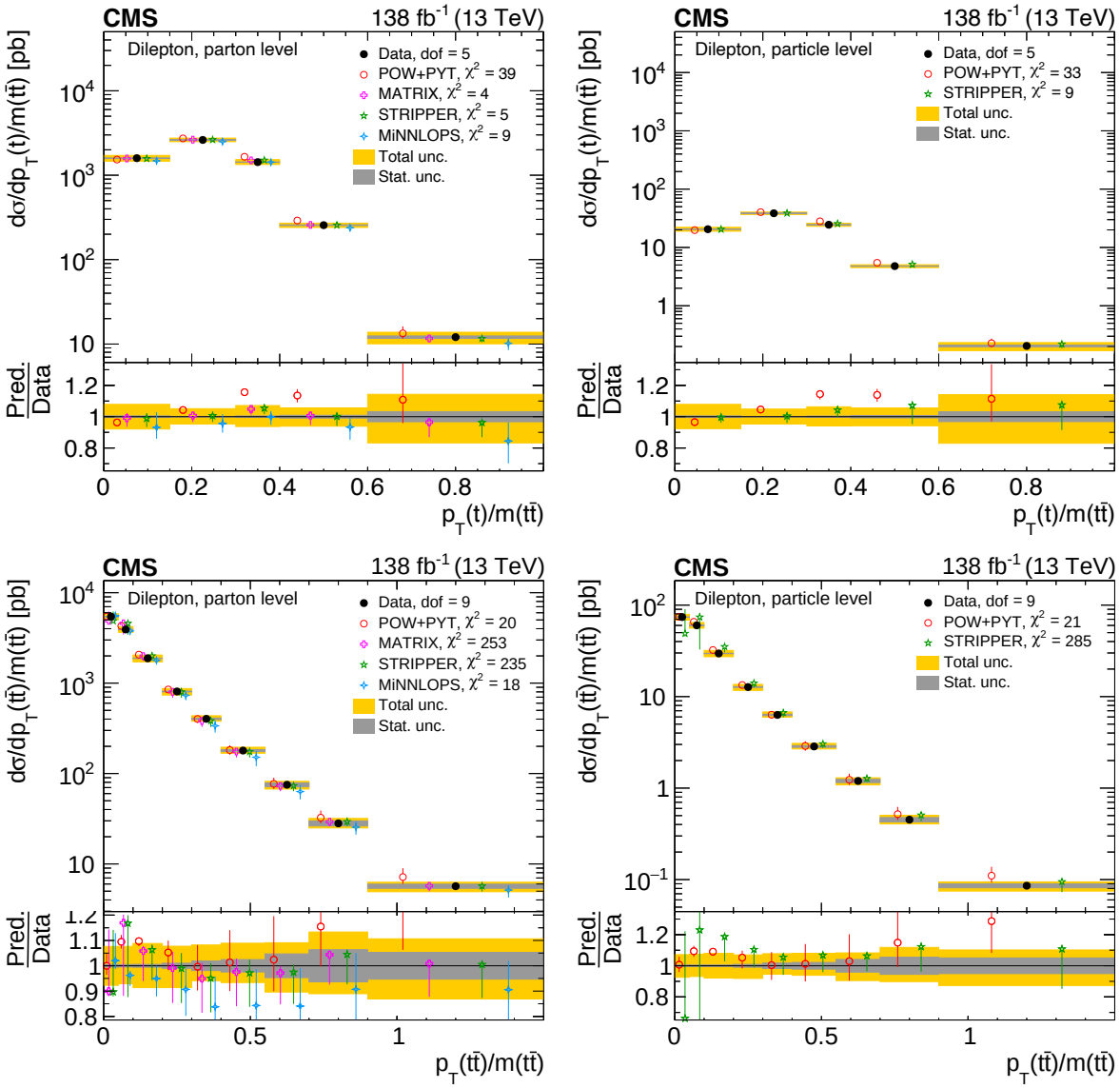

Figure 102: Absolute differential $t\bar{t}$ production cross sections as functions of $p_T(t)/m(t\bar{t})$ (upper) and $p_T(t\bar{t})/m(t\bar{t})$ (lower) are shown for data (filled circles), POWHEG+PYTHIA 8 ('POWPYT', open circles) simulation, and various theoretical predictions with beyond-NLO precision (other points). Further details can be found in the caption of Fig. 98.

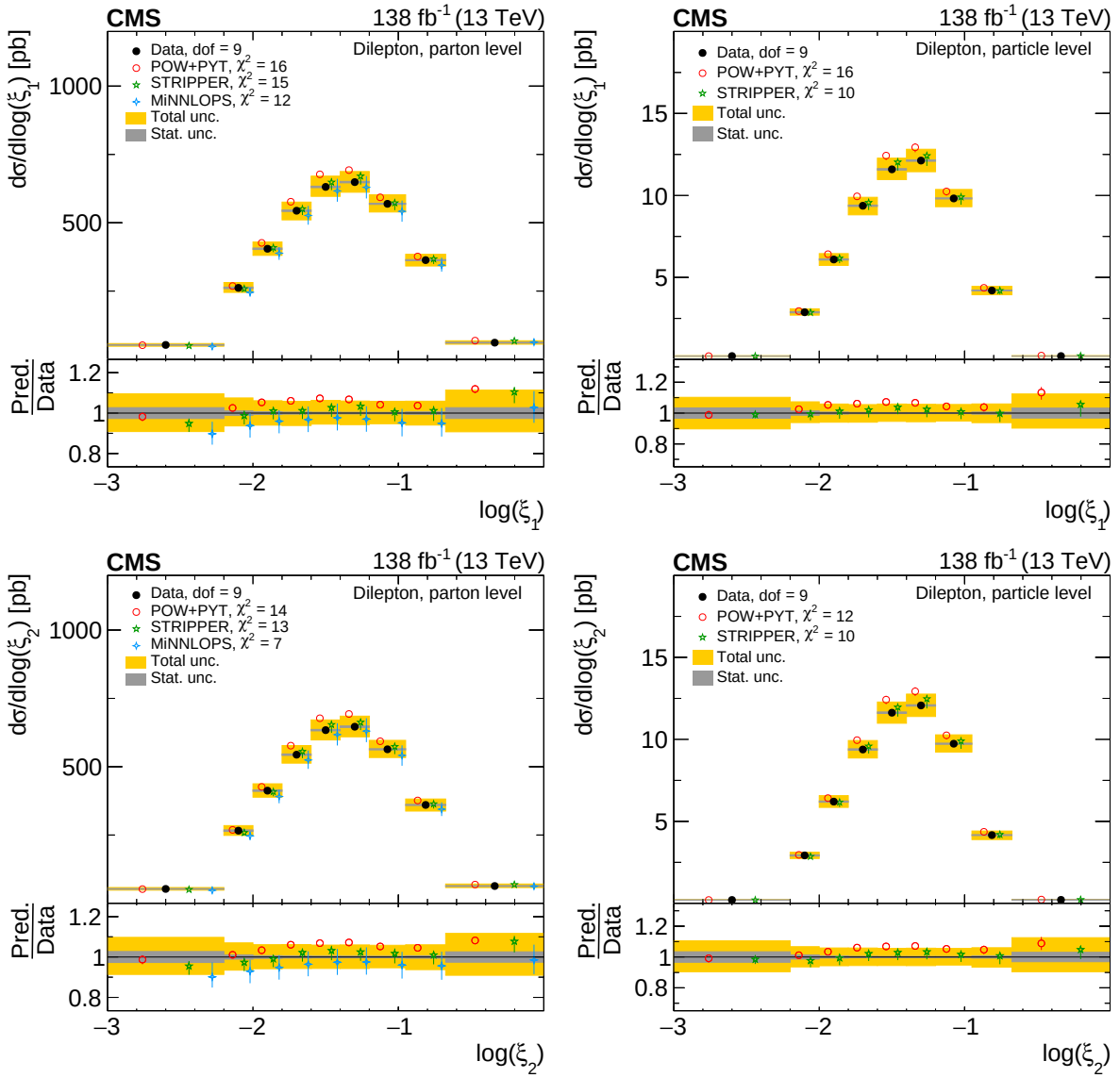

Figure 103: Absolute differential $\mathrm{t\bar{t}}$ production cross sections as functions of $\log(\xi_1)$ (upper) and $\log(\xi_2)$ (lower) are shown for data (filled circles), POWHEG+PYTHIA 8 ('POW-PYT', open circles) simulation, and STRIPPER NNLO calculation (stars). Further details can be found in the caption of Fig. 98.

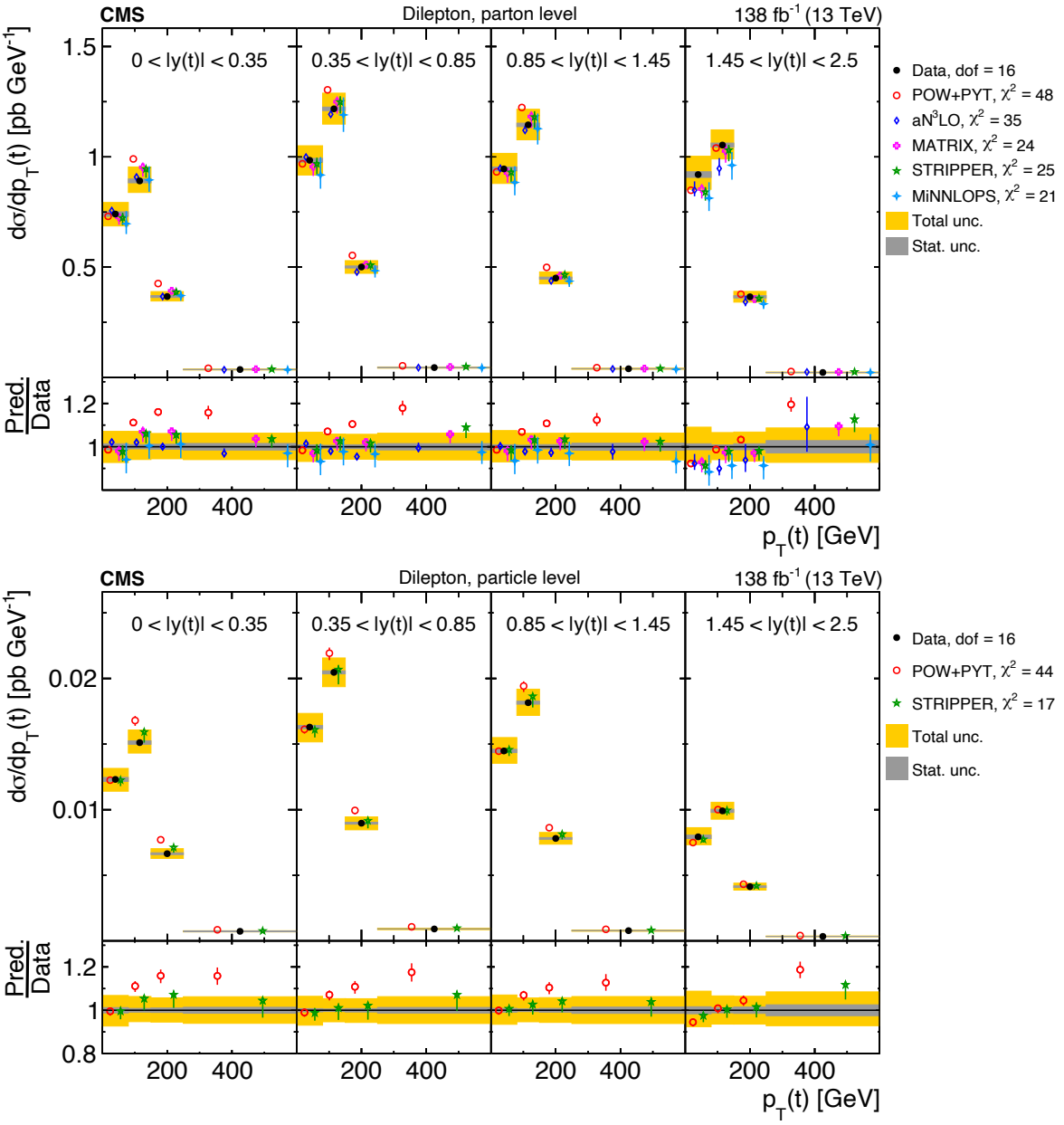

Figure 104: Absolute $[|y(t)|, p_T(t)]$ cross sections measured at the parton level in the full phase space (upper) and at the particle level in a fiducial phase space (lower). The data are shown as filled circles with grey and yellow bands indicating the statistical and total uncertainties (statistical and systematic uncertainties added in quadrature), respectively. For each distribution, the number of degrees of freedom (dof) is also provided. The cross sections are compared to predictions from the POWHEG+PYTHIA8 ('POW-PYT', open circles) simulation and various theoretical predictions with beyond-NLO precision (other points). The estimated uncertainties in the predictions are represented by a vertical bar on the corresponding points. For each model, a value of χ^2 is reported that takes into account the measurement uncertainties. The lower panel in each plot shows the ratios of the predictions to the data.

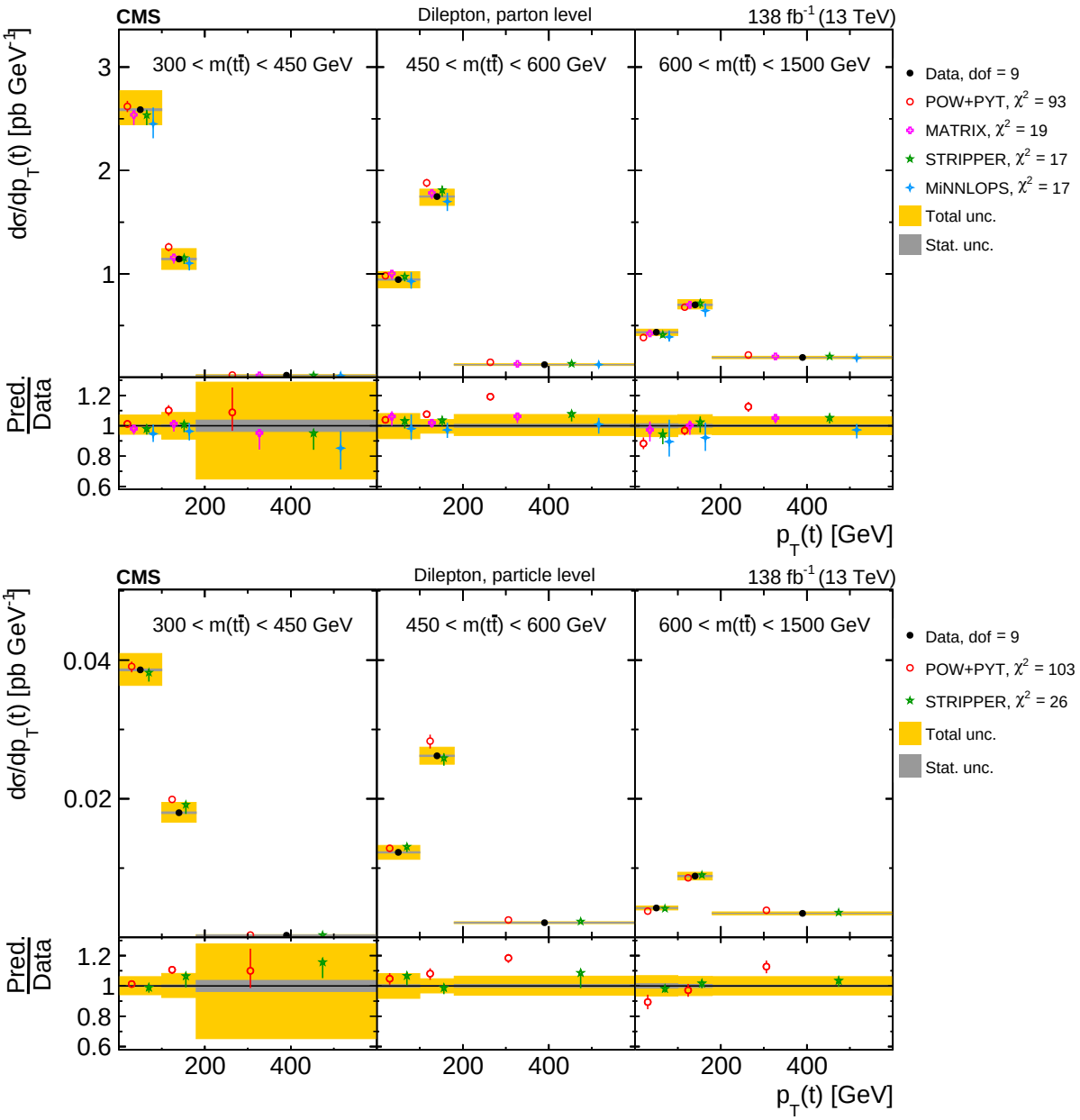

Figure 105: Absolute $[m(\mathrm{t\bar{t}}), p_{\mathrm{T}}(\mathrm{t})]$ cross sections are shown for data (filled circles), POWHEG+PYTHIA 8 ('POW-PYT', open circles) simulation, and various theoretical predictions with beyond-NLO precision (other points). Further details can be found in the caption of Fig. 104.

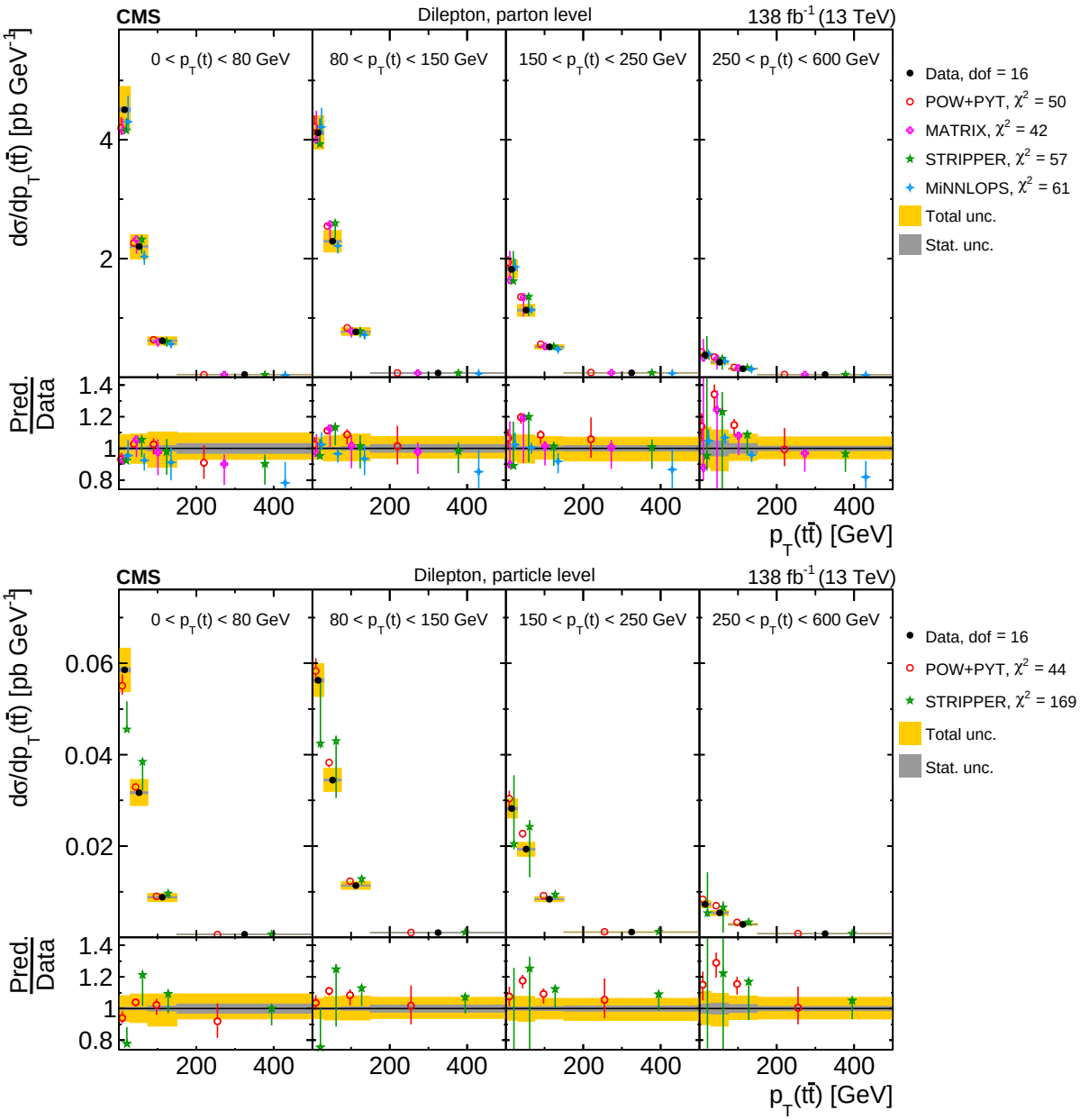

Figure 106: Absolute $[p_T(t), p_T(t\bar{t})]$ cross sections are shown for data (filled circles), POWHEG+PYTHIA 8 ('POW-PYT', open circles) simulation, and various theoretical predictions with beyond-NLO precision (other points). Further details can be found in the caption of Fig. 104.

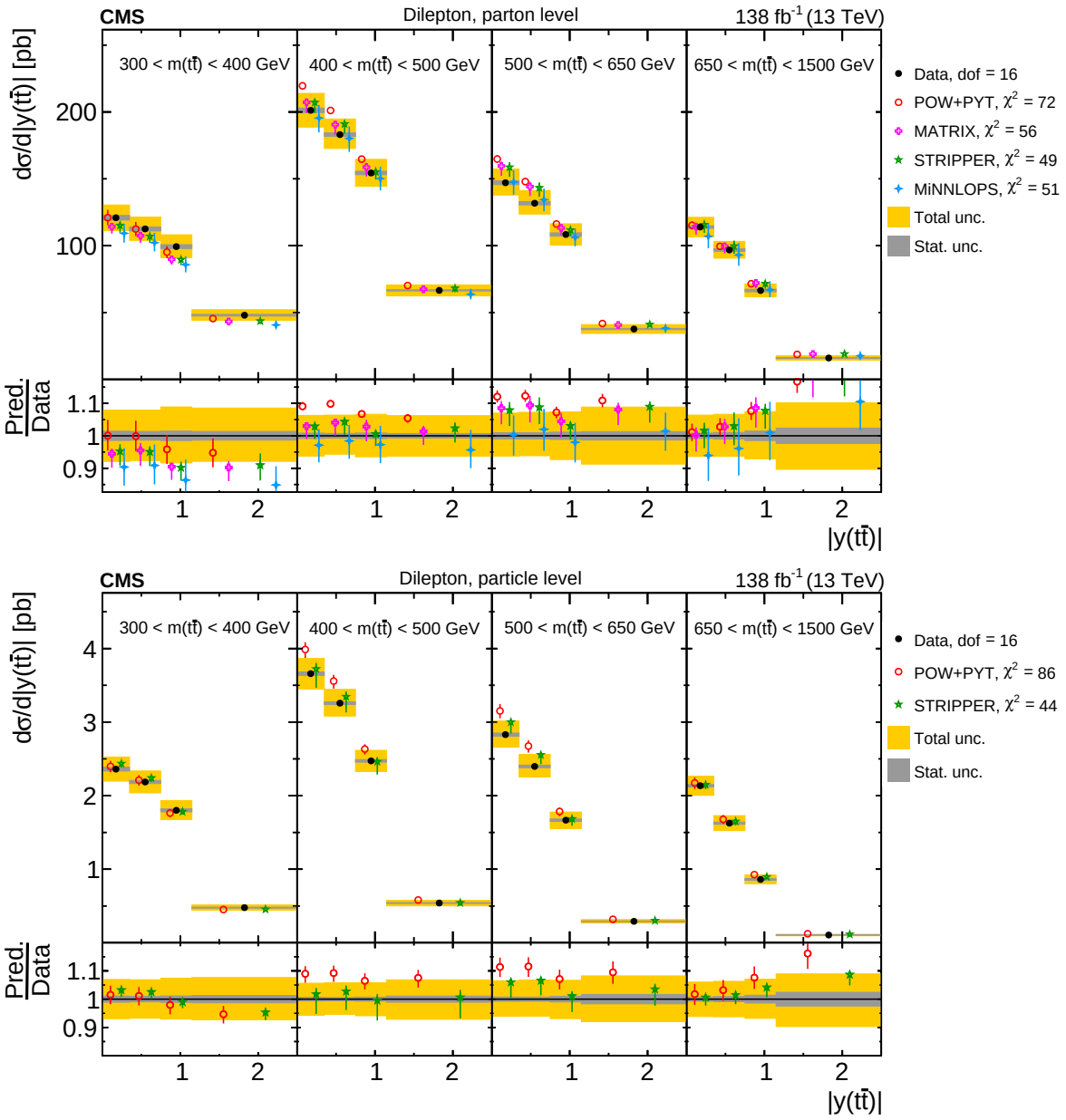

Figure 107: Absolute $[m(\mathrm{t\bar{t}}), |y(\mathrm{t\bar{t}})|]$ cross sections are shown for data (filled circles), POWHEG+PYTHIA 8 ('POW-PYT', open circles) simulation, and various theoretical predictions with beyond-NLO precision (other points). Further details can be found in the caption of Fig. 104.

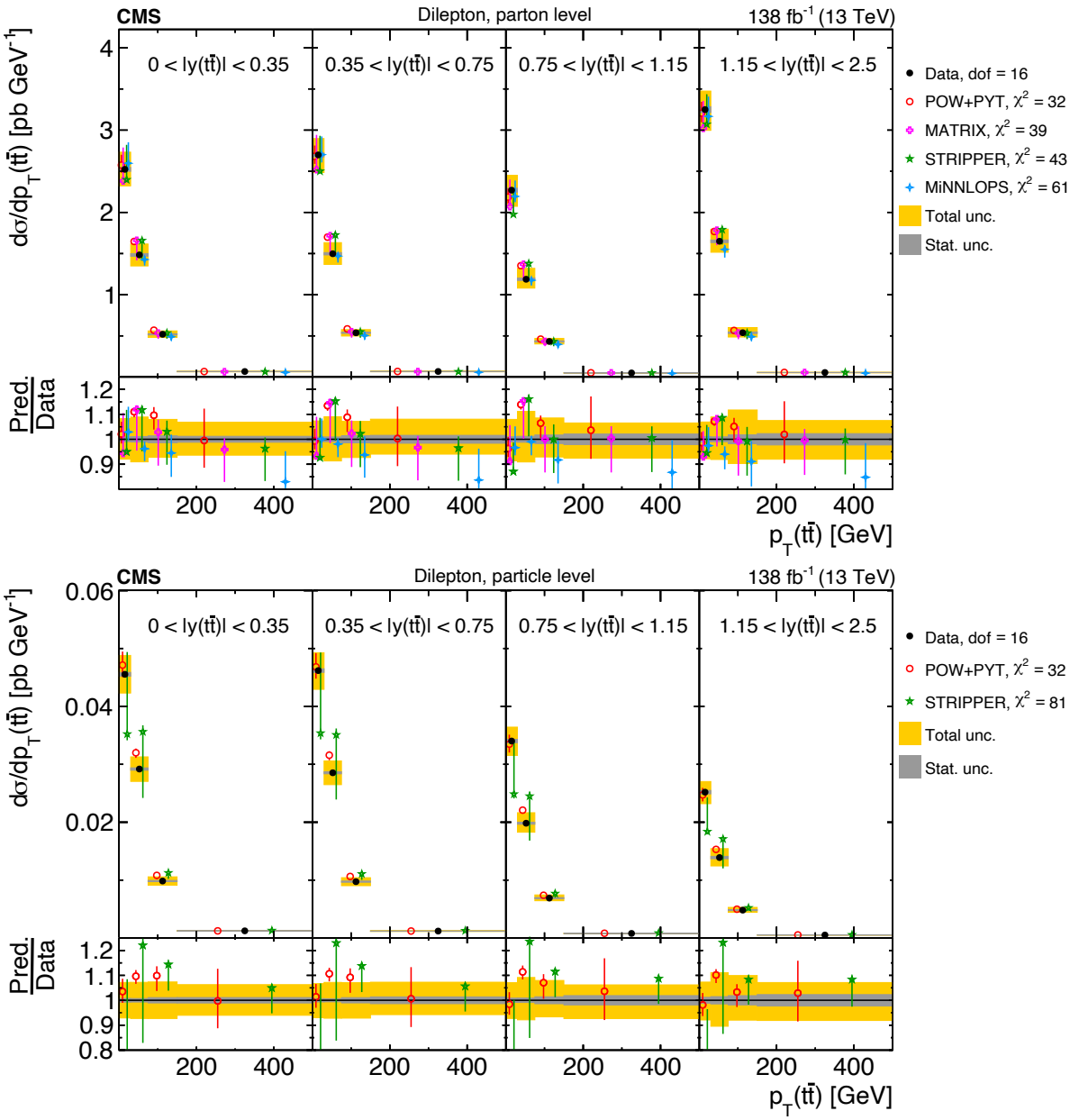

Figure 108: Absolute $[|y(\mathrm{t\bar{t}})|, p_{\mathrm{T}}(\mathrm{t\bar{t}})]$ cross sections are shown for data (filled circles), POWHEG+PYTHIA 8 ('POW-PYT', open circles) simulation, and various theoretical predictions with beyond-NLO precision (other points). Further details can be found in the caption of Fig. 104.

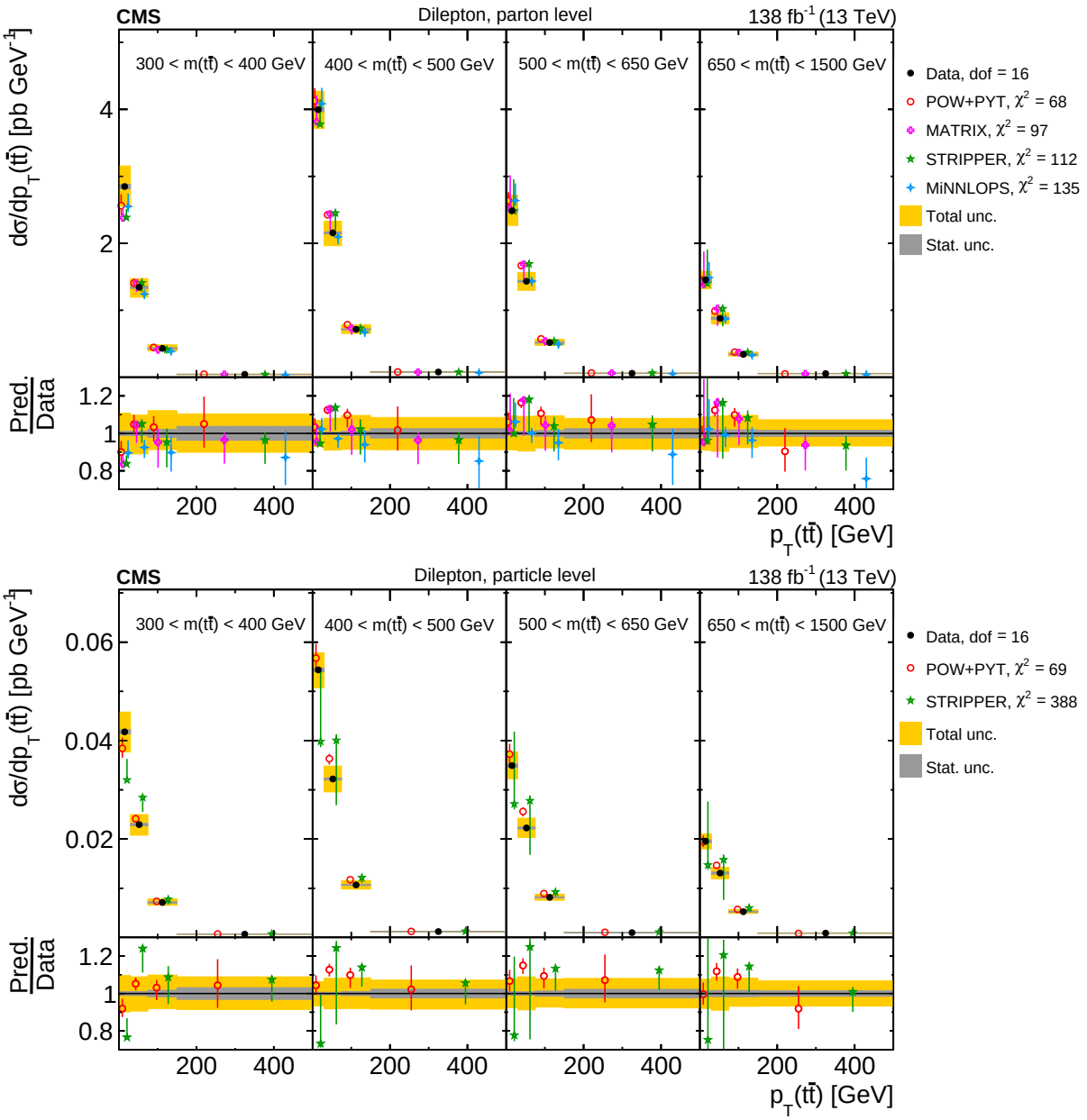

Figure 109: Absolute $[m(\mathrm{t\bar{t}}), p_{\mathrm{T}}(\mathrm{t\bar{t}})]$ cross sections are shown for data (filled circles), POWHEG+PYTHIA 8 ('POW-PYT', open circles) simulation, and various theoretical predictions with beyond-NLO precision (other points). Further details can be found in the caption of Fig. 104.

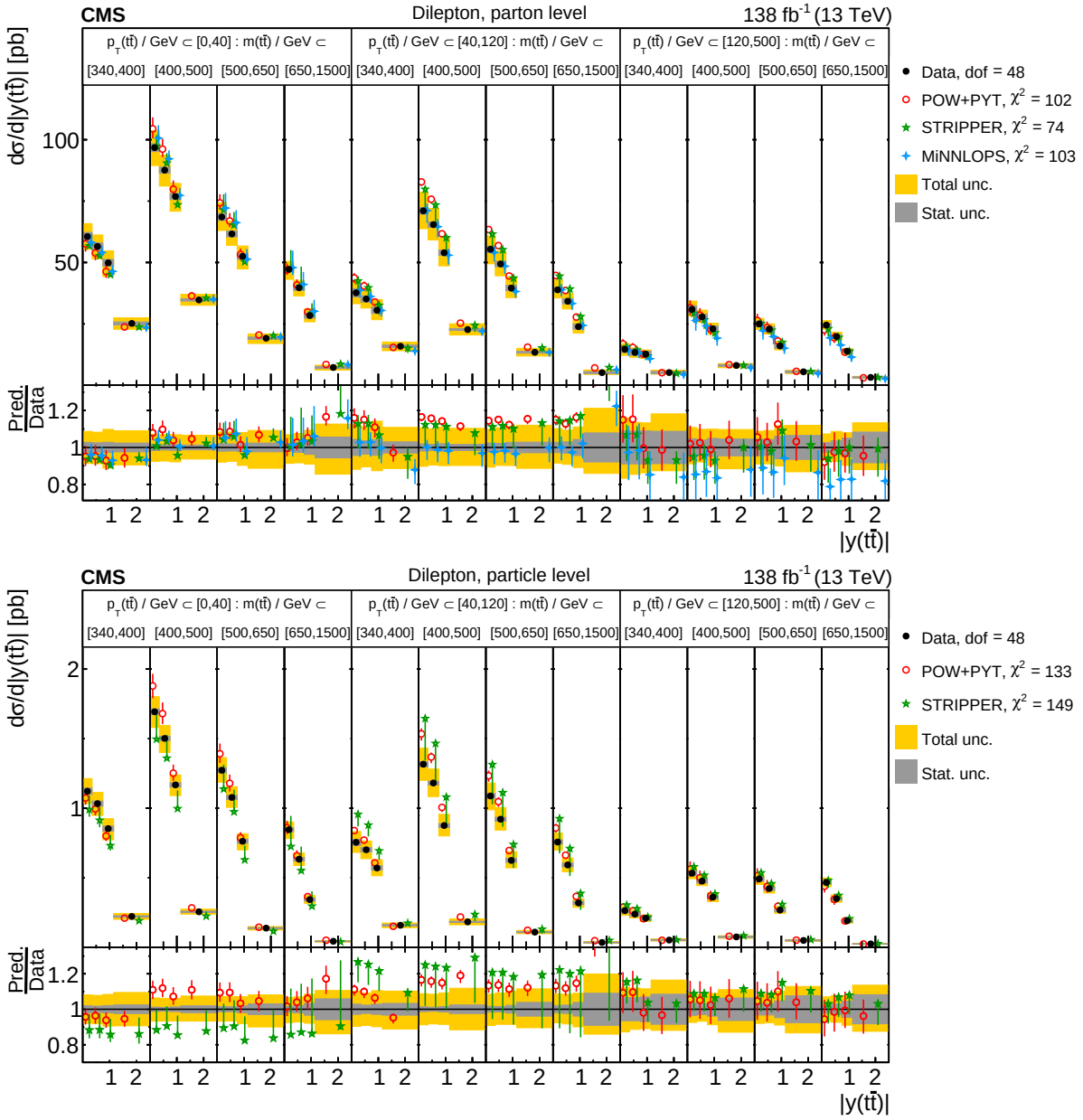

Figure 110: Absolute $[p_{\mathrm{T}}(\mathrm{t\bar{t}}), m(\mathrm{t\bar{t}}), |y(\mathrm{t\bar{t}})|]$ cross sections are shown for data (filled circles), POWHEG+PYTHIA 8 ('POW-PYT', open circles) simulation, and various theoretical predictions with beyond-NLO precision (other points). Further details can be found in the caption of Fig. 104.

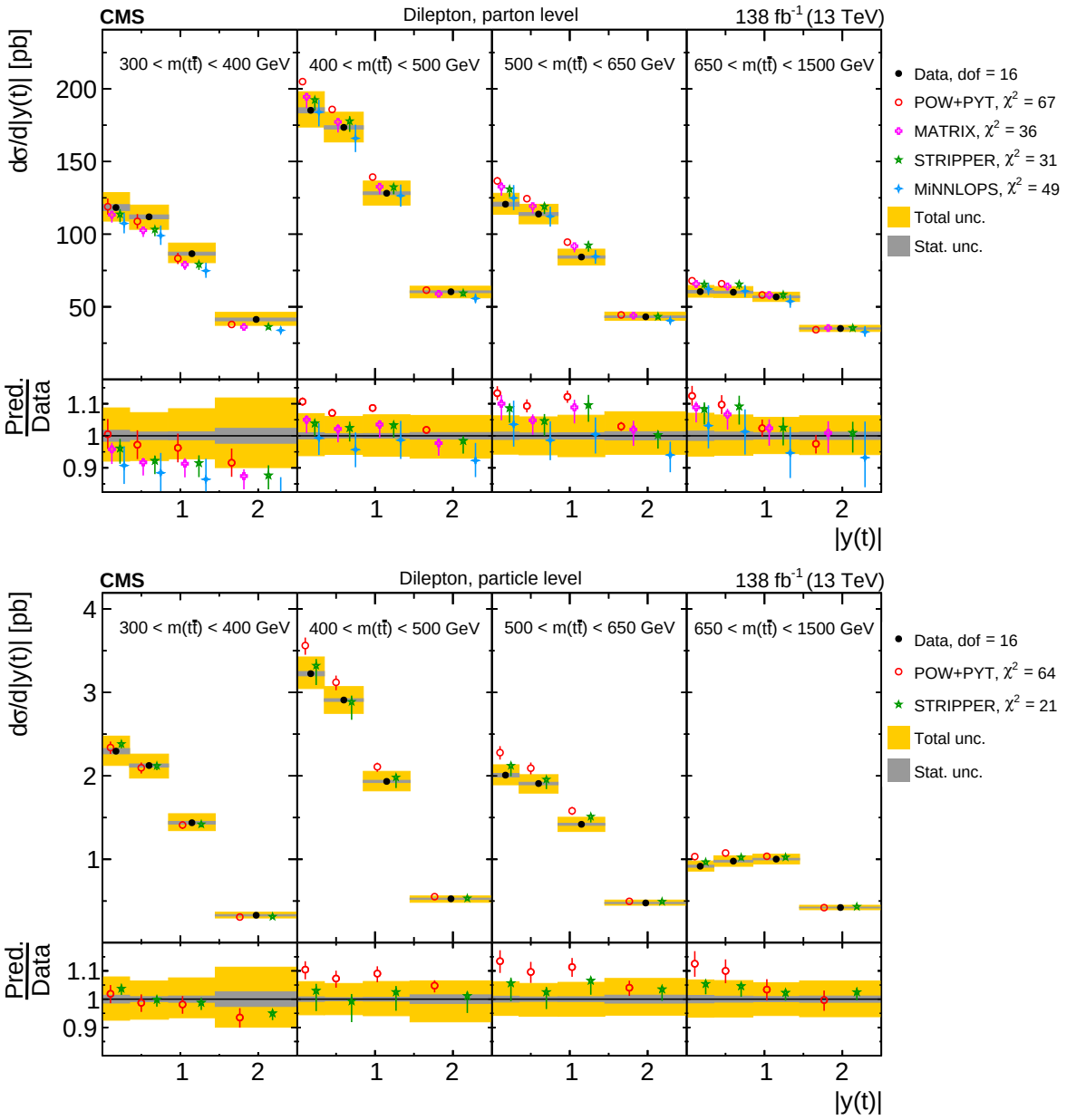

Figure 111: Absolute $[m(\mathrm{t\bar{t}}), |y(\mathrm{t})|]$ cross sections are shown for data (filled circles), POWHEG+PYTHIA 8 ('POW-PYT', open circles) simulation, and various theoretical predictions with beyond-NLO precision (other points). Further details can be found in the caption of Fig. 104.

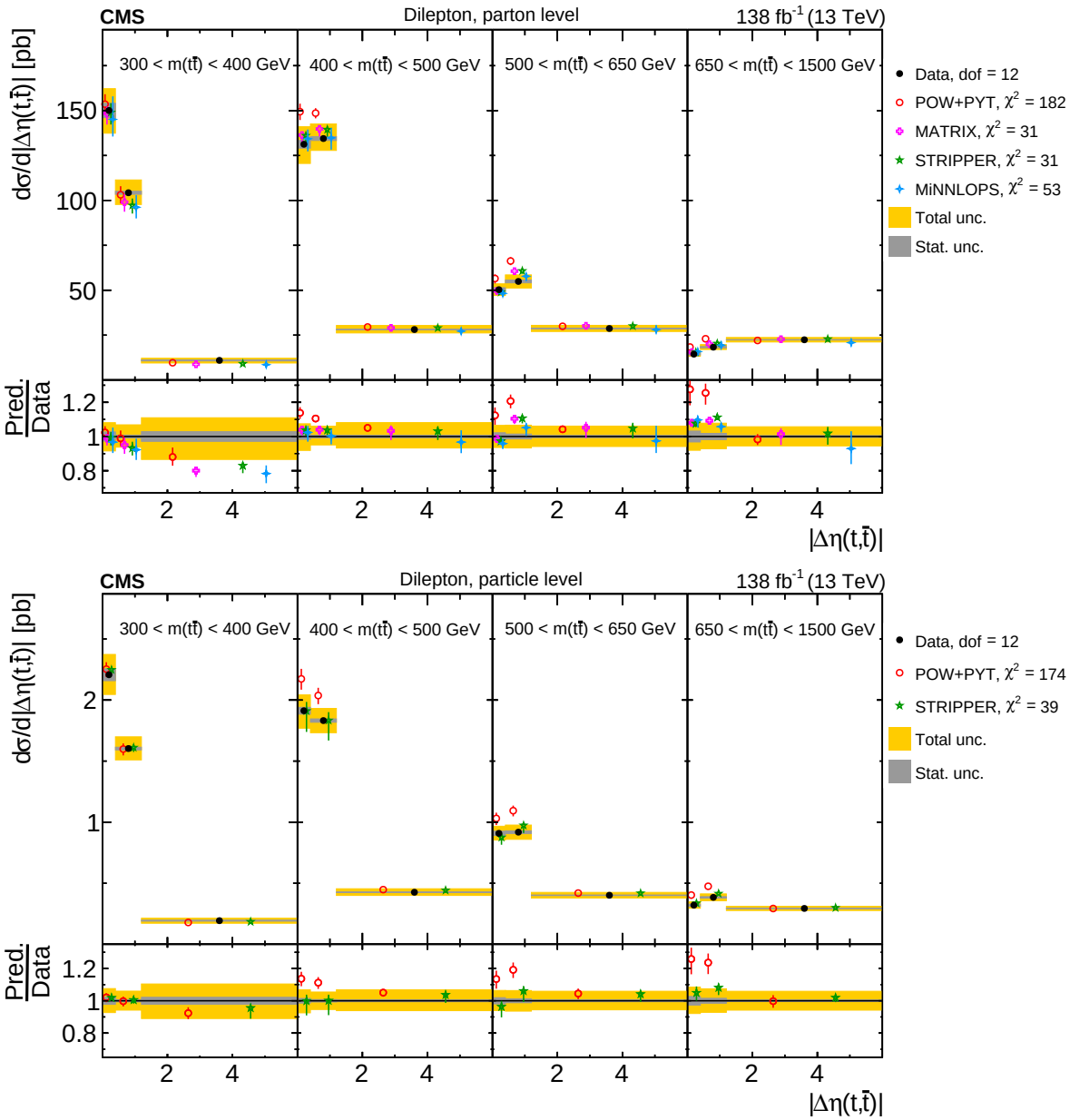

Figure 112: Absolute $[m(\mathrm{t\bar{t}}), |\Delta\eta(\mathrm{t},\bar{\mathrm{t}})|]$ cross sections are shown for data (filled circles), POWHEG+PYTHIA 8 ('POW-PYT', open circles) simulation, and various theoretical predictions with beyond-NLO precision (other points). Further details can be found in the caption of Fig. 104.

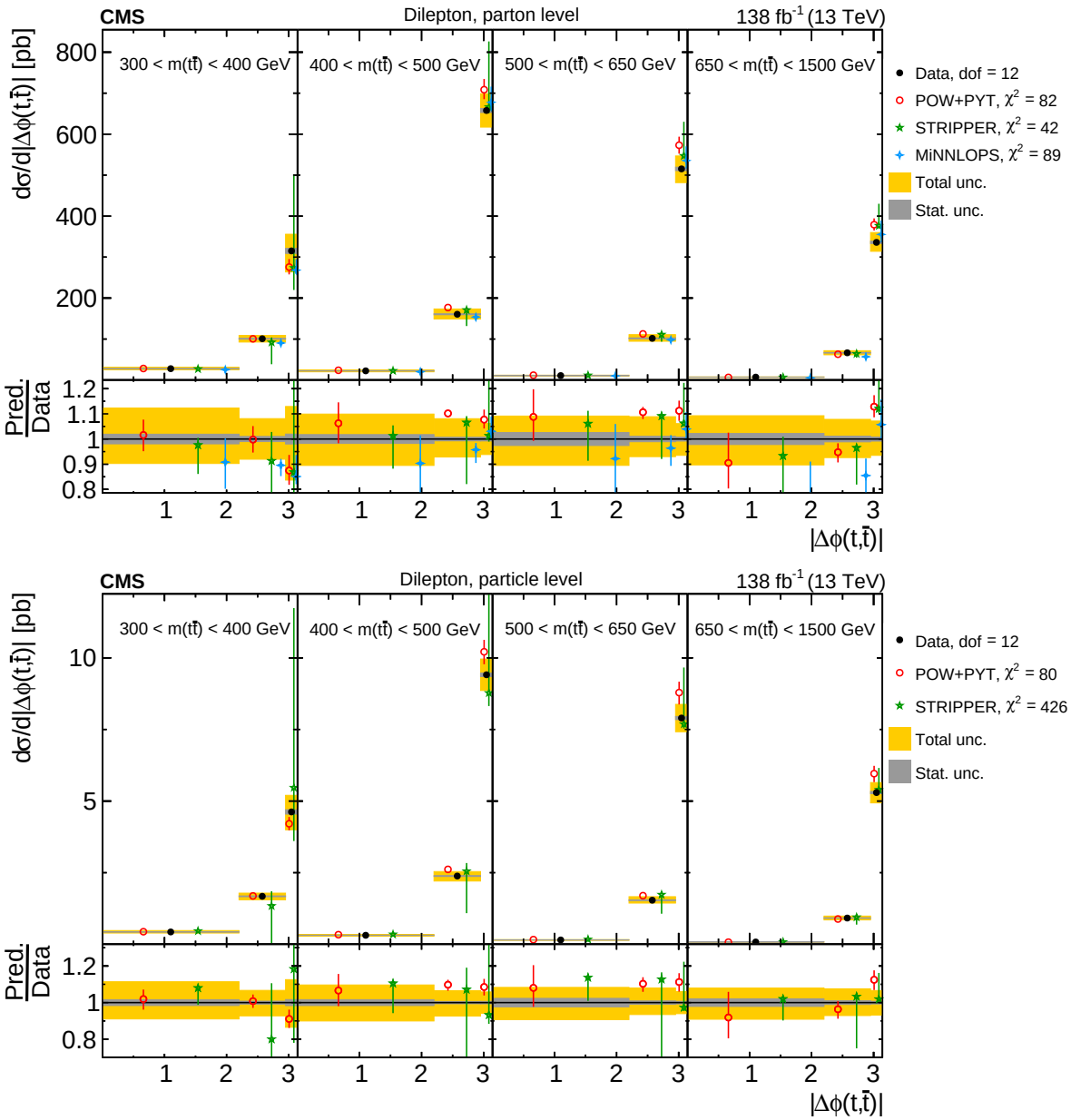

Figure 113: Absolute $[m(\mathrm{t\bar{t}}), |\Delta\phi(\mathrm{t},\bar{\mathrm{t}})|]$ cross sections are shown for data (filled circles), POWHEG+PYTHIA 8 ('POW-PYT', open circles) simulation, and various theoretical predictions with beyond-NLO precision (other points). Further details can be found in the caption of Fig. 104.

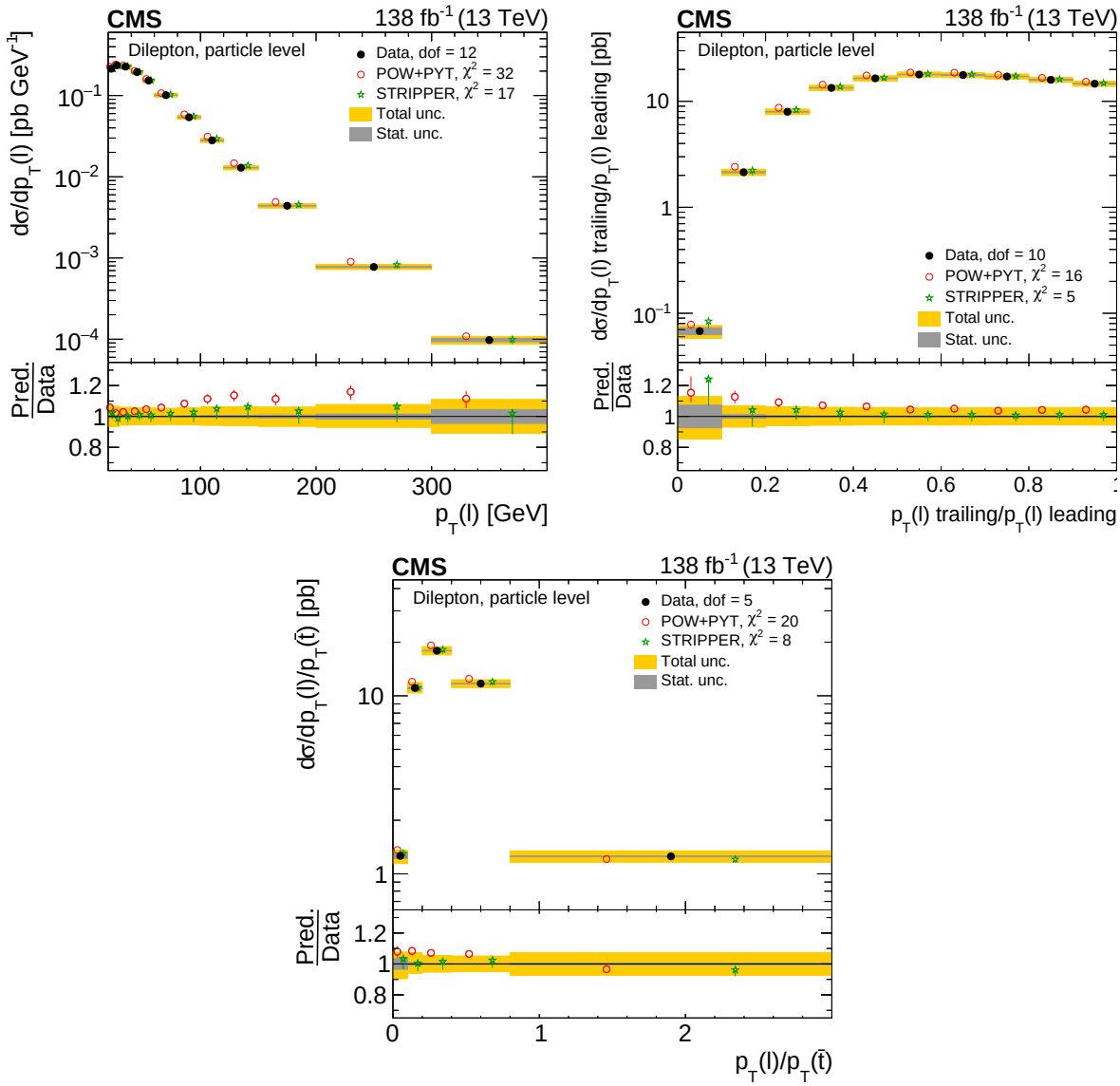

Figure 114: Absolute differential $t\bar{t}$ production cross sections as functions of p_T of the lepton (upper left), of the ratio of the trailing and leading lepton p_T (upper right), and of the ratio of lepton and top antiquark p_T (lower), measured at the particle level in a fiducial phase space. The data are shown as filled circles with grey and yellow bands indicating the statistical and total uncertainties (statistical and systematic uncertainties added in quadrature), respectively. For each distribution, the number of degrees of freedom (dof) is also provided. The cross sections are compared to predictions from the POWHEG+PYTHIA 8 ('POW-PYT', open circles) simulation and STRIPPER NNLO calculation (stars). The estimated uncertainties in the predictions are represented by a vertical bar on the corresponding points. For each model, a value of χ^2 is reported that takes into account the measurement uncertainties. The lower panel in each plot shows the ratios of the predictions to the data.

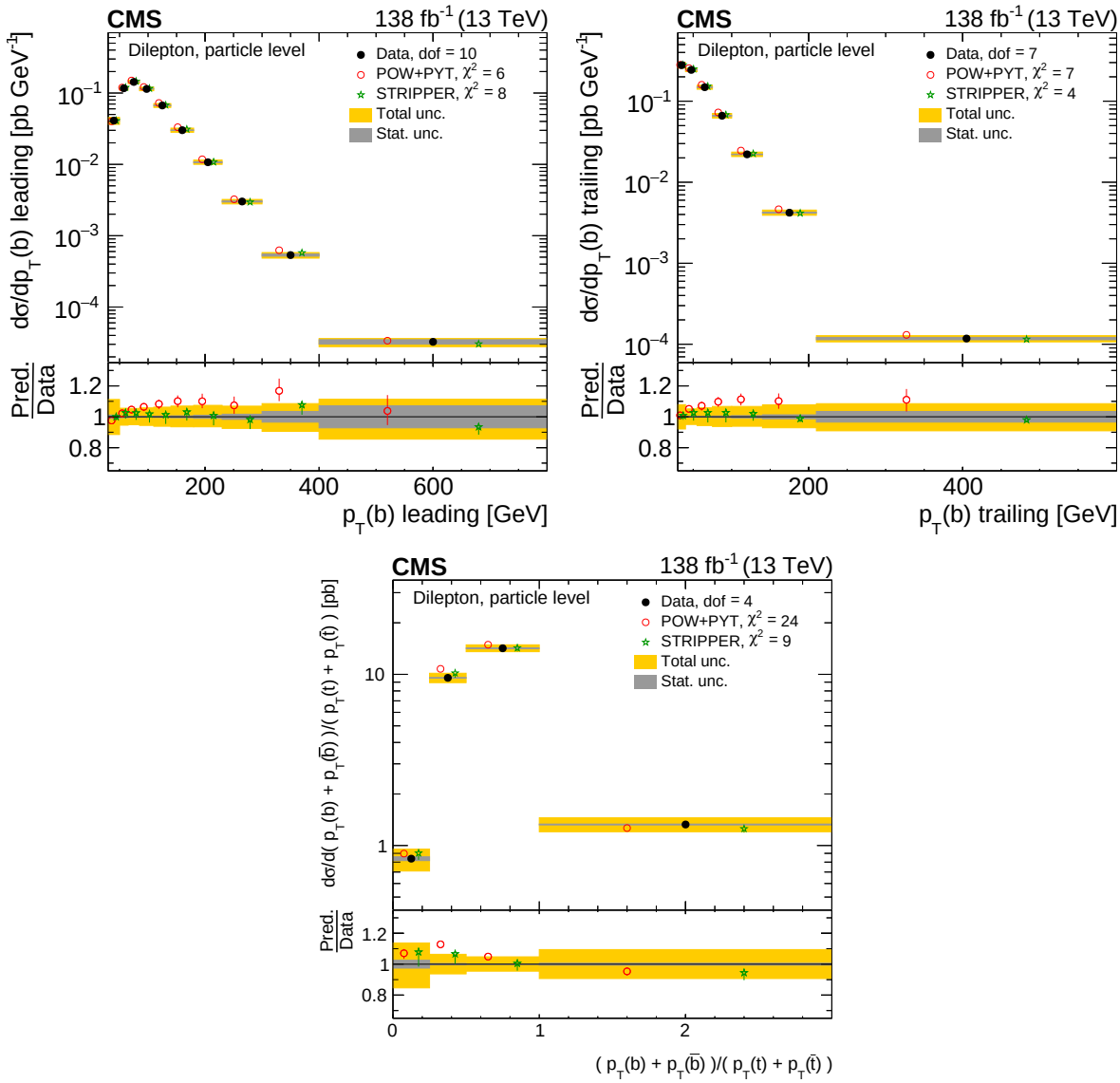

Figure 115: Absolute differential $\mathrm{t\bar{t}}$ production cross sections as functions of the p_{T} of the leading (upper left) and trailing (upper right) b jet, and $(p_{\mathrm{T}}(\mathrm{b}) + p_{\mathrm{T}}(\bar{\mathrm{b}}))/(p_{\mathrm{T}}(\mathrm{t}) + p_{\mathrm{T}}(\bar{\mathrm{t}}))$ (lower) d-NLO precision (other points). are shown for data (filled circles), POWHEG+PYTHIA 8 ('POWPYT', open circles) simulation, and STRIPPER NNLO calculation (stars). Further details can be found in the caption of Fig. 114.

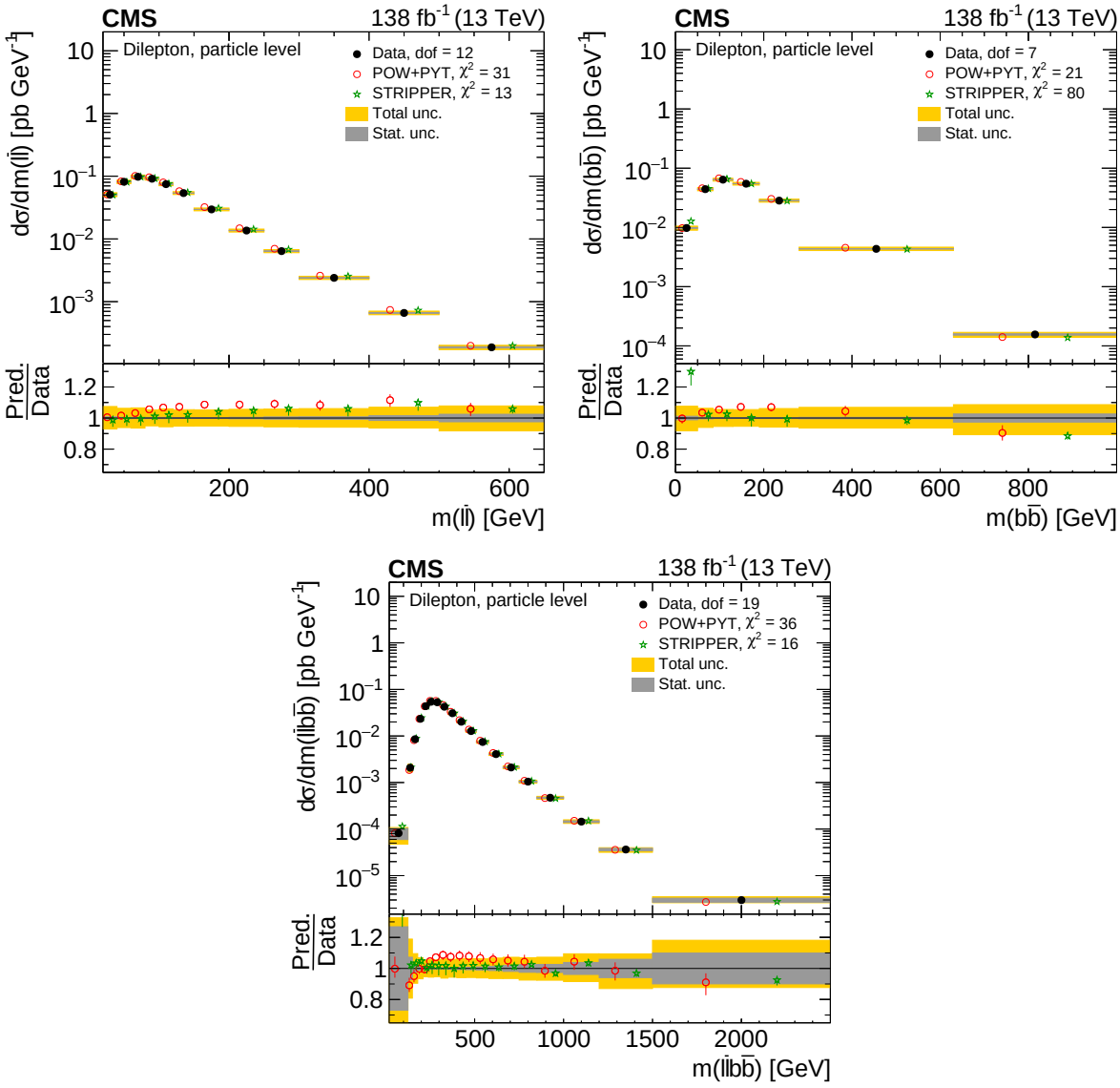

Figure 116: Absolute differential $\mathrm{t\bar{t}}$ production cross sections as functions of $m(\ell\bar{\ell})$ (upper left), $m(\mathrm{b\bar{b}})$ (upper right), and $m(\ell\bar{\ell}\mathrm{b\bar{b}})$ (lower) are shown for data (filled circles), POWHEG+PYTHIA 8 ('POW-PYT', open circles) simulation, and STRIPPER NNLO calculation (stars). Further details can be found in the caption of Fig. 114.

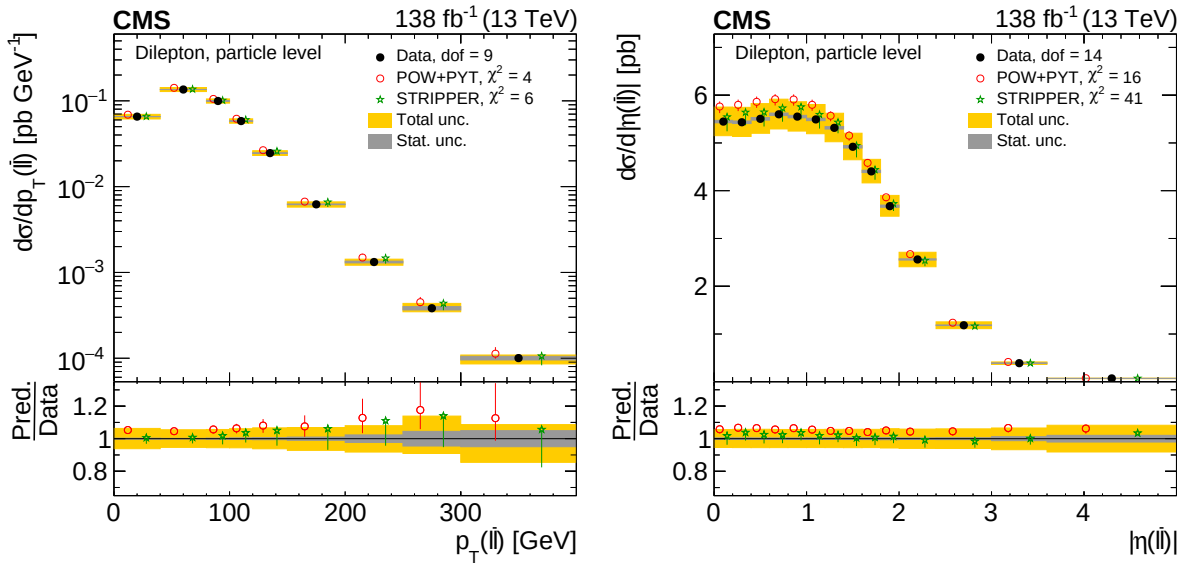

Figure 117: Absolute differential $\mathrm{t\bar{t}}$ production cross sections as functions of $p_{\mathrm{T}}(\ell\bar{\ell})$ (left) and $|\eta(\ell\bar{\ell})|$ (right) are shown for data (filled circles), POWHEG+PYTHIA 8 ('POW-PYT', open circles) simulation, and STRIPPER NNLO calculation (stars). Further details can be found in the caption of Fig. 114.

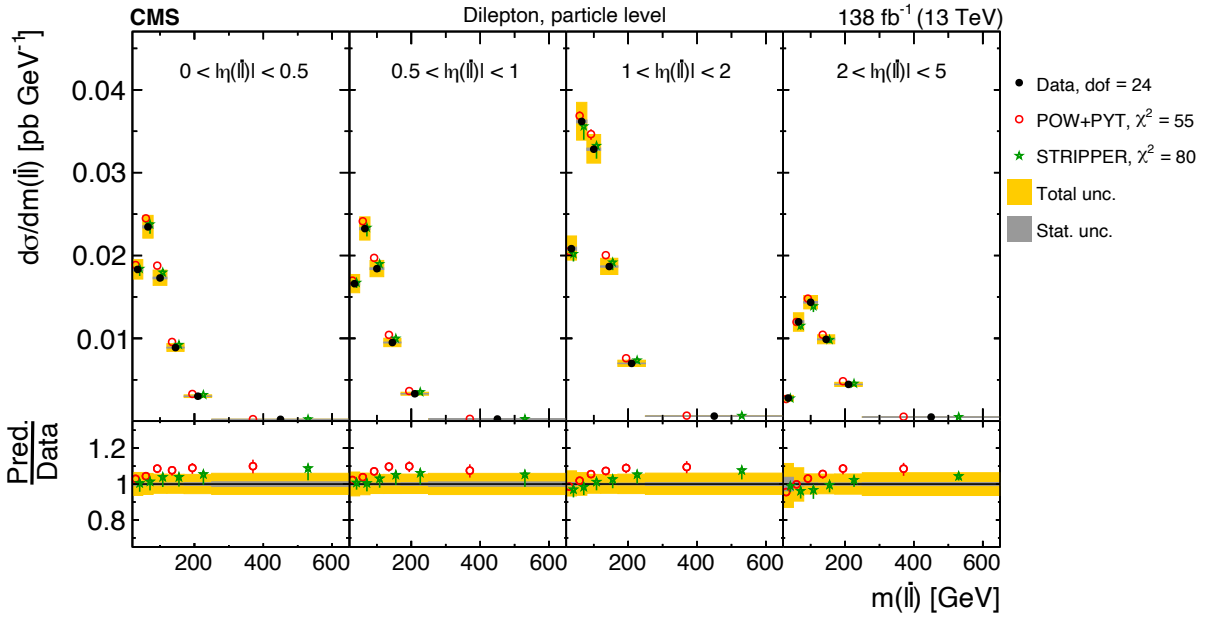

Figure 118: Absolute $[|\eta(\ell\bar{\ell})|, m(\ell\bar{\ell})]$ cross sections are shown for data (filled circles), POWHEG+PYTHIA 8 ('POW-PYT', open circles) simulation, and STRIPPER NNLO calculation (stars). Further details can be found in the caption of Fig. 114.

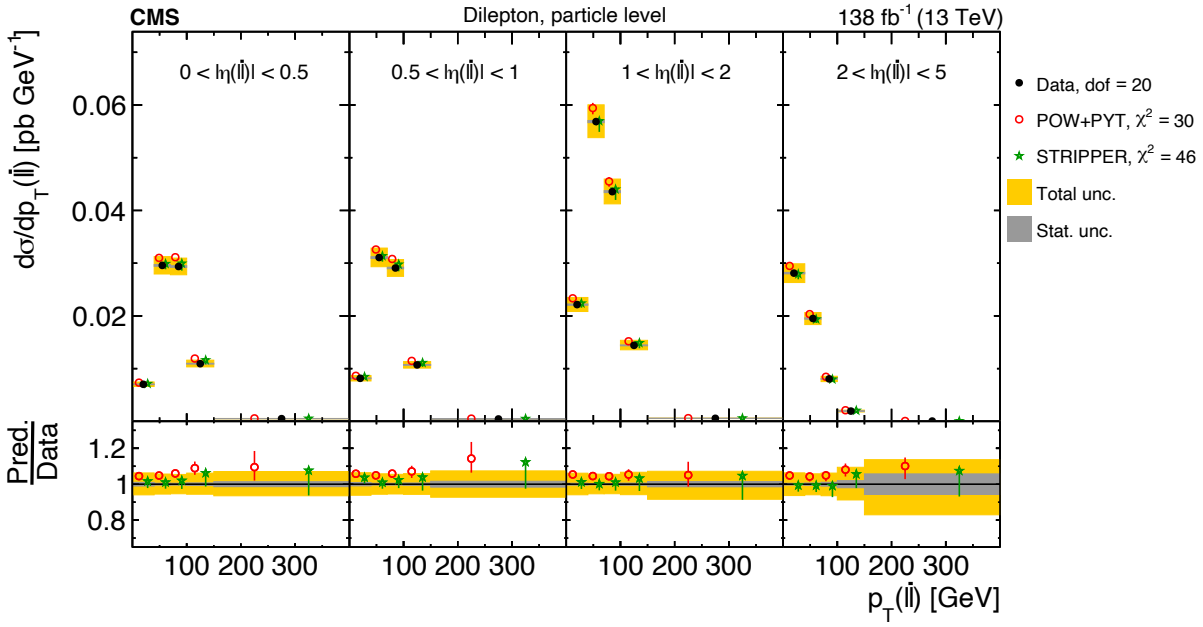

Figure 119: Absolute $[|\eta(\ell\bar{\ell})|, p_{\mathrm{T}}(\ell\bar{\ell})]$ cross sections are shown for data (filled circles), POWHEG+PYTHIA 8 ('POW-PYT', open circles) simulation, and STRIPPER NNLO calculation (stars). Further details can be found in the caption of Fig. 114.

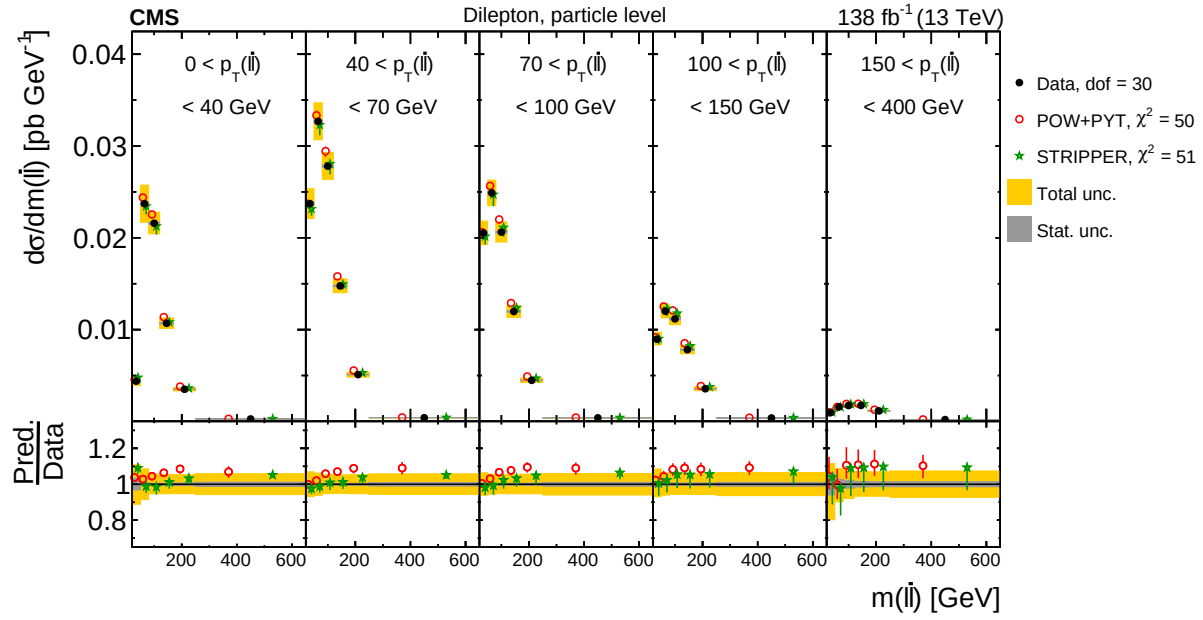

Figure 120: Absolute $[p_{\mathrm{T}}(\ell\bar{\ell}), m(\ell\bar{\ell})]$ cross sections are shown for data (filled circles), POWHEG+PYTHIA 8 ('POW-PYT', open circles) simulation, and STRIPPER NNLO calculation (stars). Further details can be found in the caption of Fig. 114.

Table 20: The χ^2 values and dof of the measured absolute single-differential cross sections for $t\bar{t}$ and top quark kinematic observables at the parton level are shown with respect to the POWHEG+PYTHIA 8 ('POW-PYT') simulation and various theoretical predictions with beyond-NLO precision. The χ^2 values are calculated taking only measurement uncertainties into account and excluding theory uncertainties. The corresponding χ^2 values including theory uncertainties are indicated with the brackets (w. unc.).

Cross section variables	dof	χ^2				
		POW+PYT (w. unc.)	aN^{3}LO (w. unc.)	MATRIX (w. unc.)	STRIPPER (w. unc.)	MiNNLOPS (w. unc.)
$p_T(t)$	7	21 (13)	47 (33)	3 (3)	15 (6)	6 (5)
$p_T(\bar{t})$	7	19 (12)	—	5 (4)	10 (10)	7 (5)
$y(t)$	10	28 (24)	24 (13)	17 (17)	17 (17)	14 (14)
$y(\bar{t})$	10	33 (28)	—	15 (14)	26 (24)	22 (19)
$p_T(t\bar{t})$	7	24 (8)	—	7 (3)	10 (3)	51 (15)
$y(t\bar{t})$	12	13 (9)	—	7 (7)	10 (9)	9 (9)
$m(t\bar{t})$	7	6 (4)	—	6 (4)	5 (4)	2 (2)
$\lvert\Delta\phi(t,\bar{t})\rvert$	4	4 (2)	—	91 (0)	78 (1)	5 (4)
$\lvert y(t)\rvert - \lvert y(\bar{t})\rvert$	8	18 (10)	—	2 (2)	3 (3)	12 (10)
$p_T(t)/m(t\bar{t})$	5	39 (21)	—	4 (3)	5 (5)	9 (3)
$p_T(t\bar{t})/m(t\bar{t})$	9	20 (7)	—	253 (9)	235 (10)	18 (6)
$\log(\xi_1)$	9	16 (12)	—	—	15 (14)	12 (11)
$\log(\xi_2)$	9	14 (9)	—	—	13 (11)	7 (6)

Table 21: The χ^2 values and dof of the measured absolute single-differential cross sections for $t\bar{t}$ and top quark kinematic observables at the particle level are shown with respect to the POWHEG+PYTHIA8 ('POW-PYT') simulation and the STRIPPER NNLO calculation. The χ^2 values are calculated taking only measurement uncertainties into account and excluding theory uncertainties. The corresponding χ^2 values including theory uncertainties are indicated with the brackets (w. unc.).

Cross section variables	dof	χ^2	
		POW+PYT (w. unc.)	STRIPPER (w. unc.)
$p_T(t)$	7	22 (13)	3 (2)
$p_T(\bar{t})$	7	20 (12)	4 (2)
$y(t)$	10	24 (18)	11 (11)
$y(\bar{t})$	10	28 (23)	10 (9)
$p_T(t\bar{t})$	7	23 (8)	87 (8)
$y(t\bar{t})$	12	13 (8)	20 (18)
$m(t\bar{t})$	7	7 (4)	4 (2)
$\lvert\Delta\phi(t,\bar{t})\rvert$	4	4 (1)	1412 (6)
$\lvert y(t)\rvert - \lvert y(\bar{t})\rvert$	8	17 (11)	4 (3)
$p_T(t)/m(t\bar{t})$	5	33 (23)	9 (6)
$p_T(t\bar{t})/m(t\bar{t})$	9	21 (7)	285 (8)
$\log(\xi_1)$	9	16 (10)	10 (10)
$\log(\xi_2)$	9	12 (7)	10 (10)

Table 22: The χ^2 values and dof of the measured absolute multi-differential cross sections for $t\bar{t}$ and top quark kinematic observables at the parton level are shown with respect to the POWHEG+PYTHIA 8 ('POW-PYT') simulation and various theoretical predictions with beyond-NLO precision. The χ^2 values are calculated taking only measurement uncertainties into account and excluding theory uncertainties. The corresponding χ^2 values including theory uncertainties are indicated with the brackets (w. unc.).

Cross section variables	dof	χ^2				
		POW+PYT (w. unc.)	aN^{3}LO (w. unc.)	MATRIX (w. unc.)	STRIPPER (w. unc.)	MiNNLOPS (w. unc.)
$[\lvert y(t)\rvert,\ p_T(t)]$	16	48 (36)	35 (35)	24 (24)	25 (24)	21 (21)
$[m(t\bar{t}),\ p_T(t)]$	9	93 (36)	—	19 (16)	17 (14)	17 (9)
$[p_T(t),\ p_T(t\bar{t})]$	16	50 (25)	—	42 (37)	57 (56)	61 (31)
$[m(t\bar{t}),\ \lvert y(t\bar{t})\rvert]$	16	72 (46)	—	56 (53)	49 (48)	51 (42)
$[\lvert y(t\bar{t})\rvert,\ p_T(t\bar{t})]$	16	32 (17)	—	39 (35)	43 (40)	61 (28)
$[m(t\bar{t}),\ p_T(t\bar{t})]$	16	68 (47)	—	97 (81)	112 (91)	135 (37)
$[p_T(t\bar{t}),\ m(t\bar{t}),\ \lvert y(t\bar{t})\rvert]$	48	102 (71)	—	—	74 (74)	103 (83)
$[m(t\bar{t}),\ \lvert y(t)\rvert]$	16	67 (39)	—	36 (36)	31 (31)	49 (45)
$[m(t\bar{t}),\ \lvert \Delta\eta(t,\bar{t})\rvert]$	12	182 (34)	—	31 (30)	31 (31)	53 (20)
$[m(t\bar{t}),\ \lvert \Delta\phi(t,\bar{t})\rvert]$	12	82 (51)	—	—	42 (27)	89 (68)

Table 23: The χ^2 values and dof of the measured absolute multi-differential cross sections for $t\bar{t}$ and top quark kinematic observables at the particle level are shown with respect to the POWHEG+PYTHIA 8 ('POW-PYT') simulation and the STRIPPER NNLO calculation. The χ^2 values are calculated taking only measurement uncertainties into account and excluding theory uncertainties. The corresponding χ^2 values including theory uncertainties are indicated with the brackets (w. unc.).

Cross section variables	dof	χ^2	
		POW+PYT (w. unc.)	STRIPPER (w. unc.)
$[\lvert y(t)\rvert,\ p_T(t)]$	16	44 (28)	17 (16)
$[m(t\bar{t}),\ p_T(t)]$	9	103 (37)	26 (17)
$[p_T(t),\ p_T(t\bar{t})]$	16	44 (21)	169 (106)
$[m(t\bar{t}),\ \lvert y(t\bar{t})\rvert]$	16	86 (41)	44 (43)
$[\lvert y(t\bar{t})\rvert,\ p_T(t\bar{t})]$	16	32 (19)	81 (38)
$[m(t\bar{t}),\ p_T(t\bar{t})]$	16	69 (37)	388 (145)
$[p_T(t\bar{t}),\ m(t\bar{t}),\ \lvert y(t\bar{t})\rvert]$	48	133 (69)	149 (82)
$[m(t\bar{t}),\ \lvert y(t)\rvert]$	16	64 (27)	21 (20)
$[m(t\bar{t}),\ \lvert \Delta\eta(t,\bar{t})\rvert]$	12	174 (32)	39 (25)
$[m(t\bar{t}),\ \lvert \Delta\phi(t,\bar{t})\rvert]$	12	80 (44)	426 (327)

Table 24: The χ^2 values and dof of the measured absolute single-differential cross sections for lepton and b-jet kinematic observables at the particle level are shown with respect to the POWHEG+PYTHIA8 ('POW-PYT') simulation and the STRIPPER NNLO calculation. The χ^2 values are calculated taking only measurement uncertainties into account and excluding theory uncertainties. The corresponding χ^2 values including theory uncertainties are indicated with the brackets (w. unc.).

Cross section variables	dof	χ^2	
		POW+PYT (w. unc.)	STRIPPER (w. unc.)
$p_{\mathrm{T}}(\ell)$	12	32 (19)	17 (17)
$p_{\mathrm{T}}(\ell)$ trailing/$p_{\mathrm{T}}(\ell)$ leading	10	16 (11)	5 (5)
$p_{\mathrm{T}}(\ell)/p_{\mathrm{T}}(\bar{\mathrm{t}})$	5	20 (17)	8 (6)
$p_{\mathrm{T}}(\mathrm{b})$ leading	10	6 (5)	8 (8)
$p_{\mathrm{T}}(\mathrm{b})$ trailing	7	7 (5)	4 (1)
$(p_{\mathrm{T}}(\mathrm{b}) + p_{\mathrm{T}}(\bar{\mathrm{b}}))/(p_{\mathrm{T}}(\mathrm{t}) + p_{\mathrm{T}}(\bar{\mathrm{t}}))$	4	24 (19)	9 (8)
$m(\ell\bar{\ell})$	12	31 (25)	13 (13)
$m(\mathrm{b}\bar{\mathrm{b}})$	7	21 (16)	80 (72)
$m(\ell\bar{\ell}\mathrm{b}\bar{\mathrm{b}})$	19	36 (19)	16 (15)
$p_{\mathrm{T}}(\ell\bar{\ell})$	9	4 (3)	6 (3)
$\lvert\eta(\ell\bar{\ell})\rvert$	14	16 (10)	41 (24)
$[\lvert\eta(\ell\bar{\ell})\rvert, m(\ell\bar{\ell})]$	24	55 (29)	80 (59)
$[\lvert\eta(\ell\bar{\ell})\rvert, p_{\mathrm{T}}(\ell\bar{\ell})]$	20	30 (15)	46 (28)
$[p_{\mathrm{T}}(\ell\bar{\ell}), m(\ell\bar{\ell})]$	30	50 (39)	51 (51)

Table 25: The p-values are shown for the χ^2 tests of the measured normalized single-differential cross sections for $t\bar{t}$ and top quark kinematic observables at the parton level with respect to the predictions of various MC generators. The χ^2 values are calculated taking only measurement uncertainties into account and excluding theory uncertainties. For POW+PYT, the p-values of the χ^2 tests including theory uncertainties are indicated with the brackets (w. unc.).

Cross section	p-values of χ^2 (in %)		
variables	POW+PYT (w. unc.)	FxFx+PYT	POW+HER
$p_T(t)$	2 (10)	<1	51
$p_T(\bar{t})$	5 (16)	<1	41
$y(t)$	<1 (2)	<1	1
$y(\bar{t})$	<1 (<1)	<1	<1
$p_T(t\bar{t})$	<1 (32)	<1	<1
$y(t\bar{t})$	51 (74)	7	73
$m(t\bar{t})$	56 (77)	30	70
$\lvert\Delta\phi(t,\bar{t})\rvert$	82 (97)	15	7
$\lvert y(t)\rvert - \lvert y(\bar{t})\rvert$	3 (22)	<1	6
$p_T(t)/m(t\bar{t})$	<1 (<1)	<1	3
$p_T(t\bar{t})/m(t\bar{t})$	3 (62)	<1	<1
$\log(\xi_1)$	9 (26)	3	15
$\log(\xi_2)$	24 (54)	<1	51

C Tables with p-values of χ^2 tests

Tables 25–48 present the p-values of the performed χ^2 tests between the measured differential cross sections for $t\bar{t}$ production and various predictions. The corresponding χ^2 values and number of degrees of freedom can be found in the Tables 1–24.

Table 26: The p-values are shown for the χ^2 tests of the measured normalized single-differential cross sections for $t\bar{t}$ and top quark kinematic observables at the particle level with respect to the predictions of various MC generators. The χ^2 values are calculated taking only measurement uncertainties into account and excluding theory uncertainties. For POW+PYT, the p-values of the χ^2 tests including theory uncertainties are indicated with the brackets (w. unc.).

Cross section	p-values of χ^2 (in %)		
variables	POW+PYT (w. unc.)	FxFx+PYT	POW+HER
$p_T(t)$	<1 (7)	<1	47
$p_T(\bar{t})$	3 (15)	<1	59
$y(t)$	3 (7)	<1	2
$y(\bar{t})$	<1 (2)	<1	<1
$p_T(t\bar{t})$	<1 (33)	<1	<1
$y(t\bar{t})$	51 (81)	3	64
$m(t\bar{t})$	59 (81)	60	28
$\lvert\Delta\phi(t,\bar{t})\rvert$	82 (97)	36	10
$\lvert y(t)\rvert - \lvert y(\bar{t})\rvert$	4 (20)	4	1
$p_T(t)/m(t\bar{t})$	<1 (<1)	<1	2
$p_T(t\bar{t})/m(t\bar{t})$	2 (57)	<1	<1
$\log(\xi_1)$	8 (34)	3	2
$\log(\xi_2)$	32 (67)	3	29

Table 27: The p-values are shown for the χ^2 tests of the measured normalized multi-differential cross sections for $t\bar{t}$ and top quark kinematic observables at the parton level with respect to the predictions of various MC generators. The χ^2 values are calculated taking only measurement uncertainties into account and excluding theory uncertainties. For POW+PYT, the p-values of the χ^2 tests including theory uncertainties are indicated with the brackets (w. unc.).

Cross section	p-values of χ^2 (in %)		
variables	POW+PYT (w. unc.)	FxFx+PYT	POW+HER
$[\lvert y(t)\rvert,\ p_T(t)]$	<1 (<1)	<1	1
$[m(t\bar{t}),\ p_T(t)]$	<1 (<1)	<1	<1
$[p_T(t),\ p_T(t\bar{t})]$	<1 (14)	<1	<1
$[m(t\bar{t}),\ \lvert y(t\bar{t})\rvert]$	<1 (<1)	<1	<1
$[\lvert y(t\bar{t})\rvert,\ p_T(t\bar{t})]$	2 (44)	<1	<1
$[m(t\bar{t}),\ p_T(t\bar{t})]$	<1 (<1)	<1	<1
$[p_T(t\bar{t}),\ m(t\bar{t}),\ \lvert y(t\bar{t})\rvert]$	<1 (5)	<1	<1
$[m(t\bar{t}),\ \lvert y(t)\rvert]$	<1 (<1)	<1	<1
$[m(t\bar{t}),\ \lvert\Delta\eta(t,\bar{t})\rvert]$	<1 (<1)	<1	<1
$[m(t\bar{t}),\ \lvert\Delta\phi(t,\bar{t})\rvert]$	<1 (<1)	<1	<1

Table 28: The p-values are shown for the χ^2 tests of the measured normalized multi-differential cross sections for $t\bar{t}$ and top quark kinematic observables at the particle level with respect to the predictions of various MC generators. The χ^2 values are calculated taking only measurement uncertainties into account and excluding theory uncertainties. For POW+PYT, the p-values of the χ^2 tests including theory uncertainties are indicated with the brackets (w. unc.).

Cross section	p-values of χ^2 (in %)		
variables	POW+PYT (w. unc.)	FxFx+PYT	POW+HER
$[\lvert y(t)\rvert,\ p_T(t)]$	<1 (5)	<1	2
$[m(t\bar{t}),\ p_T(t)]$	<1 (<1)	<1	<1
$[p_T(t),\ p_T(t\bar{t})]$	<1 (21)	<1	<1
$[m(t\bar{t}),\ \lvert y(t\bar{t})\rvert]$	<1 (<1)	<1	<1
$[\lvert y(t\bar{t})\rvert,\ p_T(t\bar{t})]$	3 (28)	<1	<1
$[m(t\bar{t}),\ p_T(t\bar{t})]$	<1 (<1)	<1	<1
$[p_T(t\bar{t}),\ m(t\bar{t}),\ \lvert y(t\bar{t})\rvert]$	<1 (3)	<1	<1
$[m(t\bar{t}),\ \lvert y(t)\rvert]$	<1 (4)	<1	<1
$[m(t\bar{t}),\ \lvert\Delta\eta(t,\bar{t})\rvert]$	<1 (<1)	<1	<1
$[m(t\bar{t}),\ \lvert\Delta\phi(t,\bar{t})\rvert]$	<1 (<1)	<1	<1

Table 29: The p-values are shown for the χ^2 tests of the measured normalized single-differential cross sections for lepton and b-jet kinematic observables at the particle level with respect to the predictions of various MC generators. The χ^2 values are calculated taking only measurement uncertainties into account and excluding theory uncertainties. For POW+PYT, the p-values of the χ^2 tests including theory uncertainties are indicated with the brackets (w. unc.).

Cross section	p-values of χ^2 (in %)		
variables	POW+PYT (w. unc.)	FxFx+PYT	POW+HER
$p_{\mathrm{T}}(\ell)$	<1 (8)	<1	9
$p_{\mathrm{T}}(\ell)$ trailing/$p_{\mathrm{T}}(\ell)$ leading	10 (30)	<1	66
$p_{\mathrm{T}}(\ell)/p_{\mathrm{T}}(\bar{\mathrm{t}})$	4 (6)	<1	2
$p_{\mathrm{T}}(\mathrm{b})$ leading	86 (92)	<1	55
$p_{\mathrm{T}}(\mathrm{b})$ trailing	48 (70)	<1	35
$(p_{\mathrm{T}}(\mathrm{b}) + p_{\mathrm{T}}(\bar{\mathrm{b}}))/(p_{\mathrm{T}}(\mathrm{t}) + p_{\mathrm{T}}(\bar{\mathrm{t}}))$	<1 (<1)	<1	<1
$m(\ell\bar{\ell})$	2 (5)	<1	2
$m(\mathrm{b}\bar{\mathrm{b}})$	2 (7)	2	3
$m(\ell\bar{\ell}\mathrm{b}\bar{\mathrm{b}})$	2 (45)	6	6
$p_{\mathrm{T}}(\ell\bar{\ell})$	86 (96)	9	31
$\lvert\eta(\ell\bar{\ell})\rvert$	40 (77)	7	58
$[\lvert\eta(\ell\bar{\ell})\rvert,\, m(\ell\bar{\ell})]$	<1 (23)	<1	4
$[\lvert\eta(\ell\bar{\ell})\rvert,\, p_{\mathrm{T}}(\ell\bar{\ell})]$	10 (78)	<1	19
$[p_{\mathrm{T}}(\ell\bar{\ell}),\, m(\ell\bar{\ell})]$	3 (15)	<1	<1

Table 30: The p-values are shown for the χ^2 tests of the measured normalized differential cross sections as a function of the additional-jet multiplicity in the events, at the parton level of the top quark and antiquark, with respect to the predictions of various MC generators. The χ^2 values are calculated taking only measurement uncertainties into account and excluding theory uncertainties. For POW+PYT, the p-values of the χ^2 tests including theory uncertainties are indicated with the brackets (w. unc.).

Cross section variables	p-values of χ^2 (in %)		
	POW+PYT (w. unc.)	FxFx+PYT	POW+HER
$N_{\text{jet}}(p_{\text{T}} > 40\,\text{GeV})$	34 (64)	<1	<1
$N_{\text{jet}}(p_{\text{T}} > 100\,\text{GeV})$	<1 (11)	<1	<1
$[N_{\text{jet}},\, p_{\text{T}}(\text{t})]$	<1 (14)	<1	<1
$[N_{\text{jet}},\, \lvert y(\text{t})\rvert]$	<1 (<1)	<1	<1
$[N_{\text{jet}},\, p_{\text{T}}(\text{t}\bar{\text{t}})]$	<1 (<1)	<1	<1
$[N_{\text{jet}},\, m(\text{t}\bar{\text{t}})]$	<1 (<1)	<1	<1
$[N_{\text{jet}},\, \lvert y(\text{t}\bar{\text{t}})\rvert]$	46 (94)	<1	<1
$[N_{\text{jet}},\, \lvert \Delta\eta(\text{t},\bar{\text{t}})\rvert]$	<1 (<1)	<1	<1
$[N_{\text{jet}}^{0,1+},\, m(\text{t}\bar{\text{t}}),\, \lvert y(\text{t}\bar{\text{t}})\rvert]$	<1 (5)	<1	<1
$[N_{\text{jet}}^{0,1,2+},\, m(\text{t}\bar{\text{t}}),\, \lvert y(\text{t}\bar{\text{t}})\rvert]$	<1 (1)	<1	<1
$[N_{\text{jet}}^{0,1,2,3+},\, m(\text{t}\bar{\text{t}}),\, \lvert y(\text{t}\bar{\text{t}})\rvert]$	<1 (<1)	<1	<1

Table 31: The p-values are shown for the χ^2 tests of the measured normalized differential cross sections as a function of the additional-jet multiplicity in the events, at the particle level of the top quark and antiquark, with respect to the predictions of various MC generators. The χ^2 values are calculated taking only measurement uncertainties into account and excluding theory uncertainties. For POW+PYT, the p-values of the χ^2 tests including theory uncertainties are indicated with the brackets (w. unc.).

Cross section variables	p-values of χ^2 (in %)		
	POW+PYT (w. unc.)	FxFx+PYT	POW+HER
$N_{\text{jet}}(p_{\text{T}} > 40\,\text{GeV})$	30 (63)	<1	12
$N_{\text{jet}}(p_{\text{T}} > 100\,\text{GeV})$	<1 (8)	<1	19
$[N_{\text{jet}},\, p_{\text{T}}(\text{t})]$	<1 (12)	<1	<1
$[N_{\text{jet}},\, \lvert y(\text{t})\rvert]$	<1 (1)	<1	<1
$[N_{\text{jet}},\, p_{\text{T}}(\text{t}\bar{\text{t}})]$	<1 (<1)	<1	<1
$[N_{\text{jet}},\, m(\text{t}\bar{\text{t}})]$	<1 (<1)	<1	<1
$[N_{\text{jet}},\, \lvert y(\text{t}\bar{\text{t}})\rvert]$	22 (94)	<1	65
$[N_{\text{jet}},\, \lvert \Delta\eta(\text{t},\bar{\text{t}})\rvert]$	<1 (<1)	<1	<1
$[N_{\text{jet}}^{0,1+},\, m(\text{t}\bar{\text{t}}),\, \lvert y(\text{t}\bar{\text{t}})\rvert]$	<1 (<1)	<1	<1
$[N_{\text{jet}}^{0,1,2+},\, m(\text{t}\bar{\text{t}}),\, \lvert y(\text{t}\bar{\text{t}})\rvert]$	<1 (<1)	<1	<1
$[N_{\text{jet}}^{0,1,2,3+},\, m(\text{t}\bar{\text{t}}),\, \lvert y(\text{t}\bar{\text{t}})\rvert]$	<1 (<1)	<1	<1

Table 32: The p-values are shown for the χ^2 tests of the measured normalized single-differential cross sections for $t\bar{t}$ and top quark kinematic observables at the parton level with respect to various fixed-order predictions. The χ^2 values are calculated taking only measurement uncertainties into account and excluding theory uncertainties. The p-values of the χ^2 tests including theory uncertainties are indicated with the brackets (w. unc.).

Cross section	p-values of χ^2 (in %)				
variables	POW+PYT (w. unc.)	aN^{3}LO (w. unc.)	MATRIX (w. unc.)	STRIPPER (w. unc.)	MINNLOPS (w. unc.)
$p_T(t)$	2 (10)	<1 (<1)	78 (85)	22 (51)	62 (64)
$p_T(\bar{t})$	5 (16)	—	69 (75)	14 (15)	49 (53)
$y(t)$	<1 (2)	<1 (22)	6 (6)	6 (7)	8 (17)
$y(\bar{t})$	<1 (<1)	—	10 (15)	<1 (<1)	<1 (5)
$p_T(t\bar{t})$	<1 (32)	—	33 (90)	15 (86)	<1 (4)
$y(t\bar{t})$	51 (74)	—	84 (85)	61 (65)	61 (62)
$m(t\bar{t})$	56 (77)	—	49 (69)	59 (73)	90 (94)
$\lvert\Delta\phi(t,\bar{t})\rvert$	82 (97)	—	<1 (93)	<1 (90)	14 (29)
$\lvert y(t)\rvert - \lvert y(\bar{t})\rvert$	3 (22)	—	94 (94)	86 (86)	10 (22)
$p_T(t)/m(t\bar{t})$	<1 (<1)	—	58 (64)	41 (44)	28 (68)
$p_T(t\bar{t})/m(t\bar{t})$	3 (62)	—	<1 (32)	<1 (28)	1 (75)
$\log(\xi_1)$	9 (26)	—	—	6 (7)	16 (18)
$\log(\xi_2)$	24 (54)	—	—	17 (18)	52 (59)

Table 33: The p-values are shown for the χ^2 tests of the measured normalized single-differential cross sections for $\mathrm{t\bar{t}}$ and top quark kinematic observables at the particle level with respect to the POWHEG+PYTHIA 8 ('POW-PYT') simulation and the STRIPPER NNLO calculation. The χ^2 values are calculated taking only measurement uncertainties into account and excluding theory uncertainties. The p-values of the χ^2 tests including theory uncertainties are indicated with the brackets (w. unc.).

Cross section	p-values of χ^2 (in %)	
variables	POW+PYT (w. unc.)	STRIPPER (w. unc.)
$p_{\mathrm{T}}(\mathrm{t})$	<1 (7)	83 (95)
$p_{\mathrm{T}}(\bar{\mathrm{t}})$	3 (15)	82 (94)
$y(\mathrm{t})$	3 (7)	29 (29)
$y(\bar{\mathrm{t}})$	<1 (2)	37 (44)
$p_{\mathrm{T}}(\mathrm{t\bar{t}})$	<1 (33)	<1 (25)
$y(\mathrm{t\bar{t}})$	51 (81)	6 (23)
$m(\mathrm{t\bar{t}})$	59 (81)	73 (95)
$\lvert\Delta\phi(\mathrm{t},\bar{\mathrm{t}})\rvert$	82 (97)	<1 (65)
$\lvert y(\mathrm{t})\rvert - \lvert y(\bar{\mathrm{t}})\rvert$	4 (20)	81 (88)
$p_{\mathrm{T}}(\mathrm{t})/m(\mathrm{t\bar{t}})$	<1 (<1)	9 (39)
$p_{\mathrm{T}}(\mathrm{t\bar{t}})/m(\mathrm{t\bar{t}})$	2 (57)	<1 (56)
$\log(\xi_1)$	8 (34)	28 (28)
$\log(\xi_2)$	32 (67)	33 (33)

Table 34: The p-values are shown for the χ^2 tests of the measured normalized multi-differential cross sections for $t\bar{t}$ and top quark kinematic observables at the parton level with respect to various fixed-order predictions. The χ^2 values are calculated taking only measurement uncertainties into account and excluding theory uncertainties. The p-values of the χ^2 tests including theory uncertainties are indicated with the brackets (w. unc.).

Cross section variables	p-values of χ^2 (in %)				
	POW+PYT (w. unc.)	aN^{3}LO (w. unc.)	MATRIX (w. unc.)	STRIPPER (w. unc.)	MINNLOPS (w. unc.)
$[\lvert y(t)\rvert, p_T(t)]$	<1 (<1)	<1 (<1)	7 (7)	6 (7)	9 (10)
$[m(t\bar{t}), p_T(t)]$	<1 (<1)	—	7 (15)	4 (13)	6 (47)
$[p_T(t), p_T(t\bar{t})]$	<1 (14)	—	<1 (<1)	<1 (<1)	<1 (2)
$[m(t\bar{t}), \lvert y(t\bar{t})\rvert]$	<1 (<1)	—	<1 (<1)	<1 (<1)	<1 (<1)
$[\lvert y(t\bar{t})\rvert, p_T(t\bar{t})]$	2 (44)	—	<1 (<1)	<1 (<1)	<1 (5)
$[m(t\bar{t}), p_T(t\bar{t})]$	<1 (<1)	—	<1 (<1)	<1 (<1)	<1 (<1)
$[p_T(t\bar{t}), m(t\bar{t}), \lvert y(t\bar{t})\rvert]$	<1 (5)	—	—	2 (3)	<1 (<1)
$[m(t\bar{t}), \lvert y(t)\rvert]$	<1 (<1)	—	<1 (<1)	1 (1)	<1 (<1)
$[m(t\bar{t}), \lvert \Delta\eta(t,\bar{t})\rvert]$	<1 (<1)	—	<1 (<1)	<1 (<1)	<1 (10)
$[m(t\bar{t}), \lvert \Delta\phi(t,\bar{t})\rvert]$	<1 (<1)	—	—	<1 (8)	<1 (<1)

Table 35: The p-values are shown for the χ^2 tests of the measured normalized multi-differential cross sections for $t\bar{t}$ and top quark kinematic observables at the particle level with respect to the POWHEG+PYTHIA 8 ('POW-PYT') simulation and the STRIPPER NNLO calculation. The χ^2 values are calculated taking only measurement uncertainties into account and excluding theory uncertainties. The p-values of the χ^2 tests including theory uncertainties are indicated with the brackets (w. unc.).

Cross section	p-values of χ^2 (in %)	
variables	POW+PYT (w. unc.)	STRIPPER (w. unc.)
$[\lvert y(t)\rvert,\ p_T(t)]$	<1 (5)	38 (39)
$[m(t\bar{t}),\ p_T(t)]$	<1 (<1)	2 (32)
$[p_T(t),\ p_T(t\bar{t})]$	<1 (21)	<1 (<1)
$[m(t\bar{t}),\ \lvert y(t\bar{t})\rvert]$	<1 (<1)	<1 (<1)
$[\lvert y(t\bar{t})\rvert,\ p_T(t\bar{t})]$	3 (28)	<1 (<1)
$[m(t\bar{t}),\ p_T(t\bar{t})]$	<1 (<1)	<1 (<1)
$[p_T(t\bar{t}),\ m(t\bar{t}),\ \lvert y(t\bar{t})\rvert]$	<1 (3)	<1 (<1)
$[m(t\bar{t}),\ \lvert y(t)\rvert]$	<1 (4)	18 (25)
$[m(t\bar{t}),\ \lvert \Delta\eta(t,\bar{t})\rvert]$	<1 (<1)	<1 (3)
$[m(t\bar{t}),\ \lvert \Delta\phi(t,\bar{t})\rvert]$	<1 (<1)	<1 (<1)

Table 36: The p-values are shown for the χ^2 tests of the measured normalized single-differential cross sections for lepton and b-jet kinematic observables at the particle level with respect to the POWHEG+PYTHIA 8 ('POW-PYT') simulation and the STRIPPER NNLO calculation. The χ^2 values are calculated taking only measurement uncertainties into account and excluding theory uncertainties. The p-values of the χ^2 tests including theory uncertainties are indicated with the brackets (w. unc.).

Cross section	p-values of χ^2 (in %)	
variables	POW+PYT (w. unc.)	STRIPPER (w. unc.)
$p_{\mathrm{T}}(\ell)$	<1 (8)	12 (13)
$p_{\mathrm{T}}(\ell)$ trailing/$p_{\mathrm{T}}(\ell)$ leading	10 (30)	81 (82)
$p_{\mathrm{T}}(\ell)/p_{\mathrm{T}}(\bar{\mathrm{t}})$	4 (6)	33 (34)
$p_{\mathrm{T}}(\mathrm{b})$ leading	86 (92)	64 (76)
$p_{\mathrm{T}}(\mathrm{b})$ trailing	48 (70)	81 (97)
$(p_{\mathrm{T}}(\mathrm{b}) + p_{\mathrm{T}}(\bar{\mathrm{b}}))/(p_{\mathrm{T}}(\mathrm{t}) + p_{\mathrm{T}}(\bar{\mathrm{t}}))$	<1 (<1)	4 (5)
$m(\ell\bar{\ell})$	2 (5)	32 (34)
$m(\mathrm{b}\bar{\mathrm{b}})$	2 (7)	<1 (<1)
$m(\ell\bar{\ell}\mathrm{b}\bar{\mathrm{b}})$	2 (45)	68 (76)
$p_{\mathrm{T}}(\ell\bar{\ell})$	86 (96)	73 (93)
$\lvert\eta(\ell\bar{\ell})\rvert$	40 (77)	<1 (7)
$[\lvert\eta(\ell\bar{\ell})\rvert, m(\ell\bar{\ell})]$	<1 (23)	<1 (<1)
$[\lvert\eta(\ell\bar{\ell})\rvert, p_{\mathrm{T}}(\ell\bar{\ell})]$	10 (78)	<1 (11)
$[p_{\mathrm{T}}(\ell\bar{\ell}), m(\ell\bar{\ell})]$	3 (15)	2 (2)

Table 37: The p-values are shown for the χ^2 tests of the measured absolute single-differential cross sections for $t\bar{t}$ and top quark kinematic observables at the parton level with respect to the predictions of various MC generators. The χ^2 values are calculated taking only measurement uncertainties into account and excluding theory uncertainties. For POW+PYT, the p-values of the χ^2 tests including theory uncertainties are indicated with the brackets (w. unc.).

Cross section	p-values of χ^2 (in %)		
variables	POW+PYT (w. unc.)	FxFx+PYT	POW+HER
$p_T(t)$	<1 (7)	<1	61
$p_T(\bar{t})$	<1 (9)	<1	50
$y(t)$	<1 (<1)	<1	2
$y(\bar{t})$	<1 (<1)	<1	<1
$p_T(t\bar{t})$	<1 (35)	<1	<1
$y(t\bar{t})$	38 (67)	9	78
$m(t\bar{t})$	55 (78)	28	76
$\lvert\Delta\phi(t,\bar{t})\rvert$	40 (81)	14	3
$\lvert y(t)\rvert - \lvert y(\bar{t})\rvert$	2 (23)	2	9
$p_T(t)/m(t\bar{t})$	<1 (<1)	<1	3
$p_T(t\bar{t})/m(t\bar{t})$	2 (66)	<1	<1
$\log(\xi_1)$	7 (23)	4	20
$\log(\xi_2)$	14 (47)	<1	60

Table 38: The p-values are shown for the χ^2 tests of the measured absolute single-differential cross sections for $t\bar{t}$ and top quark kinematic observables at the particle level with respect to the predictions of various MC generators. The χ^2 values are calculated taking only measurement uncertainties into account and excluding theory uncertainties. For POW+PYT, the p-values of the χ^2 tests including theory uncertainties are indicated with the brackets (w. unc.).

Cross section	p-values of χ^2 (in %)		
variables	POW+PYT (w. unc.)	FxFx+PYT	POW+HER
$p_T(t)$	<1 (7)	<1	46
$p_T(\bar{t})$	<1 (11)	<1	68
$y(t)$	<1 (5)	<1	4
$y(\bar{t})$	<1 (1)	<1	<1
$p_T(t\bar{t})$	<1 (37)	<1	<1
$y(t\bar{t})$	35 (78)	3	74
$m(t\bar{t})$	46 (80)	67	39
$\lvert\Delta\phi(t,\bar{t})\rvert$	40 (85)	43	13
$\lvert y(t)\rvert - \lvert y(\bar{t})\rvert$	3 (23)	5	2
$p_T(t)/m(t\bar{t})$	<1 (<1)	<1	1
$p_T(t\bar{t})/m(t\bar{t})$	1 (59)	<1	<1
$\log(\xi_1)$	7 (35)	4	3
$\log(\xi_2)$	22 (67)	3	36

Table 39: The p-values are shown for the χ^2 tests of the measured absolute multi-differential cross sections for $t\bar{t}$ and top quark kinematic observables at the parton level with respect to the predictions of various MC generators. The χ^2 values are calculated taking only measurement uncertainties into account and excluding theory uncertainties. For POW+PYT, the p-values of the χ^2 tests including theory uncertainties are indicated with the brackets (w. unc.).

Cross section	p-values of χ^2 (in %)		
variables	POW+PYT (w. unc.)	FxFx+PYT	POW+HER
$[\|y(t)\|, p_T(t)]$	<1 (<1)	<1	2
$[m(t\bar{t}), p_T(t)]$	<1 (<1)	<1	<1
$[p_T(t), p_T(t\bar{t})]$	<1 (6)	<1	<1
$[m(t\bar{t}), \|y(t\bar{t})\|]$	<1 (<1)	<1	<1
$[\|y(t\bar{t})\|, p_T(t\bar{t})]$	<1 (37)	<1	<1
$[m(t\bar{t}), p_T(t\bar{t})]$	<1 (<1)	<1	<1
$[p_T(t\bar{t}), m(t\bar{t}), \|y(t\bar{t})\|]$	<1 (2)	<1	<1
$[m(t\bar{t}), \|y(t)\|]$	<1 (<1)	<1	<1
$[m(t\bar{t}), \|\Delta\eta(t,\bar{t})\|]$	<1 (<1)	<1	<1
$[m(t\bar{t}), \|\Delta\phi(t,\bar{t})\|]$	<1 (<1)	<1	<1

Table 40: The p-values are shown for the χ^2 tests of the measured absolute multi-differential cross sections for $t\bar{t}$ and top quark kinematic observables at the particle level with respect to the predictions of various MC generators. The χ^2 values are calculated taking only measurement uncertainties into account and excluding theory uncertainties. For POW+PYT, the p-values of the χ^2 tests including theory uncertainties are indicated with the brackets (w. unc.).

Cross section	p-values of χ^2 (in %)		
variables	POW+PYT (w. unc.)	FxFx+PYT	POW+HER
$[\|y(t)\|, p_T(t)]$	<1 (3)	<1	4
$[m(t\bar{t}), p_T(t)]$	<1 (<1)	<1	<1
$[p_T(t), p_T(t\bar{t})]$	<1 (17)	<1	<1
$[m(t\bar{t}), \|y(t\bar{t})\|]$	<1 (<1)	<1	<1
$[\|y(t\bar{t})\|, p_T(t\bar{t})]$	1 (27)	<1	<1
$[m(t\bar{t}), p_T(t\bar{t})]$	<1 (<1)	<1	<1
$[p_T(t\bar{t}), m(t\bar{t}), \|y(t\bar{t})\|]$	<1 (3)	<1	<1
$[m(t\bar{t}), \|y(t)\|]$	<1 (5)	<1	<1
$[m(t\bar{t}), \|\Delta\eta(t,\bar{t})\|]$	<1 (<1)	<1	<1
$[m(t\bar{t}), \|\Delta\phi(t,\bar{t})\|]$	<1 (<1)	<1	<1

Table 41: The p-values are shown for the χ^2 tests of the measured absolute single-differential cross sections for lepton and b-jet kinematic observables at the particle level with respect to the predictions of various MC generators. The χ^2 values are calculated taking only measurement uncertainties into account and excluding theory uncertainties. For POW+PYT, the p-values of the χ^2 tests including theory uncertainties are indicated with the brackets (w. unc.).

Cross section	p-values of χ^2 (in %)		
variables	POW+PYT (w. unc.)	FxFx+PYT	POW+HER
$p_{\mathrm{T}}(\ell)$	<1 (9)	<1	6
$p_{\mathrm{T}}(\ell)$ trailing/$p_{\mathrm{T}}(\ell)$ leading	9 (34)	<1	70
$p_{\mathrm{T}}(\ell)/p_{\mathrm{T}}(\bar{\mathrm{t}})$	<1 (<1)	<1	2
$p_{\mathrm{T}}(\mathrm{b})$ leading	85 (91)	<1	64
$p_{\mathrm{T}}(\mathrm{b})$ trailing	46 (64)	<1	41
$(p_{\mathrm{T}}(\mathrm{b}) + p_{\mathrm{T}}(\bar{\mathrm{b}}))/(p_{\mathrm{T}}(\mathrm{t}) + p_{\mathrm{T}}(\bar{\mathrm{t}}))$	<1 (<1)	<1	<1
$m(\ell\bar{\ell})$	<1 (2)	<1	3
$m(\mathrm{b}\bar{\mathrm{b}})$	<1 (2)	2	4
$m(\ell\bar{\ell}\mathrm{b}\bar{\mathrm{b}})$	<1 (48)	6	10
$p_{\mathrm{T}}(\ell\bar{\ell})$	88 (97)	6	34
$\lvert\eta(\ell\bar{\ell})\rvert$	32 (77)	7	63
$[\lvert\eta(\ell\bar{\ell})\rvert, m(\ell\bar{\ell})]$	<1 (22)	<1	7
$[\lvert\eta(\ell\bar{\ell})\rvert, p_{\mathrm{T}}(\ell\bar{\ell})]$	7 (80)	<1	24
$[p_{\mathrm{T}}(\ell\bar{\ell}), m(\ell\bar{\ell})]$	1 (12)	<1	<1

Table 42: The p-values are shown for the χ^2 tests of the measured absolute differential cross sections as a function of the additional-jet multiplicity in the events, at the parton level of the top quark and antiquark, with respect to the predictions of various MC generators. The χ^2 values are calculated taking only measurement uncertainties into account and excluding theory uncertainties. For POW+PYT, the p-values of the χ^2 tests including theory uncertainties are indicated with the brackets (w. unc.).

Cross section	p-values of χ^2 (in \$)		
variables	POW+PYT (w. unc.)	FxFx+PYT	POW+HER
$N_{\text{jet}}(p_{\text{T}} > 40\,\text{GeV})$	30 (56)	<1	<1
$N_{\text{jet}}(p_{\text{T}} > 100\,\text{GeV})$	<1 (5)	<1	<1
$[N_{\text{jet}},\, p_{\text{T}}(\text{t})]$	<1 (5)	<1	<1
$[N_{\text{jet}},\, \lvert y(\text{t})\rvert]$	<1 (<1)	<1	<1
$[N_{\text{jet}},\, p_{\text{T}}(\text{t}\bar{\text{t}})]$	<1 (<1)	<1	<1
$[N_{\text{jet}},\, m(\text{t}\bar{\text{t}})]$	<1 (<1)	<1	<1
$[N_{\text{jet}},\, \lvert y(\text{t}\bar{\text{t}})\rvert]$	32 (87)	<1	<1
$[N_{\text{jet}},\, \lvert \Delta\eta(\text{t},\bar{\text{t}})\rvert]$	<1 (<1)	<1	<1
$[N_{\text{jet}}^{0,1+},\, m(\text{t}\bar{\text{t}}),\, \lvert y(\text{t}\bar{\text{t}})\rvert]$	<1 (3)	<1	<1
$[N_{\text{jet}}^{0,1,2+},\, m(\text{t}\bar{\text{t}}),\, \lvert y(\text{t}\bar{\text{t}})\rvert]$	<1 (<1)	<1	<1
$[N_{\text{jet}}^{0,1,2,3+},\, m(\text{t}\bar{\text{t}}),\, \lvert y(\text{t}\bar{\text{t}})\rvert]$	<1 (<1)	<1	<1

Table 43: The p-values are shown for the χ^2 tests of the measured absolute differential cross sections as a function of the additional-jet multiplicity in the events, at the particle level of the top quark and antiquark, with respect to the predictions of various MC generators. The χ^2 values are calculated taking only measurement uncertainties into account and excluding theory uncertainties. For POW+PYT, the p-values of the χ^2 tests including theory uncertainties are indicated with the brackets (w. unc.).

Cross section	p-values of χ^2 (in %)		
variables	POW+PYT (w. unc.)	FxFx+PYT	POW+HER
$N_{\text{jet}}(p_{\text{T}} > 40\,\text{GeV})$	29 (66)	<1	22
$N_{\text{jet}}(p_{\text{T}} > 100\,\text{GeV})$	<1 (5)	<1	25
$[N_{\text{jet}},\, p_{\text{T}}(\text{t})]$	<1 (9)	<1	<1
$[N_{\text{jet}},\, \lvert y(\text{t})\rvert]$	<1 (1)	<1	<1
$[N_{\text{jet}},\, p_{\text{T}}(\text{t}\bar{\text{t}})]$	<1 (<1)	<1	<1
$[N_{\text{jet}},\, m(\text{t}\bar{\text{t}})]$	<1 (<1)	<1	<1
$[N_{\text{jet}},\, \lvert y(\text{t}\bar{\text{t}})\rvert]$	13 (91)	<1	75
$[N_{\text{jet}},\, \lvert \Delta\eta(\text{t},\bar{\text{t}})\rvert]$	<1 (<1)	<1	<1
$[N_{\text{jet}}^{0,1+},\, m(\text{t}\bar{\text{t}}),\, \lvert y(\text{t}\bar{\text{t}})\rvert]$	<1 (<1)	<1	<1
$[N_{\text{jet}}^{0,1,2+},\, m(\text{t}\bar{\text{t}}),\, \lvert y(\text{t}\bar{\text{t}})\rvert]$	<1 (<1)	<1	<1
$[N_{\text{jet}}^{0,1,2,3+},\, m(\text{t}\bar{\text{t}}),\, \lvert y(\text{t}\bar{\text{t}})\rvert]$	<1 (<1)	<1	<1

Table 44: The p-values are shown for the χ^2 tests of the measured absolute single-differential cross sections for $\mathrm{t\bar{t}}$ and top quark kinematic observables at the parton level with respect to various fixed-order predictions. The χ^2 values are calculated taking only measurement uncertainties into account and excluding theory uncertainties. The p-values of the χ^2 tests including theory uncertainties are indicated with the brackets (w. unc.).

Cross section	p-values of χ^2 (in %)				
variables	POW+PYT (w. unc.)	$a\mathrm{N^3LO}$ (w. unc.)	MATRIX (w. unc.)	STRIPPER (w. unc.)	MiNNLOPS (w. unc.)
$p_\mathrm{T}(\mathrm{t})$	<1 (7)	<1 (<1)	84 (87)	4 (58)	55 (68)
$p_\mathrm{T}(\bar{\mathrm{t}})$	<1 (9)	—	71 (74)	17 (20)	47 (60)
$y(\mathrm{t})$	<1 (<1)	<1 (20)	8 (9)	7 (8)	17 (20)
$y(\bar{\mathrm{t}})$	<1 (<1)	—	13 (15)	<1 (<1)	2 (5)
$p_\mathrm{T}(\mathrm{t\bar{t}})$	<1 (35)	—	42 (90)	21 (85)	<1 (4)
$y(\mathrm{t\bar{t}})$	38 (67)	—	86 (87)	65 (72)	72 (73)
$m(\mathrm{t\bar{t}})$	55 (78)	—	51 (72)	61 (76)	94 (97)
$\lvert\Delta\phi(\mathrm{t},\bar{\mathrm{t}})\rvert$	40 (81)	—	<1 (98)	<1 (96)	25 (45)
$\lvert y(\mathrm{t})\rvert - \lvert y(\bar{\mathrm{t}})\rvert$	2 (23)	—	97 (97)	90 (91)	15 (28)
$p_\mathrm{T}(\mathrm{t})/m(\mathrm{t\bar{t}})$	<1 (<1)	—	60 (74)	38 (47)	9 (76)
$p_\mathrm{T}(\mathrm{t\bar{t}})/m(\mathrm{t\bar{t}})$	2 (66)	—	<1 (40)	<1 (37)	3 (76)
$\log(\xi_1)$	7 (23)	—	—	8 (11)	23 (27)
$\log(\xi_2)$	14 (47)	—	—	18 (26)	66 (71)

Table 45: The p-values are shown for the χ^2 tests of the measured absolute single-differential cross sections for $t\bar{t}$ and top quark kinematic observables at the particle level with respect to the POWHEG+PYTHIA 8 ('POW-PYT') simulation and the STRIPPER NNLO calculation. The χ^2 values are calculated taking only measurement uncertainties into account and excluding theory uncertainties. The p-values of the χ^2 tests including theory uncertainties are indicated with the brackets (w. unc.).

Cross section	p-values of χ^2 (in %)	
variables	POW+PYT (w. unc.)	STRIPPER (w. unc.)
$p_{\mathrm{T}}(\mathrm{t})$	<1 (7)	88 (97)
$p_{\mathrm{T}}(\bar{\mathrm{t}})$	<1 (11)	82 (97)
$y(\mathrm{t})$	<1 (5)	33 (34)
$y(\bar{\mathrm{t}})$	<1 (1)	43 (53)
$p_{\mathrm{T}}(\mathrm{t}\bar{\mathrm{t}})$	<1 (37)	<1 (35)
$y(\mathrm{t}\bar{\mathrm{t}})$	35 (78)	6 (11)
$m(\mathrm{t}\bar{\mathrm{t}})$	46 (80)	80 (94)
$\lvert\Delta\phi(\mathrm{t},\bar{\mathrm{t}})\rvert$	40 (85)	<1 (18)
$\lvert y(\mathrm{t})\rvert - \lvert y(\bar{\mathrm{t}})\rvert$	3 (23)	87 (91)
$p_{\mathrm{T}}(\mathrm{t})/m(\mathrm{t}\bar{\mathrm{t}})$	<1 (<1)	11 (28)
$p_{\mathrm{T}}(\mathrm{t}\bar{\mathrm{t}})/m(\mathrm{t}\bar{\mathrm{t}})$	1 (59)	<1 (51)
$\log(\xi_1)$	7 (35)	34 (35)
$\log(\xi_2)$	22 (67)	37 (39)

Table 46: The p-values are shown for the χ^2 tests of the measured absolute multi-differential cross sections for $\mathrm{t\bar{t}}$ and top quark kinematic observables at the parton level with respect to various fixed-order predictions. The χ^2 values are calculated taking only measurement uncertainties into account and excluding theory uncertainties. The p-values of the χ^2 tests including theory uncertainties are indicated with the brackets (w. unc.).

Cross section	p-values of χ^2 (in %)				
variables	POW+PYT (w. unc.)	$a\mathrm{N^3LO}$ (w. unc.)	MATRIX (w. unc.)	STRIPPER (w. unc.)	MINNLOPS (w. unc.)
$[\lvert y(\mathrm{t})\rvert, p_\mathrm{T}(\mathrm{t})]$	<1 (<1)	<1 (<1)	8 (10)	6 (10)	19 (19)
$[m(\mathrm{t\bar{t}}), p_\mathrm{T}(\mathrm{t})]$	<1 (<1)	—	2 (6)	5 (13)	4 (46)
$[p_\mathrm{T}(\mathrm{t}), p_\mathrm{T}(\mathrm{t\bar{t}})]$	<1 (6)	—	<1 (<1)	<1 (<1)	<1 (1)
$[m(\mathrm{t\bar{t}}), \lvert y(\mathrm{t\bar{t}})\rvert]$	<1 (<1)	—	<1 (<1)	<1 (<1)	<1 (<1)
$[\lvert y(\mathrm{t\bar{t}})\rvert, p_\mathrm{T}(\mathrm{t\bar{t}})]$	<1 (37)	—	<1 (<1)	<1 (<1)	<1 (4)
$[m(\mathrm{t\bar{t}}), p_\mathrm{T}(\mathrm{t\bar{t}})]$	<1 (<1)	—	<1 (<1)	<1 (<1)	<1 (<1)
$[p_\mathrm{T}(\mathrm{t\bar{t}}), m(\mathrm{t\bar{t}}), \lvert y(\mathrm{t\bar{t}})\rvert]$	<1 (2)	—	—	<1 (<1)	<1 (<1)
$[m(\mathrm{t\bar{t}}), \lvert y(\mathrm{t})\rvert]$	<1 (<1)	—	<1 (<1)	1 (1)	<1 (<1)
$[m(\mathrm{t\bar{t}}), \lvert \Delta\eta(\mathrm{t},\bar{\mathrm{t}})\rvert]$	<1 (<1)	—	<1 (<1)	<1 (<1)	<1 (7)
$[m(\mathrm{t\bar{t}}), \lvert \Delta\phi(\mathrm{t},\bar{\mathrm{t}})\rvert]$	<1 (<1)	—	—	<1 (<1)	<1 (<1)

Table 47: The p-values are shown for the χ^2 tests of the measured absolute multi-differential cross sections for $t\bar{t}$ and top quark kinematic observables at the particle level with respect to the POWHEG+PYTHIA 8 ('POW-PYT') simulation and the STRIPPER NNLO calculation. The χ^2 values are calculated taking only measurement uncertainties into account and excluding theory uncertainties. The p-values of the χ^2 tests including theory uncertainties are indicated with the brackets (w. unc.).

Cross section	p-values of χ^2 (in %)	
variables	POW+PYT (w. unc.)	STRIPPER (w. unc.)
$[\lvert y(t)\rvert,\ p_T(t)]$	<1 (3)	39 (45)
$[m(t\bar{t}),\ p_T(t)]$	<1 (<1)	<1 (4)
$[p_T(t),\ p_T(t\bar{t})]$	<1 (17)	<1 (<1)
$[m(t\bar{t}),\ \lvert y(t\bar{t})\rvert]$	<1 (<1)	<1 (<1)
$[\lvert y(t\bar{t})\rvert,\ p_T(t\bar{t})]$	1 (27)	<1 (<1)
$[m(t\bar{t}),\ p_T(t\bar{t})]$	<1 (<1)	<1 (<1)
$[p_T(t\bar{t}),\ m(t\bar{t}),\ \lvert y(t\bar{t})\rvert]$	<1 (3)	<1 (<1)
$[m(t\bar{t}),\ \lvert y(t)\rvert]$	<1 (5)	20 (23)
$[m(t\bar{t}),\ \lvert \Delta\eta(t,\bar{t})\rvert]$	<1 (<1)	<1 (2)
$[m(t\bar{t}),\ \lvert \Delta\phi(t,\bar{t})\rvert]$	<1 (<1)	<1 (<1)

Table 48: The p-values are shown for the χ^2 tests of the measured absolute single-differential cross
sections for lepton and b-jet kinematic observables at the particle level with respect to the POWHEG+PYTHIA 8 ('POW-PYT') simulation and the STRIPPER NNLO calculation. The χ^2 values are calculated taking only measurement uncertainties into account and excluding theory uncertainties. The p-values of the χ^2 tests including theory uncertainties are indicat ed with the brackets (w. unc.).

Cross section	p-values of χ^2 (in %)	
variables	POW+PYT (w. unc.)	STRIPPER (w. unc.)
$p_{\mathrm{T}}(\ell)$	<1 (9)	14 (14)
$p_{\mathrm{T}}(\ell)$ trailing/$p_{\mathrm{T}}(\ell)$ leading	9 (34)	86 (87)
$p_{\mathrm{T}}(\ell)/p_{\mathrm{T}}(\bar{\mathrm{t}})$	<1 (<1)	14 (32)
$p_{\mathrm{T}}(\mathrm{b})$ leading	85 (91)	61 (65)
$p_{\mathrm{T}}(\mathrm{b})$ trailing	46 (64)	78 (98)
$(p_{\mathrm{T}}(\mathrm{b}) + p_{\mathrm{T}}(\bar{\mathrm{b}}))/(p_{\mathrm{T}}(\mathrm{t}) + p_{\mathrm{T}}(\bar{\mathrm{t}}))$	<1 (<1)	7 (9)
$m(\ell\bar{\ell})$	<1 (2)	36 (40)
$m(\mathrm{b}\bar{\mathrm{b}})$	<1 (2)	<1 (<1)
$m(\ell\bar{\ell}\mathrm{b}\bar{\mathrm{b}})$	<1 (48)	66 (75)
$p_{\mathrm{T}}(\ell\bar{\ell})$	88 (97)	78 (96)
$\lvert\eta(\ell\bar{\ell})\rvert$	32 (77)	<1 (4)
$[\lvert\eta(\ell\bar{\ell})\rvert,\, m(\ell\bar{\ell})]$	<1 (22)	<1 (<1)
$[\lvert\eta(\ell\bar{\ell})\rvert,\, p_{\mathrm{T}}(\ell\bar{\ell})]$	7 (80)	<1 (12)
$[p_{\mathrm{T}}(\ell\bar{\ell}),\, m(\ell\bar{\ell})]$	1 (12)	<1 (<1)